# Crystal Engineering and Structural Solutions of Organic Molecular Materials

Chloe Jenine Pugh

Department of Chemistry, University of Liverpool

Thesis submitted in accordance with the requirements of the University of Liverpool for the degree of Doctor of Philosophy.

September 2018

Supervisor: Prof Andy Cooper

Co-supervisors: Dr Alexander Steiner

# *Abstract*

Organic molecular materials have been studied for decades, with a strong focus on their application within gas uptake and selective separations. Porous organic molecules can come in multiple forms, whether a discrete molecule such as a macrocycle or cage, or an infinite framework, such as a hydrogen bonded organic framework (HOF). In this thesis, we will examine the benefits of crystal engineering as an alternative route towards the formation of new organic molecular structures. The molecular structures discussed in this thesis include organic molecular cages, hydrogen bonded organic frameworks and organic co-crystals. Crystal engineering has been posed as an impressive method for the discovery of new materials, without the time costly effort of finding alternative precursors, or finding the best possible reaction conditions. There are multiple routes towards recrystallisation, which are suitable whether soluble or insoluble, which can be utilised to direct alternative crystal packing, hence, alternative functionality.

The dynamic nature of organic molecular cages, which are synthesised via reversible imine condensation reactions, is discussed in detail in chapter 2. **TCC1**$_{[3+6]}$, a trigonal prismatic cage underwent re-equilibration in solution to the truncated tetrahedron cage, stoichiometrically twice the equivalent, **TCC1**$_{[6+12]}$. The cage formation was optimised synthetically, and furthermore experimental observations were rationalised through computational analyses.

A series of organic molecular cages were synthesised via high throughput techniques using robotics, which were then fully characterised and their crystal structures determined. From this, a series of discoveries were made, including further illustration of re-equilibration in **C21**, from a [3+2] cage to a [6+4]. The formation of a new topology for **C18** was also discovered, a bridged catenane with a novel topology not previously seen in literature. High throughput methods were also used in Chapter 4. However as opposed to the modelling the potential structure *in silico*, as in Chapter 3, the cages were chosen based on precursors capable of hydrogen bonding or organic salt formation. We showed it is possible to synthesised porous co-crystals from small organics, and furthermore discuss the benefits of using a bespoke high throughput infra-red kit, capable of determining the isosteric heat of adsorption.

Porous structures by strategic design are also discussed in chapter 4, focusing on an alternative method using both crystal structure prediction (CSP) and energy-structure-function maps (ESFs) to increase the rate of porous material discovery. **T1** and **T2** are both triptycene-based hydrogen bonding tectons, which are capable of forming hydrogen-bonded organic frameworks. The ESFs enabled rationalisation of the experimental findings, and furthermore provided insight into the importance of hydrogen bond donors and acceptors through comparison of **T1** and **T2**.

# *Acknowledgements*

Firstly, I'd like to express my gratitude to my supervisor, Professor Andy Cooper, who without his support this thesis would not have been possible. I'd also to thank my research co-ordinators, Dr Marc Little, who has been by my side from day one patiently teaching me the art of crystallography. Dr Michael Briggs, another research coordinator, who has always shown patience, empathy and most of all someone who I could rely on to be brutally honest.

Work presented in this thesis would not have been possible without the following people: Dr Rebecca Greenaway, for all her time taken to synthesise precursors, as well as her guidance, Dr Ben Slater, for the synthesis of **T1** and assistance in TGA and DSC, Valentina Santolini, for the computational calculations, which were vital to multiple projects in this thesis, Dr Marc Little, for all his help and guidance in X-ray crystallography, Dr Michael Briggs, for helping to teach me HPLC and further develop a project and Dr Ben Alston for his continued input and guidance. I'd also like to mention Charlotte Smith, a truly amazing friend who has always been there when I needed her most.

I'd like to also thank my family, who have always encouraged me in every way, and my parents for encouraging me to believe in myself. And last, but in no way least, I'd like to write a heartfelt thank you to my amazing husband. Despite completing his own thesis many years ago (but not too many), he sat patiently many evenings reading through my own, giving me ideas for improvement, and always having a shoulder to cry on (more times than I care to admit).

# *List of Publications*

1. *Functional materials discovery using energy-structure-function maps, Nature*

Angeles Pulido, Linjiang Chen, Tomasz Kaczorowski, Daniel Holden, Marc A. Little, Samantha Y. Chong, Benjamin Slater, David P. McMahon, Baltasar Bonillo, ***Chloe Stackhouse***, Andrew Stephenson, Christopher M. Kane, Rob Clowes, Tom Hasell, Andrew I. Cooper and Graeme Day.

DOI: 10.1038/nature21419

2. *Structural water as an essential comonomer in supramolecular polymerization, Science Advances*

Shengyi Dong, Jing Leng, Yexin Feng, Ming Liu, ***Chloe J. Stackhouse***, Andreas Schönhals, Leanardo Chiapissi, Lingyan Gao, Wei Chen, Jie Sheng, Lin Jin, Zhenhui Qi and Christopher A. Schalley

DOI: 10.1126/sciadv.aao0900

3. *Cage Doubling: Solvent mediated re-equilibration of a [3+6] prismatic organic cage to a large [6+12] truncated tetrahedron, Crystal Growth and Design*

***Chloe J. Pugh***, Valentina Santolini, Rebecca L. Greenaway, Marc A. Little, Michael E. Briggs, Kim E. Jelfs and Andrew I. Cooper

DOI: 10.1021/acs.cgd.7b01422

4. *High throughput discovery of organic cages and covalently bridged catenanes using computational screening fused with automated synthesis*

Rebecca L. Greenaway, Valentina Santolini, Michael J. Bennison, Ben Alston, ***Chloe J. Pugh***, Marc A. Little, Marcin Miklitz, Edward G. B. Eden, Rob Clowes, Helen J. Cuthbertson, Anika Shakil, Heather Armstrong, Michael E. Briggs, Kim E. Jelfs and Andrew I. Cooper

DOI: 10.1038/s41467-018-05271-9

5. *The Simplest Supramolecular Helix*

Felix Hanke, ***Chloe J. Pugh***, Ellis Kay, Joshua Taylor, Stephen M. Todd, Craig M. Robertson, Benjamin Slater and Alexander Steiner

DOI: 10.1039/c8cc03295e

## *List of Abbreviations*

| | |
|---|---|
| OMCs | Organic molecular cages |
| POCs | Porous organic cages |
| MOFs | Metal organic frameworks |
| MOPs | Metal organic polyhedra |
| COFs | Covalent organic frameworks |
| HOFs | Hydrogen-bonded organic frameworks |
| WTW | Window-to-window |
| WTE | Window-to-edge |
| $\Delta S$ | Entropy |
| $\Delta H$ | Enthalpy |
| $\Delta G$ | Gibbs free energy |
| MIMS | Mechanically interlocked molecules |
| PET | Photoinduced electron transfer |
| MRI | Magnetic resonance imaging |
| TON | Turn over number |
| CCS | Carbon capture storage |
| BET | Brunauer-Emmett-Teller |
| $SA_{BET}$ | BET surface area |
| $SA_{Langmuir}$ | Langmuir surface area |
| DCC | Dynamic covalent chemistry |
| RDS | Rate determining step |
| VdW | Van der Waals |
| PXRD | Powder X-ray diffraction |
| SCXRD | Single crystal X-ray diffraction |
| EDA | Ethylenediamine |
| TFB | Triformylbenzene |
| HPLC | High performance liquid chromatography |
| Prep-HPLC | Preparative high performance liquid chromatography |
| NMR | Nuclear magnetic resonance |
| CC1 | Covalent cage 1 |
| CC3 | Covalent cage 3 |
| RCC3 | Reduced cage 3 |
| FTRCC3 | Formaldehyde tied reduced cage 3 |
| DCM | Dichloromethane |
| CHCl3 | Chloroform |
| MeOH | Methanol |
| EtOH | Ethanol |
| LCMS | Liquid chromatography mass spectrometry |
| DAD | Diode array detector |
| UV | Ultra-violet |
| EIC | Extracted ion count |
| MD | Molecular dynamic |

|  |  |
|---|---|
| DFT | Density functional theory |
| HTS | High-throughput screening |
| HT | High-throughput |
| IR | Infra-red |
| TFA | Trifluoroacetic acid |
| MAS | Magic angle spin |
| HSQCS | Heteronuclear single-quantum correlation spectroscopy |
| DLS | Diamond light source |
| ADP | Atomic displacement parameters |
| TTBI/T2 | Triptycenetrisbenzimidazolone |
| T1 | Triptycene-2,3,6,7,14,15-hexacarboxytriimide |
| T0 | Triptycene |
| DMAC | Dimethylacetamide |
| ESF | Energy structure function map |
| TGA | Thermogravimetric analysis |
| DSC | Differential scanning calorimetry |
| HTIR | High throughput infra-Red |
| CPOS | Crystalline porous organic salt |
| SMs | Starting materials |
| RMSD | Root-mean-square deviation |
| DMSO | Dimethylsulfoxide |
| TCCX | Terphenyl Covalent Cage X (X = 1 - 3) |

## *Colour Key*

|  |  |
|---|---|
| ● | Carbon |
| 🔵 | Nitrogen |
| 🔴 | Oxygen |
| 🟡 | Sulphur |

# *Contents*

## *Chapter 1: Introduction*

## *Chapter 2: Cage Doubling: Solvent Mediated Re-equilibration of a [3+6] Prismatic Organic Cage to a Large [6+12] Truncated Tetrahedron*

## *Chapter 3: The role of Crystallography in High-throughput Discovery in Organic Molecular Cages*

## *Chapter 4: Functional Material Discovery: By Strategic Design and High Throughput Screening*

## *Chapter 5: Materials and Methods*

## Chapter 6: Conclusions and Future Work

# Chapter 1

## Introduction:

# *1 Supramolecular Chemistry*

Supramolecular chemistry is the study of ‘chemistry beyond the molecule', focusing on a system which is composed of assembled molecular units, as opposed to ‘traditional’ chemistry, which focuses on a single molecule.[1,2] In 1987 Lehn, Cram, and Pedersen were awarded the Nobel Prize for their seminal work in this area of chemistry.[3] Supramolecular chemistry is heavily influenced by thermodynamics, as self-assembled structures are typically held together by weak non-covalent interactions; consequently entropy and enthalpy play an important role in the systems.[4,5] For example, due to the weak non-covalent interactions there is only a small activation energy barrier to overcome to ‘break apart’ the supramolecular assembly. Therefore, the systems are typically under thermodynamic control.[6]

The driving force of supramolecular chemistry is heavily influenced by the thermodynamics of the system, for example, when a hydrated metal undergoes complexation, coordinated water is released in a process that is entropically favourable, hence, driving equilibrium towards the formation of complex molecules.[7] Guest binding in host guest complexes (section *1.1.2*) is driven by both enthalpy ($\Delta H$) and entropy ($\Delta S$), with a negative shift of $\Delta S$ upon binding, but a gain in the enthalpy, due to the formation of an energetically favourable system.[8] Leung et al. synthesised a metal-organic cage comprised of 4 metals and 6 ligands ($M_4L_6$), which was capable of supramolecular encapsulation.[9] In that study, they demonstrated that enthalpy-entropy compensation was the driving force for guest encapsulation through solvent reorganisation, whereby the entropy was negatively impacted, however this was overcome by the preferential enthalpy of complexation.

Self-assembly (section 1.1.1) is the formation of one molecule from multiple components without any intervention, such as the formation of the hydrogen bonded helical structure, DNA.[10] This process is reliant on enthalpy, as this has a negative impact on the entropy.[11] Self-assembly is a spontaneous process; if we consider $\Delta G$, $\Delta S$ becomes more negative, as the total number of components is reduced, therefore, the enthalpic gain, $\Delta H$, must be greater than the combined terms $T\Delta S$.[26] Therefore, self-assembly is an exothermic process where heat is released from the system, with the main influence of self-assembly reducing the overall energy of the system.[12]

$\Delta S$ is a property of a thermodynamic system, whereby it can be loosely defined as a measure of disorder in a system, therefore, as supramolecular complexes are composed of a large numbers of discrete molecules, $\Delta S < 0$. $\Delta H$ is the quantity equivalent to the total heat content of the system, equal to the internal energy plus the product of the total pressure and volume.[13] Hence, assemblies tend to be considered thermodynamically favourable according to Gibbs free energy $\Delta G$ when the term $\Delta H < T\Delta S$: $\Delta G = \Delta H - T\Delta S \leq 0$. In order for a reaction to be spontaneous, $\Delta G$ must be $\leq 0$. Hence enthalpy, $\Delta H$, and entropy, $\Delta S$, are governing factors in supramolecular chemistry and the formation of large assemblies.

## *1.1 Concepts within Supramolecular Chemistry*

### *1.1.1 Molecular Self-assembly*

By definition, molecular self-assembly is when an assembly self-constructs without any external influence.[14,15] Self-assembly is a useful tool for the construction of larger molecules, as well as the design of functional molecules based on the understanding of intermolecular interactions.[16] Self-assembly has been seen from both synthetic experiments, for example micelles and surfactants, and in nature, such as the double helix formed in DNA through hydrogen bonding.[17–20] Self-assembly is a principle factor in crystal engineering (section 5), whereby structure-property relationships can be better controlled by design based on the understanding of intermolecular interactions in a crystal structure.[11,21,22] This could be achieved by various methods, for example, by attempting to disrupt the $\pi$–$\pi$ or hydrogen bonding interactions between molecules through the use of solvent.[23–25]

### *1.1.2 Molecular Recognition and Complexation*

Host-guest interactions can be used to bind a specific guest to a host molecule.[26] The thermodynamic driving force of complexation is the overall reduction of Gibbs free energy in the system.[27] In host-guest chemistry, $S < 0$ and the process is enthalpically favoured. The first demonstration of host-guest chemistry was in 1967 by Pedersen and co-workers, who showed that a larger 'crown' shaped system could behave as a host to smaller species, for example a smaller metal cation.[28] The first crown ether, dibenzo-18-crown-6, is an 18 atom heterocycle (**Figure 1**), which can contain a cation guest such as potassium or sodium.[29]

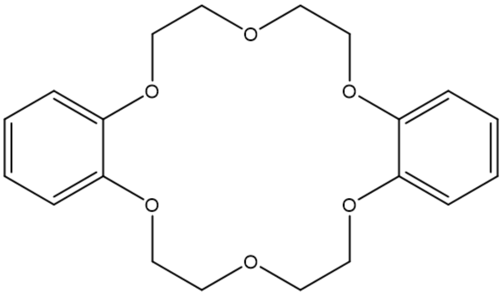

**Figure 1** Dibenzo-18-crown-6, the first reported crown ether with a diameter of 2.6–3.2 Å.[29]

Host-guest chemistry is commonly seen in enzymatic catalysis, a process whereby the rate of a chemical reaction can be increased by the active site of a protein, commonly referred to as a 'lock and key' reaction.[30] Synthesised cyclodextrins exhibit the same behaviour.[31] The most common method of binding in a host-guest system is through hydrogen-bonding, a strong non-covalent bond.[32–34] Hosts can be fine-tuned in order to selectively uptake a specific guest, improving the selectivity for specific anions or other hydrogen-bonding guests.[35,36] Host-solvent interactions can inhibit the formation of a host-guest complex. This can be overcome through the use of non-competitive solvents i.e., avoiding solvents which can form either hydrogen-bonds with the host, or $\pi$–$\pi$ stacking.

### *1.1.3 Templated-Directed Synthesis*

Template-directed syntheses occur by using a reversible, non-covalent species to pre-organise a system for chemical reaction, this differs from molecular recognition as the product will typically contain one or more covalent bonds, whereas in host-guest chemistry the interactions are non-covalent.[37] The reactants are 'held together' by the templating atom or molecule, which facilitates the reaction. [38] Pre-organisation in a reaction can result in fewer side reactions, avoid formation of undesired by-products, and promote the formation of the desired molecule.[39] This approach can be used for the synthesis of a variety of materials including rotaxanes, macrocycles, catenanes, and core-shell particles.[40–44]

### *1.1.4 Mechanically Interlocked Molecules*

Mechanically interlocked molecules (MIMs) are molecular species that interlock; these mechanical bonds allow the formation of new and interesting topologies and functionalities. Examples include, but are not limited to, catenanes[45], molecular knots[46], Borromean rings[47] and rotaxanes[48]. MIMs can be synthesised using templating methods, or through the use of alternative reaction conditions, for example the addition of an acid catalyst.[49,50] These interlocked molecules are thermodynamically stable, for example Hasell et al. demonstrated that an organic molecule cage (OMC) re-equilibrates to a triply interlocked catenane, a more thermodynamically stable species.[50] Shown in **Figure 2** are simplistic topological models of two MIMs, **2A** shows a catenane, composed of two rings which interlock. **2B**, shows a Borromean ring topology in which the three 'rings' interlock with one another to form this complex topology.

These materials can be synthesised through a variety of methods, including self-assembly,[51] template-directed synthesis,[52] and crystal engineering.[53] MIMs have been utilised in multiple fields, such as catalysis, porous materials, molecular machines, and molecular sensors.[52,54–56]

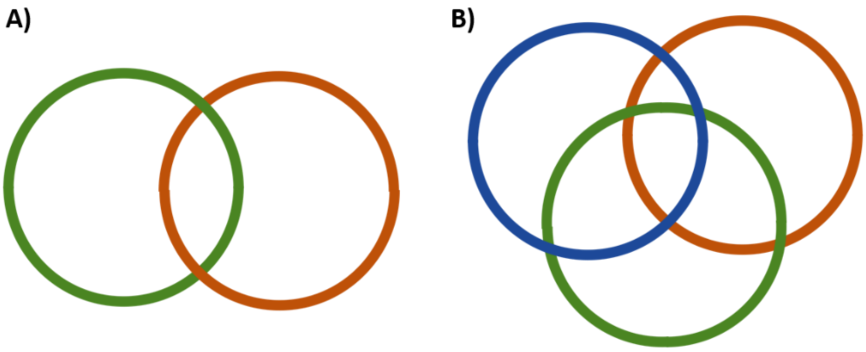

**Figure 2 A)** Two rings illustrating a catenane; **B)** A Borromean ring topology

### *1.1.5 Molecular Machinery*

Molecular machines are materials which have the ability to perform quasi-mechanical movements when responding to stimuli.[57] This emerging field was awarded the Nobel Prize for Chemistry in 2016, based on the significant advances it has made in the field of chemistry. The research into molecular machinery has grown significantly since the initial example of catenane synthesis via templation by Jean-Pierre Sauvage in 1983, who showed a catenane structure, which inspired future work.[58] Following this, in 1991 Stoddart showed it was possible to generate a molecular shuttle using a rotaxane.[59] The third recipient, Ben L. Feringa showed a light-driven molecular rotor.[60] Molecular machines are currently in the early stages of development, however they show incredible promise as new materials for molecular sensors and information storage and processing.[61–64]

## *2 Applications of Supramolecular Chemistry*

For over 50 years the field of supramolecular chemistry has gone through a significant evolution, we have already mentioned a few of the fields in which it has developed leading into multiple sub-categories.[65] Here we will discuss some of the categories in which supramolecular chemistry has influenced research, and furthermore illustrate the substantial impact it holds within the scientific community.

### *2.1 Sensing*

In the early to mid-1990's de Silva was one of the first chemists to highlight chemical sensing, taking advantage of fluorescence responsive host-guest chemistry, leading the field in optical sensing. This ground-breaking concept was demonstrated using crown ethers with a fluorophore, which was able to display photoinduced electron transfer (PET).[66–68] As well as optical sensing, chiral sensing has been demonstrated using circular dichroism for secondary alcohols.[69] This was achieved by using a dynamic multi-component assembly for reversible binding, which has since been termed 'supramolecular analytical chemistry'.[70] As well as examples in research, supramolecular sensing is currently being used in medicinal applications. James et al.

developed a system utilising PET, which could more accurately determine blood glucose levels than previous methods in intensive care patients.[71–73]

## *2.2 Molecular Imaging*

Molecular imaging allows us to visualise cellular function in living organisms without disturbing them, and a well-known example of this is magnetic resonance imaging (MRI).[74] Hmaichi et al. introduced rotaxanes that were built on fluorescent probes and attached to anionic receptors; these are considered to be the first example of artificial receptors and chemosensors.[75] Further from this, Smith et al. developed a more stable squarine rotaxane, which is currently in preclinical trials (**Figure 3**).[76–78] Hydrogels and hydrogelators have also been developed for biomaterials within the field of molecular imaging.[79–81] Most notably, the improvement of molecular imaging is enhancing current chances of detecting cancer, through both recognition and improvement of current technologies.[82,83]

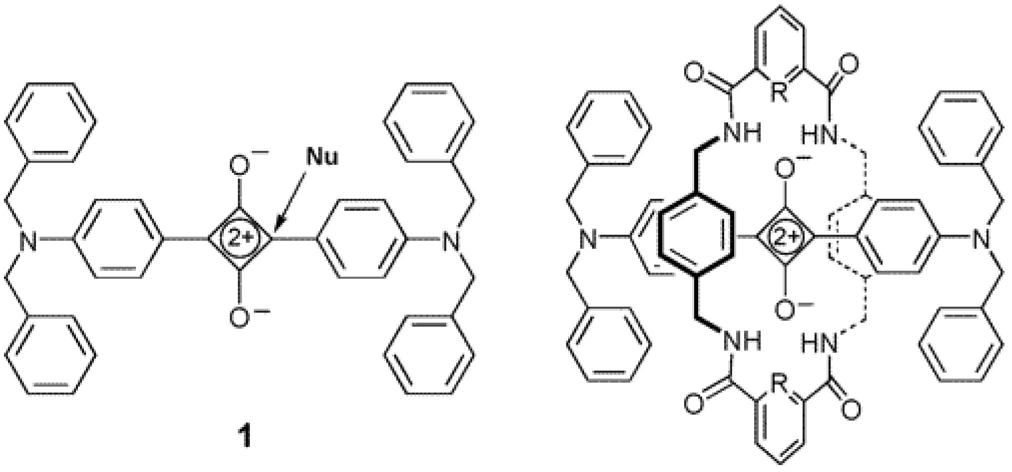

**1**

**2** R= CH
**3** R = N

**Figure 3** Squarine rotaxane used in research by Smith et al. Reprinted with permission from *J. Am. Chem. Soc.*, 2005, **127**, 3288–3289. Copyright 2005 American Chemical Society.

## *2.3 Drug Formulation and Delivery*

Improvement of drug delivery would enable researchers to improve current pharmaceuticals by creating a material which can be selectively released at the targeted area.[84] Areas of supramolecular chemistry which could have great potential within this application include host-guest complexes such as curcubit[*n*]urils (monomer and curcurbit[7]uril shown in **Figure 4**)[85] and macrocycles, as well as hyper-branched polymers.[86–89]

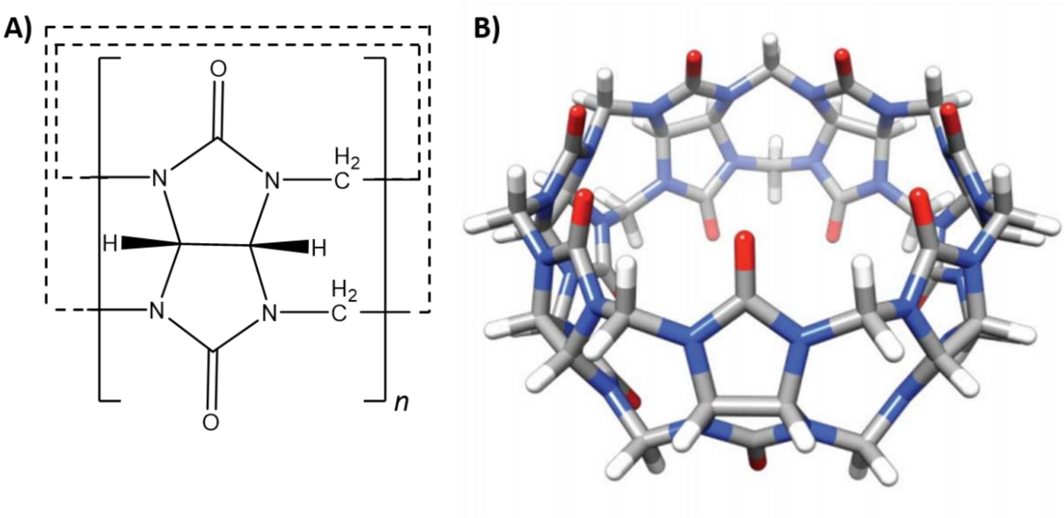

**Figure 4 A)** Curcubit[*n*]uril monomer, with n representing the number of monomers present in each macrocycle. The monomer is a glycoluril linked with methylene bridges; **B)** Curcurbit[7]uril, taken from reference 87, with permission from The Royal Society of Chemistry.[85]

Research is growing significantly in the area of supramolecular materials for drug discovery, particularly for potentially terminal illnesses such as cancer and AIDS/HIV. Despite decades of research, these illnesses are still proving difficult to treat, and the current medication used has extensive side effects making the patient extremely uncomfortable.[90–94] Dai et al. showed in 2007 that by using carbon nanotubes, it was possible to efficiently load and deliver drugs effectively. This was controlled through pH, while the strength of the $\pi$-stacking in the aromatic molecules can be varied through the diameter of the nanotube, therefore, the materials can be fine-tuned for this purpose.[95] Other researchers have demonstrated that it is possible to induce cancer cell death by intracellular self-assembly of an enzyme-responsive supramolecular gelator.[96] This method of cytotoxicity to the cancer cell would reduce these unwanted side-effects further, targeting the cancer directly.

### 2.4 Catalysis

By utilising host-guest chemistry, supramolecular molecules have been emerging as successful catalysts which are, in some examples, capable of out-performing the current catalysts commercially available, as the host can be tailor-made for a specific reaction.[85,97,98]

Curcurbit[*n*]urils have been proven to be successful materials for many applications, including catalysis. As well as high turn-over numbers (TONs), one particular example which involved a curcubit[6]uril acting as a protecting agent for palladium nanoparticles afforded high yields in reactions, as well as effective catalyst recovery after several reactions.[99]

These examples, which are only a drop in the ocean of the number of ways in which supramolecular science is evolving chemistry, illustrates the vast number of areas in which this field impacts us; from the future of medicine to the improvement of computational technology.

## 3 Porous materials

A porous material is one which contains a guest accessible pore, or void. These can be crystalline or amorphous, comprised of a framework, or discrete molecules. These materials are capable of gas or liquid uptake and storage. Porous materials are well-researched in areas such as the capture of greenhouse gases, toxic materials, and gas separations.[28,100]

One of the most pressing issues of our age is controlling the release of greenhouse gases, or their effective removal from the atmosphere, to decrease the current rate of global warming. Global warming effects everyone, whether from rising sea-levels, more dramatic and extreme weather or reduced crop growth and yields for basic food sources such as rice and wheat.[101–108] Utilising porous materials which are selective to gas uptake has proven to be a suitable method, with one of the most well-known methods being carbon-capture and storage (CCS) for the effective removal of $CO_2$ from the atmosphere, as well as selective methane capture and storage.[109–113]

Gaseous toxic materials in the atmosphere can have significant health impacts on the population, for example only small amounts of carbon monoxide, CO, can be fatal if inhaled, with only 1,600 ppm, or 0.16%, of total air volume within a confined space resulting in death within 2 hours.[114] Porous materials can be applied to both the sensing of CO, and it's effective removal removing the risk of unpleasant symptoms associated with exposure or potential fatality.[115–117] Formaldehyde presents a risk of cancer in humans through constant exposure, and those most at risk are people who are regularly exposed.[118–121] Formaldehyde is used in a number of industries including building materials and household products such as paints, disinfectants, and germicides. Not only can we effectively remove formaldehyde from the atmosphere, porous materials can chemically react with formaldehyde, removing the risk of exposure and removing the risk factors.[122,123] Toxic materials which are present as either volatile liquids or gases are considerably more high risk to the general population, hence the development of more porous materials with similar functionality to safely remove these is vital.[124]

By nature, gases are incredibly difficult to capture and separate. Therefore by creating materials which are capable of 'sieving' a mixture selectively enables us to safely capture selected gases, using them for other processes such as using $H_2$ for clean energy, or safely disposing of them through secondary reactions.[125,126] Although nuclear energy is generally accepted as a cleaner energy source when compared with other sources such as coal or oil, there are still unwanted by-products, for example dangerous gases such as radon.[127] Typically, waste gases from the nuclear industry include xenon, radon and krypton which have a very similar atomic radii. These gases are typically observed only in very low concentrations, therefore selectivity is key for their separation.[128] Literature already shows that we can selectively separate these gases, and furthermore utilise them for future purposes. For instance xenon has been used in satellites and to etch surfaces.[129–133]

Porous materials come under three different classifications (**Table 1**), micro-, meso- and macro-porous. Framework materials and discrete porous materials tend to fall under the microporous range, however some larger ones will fit into the lower end of mesoporous.[134,135] Microporous materials can be polymeric, amorphous, and/or crystalline.[136–138] Applications of these smaller pore materials include methane storage, small molecule and gas separations.[139–141] Mesopores cover a wide range, from 2 to 50 nm, meaning applications vary greatly from catalysis to microelectronics.[142–144] Macroporous materials are commonly seen in the fuel industry for catalytic cracking of hydrocarbons, as well as for Fischer-Tropsch reactions for the conversion of $H_2$ and CO to hydrocarbons.[145–147] As macropores have a pore similar in diameter to the wavelength of light, they can be applied within photocatalysis, for example the degradations of NO under UV light.[148]

**Table 1** IUPAC defined categories of porosity.

| **Microporous** | **0.2–2.0 nm** |
|---|---|
| **Mesoporous** | 2–50 nm |
| **Macroporous** | 50–1000 nm |

Researchers have been attempting for years to synthesise materials capable of improved gas uptake, requiring less material for significant guest uptake. There is a plethora of literature showing the impressive capabilities of materials ranging from a wide range of discrete molecules to framework materials. Metal organic frameworks (MOFs) are possibly one of the most well-known porous materials, and an example of a discrete porous material are porous organic cages (POCs).[149] In 2015 the first ever porous liquid was reported, synthesised using porous organic cages dissolved in a bulky solvent incapable of entering their intrinsic void.[150] Discrete porous materials have two distinct types of porosity, intrinsic and extrinsic.

**Intrinsic**: The void which exists inside the molecule, the molecular structure of the discrete molecule generates the intrinsic porosity *i.e.*, a void within the molecule. Examples include curcubit[*n*]urils and cages.

**Extrinsic**: The void space which exists between the discrete molecules, inefficient crystal packing of the materials encourages the formation of extrinsic voids. Examples include framework materials such as HOFs and COFs.

## *3.1 Framework Materials*

Framework materials are well studied in the field of host-guest chemistry, gas storage, separations, and catalysis. These materials can be either 1-, 2- or 3-dimensional, depending on the network throughout the system.[151] Frameworks are well-known, established molecular architectures, with their initial discovery made in 1756, the first reported zeolite.[152] These materials occur naturally, and have since been developed synthetically for specific uses. Well-known uses of zeolites include molecular sieves in chemical synthesis for removal of water, use in catalysis including hydrocracking, and even in surfactants to aid in the removal of $Ca^{2+}$ from hard water sources.[153–155]

### *3.1.1 Metal Organic Frameworks*

The first permanently porous Metal Organic Frameworks (MOFs) was published in 1999 by Yaghi.[156] MOFs are hybrid materials, composed of organic ligands co-ordinated to metal clusters, generating an infinite framework material which remained open when evacuated.

MOFs are synthesised using bridging organic ligands which are coordinated to metals, forming infinite framework structures[157] The size of the pores in MOFs can be determined by the length of the ligand linker used i.e., the longer the linker, the larger the pore. As with other open frameworks, when the pores are evacuated they are prone to collapse. MOFs have started to be developed for proton conduction, an important development for fuel cell technology.[158]

### *3.1.2 Covalent Organic Frameworks*

Comparatively, covalent organic frameworks (COFs) are a relatively new framework material with fewer examples by comparison to MOFs. These framework materials only contain organic elements within them, relying on the formation of rigid covalent bonding throughout the system.[159]

The first well-ordered COF, which formed a crystalline hexagonal layered structure, was reported in 2005 by Yaghi, which was synthesised using hexahydroxytriphenylene and phenyldiboronic acid.[160] The synthesis of the material took advantage of the rigidity of the boroxonate ester linkage, resulting in a COF with a large pore diameter, corresponding to a potentially mesoporous material.[161,162] The COF was found to have a high thermal stability, maintaining its structure at temperatures reaching 600 °C.

This initial work presented the possibility of crystalline, mesoporous organic frameworks. From this ground-breaking discovery, the number of reported COFs has increased significantly, with both two and three-dimension structure, and applications within both gas storage and separation, as well as catalysis.[163–165] More recently, the Yaghi group. reported two COFs which were synthesised through irreversible synthesis, using nucleophilic substitution reactions.[166] Typical COF syntheses are performed under reversible conditions, this work showed it was possible through reticular design to achieve a crystalline COF under irreversible conditions.

### *3.1.3 Hydrogen-bonded Organic Frameworks*

Finally, the most recent development in framework materials is the hydrogen-bonded organic framework (HOF). These frameworks are comprised of individual hydrogen-bonding building blocks, or tectons, which interact with one another forming a supramolecular assembly. HOFs are an exciting material for several reasons, one of which is the ease of structural elucidation via single crystal X-ray diffraction. Compared with their counterparts, HOFs have improved solubility, as a result more crystallisation methods are accessible.[167] They can have a high thermal stability, in some cases up to 300 °C, comparatively COFs can show a thermal stability in temperatures up to 600 °C, however covalent bonds are much stronger therefore this would be expected.[160,168]

HOFs can be fine-tuned for host-guest chemistry, by using a tecton of a specific size, the pore can be tailored to the desired guest.[34] Activation of the material, i.e., the removal of the guest from the pore, is typically done at relatively low temperatures, but this is also dependent on the guest and the strength of the intramolecular interactions.[169] Unless there is a strong interaction between the guest and the host, the activation and reactivation of HOFs is a low energy consuming process, due to the low temperatures required for complete evacuation.[170] The typical approach to this is to place the material in a vacuum oven at lower temperature, typically around 40–50 °C for around 24 hours.[171]

Proton conduction has been hailed as the most promising technology for clean and efficient power generation, prompting the discovery of more materials capable of such a mechanism.[172] Other framework materials have been shown to exhibit proton conduction through hydrogen bonding, which led to theories surrounding HOFs applications in this area.[173,174] Current examples in the field of proton conduction including MOFs, which exhibit this phenomena through mediation of hydrogen bonding in the existing framework.[175,176]

## *3.2 Discrete Porous Materials*

A discrete porous material is one in which the molecular species are independent of one another, comparatively a framework is an infinite and extending structure. Discrete porous materials are beneficial, as they are solution processable, i.e. improved solubility compared with non-discrete materials.[177] **Figure 5** shows a simplified illustration of a discrete porous material, where each square is representative of a discrete molecule with an intrinsic pore. For a material to be permanently porous, it must be shape persistent, i.e., when the pores are evacuated, the molecule remains ‘open’. The schematic illustrates three potential outcomes from desolvation, route A shows desolvation or guest removal leading to an amorphous material. There is potential however that this amorphous material may still be porous. Route B shows desolvation leading to the loss of the extrinsic pore, the intrinsic pore would still be accessible, so porosity would be maintained. Finally, route C shows the ‘ideal’ result, which is that the intrinsic porosity is retained and the material has permanent porosity.[100]

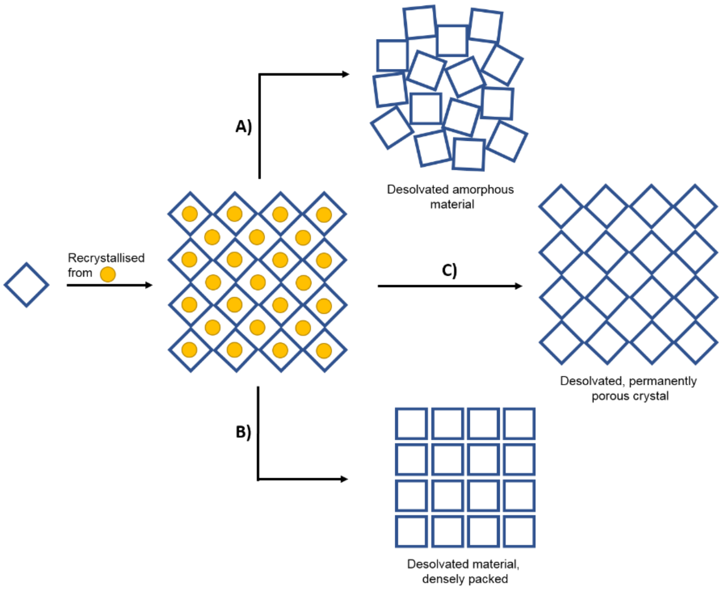

**Figure 5** Routes A, B, and C represent potential outcomes after desolvation for intrinsically porous materials.[100]

### *3.2.1 Macrocycles*

A macrocycle is a cyclic material, containing more than 12 atoms.[178] Macrocycles have been studied for several applications, including porosity. Macrocycles can be functionalised for the recognition of particular guests to be held within the macrocycle.[179,180]

Macrocycles also exist in nature, for example the enzyme inhibitor Pacritinib, which has also been successfully synthesised in a laboratory environment.[181,182] Macrocycles have been reported since the 1950s and are a well-studied field, encompassing 'sub-categories' of other materials such as curcurbit[*n*]urils and pillar[*n*]arenes. These materials have applications in medicine as building blocks for larger structures and host-guest complexation.[183–186] Macrocycles cover a larger family, some examples are discussed below in more detail.

### *3.2.2 Pillar[n]arene*

Pillar[*n*]arenes were first reported in 2008 by Ogoshi, who noted that these initial cyclic structures did not exhibit the 'tilt' seen in other cyclic structures, and instead these molecules form symmetrical cylinder structures, as opposed to a 'basket' structure.[187] **Figure 6** shows a pillar[5]arene used for host-guest complexation which shows the cyclic nature of these structures.[188] This particular example formed infinite 1-dimensional channels which were able to host a bispyridinium salt in a 1:1 ratio.

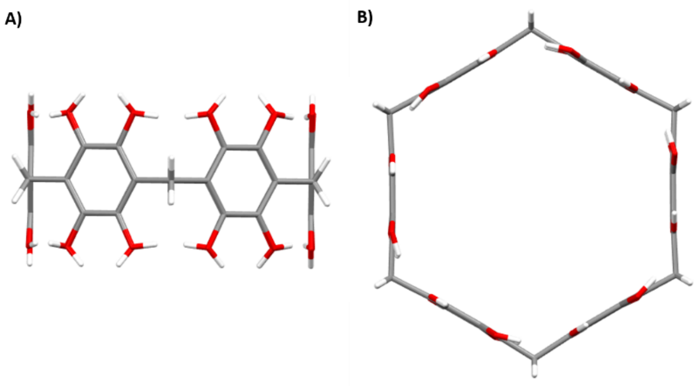

**Figure 6 A)** Sideways view of the pillar[5]arene; **B)** A ‘top-down’ view, showing the absence of any tilt in the molecule.

Pillar[*n*]arenes are synthesised from a hydroquinone monomer (**Figure 7A**), forming the cylindrical structure (**Figure 7B**). The structure was presented as a potential new host for host-guest chemistry, alongside the ability to functionalise the reactive hydroxyl groups improving possibilities of molecular recognition.[189]

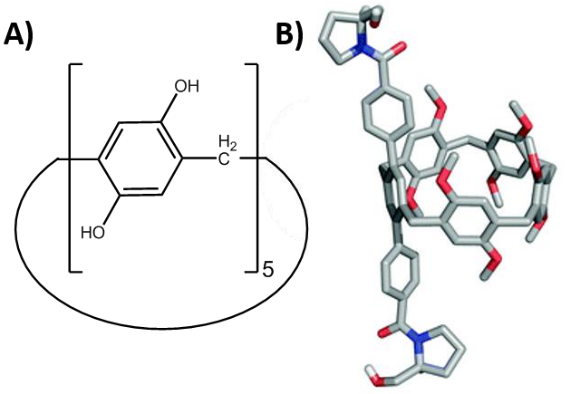

**Figure 7 A**) Chemical representation of the methylene bridge and repeating unit; **B**) A crystal structure reproduced from N. L. Strutt, H. Zhang and J. F. Stoddart, *Chem. Commun.*, 2014, **50**, 7455 with permission of The Royal Society of Chemistry.

The pillar[5]arene's high surface area of 400 $m^2g^{-1}$ provides a large enough intrinsic pore for the longer chained alkane, propane, and showed selectivity for these over methane. Tailoring the size of the pore to the size of the guest promotes thermodynamic selectivity and furthermore highlights the importance of tuning in host-guest chemistry.

### *3.2.3 Curcurbit[n]urils*

Cucurbit[*n*]urils are cyclic molecules which are synthesised from glycoluril monomers linked together with a methylene bridge. **Figure 8A** shows a cucurbituril Q5 (purple) published in 2002, with disordered solvent within the pore of Q5.[190] **Figure 8B** shows a smaller cucurbituril Q5 (red) sat inside of the larger Q10 curcurbituril (purple), which is capable up chloride uptake (represented by the gold sphere), with $Cs^+$ neutralising the charge.[191] Cucurbit[*n*]urils are partially enclosed, due to the tilting of the edges inwards. In 2013 the largest cucurbit[*n*]uril was synthesised comprising of 14 methylene bridges, with an internal cavity of 870 Å$^3$.[192]

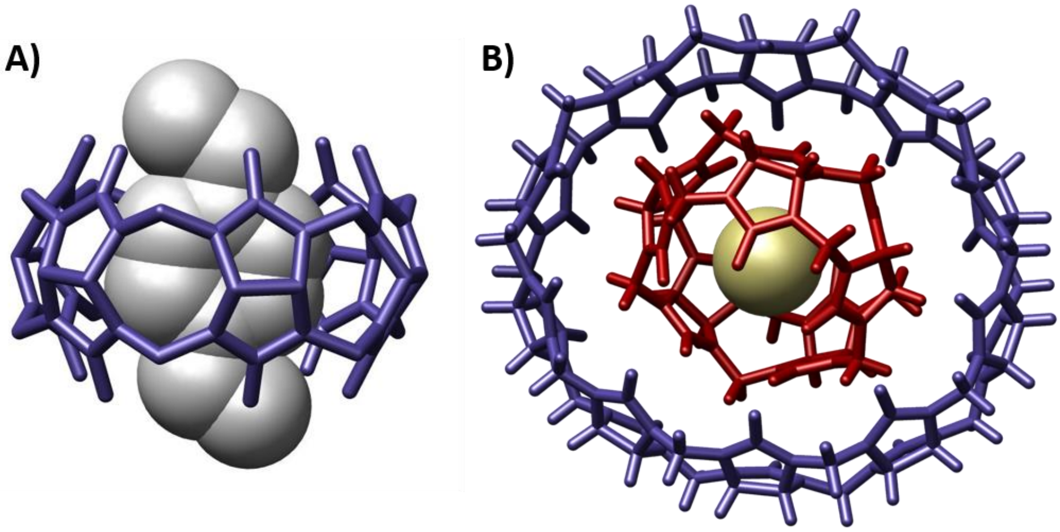

**Figure 8 A**) A macrocycle comprised of 5 methylene bridges, with toluene sitting inside the host; **B**) A more recent development, a smaller cucurbituril, Q5, sitting inside the larger Q10, with Q5 hosting a chloride ion.

### *3.2.4 Metal Organic Polyhedra*

Metal Organic Polyhedra (MOPs) form three-dimensional structures, which can pack together to form networks between the cage structures. MOPs are synthesised using principles from self-assembly, containing a metal ‘corner’ which is coordinated to ligands, whose angles control the geometry of the cages. Restrictions with topology arise from the angle and number of coordination sites of the metal used, therefore only a low number of structures can be theoretically synthesised. These cages are typically synthesised in solution at higher temperatures, using solvents such as dimethylformamide (DMF), dimethoxyethane (DME) or $H_2O$ and under an inert atmosphere.[193–195]

MOPs are a fairly new material, with much of the progress occurring within the last two decades. They have shown promise for application in a wide number of fields including bio-medical applications, catalysis, molecular sensing, and gas adsorption and separation.[196–202] In order to be applied within any of these fields, MOPs must be effectively desolvated i.e., the solvent from the reaction removed from the intrinsic pore. This requires a MOP which is architecturally robust enough to withstand removal of guests and maintain the pore. One example from Yaghi et al. highlighted a permanently porous MOP, which was desolvated under vacuum at ambient conditions in order to obtain materials with a BET surface area ($SA_{BET}$) up to 424 $m^2g^{-1}$ (**Figure 9**).[203]

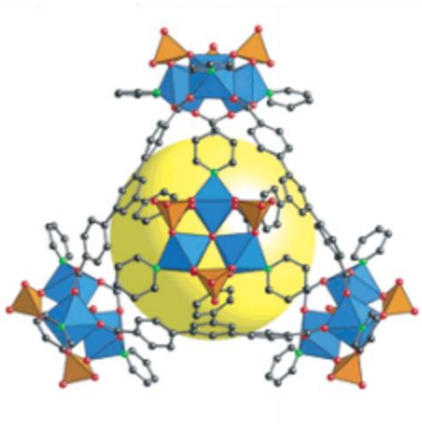

**Figure 9** MOP 54, permanently porous with a $SA_{BET}$ of 424 $m^2g^{-1}$. Reprinted with permission from A. C. Sudik, A. R. Millward, N. W. Ockwig, A. P. Côté, J. Kim and O. M. Yaghi, *J. Am. Chem. Soc.*, 2005, **127**, 7110–7118. Copyright 2005 American Chemical Society.

MOPs can form impressively large species, for example the largest to date was published by Fujita et al., who showed through X-ray diffraction studies a $M_{30}L_{60}$ MOP was synthesised and isolated.[195] Another impressively large $M_{18}L_{24}$ MOP was synthesised using 18 palladium ions and tris(4-pyridyl) ligands coordinating the metals. In 2016, a MOP (**Figure 10**) was reported with the stoichiometry $M_{30}L_{60}$ and a cage diameter of 8.2 nm.

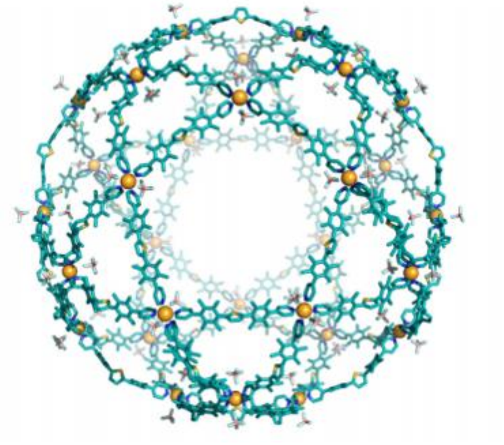

**Figure 10** Reprinted from Chem, Volume 1 Edition 1, Daishi Fujita, Yoshihiro Ueda, Sota Sato, Hiroyuki Yokoyama, Nobuhiro Mizuno, Takshgi Kumasaka, Makoto Fujita, Self-Assembly of $M_{30}L_{60}$ Icosidodecahedron, Pages No. 91 - 101, Copyright 2016, with permission from Elsevier.

## *4 Organic Cages*

### *4.1 Crystal Structure and Packing*

By IUPAC definition, a cage is a "polycyclic compound with the shape of a cage".[204] Unlike MOPs, organic cages contain no metals for coordination. Organic Molecular Cages (OMCs) are discrete molecules, which contain windows creating a network throughout the crystal structure. The cage windows allow guest access, and the packing between the cages, i.e. window to window (WTW), or window to edge (WTE), determines whether a porous network will be formed. Two potential routes to cage formation are via reversible or irreversible routes, which have a significant influence on the yield of the product. These materials are still in their infancy, however their impact has been impressive.[205]

When organic cages were initially reported, they were highlighted as new materials with remarkable potential for gas adsorption and molecular separation.[206–208] Further research has shown that these materials are in fact capable of much more; including as catalytic hosts for selective syntheses and potential applications in nonlinear optics for telecommunications and optical storage.[209,210]

Illustrated in **Figure 11A** and **11B** is the covalent cage **CC3** published by the Cooper group in 2009, which formed a 3D-network from synthesis (**Figure 8C**).[206] Cages can pack either WTW or WTE, which determines the diffusion pathway of guests in the network. The connectivity is influenced by steric hindrance arising for the bulky cage vertices, which pack together to form WTW interactions. For **CC3** pictured in **Figure 11**, a diamondoid network runs through the cage structures, allowing diffusion of guests which have a smaller radii than the cage windows. The crystal structure in **Figure 11C** packs in the Cubic space group $F2_13$, with all 4 windows showing WTW interactions.

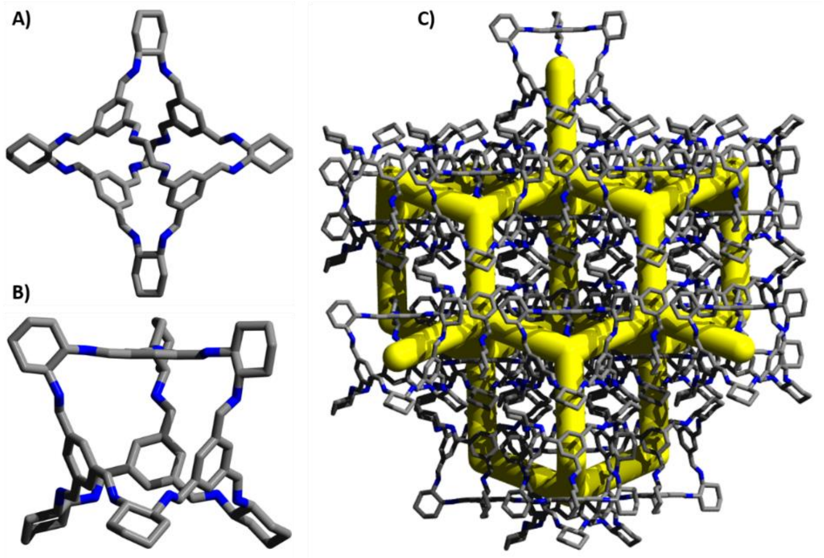

**Figure 11 A**) Molecular covalent cage **CC3**; **B**) Showing the window of **CC3**; **C**) Diamondoid network in the crystal structure of **CC3**$\alpha$.

POCs are inherently chiral, determined by the direction of the cage vertices shown in **Figure 12**. If the cage imine linkers turn to the left the cage is *S*-, and to the right *R*-. WTW packing of cages can be encouraged through chiral recognition.[211] If two racemic cages are recrystallised together, i.e. **CC3**-*R* and **CC3**-*S*, then the *R*- and *S*- windows will preferentially pack WTW. Chiral recognition can influence the packing of the materials, allowing us to influence the crystal packing and encourage WTW packing through racemic co-crystallisations. Chiral cages have also been shown to be effective in the separation of small chiral molecules.[212,130]

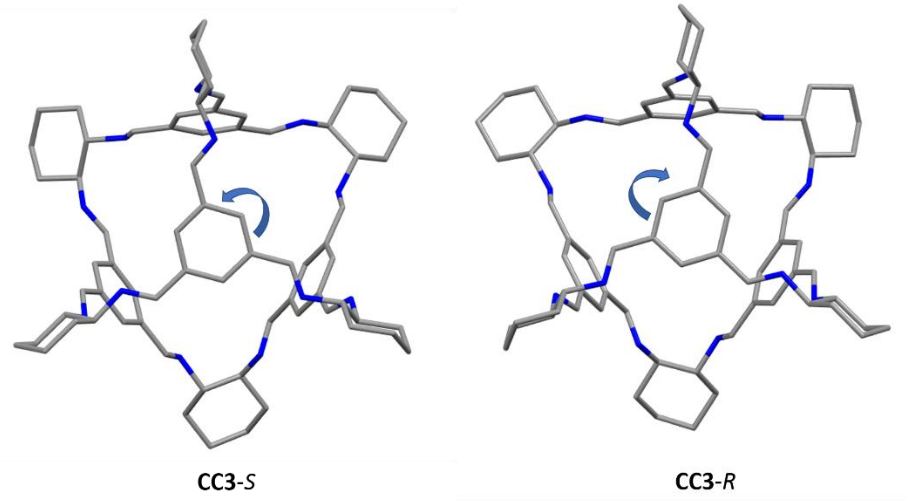

**Figure 12** Cage chirality comparing the vertices of **CC3**-*R* and **CC3**-*S*.

For organic cages, or any other molecules containing voids, shape persistency is vital for porosity. A molecule is shape persistence if it is structurally stable to guest removal e.g., removal of the crystallisation solvent does not lead to structural collapse and loss of the intrinsic cage cavity. Shape persistence in cages is not directly related to stability, for example **CC7** and **CC8**, published in 2011 was shown to be chemically stable with analysis showing the cage had collapsed but was still remained intact.[213]

### *4.2 Synthesis of Organic Cages – Dynamic Covalent Chemistry*

Cage formation relies on self-assembly, whereby the reagents react to form a larger species preferentially. As discussed at the start of this chapter, entropy and enthalpy are important factors in self-assembly. The dynamic nature of imine chemistry has been taken advantage of in the syntheses of OMCs and macrocycles, with a huge number of large assemblies comprised of imine bonded materials. The reversibility of the bond lends itself to the formation of thermodynamic products. The bond is able to continually self-correct, allowing it to form a thermodynamic minimum. This is known as dynamic covalent chemistry (DCC), which allows molecules to form under thermodynamic control.[214,215]

DCC is impacted by a number of variables, including pH, temperature, solvent and concentration. As imine condensation is a reversible reaction, equilibrium can be driven either forward to the product, or backwards to the starting materials enabling us to control the reaction. DCC is an excellent tool to generate a thermodynamically stable product, either through driving the equilibrium by using alternative reaction conditions, or using starting materials with features such as steric hindrance or electronic configuration in order to form a desired product.[214,216]

It is generally considered that the higher the concentration of reagents in solution, this will generally form the kinetic product. Therefore, in order to drive the reaction towards the thermodynamic product a high dilution method is preferable. In some cases, reagents need to be added at a slower rate, i.e. dropwise for the preferential formation of the thermodynamic product.[217]

Higher temperatures drive equilibrium forward, tending towards the formation of a thermodynamic product. If the starting materials are at a lower temperature, therefore less energy is in the system and so the reaction will tend towards the kinetic product, comparatively at higher temperatures the reactions tends towards the thermodynamic product.[218] In some cases however, if the forward reaction is too fast, this can result in a kinetic trap through polymer precipitation, which will occur prior to the full equilibration to the cage material.

Imine condensation can also be influenced by the use of an acid catalyst. The rate determining step (RDS) in imine condensation, as illustrated in **Figure 13A**, is the attack of the amine on the aldehyde carbonyl. The presence of an acid catalyst will increase the rate of this reaction. The energy of the RDS can be reduced by protonation of the oxygen on the aldehyde (**Figure 13B**), inducing a stronger dipole-dipole moment and generating a more stable leaving group.[219]

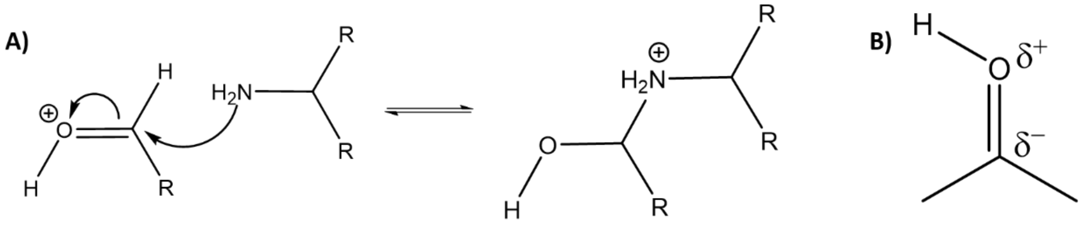

**Figure 13 A)** RDS in an imine condensation reaction; **B)** Induced stronger dipole-dipole moment when using an acid catalyst.

Solvent polarity has an impact on the rate of reaction, for example one kinetic study found that when the reaction was performed in CDCN it was approximately 3.7 times faster than in $CDCl_3$.[220] The reaction was performed in the absence of protons or metal catalysis, illustrating that the polarity of the solvent has a direct influence on the reaction, with more polar solvents supporting the rate determining polar transition state (**Figure 13A**), with this effect demonstrated in Chapter 2.[221] Similar observations are seen when studying pH effects. Under more acidic conditions reactions tend to reach equilibrium faster than neutral or alkaline conditions.[222,223]

Other dynamic covalent bonds, rather than imines, have been reported, one of which is the formation of a large organic cage using imine and boronic esters. Severin and colleagues illustrated this when they published 2 new boronic acid cages synthesised through condensation methods. Other groups have shown similar methods, including Mastalerz who demonstrated a shape persistent cage which had a BET surface area of 3758 $m^2g^{-1}$.[224–226]

### *4.3 Irreversible Cages and Macrocycles*

Irreversible cages are typically synthesised in very low yields, comparatively reversible cages can be synthesised in higher yields due to self-correction. Irreversible cages have a tendency to be more chemically stable, for example imine bonds are not stable to acidic or basic conditions.

Cages formed from carbon-carbon bonds were first reported in 1977, utilising a Wittig reaction. These cages demonstrated an attractive opportunity due to their chemical and thermal stability, furthermore they also present the possibility of photophysical properties. Unfortunately, despite many efforts to increase the yield of this reaction, which was initially 1.7%, this was never improved to more than 2%.[227–229]

Cram and Vögtle first demonstrated an irreversible, shape persistent cage in 1985. This cage was synthesised using amide bonds with a yield of 13%, however when another group employed a high dilution method, the yield increased to 27%. The group also further showed that templation-directed synthesis using iron, the yield further increased to 70%.[230,231]

In 1992, Moore made a significant breakthrough in irreversible cage syntheses, showing a cage with $D_{3h}$ symmetry which was synthesised with a 31% yield, using a Sonogashira-Hagihara coupling method (**Figure 14A**).[232] As well as C-C bonds used in irreversible cages, **Figure 14B** shows a macrocycle synthesised using imide bonds. This imide cage had the ability to access six individual redox states, therefore has potential in areas such as molecular electronics, which was demonstrated using $I_3^-$ anions.[233]

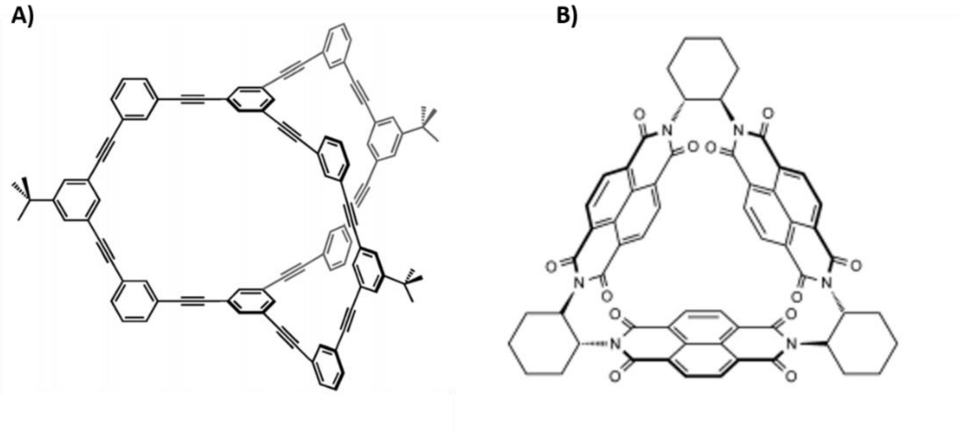

**Figure 14 A)** The irreversible cages synthesised using the Sonogashira-Hagihara coupling method; **B)** Irreversible imine-bonded cage. Figures reprinted with permission from John Wiley and Sons, copyright 2014.

More recent research in this field led to the discovery of a cage containing purely carbon, which could be synthesised with a 20% yield, which is high considering the irreversible nature of the bonding. The structure contained rigid phenyl and alkane linkers, contributing to the rigidity and proved to be an important consideration for the improved yields (**Figure 15**).[234]

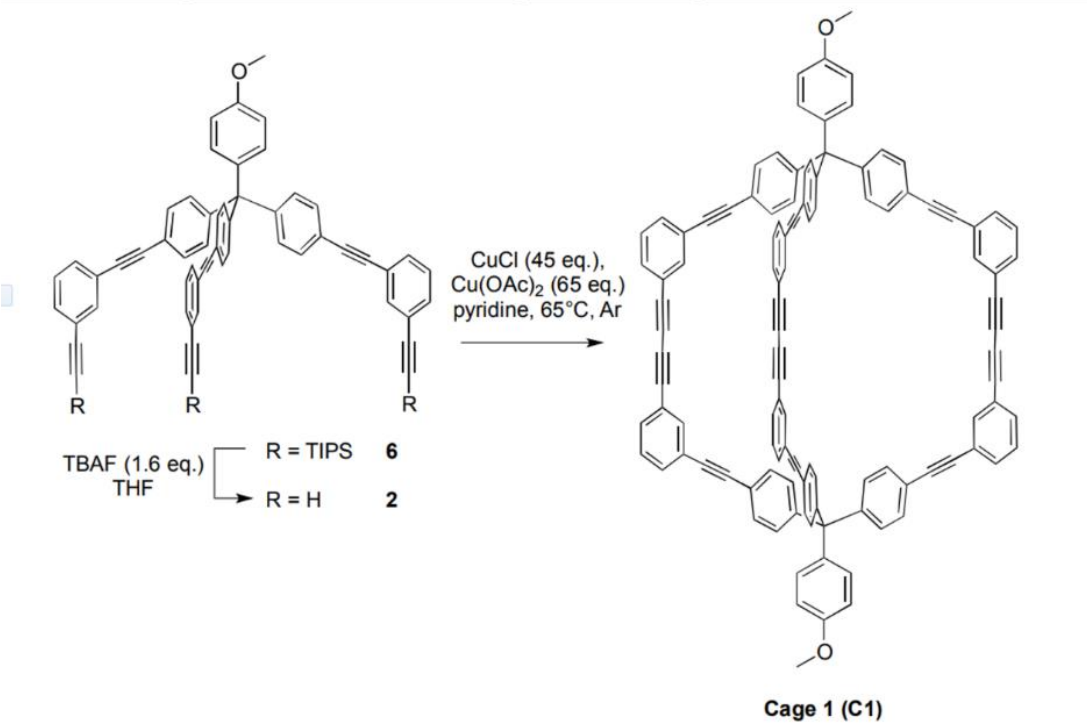

**Figure 15** The irreversible carbon cage, synthesised by Doonan et al. in 2013. Reproduced from reference 234 with permission from Angewandte Chemie.

Although we have shown the vast majority of organic cages are synthesised from reversible methods, particularly imine chemistry, there is clearly a wide breadth of chemistry which can be employed to synthesise cages which are chemically more stable, as well as the potential for applications in areas of chemistry outside of gas adsorption and separation.

# 5 Crystal Engineering

Crystal engineering provides routes to new materials by the formation of co-crystals, solvate-structures, or polymorphs.[235–237] Crystal engineering has been hailed as a potential alternative in place of traditional synthetic routes for new materials.[238] Hydrogen and halogen bonding are beneficial in crystal engineering, allowing us to utilise their directionality towards a strategic design for alternative crystal packing and/or functionality.[239–241]

Engineering with non-directional bonding, such as van der Waals (VdW), can present significant challenges. OMCs are held together in an assembly through functionality such as chiral recognition through the cage windows and weak, non-covalent interactions such as π-H .[242] Currently there are limited examples of multicomponent crystals, or co-crystals, which pack together through non-directional bonding. The co-crystallisation of **TCC1**, a cylindrical terphenyl cage, and **CC3** results in the formation of a 1:2 co-crystal with improved sorption properties than either parent cage. This can be explained from the crystal structure, their crystal densities, and pore networks. The crystalline structure of chirally pure tubular cage, **TCC1**, has no window-to-window packing. Comparatively the racemic structure shows chiral recognition which generates 1-D nanotubes. The co-crystal of **TCC1** and **CC3** shows window-to-window packing, with 3 of the 4 **CC3** windows interacting with the **CC3** cage, and one with the **TCC1** cage (**Figure 16**). Using **TCC1** and **CC3** as co-formers for co-crystallisation, the resulting material exhibited increased $N_2$ uptake.

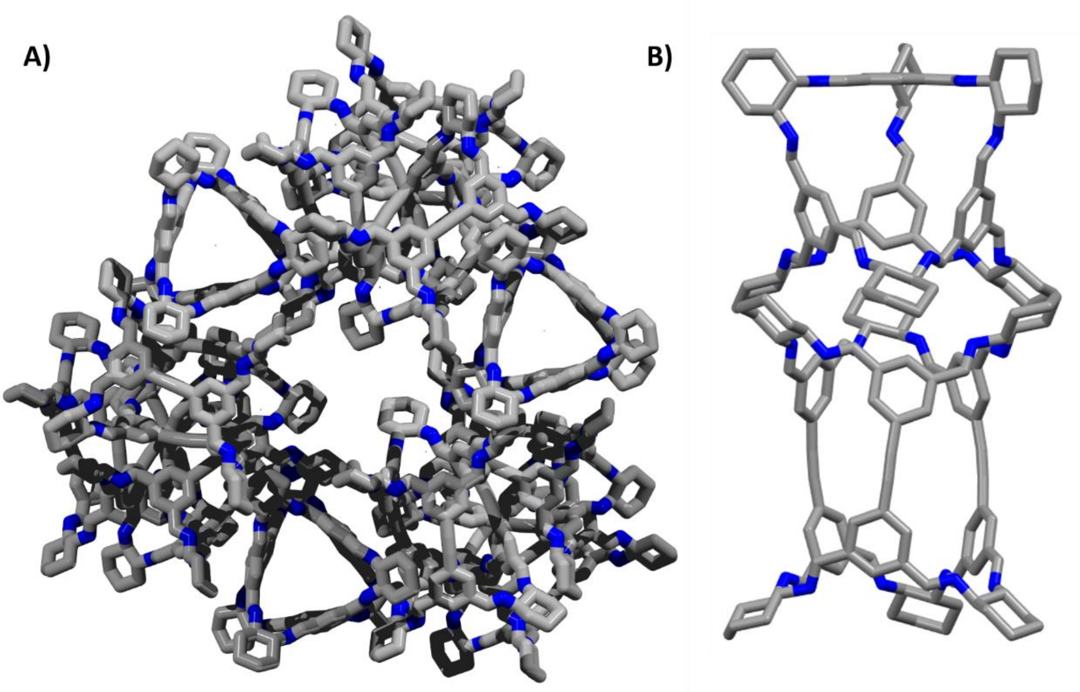

**Figure 16 A)** Crystal structure of **TCC1**, showing WTE interactions; **B)** WTW interactions between **TCC1** and **CC3**.

As well as improving the functionality of the material, recrystallising OMCs in a directional solvent can lead to alternative packing whereby the crystal packing prevents gas uptake due to the prevention of window-to-window packing.[243] **CC3** has also shown to undergo changes to the pore network by diffusing alternative solvents during recrystallization, with 1,4-dioxane directing the crystal packing and altering the pore network (**Figure 17**).[244]

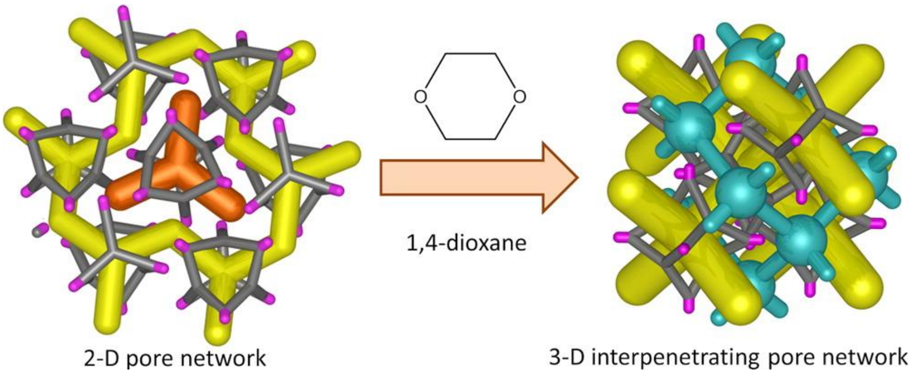

**Figure 17** Recrystallization in the directing solvent has resulted in a network variation from 2-D to 3-D. Reprinted with permission from J. Am. Chem. Soc., **2014**, 136, 1438 - 1448. Copyright 2014 American Chemical Society.

## *6 Crystallisations Methods*

Crystal growth can be a tedious and difficult challenge, there are many valid routes from both solids and solutions. Crystals in this thesis were collected using solution based methods, however we will quickly discuss solid methods. A well-known method for recrystallisation is to dissolve a molecule in hot solvent to create a saturated solution. The less solvent used the better, as the more dilute the solution the rate of nucleation will be much longer. The solution can then be left at room temperature, or in ice to crystallise in the solution. This works well for many materials; however, it doesn't always grow single crystals which are suitable for diffraction, therefore other methods need to be employed.

### *6.1 Sublimation*

Sublimation is when a solid material is heated, typically under a vacuum source, until it begins to vaporise. For this to work efficiently, the material needs to be stable to heating without decomposing. For materials discussed here, sublimation isn't suitable as they tend to decompose when heated prior to vaporisation.[245]

### *6.2 Vapour Diffusion*

A material is dissolved in a solvent which it has good solubility. This solution will be placed into a small vial, which sits inside a larger vial containing an anti-solvent which has some miscibility with the solution, but the material isn't soluble in. This method works well for anti-solvents which are highly volatile, or have a low vapour pressure.

### *6.3 Solvent Layering*

This method is similar to vapour diffusion however the anti-solvent is layered on top of the solvent. In this case, the anti-solvent should ideally be much less miscible with the solvent used for dissolution. This works well for solvents which are not very volatile, or have a high vapour pressure. This can also be used to form co-crystals as in some cases co-formers will be soluble in two different immiscible solvents. The two solutions can be layered and crystals can grow at the interface where they meet. In *Chapter 4* we will show two examples of this method working successfully.

### *6.4 Evaporation*

As the name implies, solvent evaporation using a crystallisation dish (a wide, shallow glass), which allows the solvent to evaporate quickly can be used to potentially grow single crystals. In some cases, this won't work as the rate of crystallisation will be too slow. Therefore, the rate of evaporation could be controlled, such as placing the solution into a glass vial with a lid which only allows a small amount of evaporation, or through temperature control in environments such as incubators.

# *7 X-ray Crystallography*

## *7.1 A Brief History of Crystallography*

Crystallography is the study of atomic structures using X-ray radiation. X-ray radiation was first reported in 1895 by William Röntgen, however they weren't used for the determination of atomic structures for many years.[246] Lawrence Bragg invented the first X-ray spectrometer, utilising X-ray diffraction to determine the atomic structure of crystals.[247] Crystallography can be applied to microcrystalline materials by using Powder X-ray Diffraction (PXRD), and for single crystals we can use Single Crystal X-ray Diffraction (SCXRD).

### *7.1.1 Bragg's Law*

Bragg's law explains the necessary conditions to observe diffraction from a crystal. It states that when an X-ray irradiates an atom, it interacts with the electrons within which then scatter the radiation (**Figure 18**). This can happen either constructively or destructively. When constructive, the intensity can be measured and a diffraction pattern begins to form. When destructive no peaks are seen. Diffraction is seen in crystals due to the periodic nature of the atomic arrangement.

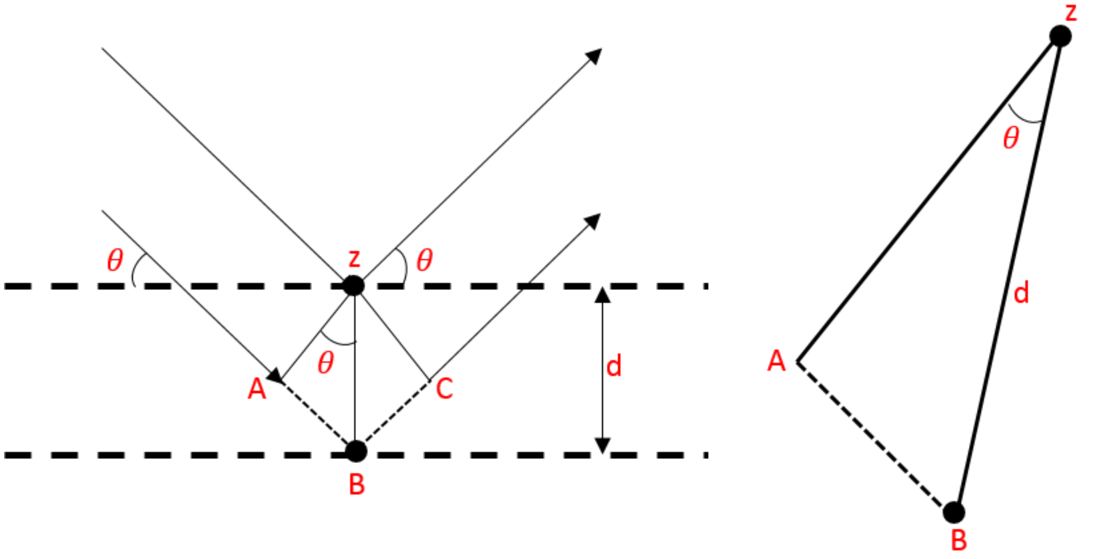

**Figure 18** Pictorial representation of Bragg's Law.

## *7.2 The phase problem*

Light waves contain not just amplitude but also a phase, however when the X-rays reach the detector, they can only measure the intensity of the light. Although much has been achieved in crystallography over the last century, we still have to account for this loss of information using complex mathematics. This is known as 'the phase problem', illustrated in **Figure 19**.

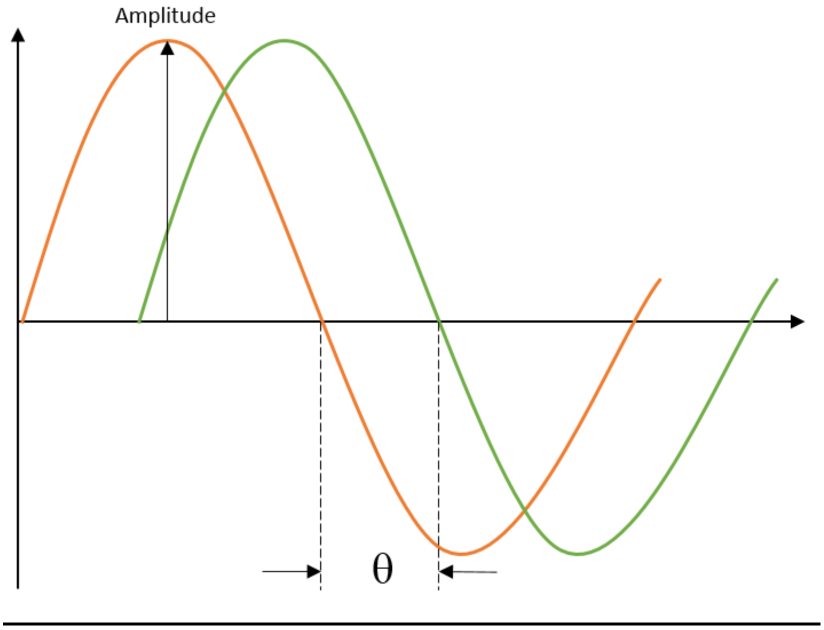

**Figure 19** Schematic to simply illustrate the phase problem. Although we can determine the amplitude, we cannot determine the phase of the light, θ.

To overcome the phase problem, different methodologies for structural solutions have been developed. For the crystal structure determination of small molecules, i.e. structures which contain less than a few hundred atoms in the unit cell, direct methods can be used. This method assumes that the crystal is made up of similarly shaped atoms, all with positive electron density and that there are statistical relationships between the structure factors. Direct methods are most commonly used for organic molecules.[248,249]

Patterson methods are used for unit cells which contain heavy atoms. The Patterson method relies on vectors between the atoms, and is related to the electron density in the cell. Heavy-heavy atom vectors are largest, followed by heavy-light and finally light-light, which will be largely unresolved.[250]

## *7.3 Space Group Determination*

Every crystal structure can be categorised into one of the 230 space groups, which are defined based on the symmetry elements present in the unit cell. Space groups can be placed into 7 distinct crystal systems as shown in **Table 2**.

**Table 2** The seven crystal systems and their corresponding rules for cell angles and lengths.

| Crystal System | Cell angle rules | Cell length rules |
|---|---|---|
| **Triclinic** | None | None |
| **Monoclinic** | $\alpha = \gamma = 90°$ | None |
| **Orthorhombic** | $\alpha = \beta = \gamma = 90°$ | None |
| **Tetragonal** | $\alpha = \beta = \gamma = 90°$ | a = b |
| **Trigonal** | $\alpha = \beta = 90°$<br>$\gamma = 120°$ | a = b |
| **Rhombohedral** | $\alpha = \beta = 90°$<br>$\gamma = 120°$ | a = b |
| **Cubic** | $\alpha = \beta = \gamma = 90°$ | a = b = c |

**Table 2** shows the crystal systems and how these are characterised based on rules for the unit cell angles and lengths. There are only 2 triclinic space groups, as these have the least symmetry. $P1$, which has no symmetry elements other than translational symmetry between the unit cells, and $P\bar{1}$ which contains an inversion centre as well as translational symmetry.

Moving from triclinic through to cubic, there is an increase in the symmetry operations. When determining a crystal structure, to develop an accurate experimental model we must collect a certain amount of data. For triclinic cells we need to collect an hemisphere of data, by comparison for the highly symmetrical cubic systems we only need 1/8th of the sphere.

The space group of a molecule is determined by the symmetry elements which are present, such as mirror planes, rotation, inversion centres, screw axes or glide planes. Systematic absences arise due to the symmetry operations in the unit cell. These absences appear as ‘0’ when calculating the structure factor, leading to the determination of which space group the crystal belongs in.

### *7.4 Twinning*

Twinned crystals are a common issue in crystal structure determination. There are many classifications of twinning in crystals, typically caused by intergrowth of two or more crystals which share the same lattice points. Merohedral or pseudo-merohedral twins can be identified from the diffraction pattern, as reflections which are lying very closely together, or are overlapping. Comparatively, non-merohedral twins produce more reflections which would cause issues when trying to auto-assign the peaks and identify the unit cell. For non-merohedral twins, it can sometimes be possible to manually separate the two domains, however in some cases software can do this automatically.

For merohedral twins however, twin laws can be applied. These twins can be related by inversion, rotation or reflection. Some crystals are more prone to twinning, for example molecules which have high point group symmetry but a low crystal symmetry.

Because reflections can overlap, the intensity of the reflection can then be incorrectly calculated. If you considered the reflection having an intensity of '1', then instead it could be '2'. Hence this leads to problems with the incorrect assignment of symmetry.

## *8 Crystallography in Supramolecular Materials*

Crystallography is the only method whereby we can obtain direct information on the molecular structure, the way in which the molecules interact with one another in their crystalline form and can provide further chemical information, such as bond lengths, angles and the chirality of the molecule.[251]

Determining the crystal structure of macromolecular or supramolecular materials is an inherently challenging task, by virtue of many factors.[252] One such issue which presents itself is that typically the unit cell is much larger, and as we discussed earlier in section 7.2, data is first obtained in reciprocal space. Therefore, the larger the cell edge the closer together reflections will appear.

Secondly, macromolecules which contain voids become more difficult to obtain effective diffraction. Diffraction relies on electron density, therefore there is an absence of density due to the presence of the void in the system, which could contain disordered solvent or, if completed desolvated a vacuum. The general principle surrounding vacuums is that ‘nature abhors a vacuum’, originally theorised by Aristotle.[253] Therefore when considering large molecular materials containing voids, these voids will have a propensity to be filled by surrounding matter, e.g. solvent, to reduce the energy of the system. If a molecular crystal contains voids, the density of the structure will decrease, and typically lower the density, the higher the lattice energy of the system.[254]

With the improvement of technology, larger crystal structures have been reported at an increasing rate over the decades.[255] Typically, the larger the crystal structure, i.e. a unit cell with edge(s) > 18 Å, the difficult associated with an accurate model of the crystal structures increases.[256] These issues arise not only from the diffraction, but also the quality of the single crystal.

Crystal growth is a complex area, discussed further in *Chapter 3, Section 1.3*. Larger materials are more prone to issues such as disorder, directly as a result of the number of possible conformations the material can exhibit.[257] Therefore, as we increase the size and complexity or the crystal structure, the chance of disorder increases significantly. Although, this can be reduced by more rigid molecules which have fewer degrees of freedom than, for example, a tert-butyl group.

## *8.1 Disorder*

Once a model for the crystal structure has been determined, there can be chemical inaccuracies, or potentially residual electron density is in the structure in an unexpected position. This is referred to as disorder, and arises as diffractometers take a ‘time-average’ picture of the crystal, due to the thermal vibration and movement of atoms structural disorder can become an issue.[258] The experimental structures found from crystallography are ‘models’, whereby data has been interpreted and a model has been calculated based on this.[259] Disorder is significantly more pronounced and difficult to manage when dealing with larger or macromolecular structures.[260]

As crystal structures are models based on experimental data, the proposed structures could show potential errors. In many cases, crystal structures will have disorder, which could apply to anything from unresolved solvent in the unit cell, to molecules having partial occupancy over multiple positions.

Disorder can be modelled using a variety of methods, two of which are using restraints and constraints. A restraint provides additional information for the model parameters to fit to. Restraints can be used to provide the model with more parameters based on known chemical information. Molecules which lie on a special symmetry position are constrained, in the sense that the co-ordinates are fixed. This is the same role as using a constraint. These are stricter, so rather than providing more data for the model to be fit to, it reduces the number of free parameters. A simple example can be seen in **Figure 13**. If a crystal contained **13A**, then we are aware that there is only one -OH in one position. However, if it lay on a 3-fold axis, then we may see crystallographically it resembles **13B**, with each -OH having an occupancy of 1/3.

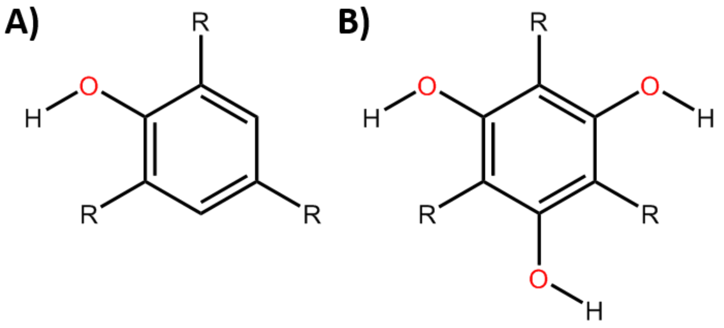

**Figure 13 A**) A molecule with one alcohol group; **B**) A molecule with 3 alcohol groups, but each has 1/3 occupancy.

Crystals which are grown using solvent methods are likely to experience issue with solvent disorder. Unless the solvent interacts with the molecule, it is unlikely that the solvent will be well resolved in the structure. There are multiple approaches to the modelling of disordered solvent, restraints to fix the solvent to known bond lengths and angles, SADI which models disordered solvent on a well-ordered model, or SQUEEZE, an algorithm which effectively removes the excess electron density.[261,248]

# *9 References*

1 J. Lehn, *Science*, 1993, **260**, 1762–1763.

2 J.-M. Lehn, *Angew. Chemie Int. Ed. English*, 1990, **29**, 1304–1319.

3 D. J. Cram, J.-M. Lehn and C. J. Pederson, The Nobel Prize in Chemistry 1987, https://www.nobelprize.org/prizes/chemistry/1987/summary/, (accessed 25 August 2018).

4 J. M. Lehn, *Supramolecular Chemistry: Concepts and Perspectives*, Wiley-VCH Verlag GmbH & Co. KGaA, Weinheim, FRG, 1995, 1-19.

5 K. JM and R. J, *Nature*, 1996, **382**, 239–241.

6 E. Mattia and S. Otto, *Nat. Nanotechnol.*, 2015, **10**, 111–119.

7 A. W. Adamson, *J. Am. Chem. Soc.*, 1954, **76**, 1578–1579.

8 H. J. Schneider, *Angew. Chemie Int. Ed.*, 2009, **48**, 3924–3977.

9 D. H. Leung, R. G. Bergman and K. N. Raymond, *J. Am. Chem. Soc.*, 2008, **130**, 2798–2805.

10 S. Sadhasivam and K. S. Yun, *J. Mater. Sci.*, 2010, **45**, 2543–2552.

11 G. M. Whitesides and B. Grzybowski, *Science*, 2002, **295**, 2418–21.

12 J. W. Steed and J. L. Atwood, *Supramolecular Chemistry, 2nd Edition*, J Wiley & Sons, Chichester, UK, 2009, 591-706.

13 H. P. Lehmann, X. Fuentes-Aderiu and L. F. Bertello, *Glossary of term in quantities and units in Clinical Chemistry*, The Scientific Journal of IUPAC, 68th edn., 1996.

14 K. Ariga, J. P. Hill, M. V Lee, A. Vinu, R. Charvet and S. Acharya, *Sci. Technol. Adv. Mater.*, 2008, **9**, 014109.

15 J. Hamacek, M. Borkovec and C. Piguet, *Dalt. Trans.*, 2006, 1473.

16 S. R. Seidel and P. J. Stang, *Acc. Chem. Res.*, 2002, **35**, 972–983.

17 J. N. Israelachvili, D. J. Mitchell and B. W. Ninham, *J. Chem. Soc. Faraday Trans. 2*, 1976, **72**, 1525-1568.

18 K. Marilyn and P. Richard, in *Applied Colloid and Surface Chemistry*, John Wiley & Sons, Ltd, Chichester, UK, 2005, pp. 61–77.

19 E. Winfree, F. Liu, L. A. Wenzler and N. C. Seeman, *Nature*, 1998, **394**, 539–544.

20 D. Philp and J. F. Stoddart, *Angew. Chemie Int. Ed. English*, 1996, **35**, 1154–1196.

21 G. R. Desiraju, *Angew. Chemie Int. Ed. English*, 1995, **34**, 2311–2327.

22 J. Perry IV, M. Perman and M. J. Zaworotko, *Chem. Soc. Rev.*, 1994, **23**, 283, 1400-1417.

23 C. G. Claessens and J. F. Stoddart, *J. Phys. Org. Chem.*, 1997, **10**, 254–272.

24 C. B. Aakeröy and K. R. Seddon, *Chem. Soc. Rev.*, 1993, **22**, 397–407.

25 C. B. Aakeröy, A. M. Beatty and B. A. Helfrich, *Angew. Chemie Int. Ed.*, 2001, **40**, 3240–3242.

26 J.-M. Lehn, *Angew. Chemie Int. Ed. English*, 1990, **29**, 1304–1319.

27 T. P. Lybrand, J. A. McCammon and G. Wipff, *Proc. Natl. Acad. Sci. U. S. A.*, 1986, **83**, 833–5.

28 G. Zhang and M. Mastalerz, *Chem. Soc. Rev.*, 2014, **43**, 1934–1947.

29 C. J. Pedersen, *Science.*, 1988, **241**, 536–540.

30 M. L. Bender, R. L. Van Etten, G. A. Clowes and J. F. Sebastian, *J. Am. Chem. Soc.*, 1966, **88**, 2318–2319.

31 D. J. Cram and J. M. Cram, *Science*, 1974, 183, 803–809.

32 G. Cooke and V. M. Rotello, *Chem. Soc. Rev.*, 2002, **31**, 275–286.

33 W. Saenger, T. Steiner and IUCr, *Acta Crystallogr. Sect. A Found. Crystallogr.*, 1998, **54**, 798–805.

34 A. M. Beatty, *Coord. Chem. Rev.*, 2003, **246**, 131–143.

35 Y. Uda, F. Kaneko and T. Kawaguchi, *Macromol. Rapid Commun.*, 2004, **25**, 1900–1904.

36 F. Fochi, P. Jacopozzi, E. Wegelius, K. Rissanen, P. Cozzini, E. Marastoni, E. Fisicaro, P. Manini, R. Fokkens and E. Dalcanale, *J. Am. Chem. Soc.*, 2001, **123**, 7539–7552.

37 J.-M. Lehn, *Science.*, 2002, **295**, 2400–2403.

38 G. Schill and A. Lüttringhaus, *Angew. Chem. Int. Ed. English*, 1964, **3**, 546–547.

39 C. D. Meyer, C. S. Joiner and J. F. Stoddart, *Chem. Soc. Rev.*, 2007, **36**, 1705-1723.

40 P. T. Glink, A. I. Oliva, J. F. Stoddart, A. J. P. White and D. J. Williams, *Angew. Chemie Int. Ed.*, 2001, **40**, 1870–1875.

41 M. J. Langton, J. D. Matichak, A. L. Thompson and H. L. Anderson, *Chem. Sci.*, 2011, **2**, 1897-1901.

42 M. Hoffmann, C. J. Wilson, B. Odell and H. L. Anderson, *Angew. Chemie Int. Ed.*, 2007, **46**, 3122–3125.

43 S. Höger and A.-D. Meckenstock, *Chem. - A Eur. J.*, 1999, **5**, 1686–1691.

44 S. Li, M. Dharmarwardana, R. P. Welch, Y. Ren, C. M. Thompson, R. A. Smaldone and J. J. Gassensmith, *Angew. Chemie Int. Ed.*, 2016, **55**, 10691–10696.

45 D. A. Leigh, R. G. Pritchard and A. J. Stephens, *Nat. Chem.*, 2014, **6**, 978–982.

46 M. W. Hosseini, *Acc. Chem. Res.*, 2005, **38**, 313–323.

47 K. S. Chichak, S. J. Cantrill, A. R. Pease, S. H. Chiu, G. W. V. Cave, J. L. Atwood and J. F. Stoddart, *Science*, 2004, **304**, 1308–1312.

48 P. L. Anelli, P. R. Ashton, R. Ballardini, V. Balzani, M. Delgado, M. T. Gandolfi, T. T. Goodnow, A. E. Kaifer and D. Philp, *J. Am. Chem. Soc.*, 1992, **114**, 193–218.

49 J. F. Stoddart, *Chem. Soc. Rev.*, 2009, **38**, 1802-1820.

50 T. Hasell, X. Wu, J. T. A. Jones, J. Bacsa, A. Steiner, T. Mitra, A. Trewin, D. J. Adams and A. I. Cooper, *Nat. Chem.*, 2010, **2**, 750–755.

51 M. C. T. Fyfe and J. F. Stoddart, *Acc. Chem. Res.*, 1997, **30**, 393–401.

52 S. F. M. van Dongen, S. Cantekin, J. A. A. W. Elemans, A. E. Rowan and R. J. M. Nolte, *Chem. Soc. Rev.*, 2014, **43**, 99–122.

53 R. L. Greenaway, V. Santolini, M. J. Bennison, B. M. Alston, C. J. Pugh, M. A. Little, M. Miklitz, E. G. B. Eden-Rump, R. Clowes, A. Shakil, H. J. Cuthbertson, H. Armstrong, M. E. Briggs, K. E. Jelfs and A. I. Cooper, *Nat. Commun.*, 2018, **9**, 2849.

54 G. Zhang, O. Presly, F. White, I. M. Oppel and M. Mastalerz, *Angew. Chemie*, 2014, **126**, 5226–5230.

55 M. J. Chmielewski, J. J. Davis and P. D. Beer, *Org. Biomol. Chem.*, 2009, **7**, 415–424.

56 D. A. Leigh, J. K. Y. Wong, F. Dehez and F. Zerbetto, *Nature*, 2003, **424**, 174–179.

57 R. Ballardini, V. Balzani, A. Crei, M. T. Gandolfi and M. Venturi, *Acc. Chem. Res.*, 2001, **34**, 445–455.

58 M. Cesario, C. O. Dietrich-Buchecker, J. Guilhem, C. Pascard and J. P. Sauvage, *J. Chem. Soc. Chem. Commun.*, 1985, 244.

59 R. A. Bissell, E. Córdova, A. E. Kaifer and J. F. Stoddart, *Nature*, 1994, **369**, 133–137.

60 N. Koumura, R. W. J. Zijlstra, R. A. van Delden, N. Harada and B. L. Feringa, *Nature*, 1999, **401**, 152–155.

61 V. Balzani, *Photochem. Photobiol. Sci.*, 2003, **2**, 459.

62 A. H. Flood, R. J. A. Ramirez, W.-Q. Deng, R. P. Muller, W. A. Goddard III and J. F. Stoddart, *Aust. J. Chem.*, 2004, **57**, 301.

63 P. L. Anelli, N. Spencer and J. F. Stoddart, *J. Am. Chem. Soc.*, 1991, **113**, 5131–5133.

64 M. M. Boyle, R. A. Smaldone, A. C. Whalley, M. W. Ambrogio, Y. Y. Botros and J. F. Stoddart, *Chem. Sci.*, 2011, **2**, 204–210.

65 I. V. Kolesnichenko and E. V. Anslyn, *Chem. Soc. Rev.*, 2017, **46**, 2385–2390.

66 A. P. de Silva, H. Q. N. Gunaratne, T. Gunnlaugsson and M. Nieuwenhuizen, *Chem. Commun.*, 1996, **0**, 1967, 2191-2192.

67 A. P. de Silva, H. Q. N. Gunaratne and C. P. McCoy, *J. Am. Chem. Soc.*, 1997, **119**, 7891–7892.

68 P. A. de Silva, N. H. Q. Gunaratne and C. P. McCoy, *Nature*, 1993, **364**, 42–44.

69 L. You, J. S. Berman and E. V. Anslyn, *Nat. Chem.*, 2011, **3**, 943–948.

70 E. V. Anslyn, *J. Org. Chem.*, 2007, **72**, 687–699.

71 T. D. James, K. R. A. S. Sandanayake and S. Shinkai, *Chem. Commun.*, 1994, **0**, 477-478.

72 T. D. James, K. R. A. S. Sandanayake, R. Iguchi and S. Shinkai, *J. Am. Chem. Soc.*, 1995, **117**, 8982–8987.

73 (IUCr) Crystallography Journals Online - supporting information, http://journals.iucr.org/j/issues/2015/01/00/aj5242/hklsup.html, (accessed 28 April 2016).

74 R. Weissleder and U. Mahmood, *Radiology*, 2001, **219**, 316–333.

75 A. Ojida, Y. Mito-oka, M. Inoue and I. Hamachi, *J. Am. Chem. Soc.*, 2002, **124**, 6256–6258.

76 B. D. Smith, *Beilstein J. Org. Chem.*, 2015, **11**, 2540–2548.

77 J. J. Gassensmith, J. M. Baumes and B. D. Smith, *Chem. Commun.*, 2009, 6329–38.

78 Easwaran Arunkumar, Christopher C. Forbes, Bruce C. Noll and B. D. Smith, *J. Am. Chem. Soc.*, 2005, **127**, 3288–3289.

79 W. G. Cox and V. L. Singer, *J. Histochem. Cytochem.*, 1999, **47**, 1443–1455.

80 Y. Zhang, B. Zhang, Y. Kuang, Y. Gao, J. Shi, X. X. Zhang and B. Xu, *J. Am. Chem. Soc.*, 2013, **135**, 5008–5011.

81 X. Du, J. Zhou, J. Shi and B. Xu, *Chem. Rev.*, 2015, **115**, 13165–13307.

82 J.-H. Xu, F.-P. Gao, X.-F. Liu, Q. Zeng, S.-S. Guo, Z.-Y. Tang, X.-Z. Zhao and H. Wang, *Chem. Commun.*, 2013, **49**, 4462.

83 G. Yu, G. Tang and F. Huang, *J. Mater. Chem. C*, 2014, **2**, 6609–6617.

84 M. J. Webber and R. Langer, *Chem. Soc. Rev.*, 2017, **46**, 6600–6620.

85 E. Masson, X. Ling, R. Joseph, L. Kyeremeh-Mensah and X. Lu, *RSC Adv.*, 2012, **2**, 1213–1247.

86 R. Oun, R. S. Floriano, L. Isaacs, E. G. Rowan and N. J. Wheate, *Toxicol. Res.*, 2014, **3**, 447–455.

87 G. Hettiarachchi, D. Nguyen, J. Wu, D. Lucas, D. Ma, L. Isaacs and V. Briken, *PLoS One*, 2010, **5**, e10514.

88 S. Walker, R. Oun, F. J. McInnes and N. J. Wheate, *Isr. J. Chem.*, 2011, **51**, 616–624.

89 C. Gao and D. Yan, *Prog. Polym. Sci.*, 2004, **29**, 183–275.

90 R. Langer, *Science*, 1990, **249**, 1527–1533.

91 U. Gupta and N. K. Jain, *Adv. Drug Deliv. Rev.*, 2010, **62**, 478–490.

92 P. A. Vasey, S. B. Kaye, R. Morrison, C. Twelves, P. Wilson, R. Duncan, A. H. Thomson, L. S. Murray, T. E. Hilditch, T. Murray, S. Burtles, D. Fraier, E. Frigerio and J. Cassidy, *Clin. Cancer Res.*, 1999, **5**, 83–94.

93 Y. Malam, M. Loizidou and A. M. Seifalian, *Trends Pharmacol. Sci.*, 2009, **30**, 592–599.

94 A. Sparreboom, O. van Tellingen, W. J. Nooijen, J. H. Beijnen, Q. Cao, X. Chen and H. Dai, *Cancer Res.*, 1996, **56**, 2112–5.

95 Z. Liu, X. Sun, N. Nakayama-Ratchford and H. Dai, *ACS Nano*, 2007, **1**, 50–56.

96 A. Tanaka, Y. Fukuoka, Y. Morimoto, T. Honjo, D. Koda, M. Goto and T. Maruyama, *J. Am. Chem. Soc.*, 2015, **137**, 770–775.

97 D. Fiedler, D. H. Leung, R. G. Bergman and K. N. Raymond, *Acc. Chem. Res.*, 2005, **38**, 349–358.

98 M. D. Pluth, R. G. Bergman and K. N. Raymond, *Science*, 2007, **316**, 85–88.

99 M. Cao, J. Lin, H. Yang and R. Cao, *Chem. Commun.*, 2010, **46**, 5088.

100 M. Mastalerz, *Chem. - A Eur. J.*, 2012, **18**, 10082–10091.

101 G.-R. Walther, E. Post, P. Convey, A. Menzel, C. Parmesan, T. J. C. Beebee, J.-M. Fromentin, O. Hoegh-Guldberg and F. Bairlein, *Nature*, 2002, **416**, 389–395.

102 J. A. Church and N. J. White, *Geophys. Res. Lett.*, 2006, **33**, 1-4.

103 M. Beniston, D. B. Stephenson, O. B. Christensen, C. A. T. Ferro, C. Frei, S. Goyette, K. Halsnaes, T. Holt, K. Jylhä, B. Koffi, J. Palutikof, R. Schöll, T. Semmler and K. Woth, *Clim. Change*, 2007, **81**, 71–95.

104 W. Cai, S. Borlace, M. Lengaigne, P. van Rensch, M. Collins, G. Vecchi, A. Timmermann, A. Santoso, M. J. McPhaden, L. Wu, M. H. England, G. Wang, E. Guilyardi and F.-F. Jin, *Nat. Clim. Chang.*, 2014, **4**, 111–116.

105 D. Coumou and S. Rahmstorf, *Nat. Clim. Chang.*, 2012, **2**, 491–496.

106 S. Peng, J. Huang, J. E. Sheehy, R. C. Laza, R. M. Visperas, X. Zhong, G. S. Centeno, G. S. Khush and K. G. Cassman, *Proc. Natl. Acad. Sci.*, 2004, **101**, 9971–9975.

107 S. Asseng, F. Ewert, P. Martre, R. P. Rötter, D. B. Lobell, D. Cammarano, B. A. Kimball, M. J. Ottman, G. W. Wall, J. W. White, M. P. Reynolds, P. D. Alderman, P. V. V. Prasad, P. K. Aggarwal, J. Anothai, B. Basso, C. Biernath, A. J. Challinor, G. De Sanctis, J. Doltra, E. Fereres, M. Garcia-Vila, S. Gayler, G. Hoogenboom, L. A. Hunt, R. C. Izaurralde, M. Jabloun, C. D. Jones, K. C. Kersebaum, A.-K. Koehler, C. Müller, S. Naresh Kumar, C. Nendel, G. O'Leary, J. E. Olesen, T. Palosuo, E. Priesack, E. Eyshi Rezaei, A. C. Ruane, M. A. Semenov, I. Shcherbak, C. Stöckle, P. Stratonovitch, T. Streck, I. Supit, F. Tao, P. J. Thorburn, K. Waha, E. Wang, D. Wallach, J. Wolf, Z. Zhao and Y. Zhu, *Nat. Clim. Chang.*, 2015, **5**, 143–147.

108 S. M. Gourdji, A. M. Sibley and D. B. Lobell, *Environ. Res. Lett.*, 2013, **8**, 1-4.

109 J.-R. Li, Y. Ma, M. C. McCarthy, J. Sculley, J. Yu, H.-K. Jeong, P. B. Balbuena and H.-C. Zhou, *Coord. Chem. Rev.*, 2011, **255**, 1791–1823.

110 T. Ben, C. Pei, D. Zhang, J. Xu, F. Deng, X. Jing and S. Qiu, *Energy Environ. Sci.*, 2011, **4**, 3991-3999.

111 G. Férey, C. Serre, T. Devic, G. Maurin, H. Jobic, P. L. Llewellyn, G. De Weireld, A. Vimont, M. Daturi and J.-S. Chang, *Chem. Soc. Rev.*, 2011, **40**, 550–562.

112 M. Eddaoudi, *Science*, 2002, **295**, 469–472.

113 H. Furukawa and O. M. Yaghi, *J. Am. Chem. Soc.*, 2009, **131**, 8875–8883.

114 M. Goldstein, *J. Emerg. Nurs.*, 2008, **34**, 538–542.

115 D. J. Wales, J. Grand, V. P. Ting, R. D. Burke, K. J. Edler, C. R. Bowen, S. Mintova and A. D. Burrows, *Chem. Soc. Rev.*, 2015, **44**, 4290–4321.

116 Z. Jin, H.-J. Zhou, Z.-L. Jin, R. F. Savinell and C.-C. Liu, *Sensors Actuators B Chem.*, 1998, **52**, 188–194.

117 R.-Q. Zou, H. Sakurai, S. Han, R.-Q. Zhong and Q. Xu, *J. Am. Chem. Soc.*, 2007, **129**, 8402–8403.

118 M. Hauptmann, P. A. Stewart, J. H. Lubin, L. E. Beane Freeman, R. W. Hornung, R. F. Herrick, R. N. Hoover, J. F. Fraumeni, A. Blair and R. B. Hayes, *JNCI J. Natl. Cancer Inst.*, 2009, **101**, 1696–1708.

119 M. Hauptmann, J. H. Lubin, P. A. Stewart, R. B. Hayes and A. Blair, *J. Natl. Cancer Inst.*, 2003, **95**, 1615–1623.

120 D. Coggon, E. C. Harris, J. Poole and K. T. Palmer, *J. Natl. Cancer Inst.*, 2003, **95**, 1608–1615.

121 L. E. Pinkerton, M. J. Hein and L. T. Stayner, *Occup. Environ. Med.*, 2004, **61**, 193–200.

122 H. Tian, J. He, X. Zhang, L. Zhou and D. Wang, *Microporous Mesoporous Mater.*, 2011, **138**, 118–122.

123 Z. Xu, J. Yu and W. Xiao, *Chem. - A Eur. J.*, 2013, **19**, 9592–9598.

124 N. A. Khan, Z. Hasan and S. H. Jhung, *J. Hazard. Mater.*, 2013, **244**–**245**, 444–456.

125 M. Dincă, A. F. Yu and J. R. Long, *J. Am. Chem. Soc.*, 2006, **128**, 8904–8913.

126 L. Schlapbach and A. Züttel, *Nature*, 2001, **414**, 353–358.

127 R. Wakeford, *J. Radiol. Prot.*, 2009, **29**, 61–79.

128 C. M. Simon, R. Mercado, S. K. Schnell, B. Smit and M. Haranczyk, *Chem. Mater.*, 2015, **27**, 4459–4475.

129 D. Banerjee, A. J. Cairns, J. Liu, R. K. Motkuri, S. K. Nune, C. A. Fernandez, R. Krishna, D. M. Strachan and P. K. Thallapally, *Acc. Chem. Res.*, 2015, **48**, 211–219.

130 L. Chen, P. S. Reiss, S. Y. Chong, D. Holden, K. E. Jelfs, T. Hasell, M. A. Little, A. Kewley, M. E. Briggs, A. Stephenson, K. M. Thomas, J. A. Armstrong, J. Bell, J. Busto, R. Noel, J. Liu, D. M. Strachan, P. K. Thallapally and A. I. Cooper, *Nat Mater*, 2014, **13**, 954–960.

131 J. S. Sovey, V. K. Rawlin and M. J. Patterson, *J. Propuls. Power*, 2001, **17**, 517–526.

132 L. J. J. Hronowski and W. A. Szarek, *Can. J. Chem.*, 1992, **70**, 1162–1169.

133 L. Li, T. Abe and M. Esashi, *J. Vac. Sci. Technol. B Microelectron. Nanom. Struct.*, 2003, **21**, 2545.

134 J. Rouquerol, D. Avnir, C. W. Fairbridge, D. H. Everett, J. M. Haynes, N. Pernicone, J. D. F. Ramsay, K. S. W. Sing and K. K. Unger, *Pure Appl. Chem.*, 2009, **66**, 1365–3075.

135 L. Peng, J. Zhang, Z. Xue, B. Han, X. Sang, C. Liu and G. Yang, *Nat. Commun.*, 2014, **5**, 4465.

136 S. Kitagawa, R. Kitaura and S. Noro, *Angew. Chemie Int. Ed.*, 2004, **43**, 2334–2375.

137 R. Dawson, A. I. Cooper and D. J. Adams, *Prog. Polym. Sci.*, 2012, **37**, 530–563.

138 S. Horike, S. Shimomura and S. Kitagawa, *Nat. Chem.*, 2009, **1**, 695–704.

139 T. Düren, L. Sarkisov, O. M. Yaghi and R. Q. Snurr, *Langmuir*, 2004, **20**, 2683–2689.

140 M. C. Das, Q. Guo, Y. He, J. Kim, C.-G. Zhao, K. Hong, S. Xiang, Z. Zhang, K. M. Thomas, R. Krishna and B. Chen, *J. Am. Chem. Soc.*, 2012, **134**, 8703–8710.

141 P. M. Budd, K. J. Msayib, C. E. Tattershall, B. S. Ghanem, K. J. Reynolds, N. B. McKeown and D. Fritsch, *J. Memb. Sci.*, 2005, **251**, 263–269.

142 P. C. Angelomé, M. C. Fuertes and G. J. A. A. Soler-Illia, *Adv. Mater.*, 2006, **18**, 2397–2402.

143 A. Corma, , DOI:10.1021/CR960406N.

144 F. Ciaramella, V. Jousseaume, S. Maitrejean, M. Verdier, B. Remiat, A. Zenasni and G. Passemard, *Thin Solid Films*, 2006, **495**, 124–129.

145 C. M. A. Parlett, K. Wilson and A. F. Lee, *Chem. Soc. Rev.*, 2013, **42**, 3876–3893.

146 W. Vermeiren and J.-P. Gilson, *Top. Catal.*, 2009, **52**, 1131–1161.

147 † Andrei Y. Khodakov, *, A. Wei Chu, † and P. Fongarland†, *Chem. Rev.*, 2007, **107**, 1692–1744.

148 F. Dong, Y. Sun, W. K. Ho and Z. Wu, *Dalton. Trans.*, 2012, **41**, 8270-8284.

149 D. Yuan, W. Lu, D. Zhao and H.-C. Zhou, *Adv. Mater.*, 2011, **23**, 3723–3725.

150 N. Giri, M. G. Del Pópolo, G. Melaugh, R. L. Greenaway, K. Rätzke, T. Koschine, L. Pison, M. F. C. Gomes, A. I. Cooper and S. L. James, *Nature*, 2015, **527**, 216–220.

151 A. K. Cheetham, C. N. R. Rao and R. K. Feller, *Chem. Commun.*, 2006, **0**, 4780–4795.

152 N. E. R. Zimmermann and M. Haranczyk, *Cryst. Growth Des.*, 2016, **16**, 3043–3048.

153 M. E. Davis and R. F. Lobo, *Chem. Mater*, 1992, **4**, 756–768.

154 P. Dufresne, A. Quesada and S. Mignard, *Stud. Surf. Sci. Catal.*, 1989, **53**, 301–315.

155 R. S. Bowman, *Microporous Mesoporous Mater.*, 2003, **61**, 43–56.

156 H. Li, M. Eddaoudi, M. O’Keeffe and O. M. Yaghi, *Nature*, 1999, **402**, 276–279.

157 A. K. Cheetham, G. Férey and T. Loiseau, *Angew. Chemie Int. Ed.*, 1999, **38**, 3268–3292.

158 J. A. Hurd, R. Vaidhyanathan, V. Thangadurai, C. I. Ratcliffe, I. L. Moudrakovski and G. K. H. Shimizu, *Nat. Chem.*, 2009, **1**, 705–710.

159 X. Feng, X. Ding and D. Jiang, *Chem. Soc. Rev.*, 2012, **41**, 6010.

160 A. P. Côté, A. I. Benin, N. W. Ockwig, M. O’Keeffe, A. J. Matzger and O. M. Yaghi, *Science*, 2005, **310**, 1166–70.

161 D. T. Vodak, M. Braun, L. Iorganidis, J. Piervert, M. Stevens, L. Beck, J. C. H. Spence, M. O’Keeffe and O. M. Yaghi, *J. Am. Chem. Soc.*, 2002, **124**, 4942–4943.

162 T. Hoang, J. W. Lauher and F. W. Fowler, *J. Am. Chem. Soc.*, 2002, **124**, 10656–10657.

163 H. El-Kaderi, J. Hunt, J. Mendoza-Cortes, A. Cote, R. Taylor, M. O’Keeffe and O. Yaghi, *Science*, 2007, **316**, 268–272.

164 S. Ding and W. Wang, *Chem. Soc. Rev.*, 2013, **42**, 548–568.

165 S. Ding, J. Gao, Q. Wang, Y. ZHang, W. Song, S. CY and W. W, *J. Am. Chem. Soc.*, 2011, **133**, 19816–19822.

166 B. Zhang, M. Wei, H. Mao, X. Pei, S. A. Alshmimri, J. A. Reimer and O. M. Yaghi, *J. Am. Chem. Soc.*, 2018, **361**, 6397, 48-52.

167 Y.F. Han, Y.X. Yuan and H.B. Wang, *Molecules*, 2017, **22**, 266-298.

168 X.Z. Luo, X.J. Jia, J.H. Deng, J.L. Zhong, H.J. Liu, K.J. Wang and D.C. Zhong, *J. Am. Chem. Soc.*, 2013, **135**, 11684–11687.

169 P. Li, Y. He, J. Guang, L. Weng, J. C.-G. Zhao, S. Xiang and B. Chen, *J. Am. Chem. Soc.*, 2014, **136**, 547–549.

170 H. J. Park, D.-W. Lim, W. S. Yang, T.-R. Oh and M. P. Suh, *Chem. - A Eur. J.*, 2011, **17**, 7251–7260.

171 Y. He, S. Xiang and B. Chen, *J. Am. Chem. Soc.*, 2011, **133**, 14570–14573.

172 S. J. Peighambardoust, S. Rowshanzamir and M. Amjadi, *Int. J. Hydrogen Energy*, 2010, **35**, 9349–9384.

173 M. Sadakiyo, T. Yamada, K. Honda, H. Matsui and H. Kitagawa, *J. Am. Chem. Soc.*, 2014, **136**, 7701–7707.

174 S. B. Tayade, S. S. Bhat, R. Illathvalappil, V. M. Dhavale, V. A. Kawade, A. S. Kumbhar, S. Kurungot and C. Näther, *CrystEngComm*, 2018, **20**, 1094–1100.

175 Q. Tang, Y. Liu, S. Liu, D. He, J. Miao, X. Wang, G. Yang, Z. Shi and Z. Zheng, *J. Am. Chem. Soc.*, 2014, **136**, 12444–12449.

176 M. Sadakiyo, T. Yamada, K. Honda, H. Matsui and H. Kitagawa, *J. Am. Chem. Soc.*, 2014, **136**, 7701–7707.

177 M. E. Briggs and A. I. Cooper, *Chem. Mater.*, 2017, **29**, 149–157.

178 A. D. Jenkins, P. Kratochvil, R. F. T. Stepto and U. W. Suter, *Pure Appl. Chem.*, 1996, **68**, 2287–231.

179 E. Macedi, A. Meli, F. De Riccardis, P. Rossi, V. J. Smith, L. J. Barbour, I. Izzo and C. Tedesco, *CrystEngComm*, 2017, **19**, 4704–4708.

180 H. Uekusa, K. Fujii, K. Johmoto, Y. Kikuchi, H. Takahagi, K. Ono, N. Iwasawa, Y. Miyauchi and K. Tanaka, *Acta Crystallogr. Sect. A Found. Adv.*, 2017, **73**, 792–792.

181 A. D. William, A. C.-H. Lee, A. Poulsen, K. C. Goh, B. Madan, S. Hart, E. Tan, H. Wang, H. Nagaraj, D. Chen, C. P. Lee, E. T. Sun, R. Jayaraman, M. K. Pasha, K. Ethirajulu, J. M. Wood and B. W. Dymock, *J. Med. Chem.*, 2012, **55**, 2623–2640.

182 E. M. M. Abdelraheem, S. Khaksar, K. Kurpiewska, J. Kalinowska-Tłuścik, S. Shaabani and A. Dömling, *J. Org. Chem.*, 2018, **83**, 1441–1447.

183 W. Zhang and J. S. Moore, *Angew. Chemie Int. Ed.*, 2006, **45**, 4416–4439.

184 C. Grave and A. D. Schlüter, *European J. Org. Chem.*, 2002, **2002**, 3075–3098.

185 P. V. Bernhardt, J. Y. Kim, Y. Kim, Y. H. Lee and S. Chow, *Comptes Rendus Chim.*, 2005, **8**, 211–214.

186 M. Iyoda, J. Yamakawa and M. J. Rahman, *Angew. Chemie Int. Ed.*, 2011, **50**, 10522–10553.

187 T. Ogoshi, S. Kanai, S. Fujinami, T. Yamagishi and Y. Nakamoto, *J. Am. Chem. Soc.*, 2008, **130**, 5022–5023.

188 Y. Ma, X. Chi, X. Yan, J. Liu, Y. Yao, W. Chen, F. Huang and J.-L. Hou, *Org. Lett.*, 2012, **14**, 1532–1535.

189 N. L. Strutt, H. Zhang and J. F. Stoddart, *Chem. Commun.*, 2014, **50**, 7455.

190 W. A. Freeman, *Acta Crystallogr. Sect. B Struct. Sci.*, 1984, **40**, 382–387.

191 A. I. Day, R. J. Blanch, A. P. Arnold, S. Lorenzo, G. R. Lewis and I. Dance, *Angew. Chemie Int. Ed.*, 2002, **41**, 275-276.

192 X.J. Cheng, L.L. Liang, K. Chen, N.N. Ji, X. Xiao, J.X. Zhang, Y.Q. Zhang, S.F. Xue, Q.-J. Zhu, X.-L. Ni and Z. Tao, *Angew. Chemie*, 2013, **125**, 7393–7396.

193 D. Fujita, Y. Ueda, S. Sato, H. Yokoyama, N. Mizuno, T. Kumasaka and M. Fujita, *Chem*, 2016, **1**, 91–101.

194 Q.F. Q.F. Sun, J. Iwasa, D. Ogawa, Y. Ishido, S. Sato, T. Ozeki, Y. Sei, K. Yamaguchi and M. Fujita, *Science*, 2010, **328**, 1144–1147.

195 D. Fujita, Y. Ueda, S. Sato, N. Mizuno, T. Kumasaka and M. Fujita, *Nature*, 2016, **540**, 563–566.

196 R. Elghanian, J. J. Storhoff, R. C. Mucic, R. L. Letsinger and C. A. Mirkin, *Science*, 1997, **277**, 1078–81.

197 M. Maeda, *Polym. J.*, 2006, **38**, 1099–1104.

198 M. Hong, X. Zhou, Z. Lu and J. Zhu, *Angew. Chemie Int. Ed.*, 2009, **48**, 9503–9506.

199 C. J. Hastings, R. G. Bergman and K. N. Raymond, *Chem. - A Eur. J.*, 2014, **20**, 3966–3973.

200 Y. Liu, X. Wu, C. He, Y. Jiao and C. Duan, *Chem. Commun.*, 2009, **0**, 7554-7559.

201 S. Hong, M. Oh, M. Park, J. W. Yoon, J. S. Chang and M. S. Lah, *Chem. Commun.*, 2009, **0**, 5397-5399.

202 R. Yun, J. Duan, J. Bai and Y. Li, *Cryst. Growth Des.*, 2013, **13**, 24–26.

203 A. C. Sudik, A. R. Millward, N. W. Ockwig, A. P. Côté, J. Kim and O. M. Yaghi, *J. Am. Chem. Soc.*, 2005, **127**, 7110–7118.

204 P. Muller, *GLOSSARY OF TERMS USED IN PHYSICAL ORGANIC CHEMISTRY*, 1994, **66**, 1077, 1094-1094.

205 T. Friščić, *Chem. Soc. Rev.*, 2012, **41**, 3493–3510.

206 T. Tozawa, J. T. A. Jones, S. I. Swamy, S. Jiang, D. J. Adams, S. Shakespeare, R. Clowes, D. Bradshaw, T. Hasell, S. Y. Chong, C. Tang, S. Thompson, J. Parker, A. Trewin, J. Bacsa, A. M. Z. Slawin, A. Steiner and A. I. Cooper, *Nat Mater*, 2009, **8**, 973–978.

207 Q. Song, S. Jiang, T. Hasell, M. Liu, S. Sun, A. K. Cheetham, E. Sivaniah and A. I. Cooper, *Adv. Mater.*, 2016, **28**, 2629–2637.

208 T. Hasell, M. Miklitz, A. Stephenson, M. A. Little, S. Y. Chong, R. Clowes, L. Chen, D. Holden, G. A. Tribello, K. E. Jelfs and A. I. Cooper, *J. Am. Chem. Soc.*, 2016, **185**, 1653–1659.

209 L. Guy, J.-P. Dutasta and A. Martinez, *Endohedral Functionalization of Molecular Cavities for Catalysis in Confined Spaces*, 2017.

210 Q. Shi, M. Sun, J. Tian, W. Zhang and G. Yang, *Comput. Theor. Chem.*, 2017, **1120**, 1–7.

211 T. Hasell, M. A. Little, S. Y. Chong, M. Schmidtmann, M. E. Briggs, V. Santolini, K. E. Jelfs, A. I. Cooper, A. Trewin, F. Schiffman, F. Cora, B. Slater, A. Steiner, G. M. Day, A. I. Cooper, J. Liu, D. M. Strachan, P. K. Thallapally and A. I. Cooper, *Nanoscale*, 2017, **9**, 6783–6790.

212 A. Kewley, A. Stephenson, L. Chen, M. E. Briggs, T. Hasell and A. I. Cooper, *Chem. Mater.*, 2015, **27**, 3207–3210.

213 K. E. Jelfs, X. Wu, M. Schmidtmann, J. T. A. Jones, J. E. Warren, D. J. Adams and A. I. Cooper, *Angew. Chemie Int. Ed.*, 2011, **50**, 10653–10656.

214 M. E. Belowich and J. F. Stoddart, *Chem. Soc. Rev.*, 2012, **41**, 2003.

215 Y. Jin, Q. Wang, P. Taynton and W. Zhang, *Acc. Chem. Res.*, 2014, **47**, 1575–1586.

216 V. Martí-Centelles, M. D. Pandey, M. I. Burguete and S. V. Luis, *Chem. Rev.*, 2015, **115**, 8736–8834.

217 R. L. E. Furlan, S. Otto and J. K. M. Sanders, *PNAS*, 2002, **99**, 4801–4804.

218 P. Taynton, K. Yu, R. K. Shoemaker, Y. Jin, H. J. Qi and W. Zhang, *Adv. Mater.*, 2014, **26**, 3938–3942.

219 E. H. Cordes and W. P. Jencks, *J. Am. Chem. Soc.*, 1962, **84**, 832–837.

220 M. Ciaccia, R. Cacciapaglia, P. Mencarelli, L. Mandolini and S. Di Stefano, *Chem. Sci.*, 2013, **4**, 2253-2261.

221 M. Ciaccia and S. Di Stefano, *Org. Biomol. Chem.*, 2015, **13**, 646–654.

222 Y. Jin, C. Yu, R. J. Denman and W. Zhang, *Chem. Soc. Rev.*, 2013, **42**, 6634-6654.

223 C. Saiz, P. Wipf, E. Manta and G. Mahler, *Org. Lett.*, 2009, **11**, 3170–3173.

224 G. Zhang, O. Presly, F. White, I. M. Oppel and M. Mastalerz, *Angew. Chem. Int. Ed. Engl.*, 2014, **53**, 1516–1520.

225 N. Christinat, R. Scopelliti and K. Severin, *Angew. Chemie Int. Ed.*, 2008, **47**, 1848–1852.

226 M. Hutin, G. Bernardinelli and J. R. Nitschke, *Chem. - A Eur. J.*, 2008, **14**, 4585–

4593.

227 H.-E. Högberg, B. Thulin and O. Wennerström, *Tetrahedron Lett.*, 1977, **18**, 931–934.

228 F. Vögtle, J. Gross, C. Seel and M. Nieger, *Angew. Chemie Int. Ed. English*, 1992, **31**, 1069–1071.

229 S. Kammermeier, P. G. Jones and R. Herges, *Angew. Chemie Int. Ed. English*, 1996, **35**, 2669–2671.

230 D. J. Cram, S. Karbach, Y. H. Kim, L. Baczynskyj and G. W. Kallemeyn, *J. Am. Chem. Soc.*, 1985, **107**, 2575–2576.

231 American Chemical Society. and Marian S. Carson Collection (Library of Congress), *Journal of the American Chemical Society.*, [American Chemical Society], 1879.

232 Z. Wu, S. Lee and J. S. Moore, *J. Am. Chem. Soc.*, 1992, **114**, 8730–8732.

233 S. T. Schneebeli, M. Frasconi, Z. Liu, Y. Wu, D. M. Gardner, N. L. Strutt, C. Cheng, R. Carmieli, M. R. Wasielewski and J. F. Stoddart, *Angew. Chemie Int. Ed.*, 2013, **52**, 13100–13104.

234 A. Avellaneda, P. Valente, A. Burgun, J. D. Evans, A. W. Markwell-Heys, D. Rankine, D. J. Nielsen, M. R. Hill, C. J. Sumby and C. J. Doonan, *Angew. Chemie Int. Ed.*, 2013, **52**, 3746–3749.

235 G. R. Desiraju, *Angew. Chemie Int. Ed. English*, 1995, **34**, 2311–2327.

236 S. Saha and G. R. Desiraju, *J. Am. Chem. Soc.*, 2017, **139**, 1975–1983.

237 B. Moulton and M. J. Zaworotko, *Chem. Rev.*, 2001, **101**, 1629–1658.

238 G. R. Desiraju, *Angew. Chemie Int. Ed. English*, 1995, **34**, 2311–2327.

239 P. Metrangolo, F. Meyer, T. Pilati, G. Resnati and G. Terraneo, *Angew. Chemie Int. Ed.*, 2008, **47**, 6114–6127.

240 G. R. Desiraju, *Acc. Chem. Res.*, 2002, **35**, 565–573.

241 G. R. Desiraju, *Angew. Chem. Int. Ed. Engl.*, 2007, **46**, 8342–8356.

242 T. Hasell, S. Y. Chong, M. Schmidtmann, D. J. Adams and A. I. Cooper, *Angew. Chemie Int. Ed.*, 2012, **51**, 7154–7157.

243 J. T. A. Jones, D. Holden, T. Mitra, T. Hasell, D. J. Adams, K. E. Jelfs, A. Trewin, D. J. Willock, G. M. Day, J. Bacsa, A. Steiner and A. I. Cooper, *Angew. Chemie*, 2011, **123**, 775–779.

244 T. Hasell, J. L. Culshaw, S. Y. Chong, M. Schmidtmann, M. A. Little, K. E. Jelfs, E. O. Pyzer-Knapp, H. Shepherd, D. J. Adams, G. M. Day and A. I. Cooper, *J. Am. Chem. Soc.*, 2014, **136**, 1438–48.

245 R. Schlesser, R. Dalmau and Z. Sitar, *J. Cryst. Growth*, 2002, **241**, 416–420.

246 Nobel Media AB 2014, Wilhelm Conrad Röntgen - Biographical, https://www.nobelprize.org/nobel_prizes/physics/laureates/1901/rontgen-bio.html, (accessed 5 June 2018).

247 D. C. Phillips, *Biogr. Mem. Fellows R. Soc.*, 1979, **25**, 74–143.

248 G. M. Sheldrick, *Acta Crystallogr. Sect. A Found. Crystallogr.*, 2008, **64**, 112–122.

249 G. M. Sheldrick, Z. Dauter, K. S. Wilson, H. Hope and L. C. Sieker, *Acta Crystallogr. Sect. D Biol. Crystallogr.*, 1993, **49**, 18–23.

250 R. A. Crowther, D. M. Blow and IUCr, *Acta Crystallogr.*, 1967, **23**, 544–548.

251 M. Hoshino, A. Khutia, H. Xing, Y. Inokuma and M. Fujita, *IUCrJ*, 2016, **3**, 139–51.

252 J. W. Steed, *Supramol. Chem.*, 2015, **27**, 731–733.

253 A. Bialas, *Phys. J.*, 1998, **54**, 641–642.

254 A. Pulido, L. Chen, T. Kaczorowski, D. Holden, M. A. Little, S. Y. Chong, B. J. Slater, D. P. McMahon, B. Bonillo, C. J. Stackhouse, A. Stephenson, C. M. Kane, R. Clowes, T. Hasell, A. I. Cooper and G. M. Day, *Nature*, 2017, **543**, 657–664.

255 F. H. Allen, *Acta Crystallogr. Sect. B Struct. Sci.*, 2002, **58**, 380–388.

256 P. Parois, R. I. Cooper and A. L. Thompson, *Chem. Cent. J.*, 2015, **9**, 30, 1-14.

257 P. Müller, *Crystallogr. Rev.*, 2009, **15**, 57–83.

258 C. Giacovazzo, *Fundamentals of crystallography*, Oxford University Press, 2002.

259 P. Müller, R. Herbst-Irmer, A. L. Spek, T. R. Schneider and M. R. Sawaya, *Crystal Structure Refinement*, Oxford University Press, 2006.

260 J. R. Helliwell, *Crystallogr. Rev.*, 2008, **14**, 189–250.

261 A. L. Spek, *Acta Crystallogr. Sect. C, Struct. Chem.*, 2015, **71**, 9–18.

# Chapter 2

## Cage doubling: Solvent mediated re-equilibration of a [3+6] prismatic organic cage to a large [6+12] truncated tetrahedron

# 1 Introduction

## 1.1 Tubular Organic Cages

*This results presented in this chapter were published in Crystal Growth & Design.*[1]

Porous organic cages (POCs) possess internal cavities, referred to as intrinsic pores, which can be accessed through openings in the cage structure, known as cage windows. Pore channels are determined by the manner in which the POCs pack in the solid state.[2] Two common ways in which cages have been observed to pack together in the crystal structure are window to window (WTW), or window to edge (WTE), which determines the packing mode, or crystal packing.[3] If the cages pack WTW, then channels are formed throughout the structure allowing the diffusion of guests. However, if the cages pack WTE, this effectively removes those channels and so the material is unlikely to exhibit the same, if any, porosity.[4] As discussed in Chapter 1 section 4.1, the WTW crystal packing of **CC3** forms a diamondoid network throughout, resulting in the high $SA_{BET}$ and guest uptake properties.

As well as their inherent intrinsic porosity, POCs can also exhibit extrinsic porosity as a direct result of inefficient packing between cages in the solid state. This arises from the bulky substituents, or vertices, of the cage shell, which prevent POCs packing close together in their crystalline state. For example, in 2016 Reiss et al*.* reported a POC decorated with anthracene groups, which promote packing inefficiency, and hence increase the extrinsic void space.[5] Amorphous **CC3** was found to have an increased surface area compared with the porous, crystalline phase.[6] This was related directly to the greater extrinsic porosity, however not all amorphous cages are subject to the same increase in surface area when crystallinity is lost. There are two potential routes to the formation of molecules that have altered functionality; alternative starting materials (SMs), or crystal engineering to change the packing mode in the solid state.[7,3]

In 2017, Slater et al. reported a new family of crystalline POCs, referred to as, **TCCX**$_{[3+6]}$ (where **X** = 1, 2 or 3, **Figure 1**), synthesised using chirally pure *trans*-1,2-dicyclohexadiamine (CHDA) and tetraaldehydes **F**, **G**, or **H**

(**Figure 1**). These trigonal primastic cages have the ability to form 1D pore channels when co-crystallised with their respective enantiomer due to chiral recognition, introduced in Chapter 1.[8,9] Cage chirality for the trigonal prismatic **TCC** cages can be visualised in **Figure 1**, showing the *R,R*-cages, with the cages 'twisting' to the right hand side.

By altering the 3-fold, 1,3,5-substituted aldehyde triformylbenzene (TFB), to the 2-fold, 1,3-substituted tetraaldehydes there is a dramatic change in topology, however it is not always obvious what the resulting topology would be. Slater et. al. found that as well as changing the cage topology, by increasing the length of the aldehyde linker it was possible to increase the length of the tubular cage.[10] The aldehyde linkers were increased by incorporating phenyl and alkyne groups, shown in **Figure 1**.

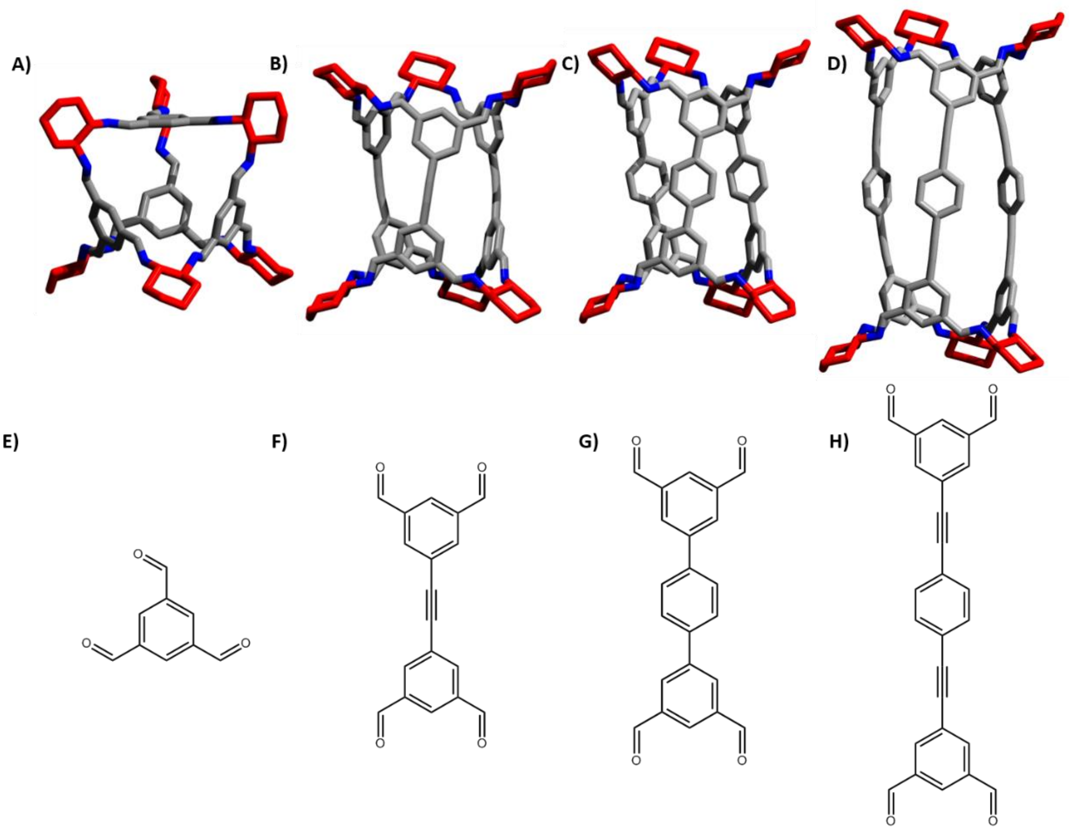

**Figure 1** Crystal structures of A) **CC3**-*R*; B) **TCC1**-*R*$_{[3+6]}$; C) **TCC2**-*R*$_{[3+6]}$; D) **TCC3**-*R*$_{[3+6]}$. Chemical structure of the corresponding aldehydes used to synthesises the cages, E) 1,3,5-triformylbenzene (TFB); F) 5,5'-(ethyne-1,2-diyl)diisophthalaldehyde; G) [1,1':4',1''-terphenyl]-3,3'',5,5''-tetracarbaldehyde; H) 5,5'-(1,4-phenylenebis(ethyne-2,1-diyl))diisophthalaldehyde.

The tubular cages have a flexible nature, with the most flexible cage being **TCC3**, due to the increased length of the aldehyde linker. Upon desolvation, 'breathing' of the molecules was observed, shown by **TCC3**-*R* in **Figure 2**. The aldehyde linker from the top of the phenyl rings measured 16.3 Å with an angle of 165.1 ° in the solvated structure, and 16.3 Å and 175.2 ° when desolvated. Angles were measured from the top of each aldehyde to the base. In the desolvated structure, the aldehyde linkers bent into the cage, whereas in the solvated they bent outwards. The **TCC** cages were shown to also behave as ultra-fast molecular rotors, which is attributed to the flexibility of the cages and their 'breathing' behaviour.[11]

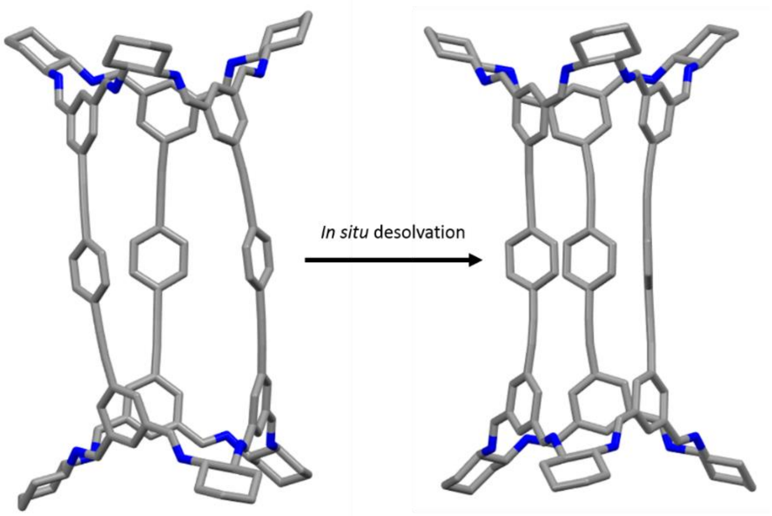

**Figure 2** Flexible breathing observed in **TCC3**-*R*, found during *in situ* desolvation.

## *1.2 Cage Topology*

The concept of reticular design for topology or geometry isn't new, with other research highlighting its application for the design of new MOFs.[12] The ability to target topologies *a priori* allows chemists to design new materials with specific structure-property relationships.[13] For example, in 2003 Yaghi introduced an isoreticular series of MOFs which exhibited the same cubic framework topology, but with increased pore volume by lengthening the organic ligands used.[14]

Zou et al. discussed topology-directed synthesis of porous organic frameworks (POFs).[15] For example, they demonstrated that as opposed to a trial and error approach, the topology of POFs can be directed by the geometry and symmetry of the tectons used. For example, a 3D diamondoid network can be directed by using a tetrahedral tecton, thus generating a porous framework.[16,17] They further discussed that a planar framework, for example a covalent organic framework (COF), can be directed using either a 'triangular' tecton or 'square' unit. For example, a combination of three-fold symmetrical tectons and linear linkers would generate a hexagonal framework, whereas a four-fold tecton with the same linear linker would form a square framework (**Figure 3**).[18]

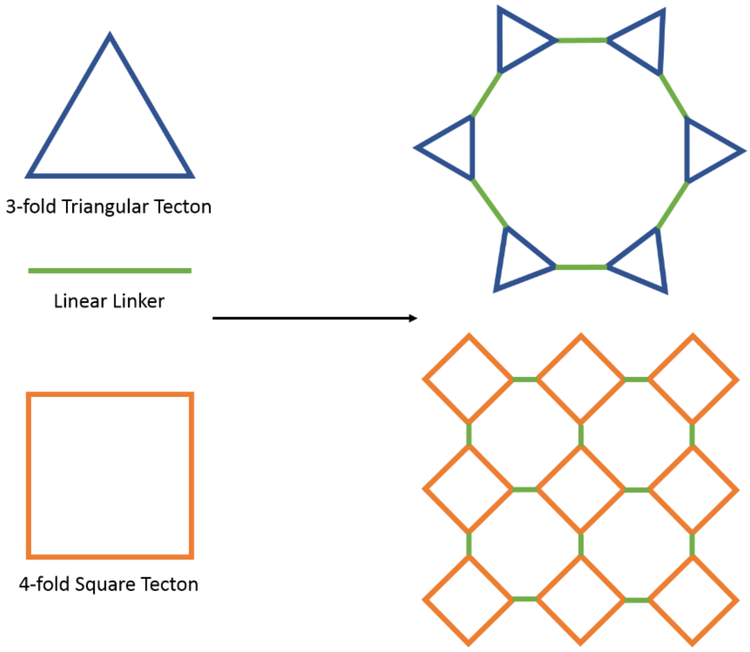

**Figure 3** Topology directed design of frameworks based on the symmetry of the tectons.

Comparatively, this same reticular design for organic molecular cages (OMCs) is an ambitious and difficult task. In 2017, Santolini et al. demonstrated that cage topology wasn't influenced by only the bond angles and length of the tectons, but also the number of functional groups.[19] In this study, a tecton with 2 functional groups is notarised as 'Di' and 3 functional groups as 'Tri'; for example **CC3**, shown in **Figure 1**, has Tri$^4$Di$^6$ topology. Their work highlighted that for the same topology, e.g., Tri$^4$Di$^6$ (4 tritopic molecules with 6 ditopic molecules), multiple geometries are accessible. Whereas topology describes the underlying connectivity of the 'skeleton' of the cage, geometry refers to its overall shape. For example, **CC3** has a tetrahedron topology, taking the centre of the highest contributing tecton, in this case the aldehyde, as the corner of the 'skeleton'.

**Figure 4** illustrates the number of geometries available from the same SMs. Despite the SMs resulting in one topology, i.e. the 'back bone' of the structure, which in this case is a tetrahedron, 6 different geometrical shapes can arise. Therefore, topological and geometrical control isn't an easy task which can be influenced by bond angles, bond lengths or functional groups alone, and reaction conditions can play a significant role.[20–22]

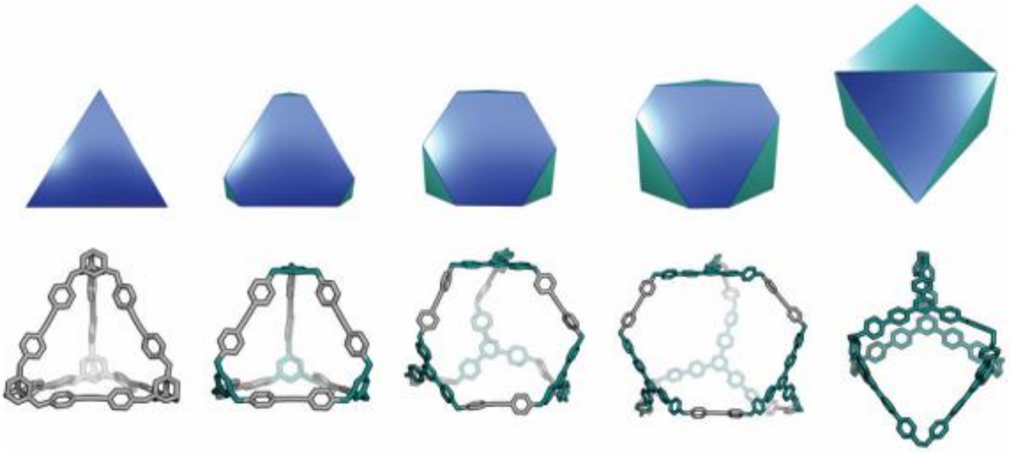

**Figure 4** Tri$^4$Di$^6$ cage topology, the same topology results in a significant number of cage geometries. Figure re-used with permission from V. Santolini, M. Miklitz, E. Berardo and K. E. Jelfs, *Nanoscale*, 2017, **9**, 5280–5298, published by The Royal Society of Chemistry.

## 1.3 Solvent-Mediated Reactions

The structure of multi-component assemblies, which are synthesised under reversible bond formation, are governed by the bond angles and symmetry of the molecular tectons, *i.e.* building blocks, which can assemble in a specific way to form a 3-dimensional molecule.[2] For example, we have shown that by using the 2-fold symmetrical linear linkers in the **TCC** series, trigonal prismatic cages were synthesised, whereas when using a 3-fold linker a tetrahedral cage is generated.[10]

Metal organic polyhedra (MOPs) have been shown to undergo topological changes when exposed to alternative experimental conditions, such as Zhou et. al. who demonstrated that by performing the reaction under solvothermal conditions generated a 38 component MOP, whereas under milder reaction conditions a 62 component MOP.[23] Subtle changes such as a small change in the ligand bend angle can also have a dramatic change in MOP topology or size.[24] The Fujita group showed that by a change in the mean bond angle of two ligands, from 133.6 ° to 131.4 ° resulted in a change from the $M_{24}L_{48}$ cage being formed, to the smaller $M_{12}L_{24}$ polyoxylemetallate.[25]

Comparatively, discrete organic species such as OMCs, have rarely been shown to undergo such dramatic changes in topology with similarly subtle changes. It is possible for POCs to undergo re-equilibration from one molecule, either a kinetic or false local-minimum, to the true thermodynamically stable species, shown through computational analyses.[26] **CC1**, a POC synthesised from TFB and 1,2-ethylenediamine, has been shown experimentally to transform dramatically from a discrete, organic cage into a triply interlocked catenane, either in the presence of an acid catalyst or through re-equilibration in a directing solvent, such as *o*-xylene.[27] Typically, only when a significant adjustment, such as the alteration of one or more linkers has been made do we observe a substantial change in molecular topology, for example Jelfs et. al. calculated that by increasing the length of the diamine linker, from ethane to pentane the cage topology changes.[5,28]

Illustrated in **Figure 5** is the work by Warmuth et al., where they demonstrated that in multiple nanocages with alternative stoichiometric equivalents could be formed from the same SMs.[29,30] **Figure 5** shows a simple schematic with the 2 SMs, tetraformylcavitand (**2**) and ethylene1,2-diamine (**3**). When the reaction was performed in $CHCl_3$, the octahedral nanocage **1** was preferentially formed in an 82 % yield. In THF, an alternative topological cage, the tetrameric nanocage **4** was synthesised in a 35% yield, and in DCM the square antiprismatic cage, nanocage **5** had a yield of 65%. All cages were then further reduced, using sodium borohydride ($NaBH_4$) and TFA, resulting in the nanocages **6** – **8**. The cages were isolated using preparative high performance liquid chromatography (prep-HPLC) and characterised using NMR.

Other research from Warmuth has shown that by changing the stoichiometry of the SMs results in the formation of two different nanocages. As well as stoichiometry, the solvent had a significant impact on the formation of the cages; with the authors proposing that the interaction between the solvent and the surface of the nanocages stabilises the formation.[30]

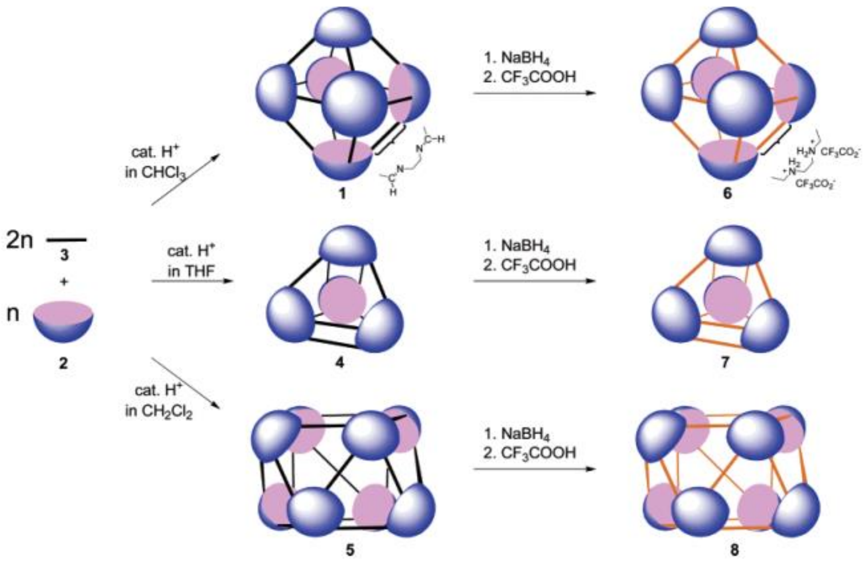

**Figure 5** Cages 1-4 were formed from the same SMs but under different conditions. Reprinted with permission from X. Liu and R. Warmuth, *J. Am. Chem. Soc.*, 2006, **43**, 14120–14127. Copyright 2006 American Chemical Society.

## 1.4 Cage Scrambling

In 2011 the Cooper group showed that two cages can undergo ‘scrambling’ when dissolved in the same solution, a process where the vertices of two cages exchange to form multiple cage species.[31] Whereas Warmuth demonstrated solvent-mediated reactions which change nanocage topology and size, cage scrambling generates new cage species through the reversible nature of imine chemistry. By exploiting the dynamic nature of the imine cages, new cage molecules with improved properties, for example, improved solubility, shown in **Figure 6**. The new cages were synthesised from ethylenediamine (EDA, **CC1**) and TFB (**CC3**).

Giri et al. demonstrated that it was possible to generate a liquid material with permanent porosity from scrambled cages.[32] Scrambled cages have improved solubility in organic solvents than cages synthesised from a single diamine.[33] The scrambled cages were dissolved in crown ether, a bulky size-excluding solvent, too large to pass through the cage windows, enabling gas to diffuse through the liquid and be encapsulated by the cages.

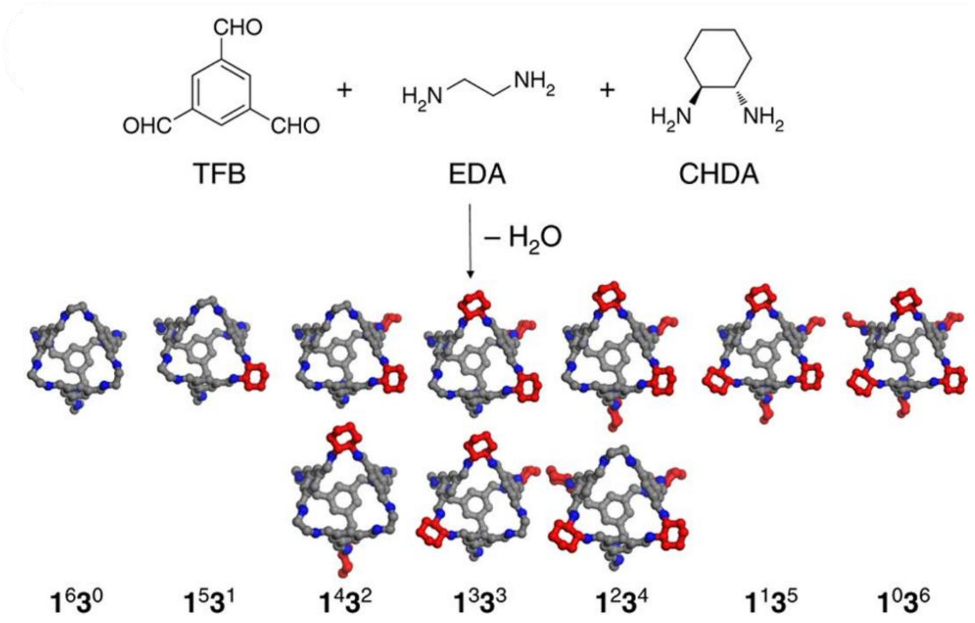

**Figure 6** Scrambled cages synthesised from SMs for **CC1** and **CC3**. Reprinted with permission from Nature: Nature Communications, Porous organic molecular solids by dynamic covalent scrambling, Shan Jiang *et. al.* Copyright 2011.

Cage scrambling further illustrates the dynamic nature of imine-bonded organic cages, something we aim to exploit in this chapter. This chapter explores the re-equilibration of a trigonal prismatic cage to a larger, truncated tetrahedron cage and how the reaction has been optimised to further understand the reaction which takes place. Computational rationalisation has been employed to provide further understanding into the formation of this molecular species.

*N.B Computational calculations were carried out by Valentina Santolini.*

# 2 Results & Discussion

## 2.1 Crystal Engineering: Co-Crystallisations with Organic Cages

As discussed in Chapter 1, cages can undergo crystal packing changes through crystal engineering, as opposed to attempting synthesis from alternative tectons. For example, **CC1** is known as a solvatomorphic cage, with 8 solvate polymorphs reported.[34] Cage co-crystallisations have also yielded impressive results, with ternary co-crystals involving **CC1**, **CC4** and **CC3** yielding microporous solids which show varied gas uptake dependent on the amount of **CC4** present in the alloy.[9]

Four solutions of **CC1**, **CC4**-*R*, **TCC1**-*S* and **TCC3**-*S* were set up in $CHCl_3$ with a concentration of 1 $mgmL^{-1}$, and co-crystallisations were set up with varying stoichiometric ratios with respect to the number of cages windows. For example, the **TCC** cages had 2 windows, whereas **CC1** and **CC4** have 4. Therefore attempts were made to enhance window to window interactions, with the cages either 1:1 or 2:1.

All chromatographs were recorded from recrystallisation, using MeOH for the mobile phase. **Co**-crystallisations were set-up using **TCC1** and **TCC3** with **CC1** and **CC4** (**Figure 7**), attempting to form a porous co-crystal with a tetrahedral network. **CC1** and **CC4** show diamonded networks when crystallised under particular recrystallisation conditions.[35,34] Hence, incorporating the tubular cages, **TCC1** and **TCC3**, to the tetrahedral **CC1** and **CC4**-*R* could create alternative networks by exploiting the two cage topologies. Typically, cages will begin to crystallise after a period of 7 days, however after this time the crystallisation experiments did not yield any precipitate, crystalline or otherwise. Therefore, high performance liquid chromatography (HPLC) was utilised, to provide insight into any processes occurring such as co-crystallisation, scrambling or if the cages show no interaction whatsoever.

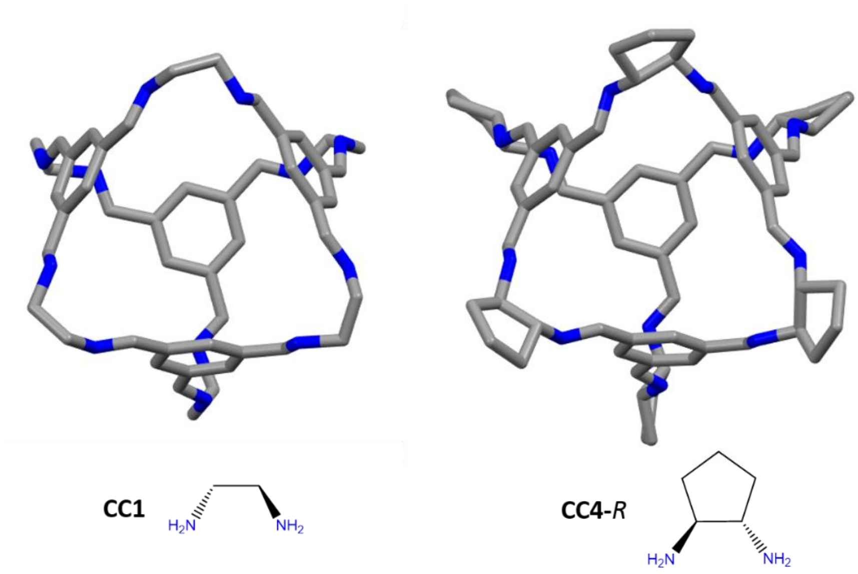

**Figure 7** Molecular structures of **CC1** and **CC4**-*R*, and the diamines which form the cage vertices.

Shown in **Figure 8** are the chromatographs for **CC1** and **TCC1**-*S*. The black line shows only one peak, which corresponds to the cage, **CC1**. The red line also shows one major peak corresponding to the cage, **TCC1**-*S*. The blue line represents the mixture after 24 hours, showing that **CC1** has split into multiple peaks across the region, and the relative amount of **TCC1** has decreased. This splitting is indicative of cage scrambling, with each peak corresponding to each cage with alternative vertices. After 2 days, more peaks are visible between the two regions where **CC1** and **TCC1**-*S* elute. The most likely explanation for this is that the cages scramble when they are mixed in solution.[31] As discussed earlier, cage scrambling is a result of DCC, whereby the dynamic reversibility of the imine bond in solution causes the cage vertices to interchange.

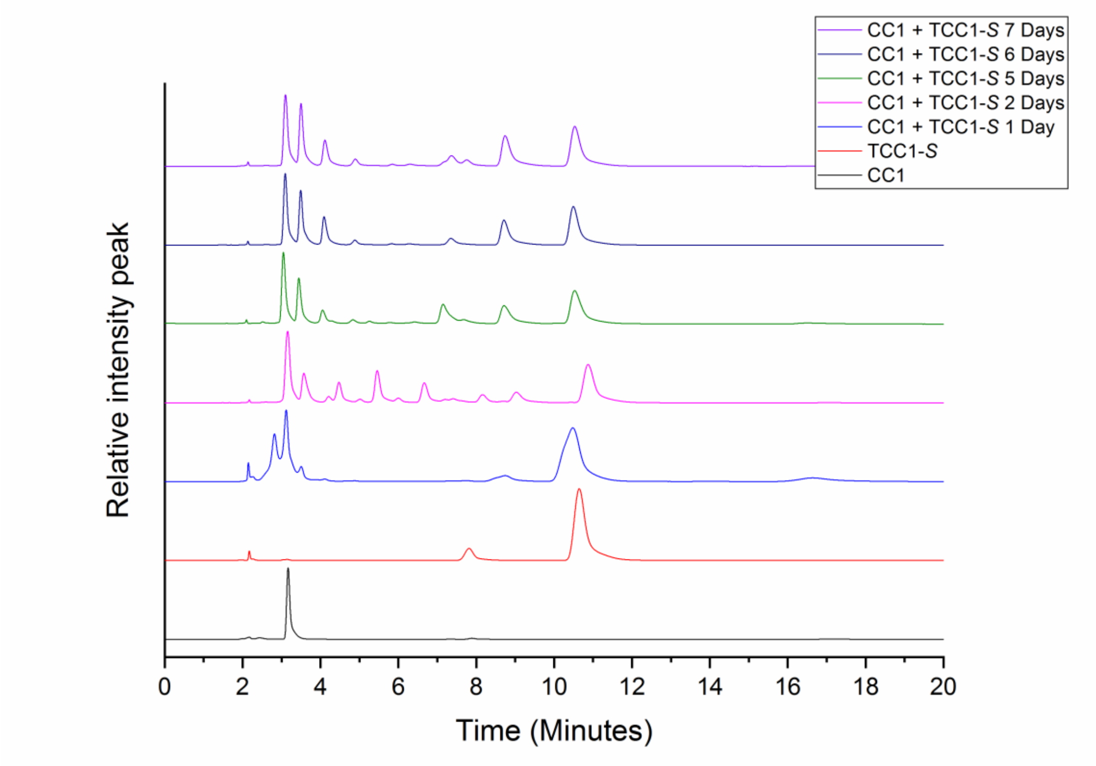

**Figure 8** Co-crystallisations of **CC1** and **TCC1**-*S*, with the top four chromatograph traces showing cage scrambling.

By comparison, the chromatographs of **CC4**-*R* and **TCC1**-*S* (**Figure 9**) only contain the two peaks, which correspond to the co-former cages. This implies that both cages are not interacting in solution, whether that be scrambling or co-crystallising. We see the same results when comparing **TCC3-***S* with **CC1** and **CC4-***R*; **TCC3**-*S* scrambled with **CC1**, but not **CC4**-*R*.

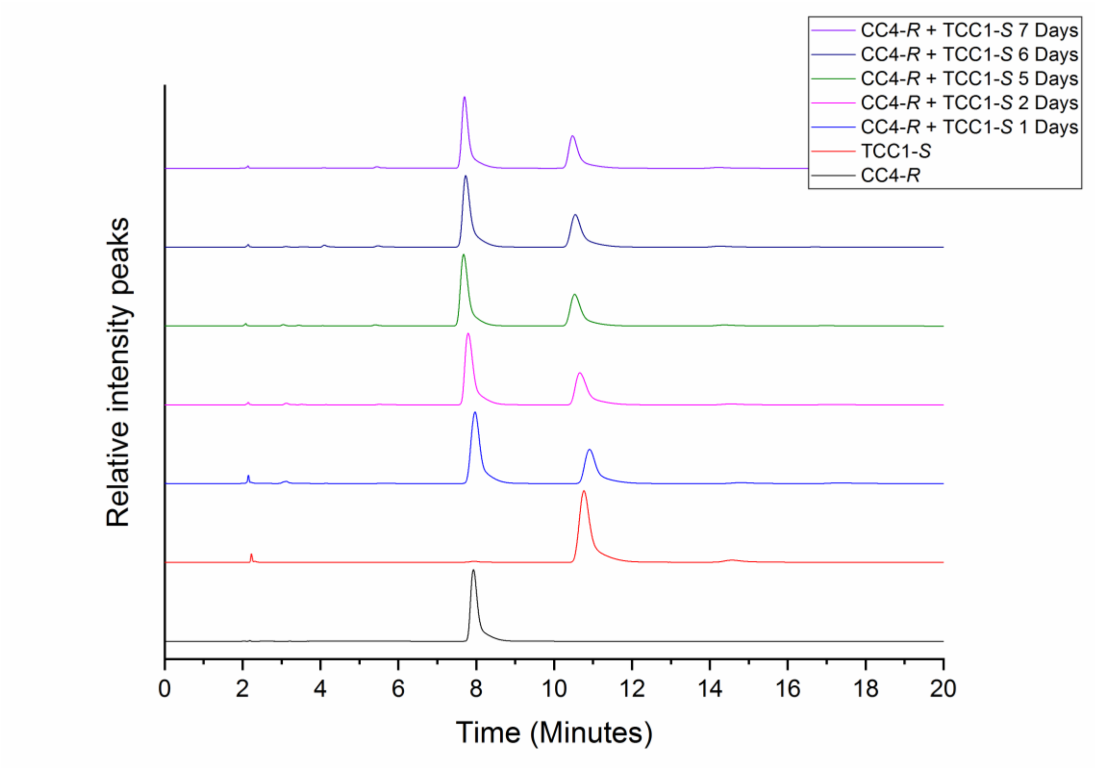

**Figure 9** Co-crystallisations of **CC4**-*R* with **TCC1**-*S*, showing no change in the number of peaks after a period of 1 week.

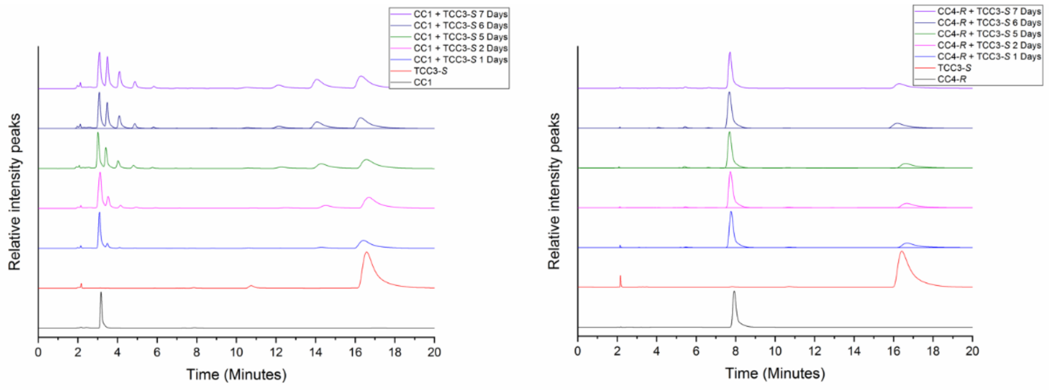

**Figure 10** Left: **CC1** co-crystallisation with **TCC3**-*S*; Right: **CC4** co-crystallisation with **TCC3**-*S*.

Work highlighted earlier in this chapter with scrambled cages showed **CC1** and **CC3** scrambled to form a series of cages which had improved sorption through desymmterisation and decreased packing efficiency.[31] With the tubular cages, it was observed that the flexible diamine vertices of **CC1** exchanging with the chirally pure cyclohexane diamine vertices of both **TCC1**-*S* and **TCC3**-*S*.

The rate determining step for cage scrambling is dependent upon the formation of an amine from the imine cages, and nucleophilic attack to another cage. All scrambling experiments were performed in aqueous solvents, with no addition of extra water or an acid catalyst. The amine used for the synthesis of **CC1**, EDA, has considerably less steric hindrance than that used for the synthesis of **CC4**, cyclopentanediamine. This leads us to believe that in these experiments we didn't see any scrambling between the **TCC** cages and **CC4** as a result of **CC4** being considerably less susceptible to nucleophilic attack, and **CC1** was more sensitive to nucleophilic attack from the small amount of water present in the solvent.

## *2.2 Crystal Engineering: Co-crystallisation with an Irreversible Cage*

As we observed cage scrambling when using the imine-bonded cages, the next step considered was to move forward with the co-crystallisation experiments using a non-reversible cage. Formaldehyde tied reduced **CC3** (**FT-RCC3**) is an irreversible, amine-bonded cage.[36] Unlike other series of POCs published by the group which contain reversible imine bonds (**Figure 11**) the cage is synthesised by initially reducing the imine bonds in **CC3**-*R/S* to form amines, which are them reacted with formaldehyde to form rigid aminal rings. The reduction of the imine removes the dynamic nature of the cages, also making them stable to acidic and basic conditions. **FT-RCC3**-*R* exhibits similar crystal packing and topology as **CC3**, which is known to form co-crystals with **TCC1**$_{[3+6]}$.[10] Chemically, the difference between the imine and amine bonded cages is that the latter are stable under acidic and basic conditions.

A series of 26 recrystallisation experiments were carried out with **FT-RCC3** in both DCM and $CHCl_3$, with 13 anti-solvents, aiming to identify a solvent system which would yield polymorphic **FT-RCC3**-*R*. The teal line shows **FTRCC3**-*R* in DCM, *o*-xylene. The difference implies that this is a different crystal phase, therefore could be a good choice for the co-crystallisation experiment. A single crystal structure of this phase was also obtained, and found to crystallise in a Monoclinic *P* space group. The structure was layered cages with solvent between the cages, however due to significant disorder it was difficult to determine the space group.

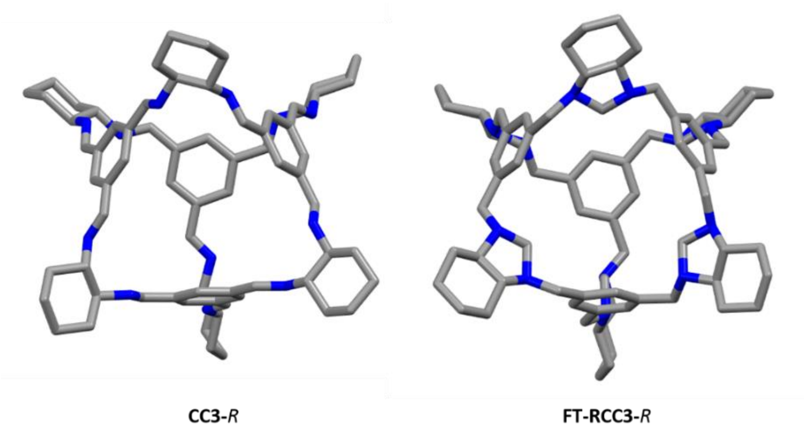

**Figure 11** Molecular structures of **CC3**-*R* and **FT-RCC3**-*R*, showing the same cage topology and geometry.

**FT-RCC3** is isolated as a crystalline solid directly from synthesis (navy line, **Figure 12**). **FT-RCC3**-*R* from reaction is isostructural to **CC3**-*R*, crystallising in the space group $F4_132$ with WTW packing throughout. Therefore, we needed to screen a series recrystallisation conditions, which wouldn't prevent co-crystallisation with other cage species by identifying polymorphs of **FT-RCC3**-*R* which would promote interactions, specifically WTW chiral recognition, between **FT-RCC3-***R* and other cage species.

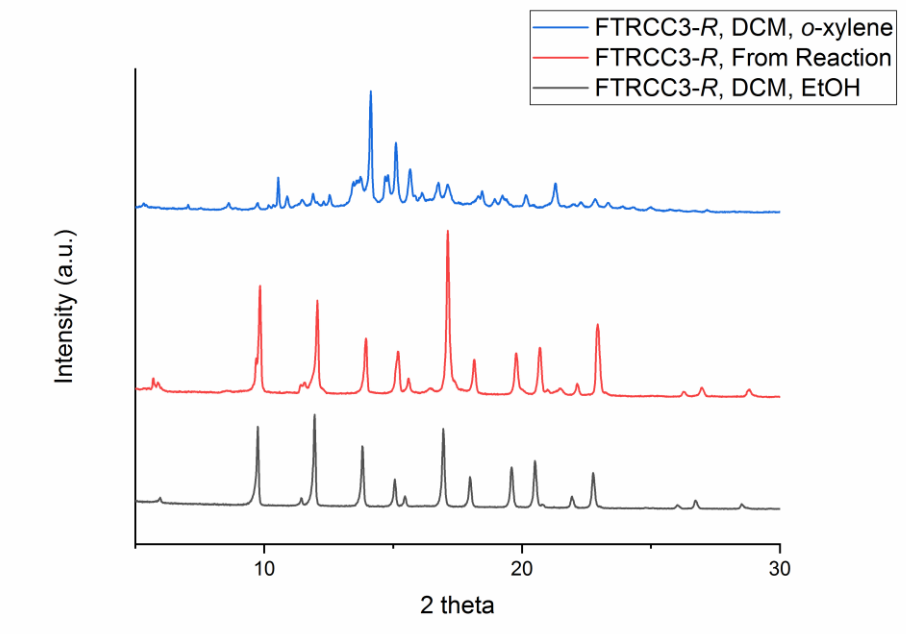

**Figure 12** Powder X-ray diffraction (PXRD) patterns of **FTRCC3**-*R*, the bottom pattern in navy is the cubic ($F4_132$) phase isolated directly from synthesis, and the top in teal is the monoclinic phase.

Co-crystallisations of **TCC1**-*S*/**TCC1**-*R* and **FT-RCC3**-*R*/**FT-RCC3**-*S* were performed by dissolving the cages in DCM and $CHCl_3$ with a combined concentration of 1 $mgmL^{-1}$ and stoichiometric ratio of 1:1 for the cages, with anti-solvents either diffused or layered. Anti-solvents *p* – xylene, *o* – xylene, and *m* – xylene were layered as opposed to diffused into the cage solutions due to the low volatility. Ideally, co-crystallisation could be encouraged through potential chiral recognition between the cage windows promoting WTW packing. The crystallisations were examined after a period of 7 days and multiple crystal habits were visually seen.

The chromatograph in **Figure 13C** was taken from a co-crystallisation of **TCC1**-*S* and **FTRCC3**-*R* in $CHCl_3$ and EtOH, which shows two peaks. Although the solution analysed contained 2 different cage species, FT-RCC3**-** *R* is not visible using HPLC (**Figure 18A**), as it only contains a very weak chromophore compared with the imine-bonded cages. Comparing this trace with data in the original publication, the first peak has the same retention time as TCC1$_{[3+6]}$ (**Figure 18B**).[10] Liquid chromatography mass spectrometry (LCMS) was used to clarify this deduction, which is discussed in more detail later in the chapter.

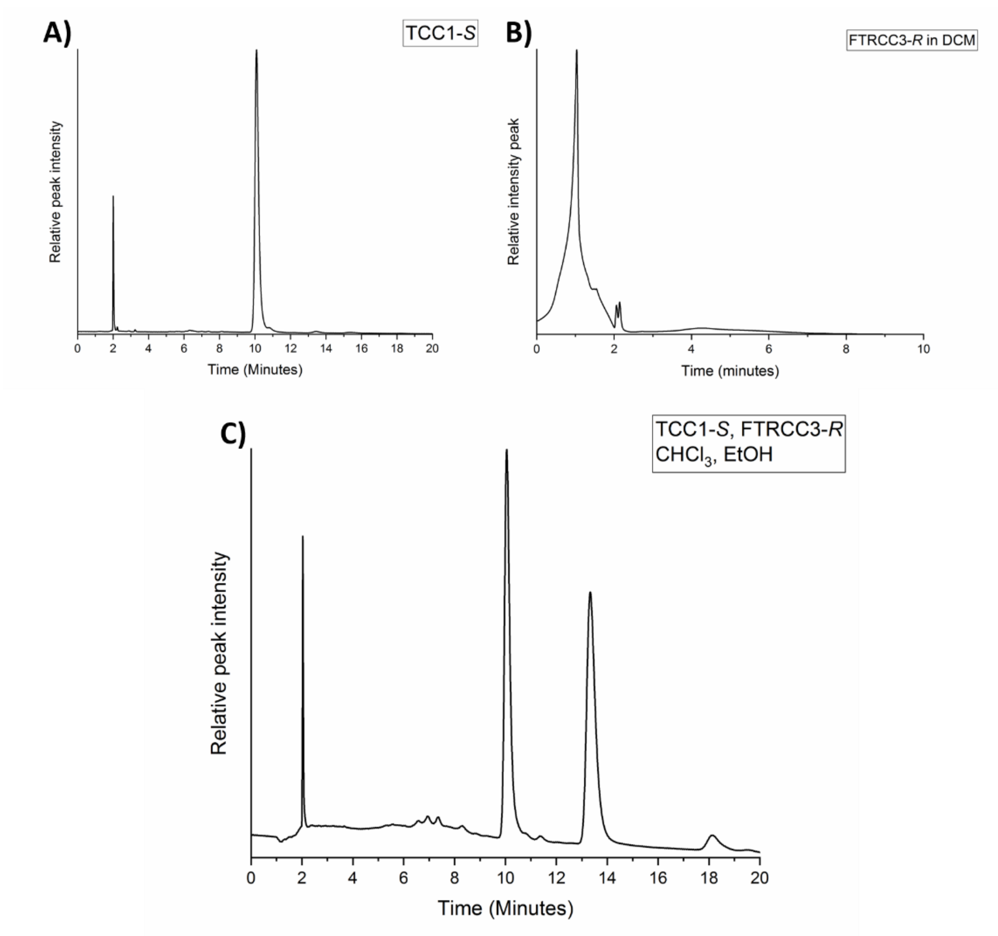

**Figure 13 A)** Chromatograph of pure **TCC1**, retention time of ~10 minutes, correlating with published data[10]; **B)** Chromatograph of **FTRCC3-***R*, the broad peak corresponds to the solvent front; **C)** Chromatograph of the co-crystallisation of **FTRCC3**-*R* and **TCC1**-*S*, showing two peaks, one of which is confirmed as being **TCC1**-*S*, and the other an unknown molecule at ~ 13.5 minutes.

## 2.3 Crystal Structure of ***TCC1***$_{[6+12]}$

Two crystal habits were identified in the co-crystallisations of **TCC1-***S* and **FTRCC3-***R*, prismatic and needle crystals from the co-crystallisation in $CHCl_3$ with EtOH as the anti-solvent, after a period of 5 days. The recrystallisation was left at room temperature, and the concentration of combined co-formers was 1 $mgmL^{-1}$ in solution. The two co-formers crystallise in cubic space groups in the same solvent system ($CHCl_3$, EtOH), with prismatic crystal habits. **FT-RCC3**-*R* crystallises in space group $F4_132$, with cell lengths $a$ = 25.316(12) Å, and **TCC1**-*S* crystallised in the space group $I2_13$, with cell length *a* = 30.095(5) Å.[10,37] Needle-shaped crystals were visually identified, and from a unit cell measurement were found to have trigonal symmetry, with the cell parameters *a* = 38.505(18) Å and *c* = 18.630(8) Å. This indicated formation of a new crystalline phase and a full data collection was recorded. Single crystal X-ray diffraction (SCXRD) revealed formation of a new cage structure, **TCC1**$_{[6+12]}\cdot$18($CHCl_3$)$\cdot$18(EtOH), that had crystallised in the trigonal space group *R*3.

A displacement ellipsoid plot for **TCC1**$_{[6+12]}$ is shown in **Figure 14**. The image in **Figure 15** shows the crystals viewed under polarised light, showing the two crystal habits as mentioned earlier. The crystals had to remain suspended in oil due to the visible desolvation forming an amorphous powder. The resulting crystal structure packed in the Trigonal space group *R*3, but was comprised of only one cage, not two as anticipated from the co-crystallisation. This cage was stoichiometrically twice the original **TCC1**$_{[3+6]}$ cage, and will henceforth be referred to as **TCC1**$_{[6+12]}$.

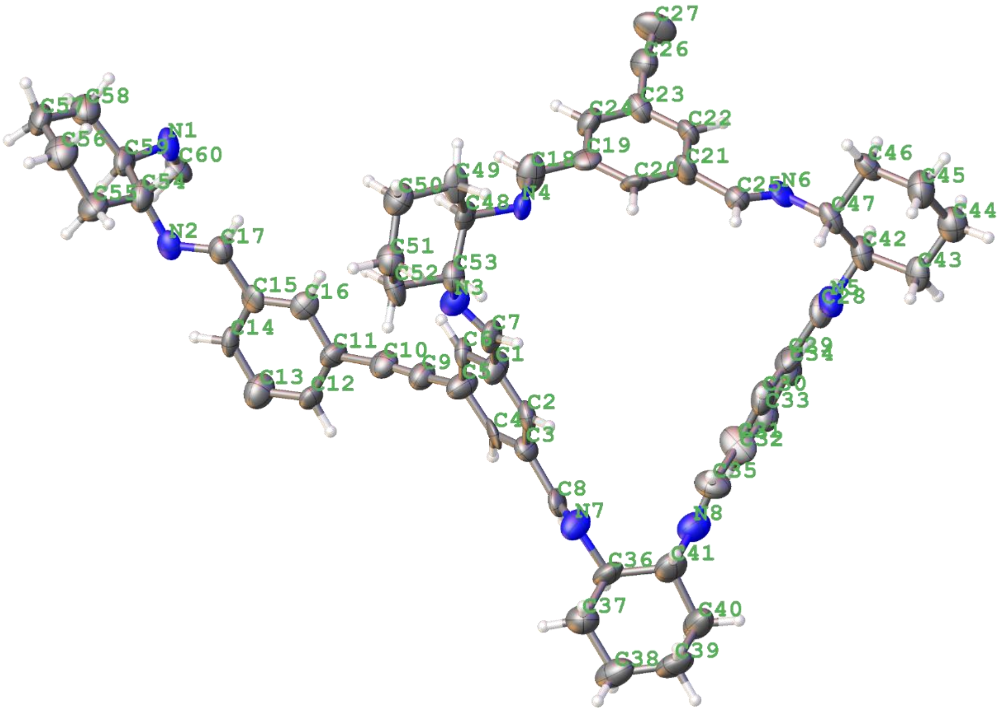

**Figure 14** Displacement ellipsoid plot of **TCC1**$_{[6+12]}$, ellipsoids displayed at 50 % occupancy level.

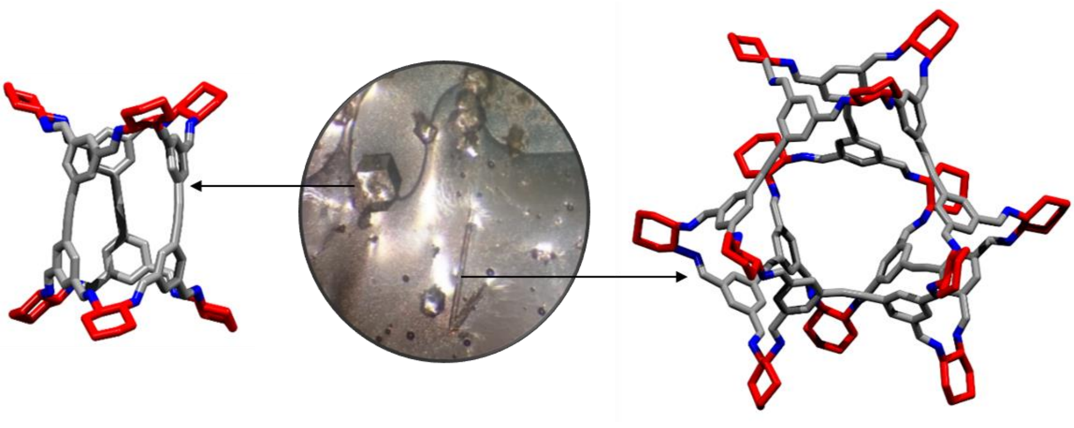

**Figure 15** Photograph of the crystals in oil, as the needle-shaped crystals are unstable when removed from the crystallisation liquor. The larger, prismatic crystals were found to be **TCC1**$_{[3+6]}$ and the fine needles **TCC1**$_{[6+12]}$.

It was not possible to model solvent molecules in the large, interconnected voids due to disorder. Therefore the SQUEEZE algorithm in PLATON was applied during the final stages of refinement.[38] A total of 4616 electrons were masked using the SQUEEZE routine in PLATON, and the solvent masked reflection file was used during the final stages of refinement. 18 $CHCl_3$ and 18 EtOH molecules per **TCC1**$_{[6+12]}$ were tentatively added to the refined formula sum. The structure also showed large atomic displacement parameters (ADP) for all the atoms, common in macromolecular structures, most likely due to the increased flexibility of the large cage increasing the atomic thermal parameters, decreasing the accuracy of atomic position.[39–41] A fixed U[iso] was applied to all H atoms, and rigid body (RIGU) restraints applied to the anisotropically atoms to improve the ADPs.[42] Some bond lengths were restrained using DFIX, producing a more accurate model.[43] **Figure 16** shows the crystal structures along the *a-, b-* and *c*-axes, illustrating the cages packing WTE along and *a*- and *b*-, and WTW along the *c*-axis.

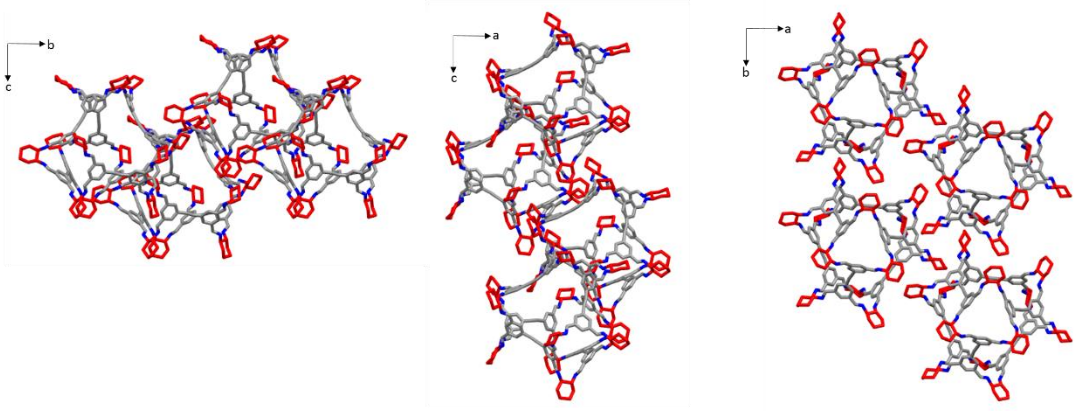

**Figure 16** Crystal packing of **TCC1**$_{[6+12]}$ along the *a*-, *b*- and *c*-axis from left to right.

**Figure 17A** shows the WTW interactions in the crystal structure, and **Figure 17B** illustrates the packing along the c-axis, which shows the WTW interactions throughout the structure forming 1-dimensional channels. Homochiral **TCC1**$_{[3+6]}$-S/R shows only WTE packing, most likely due to the cage only containing the 2 windows, whereas **TCC1**$_{[6+12]}$ contains 4 smaller and 4 larger windows, making the structure statistically more likely to exhibit WTW packing. **TCC1**$_{[6+12]}$ has two distinct window shapes, one which is the same as the triangular window of **TCC1**$_{[3+6]}$ and **CC3**, the second window, only seen in **TCC1**$_{[6+12]}$, is a larger, hexagonal window which forms as a result of the divergent imine bond angles (**Figure 18**). The bond angles for both the aldehyde linkers and imine bonds varied between the two cages, resulting in the divergent triangular windows and resulting in the formation of the large, hexagonal windows in **TCC1**$_{[6+12]}$ (**Table 1**).

**Table 1** Imine bond angles for both **TCC1**$_{[6+12]}$ and **TCC1**$_{[3+6]}$.

| **Bond** | **TCC1**$_{[3+6]}$ (°) | **TCC1**$_{[6+12]}$ (°) |
|---|---|---|
| (Ph – Diamine)C-N=C | 117.6 | 113.3 |
| N=C-C(Ph – Aldehyde) | 123.6 | 122.7 |
| Aldehyde Linker (C-C≡C) | 172.1 – 175.4 | 168.2 – 171.4 |

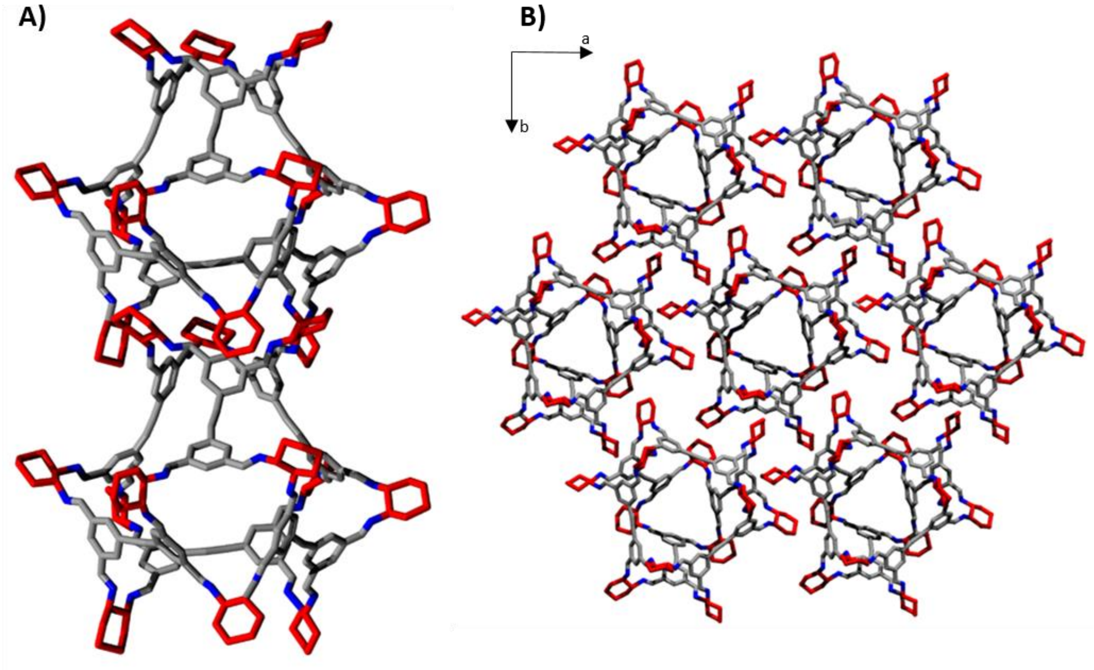

**Figure 17 A)** The WTW interactions between the two cages, viewed along the a-axis; **B)** Crystal packing of the larger cage as viewed along with c-axis.

In Section 1.1 we discussed the flexibility or **TCC3**-*R*. However, here we have shown that as well as the linkers, the flexibility of the imine bond lead to the formation of the larger, hexagonal windows shown in **Figure 18**. **Figure 18B** shows the triangular window in **TCC1**[3+6], and comparing this directly with the same window in **TCC1**[6+12] further highlights the divergent nature of the bonds.

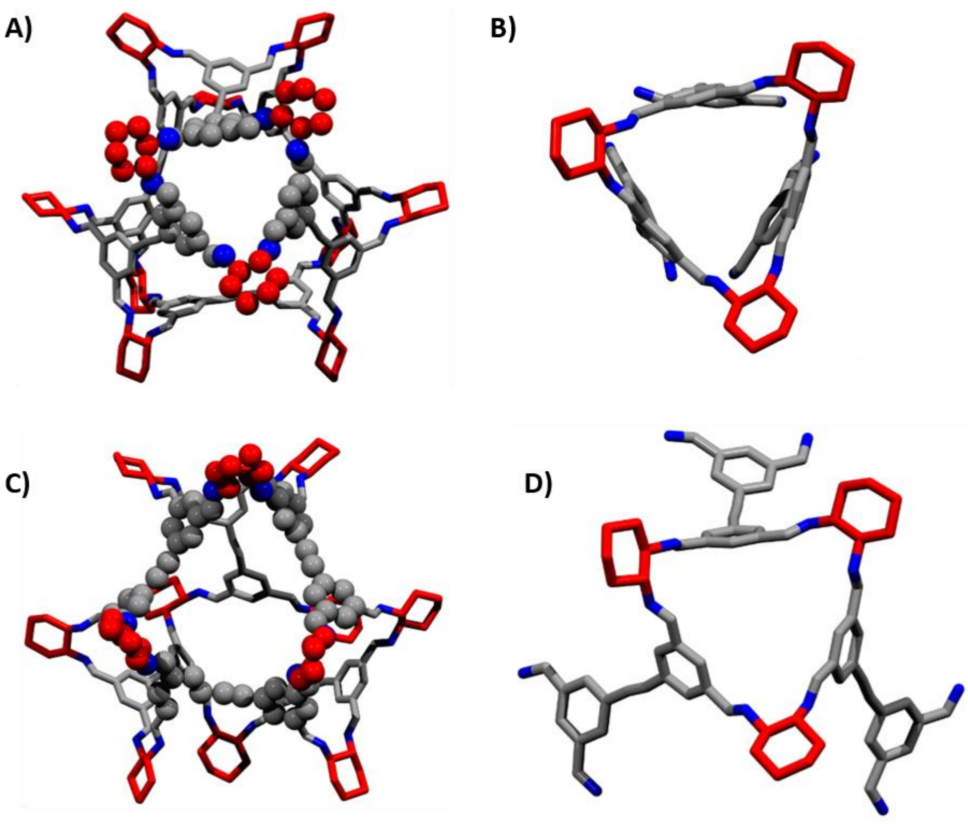

**Figure 18 A) CC3**-type window in **TCC1**$_{[6+12]}$; **B) CC3**-type window shown independently; **C)** Larger, hexagonal window seen in **TCC1**$_{[6+12]}$; **D)** Divergent imine bond angles of the large hexagonal windows, when compared with the triangular window.

## *2.4 Cage Topology*

Shown in **Figure 19A** and **Figure 19B** are the two geometries of the cages. As well as the difference in geometrical shape, the cage topology also differs significantly.[44] The topology of **TCC1**$_{[3+6]}$ and **TCC1**$_{[6+12]}$ is defined by using the centre of the aldehyde as the vertices, as the aldehyde is the building block with the highest coordination number.[19] Whilst **TCC1**$_{[3+6]}$ has the same geometry and topology (triangular prismatic), the geometry of **TCC1**$_{[6+12]}$ is truncated tetrahedron, whereas the topology is octahedron. Topology can be considered the skeleton of the molecule, therefore the geometry and topology can be substantially different.[44] **TCC1**$_{[3+6]}$ has a trigonal prismatic topology. Typically, the centre of the SM with the highest number of functional groups is chosen as the 'centre-point', so for **TCC1**$_{[3+6]}$ this would form a triangle. However, the topology is 3D and is therefore considered trigonal prismatic.

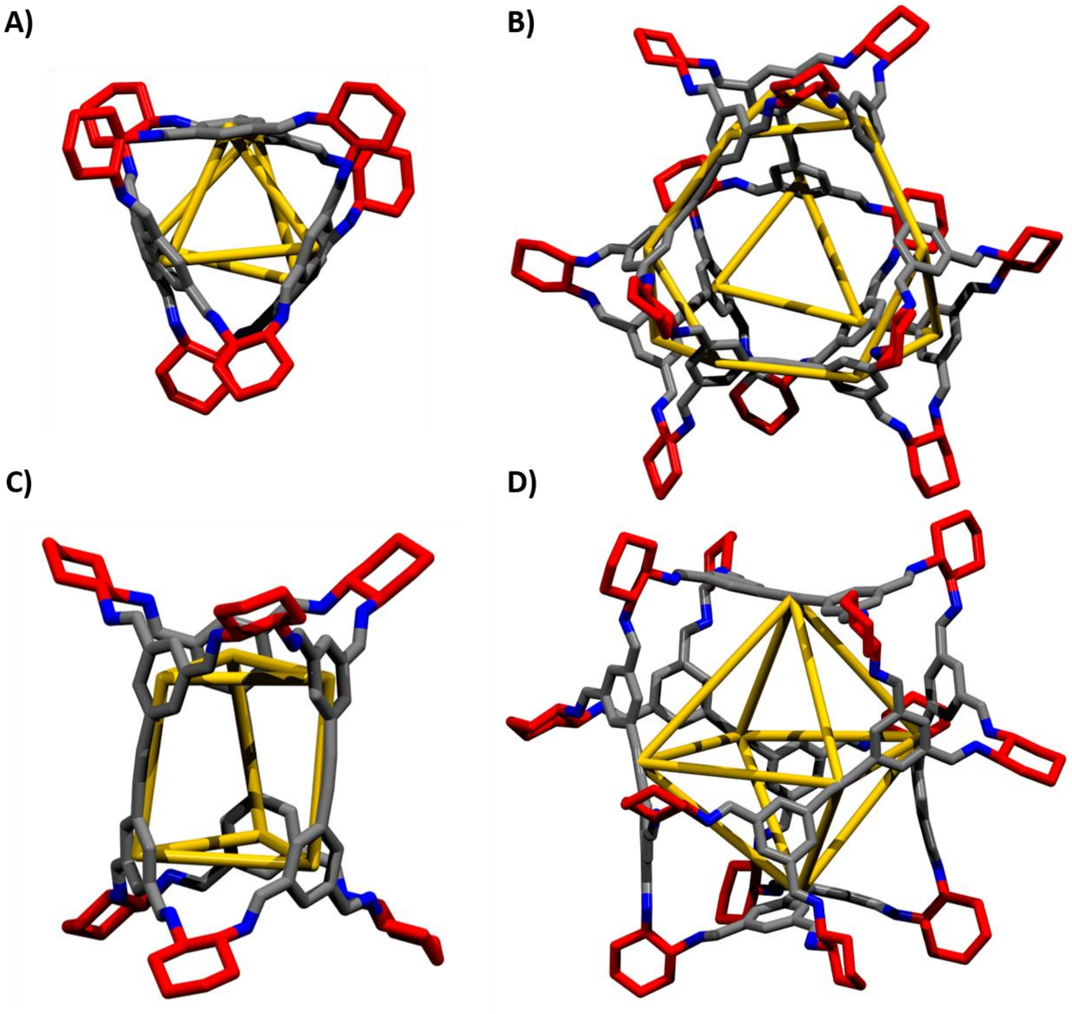

**Figure 19 A)** Illustrating the trigonal prismatic geometry and topology of **TCC1**$_{[3+6]}$ when viewed through the cage window; **B)** Truncated tetrahedron geometry of **TCC1**$_{[6+12]}$; **C)** Trigonal prismatic geometry and topology of **TCC1**$_{[3+6]}$ viewed from the side; **D)** Octahedron topology of **TCC1**$_{[6+12]}$.

The density for solvated **TCC1**$_{[6+12]}$ was calculated to be 1.186 gcm$^{-3}$, and when desolvated this reduced to around 0.558 gcm$^{-3}$, comparatively the microporous **CC3** has a density of 1.033 gcm$^{-3}$. As discussed, porosity is reliant on both a network for diffusion throughout the solid, which was observed in **TCC1**$_{[6+12]}$, as well as void space which can be roughly determined by the cage density. This property of **TCC1**$_{[6+12]}$ prompted investigations into the optimisation of the reaction, and furthermore isolation of the cage.

# *3 Cage Optimisation*

Illustrated in **Scheme 1** is a proposed schematic of **TCC1** formation. The first reversible step shows the imine condensation of 1,2-cyclohexanediamine (**I**) and 5,5'-(ethyne-1,2-diyl)diisophthalaldehyde (**II**) form **TCC1**$_{[3+6]}$, a known synthesis from publication.[10] This step is reversible under acidic or aqueous conditions, due to the dynamic nature of the imine bonds.[45] The second step shows formation of **TCC1**$_{[6+12]}$ which was observed in the crystallisation experiment in the solvents DCM and MeOH, however the actual formation was unknown at this stage. **Scheme 1** is a simplified version of the mechanism of cage formation.[46] **I** and **II** are the SMs respectively.

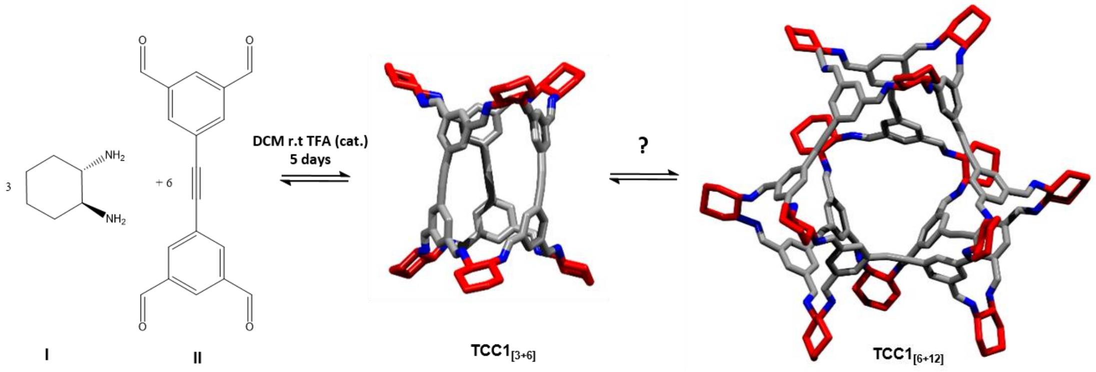

**Scheme 1** A schematic showing the generally accepted formation of the two cages. The first reversible step shows the formation of **TCC1**$_{[3+6]}$ from the SMs, which then leads to the formation of **TCC1**$_{[6+12]}$.

Recrystallisation in $CHCl_3$/EtOH and DCM/MeOH formed **TCC1**$_{[6+12],}$ Optimisation can occur *via* two potential routes, as with any new cage discovery; via crystal engineering or synthesis using alternative tectons. **TCC1**$_{[6+12]}$ was originally identified after an attempted co-crystallisation, therefore crystal engineering was deemed an ideal place to begin. The triply interlocked catenane can be isolated through crystallisation techniques, therefore the same methodology was applied.[27]

## 3.1 Optimisation through Crystal Engineering

### 3.1.1 Characterisation of ***TCC1**[6+12]*

HPLC, $^1$H NMR, $^{13}$C NMR, and LCMS were employed to further characterise and assess presence of the cage in solution. Quantitative techniques, such as NMR and LCMS would also allow us to quantify the relative amount in solution. NMR presented difficulties, there appeared to be no changes in the $^1$H NMR between a sample containing pure **TCC1**$_{[3+6]}$ and the NMR spectra containing a mixture of **TCC1**$_{[3+6]}$ and **TCC1**$_{[6+12]}$ (**Figure 20** and **21**). Although the NMR also contains **FT-RCC3**-*R*, the amine-bonded cage shows no resonances past 7 ppm. The chemical shifts 8-7ppm in **TCC1**-*S* correspond to the imine CH protons, which are absent in **FT-RCC3**-*R*. Due to the limited solubility, it was not possible to record usable $^{13}$CNMR spectra.

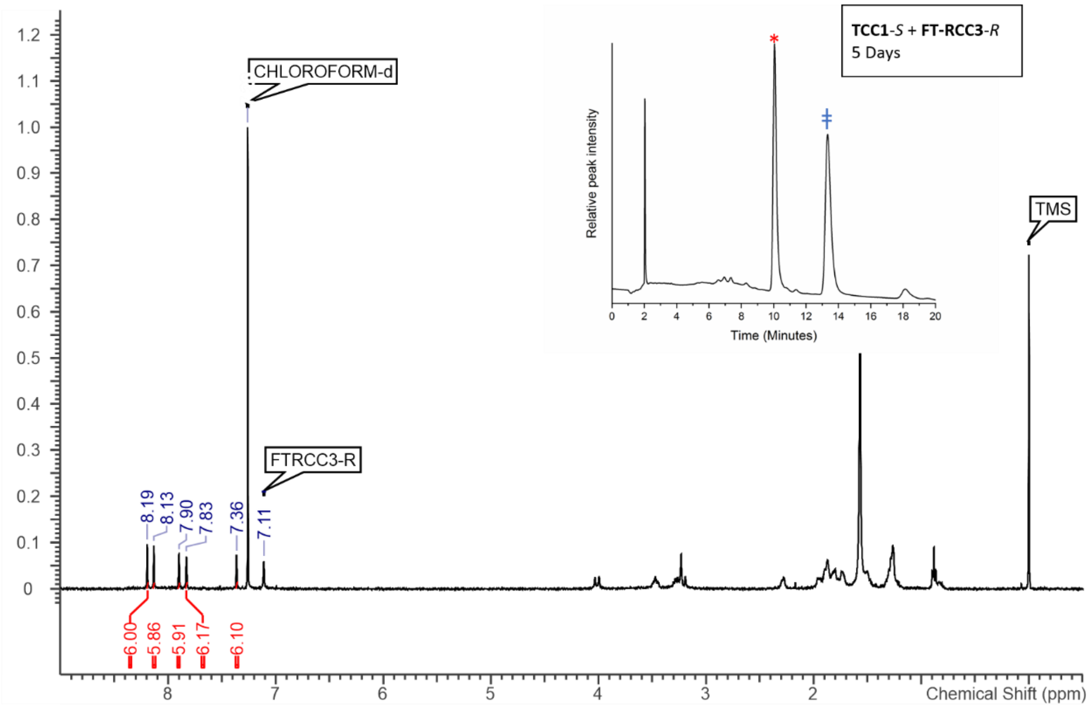

**Figure 20** NMR of the co-crystallisations of **TCC1**-*S* and **FT-RCC3**-*R* after 5 days in solution ($CHCl_3$). The HPLC corresponds to the relative ratios (2:1) of **TCC1**$_{[3+6]}$ and **TCC1**$_{[6+12]}$ in the solution.

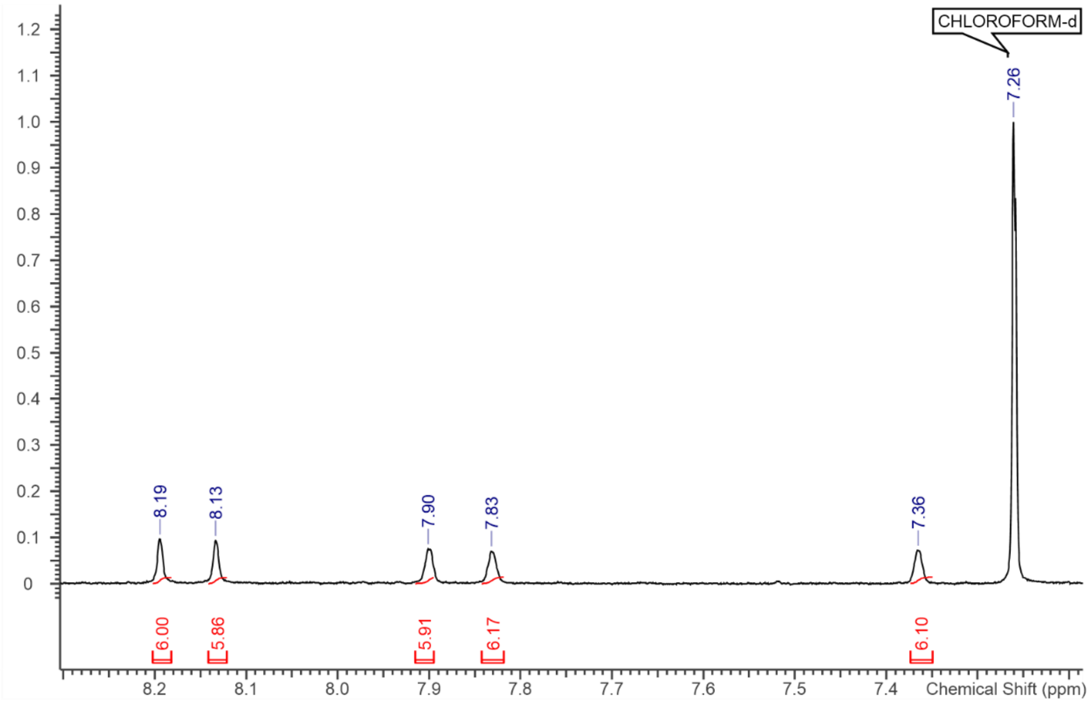

**Figure 21** 1HNMR spectra of the area corresponding to the imine bonds in **TCC1**-*S*, which shows only one set of peaks.

Variable Temperature (VTNMR) was also used to identify any potential chemical shifts when the same mixed sample was slowly cooled from 50 °C to -30 °C. VTNMR has been shown to improve the resolution of other molecules which are otherwise difficult to characterise at room temperature.[47] This method can also be further utilised for mixtures, and therefore a temperature change in temperature could result in the peak splitting and help to characterise **TCC1**$_{[6+12]}$.[48,49] **Figure 22** shows the results of the VTNMR of a mixture of **TCC1**$_{[3+6]}$ and **TCC1**$_{[6+12]}$, however we see that as the temperature was decreased there was no change, apart a shift which is attributed to MeOH at around 5.3 ppm.

Therefore, HPLC was used to determine the cages presence and relative peak area in solution by taking advantage of the UV-active chromophore, the imine, in organic molecular cages (OMCs). As the cage was active at the same wavelength, (254 nm$^{-1}$), the relative amount of cage in the reaction could be determined, however LCMS measurements were required to determine that the second peak was in fact the larger cage.

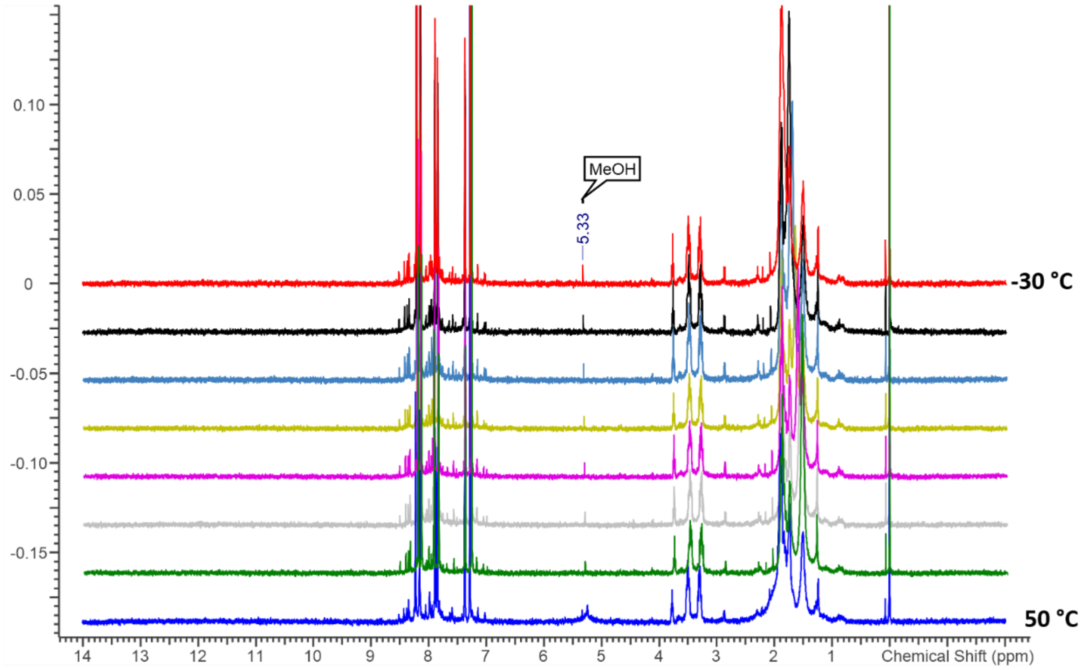

**Figure 22** VTNMR of a 2:1 **TCC1**[3+6]:**TCC1**[6+12].

This technique also enables us to accurately determine the composition of very dilute samples, for example HPLC can be used for detection of molecules in samples as dilute as 0.1 mgmL$^{-1}$. Initially LC-MS data showed that **TCC1**[6+12] fragmented, therefore the equipment was optimised with efforts to favour the **TCC1**[6+12] and prevent significant amounts of fragmentation. As there appeared to be issues with the flight of **TCC1**[6+12], the capillary voltage was set to 4000 V, and the fragmentor at 225 V. Milder ionisation conditions were employed due to the fragmentation observed, and the best data is shown in the figures.

However, these efforts did not decrease the fragmentation of **TCC1**[6+12], therefore the peak which showed masses from both **TCC1**[3+6] and **TCC1**[6+12] was assumed to be present as the large cage was fragmenting during measurement (**Figures 23**, **24** & **25**). Despite the difficulty in obtaining definite data showing just one mass, we could however determine that the second peak did in fact contain the large cage henceforth the relative peak area at 254 nm of each cage in the mixture.

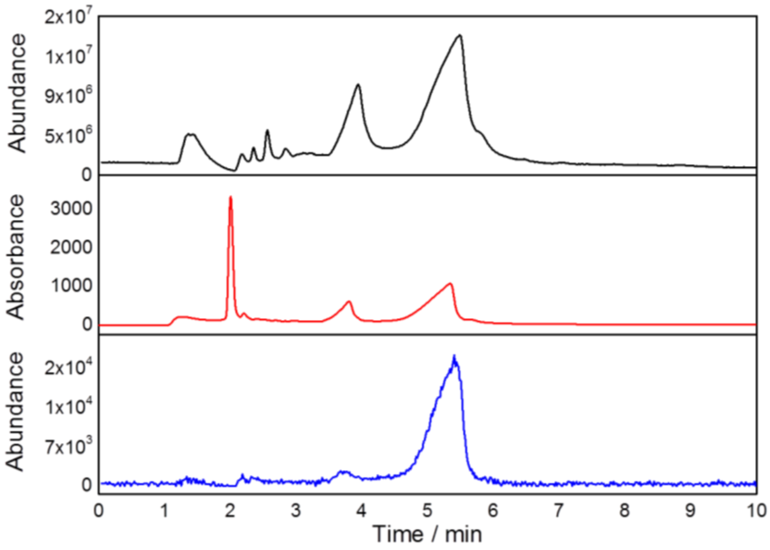

**Figure 23** LC-MS analysis of **TCC1$_{[3+6]}$** and **TCC1$_{[6+12]}$** cage mixture. Stacked TIC (total ion count, black trace), DAD (diode-array detector, UV wavelength 254 nm, red trace) and EIC (extracted ion count for **TCC1$_{[6+12]}$** doubly charged m/z ions in range 1349.1841-1349.9238, blue trace) spectra.

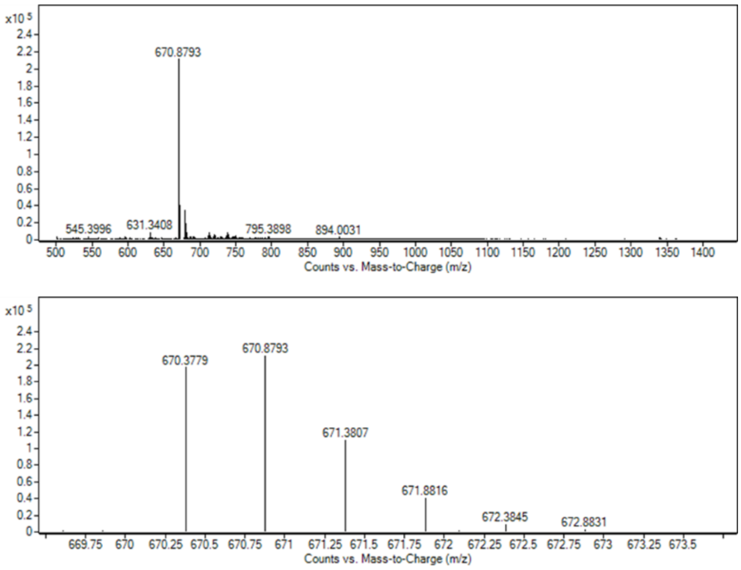

**Figure 24:** Off-line LC-MS analysis of **TCC1$_{[3+6]}$** and **TCC1$_{[6+12]}$** cage mixture. Accurate mass spectra for each peak as seen in the TIC, showing $[M+2H]^{2+}$ ions. Peak at ~3.9 min: calc. for **TCC1$_{[3+6]}$** $C_{90}H_{90}N_{12}$ 1339.7443, found $[M+2H]^{2+}$ 670.8793

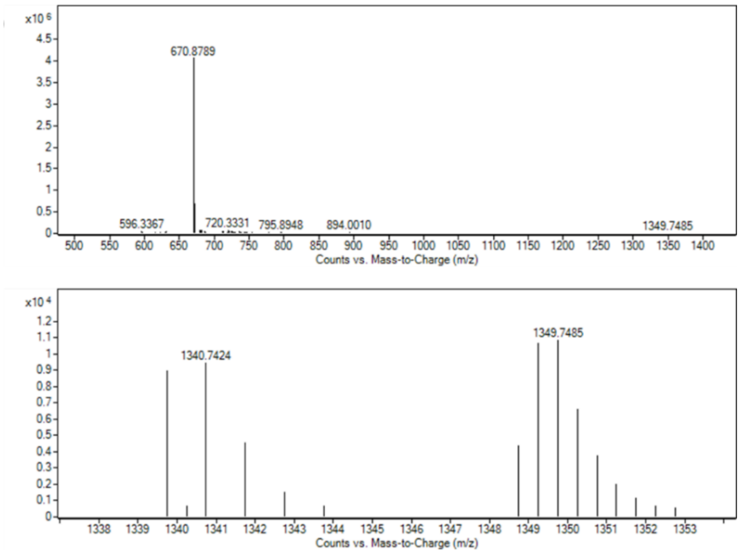

**Figure 25** peak at ~5.5 min: calc. for **TCC1$_{[6+12]}$** $C_{180}H_{180}N_{24}$ 2679.4885, found $C_{180}H_{180}N_{24}$ + $H_2O$ (calc. 2697.7991) $[M+2H]^{2+}$ 1349.7485. The large amount of **TCC1$_{[3+6]}$** observed in the peak at ~5.5 mins is thought to be due to fragmentation of the larger **TCC1$_{[6+12]}$.**

The original synthetic procedure yielded only one peak, **TCC1**$_{[3+6]}$, in the HPLC. The second peak, corresponding to **TCC1**$_{[6+12]}$ was observed after recrystallisation, with a concentration of 1 mg $mL^{-1}$, and left for a period of weeks. Crystallisations with $CHCl_3$ and DCM were set up with MeOH and EtOH to determine which crystallisation condition led to the large cage formation. Repeat experiments were run over a one week period, which showed both cages in solution, however the relative amount of large cage did not increase with time.

**Figure 26** shows the chromatographs recorded after one week of incubating the samples at 20 °C. Although some systems show preference for the formation of the larger cage, it also shows that for these conditions there is a mixture of both cages **TCC1**$_{[3+6]}$ and **TCC1**$_{[6+12]}$ in solution. An alternative method to isolate pure **TCC1**$_{[6+12]}$ was therefore attempted, by modifying the reported synthetic procedure for **TCC1**$_{[3+6]}$.

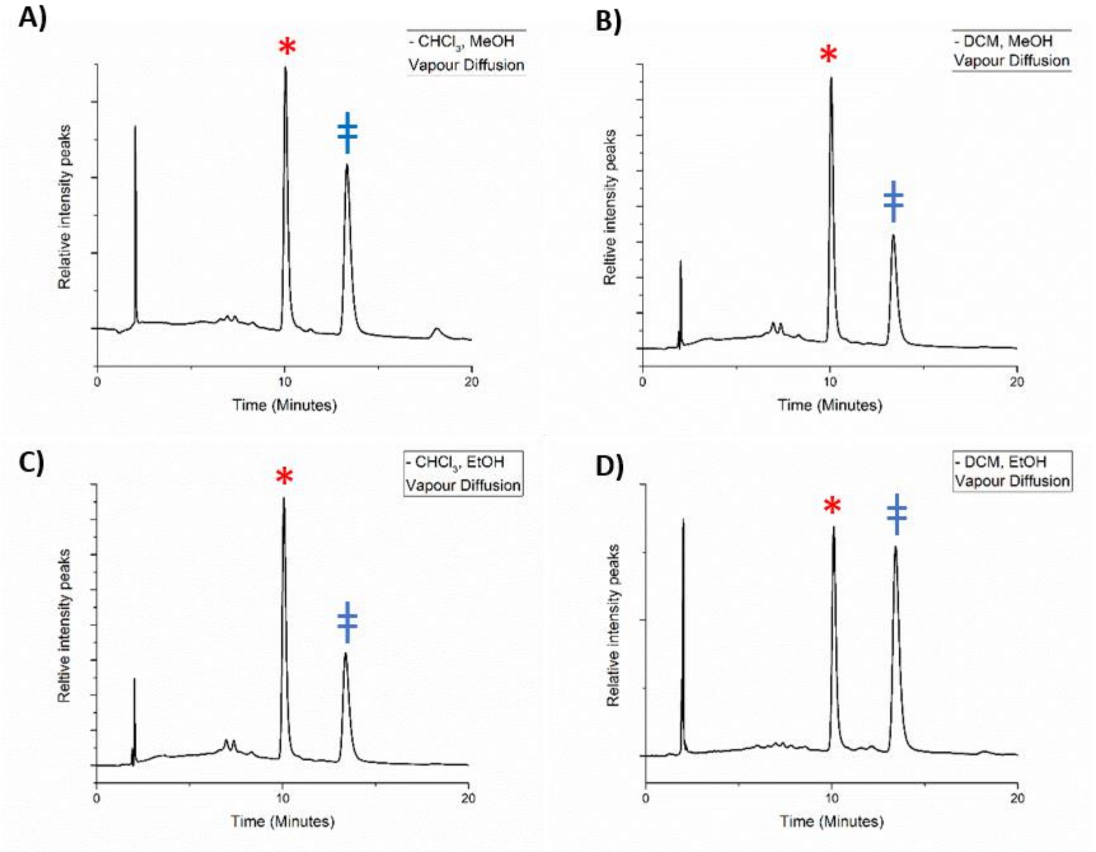

**Figure 26** a) Crystallisation in $CHCl_3$ and MeOH; b) Crystallisation in DCM and MeOH; c) Crystallisation in $CHCl_3$ and EtOH; d) Crystallisation in DCM, EtOH. * = **TCC1**$_{[3+6]}$, ǂ = **TCC1**$_{[6+12]}$.

## *3.2 Optimisation through alternative reaction conditions*

### *3.2.1 Impact of alternative conditions*

The published synthesis was found to only afford **TCC1**$_{[3+6]}$.[10] **TCC1**$_{[6+12]}$ was found through recrystallization, however we were unable to isolate a significant quantity of the cage *via* this route as **TCC1**$_{[3+6]}$ was typically the major product (**Figure 18**). The use of an acid catalyst can promote reversibility and the formation of a kinetic species by increasing the rate of reaction, therefore allowing us to trap the kinetic product.[45] We could potentially determine whether **TCC1**$_{[6+12]}$ is the thermodynamic or the kinetic product based upon the preference of the reaction under acidic conditions.[45] **Figure 27** shows the results of two reactions performed simultaneously, the left chromatograph is the reaction when performed in TFA compared with a reaction with no TFA. In *Chapter 1* section 4.2 we introduced the concept of acid catalysis promoting the formation of a thermodynamic product, in this case we see that using an acid catalyst had yielded only **TCC1**[3+6], leading us to believe that **TCC1**[6+12] could be the kinetic product of reaction.

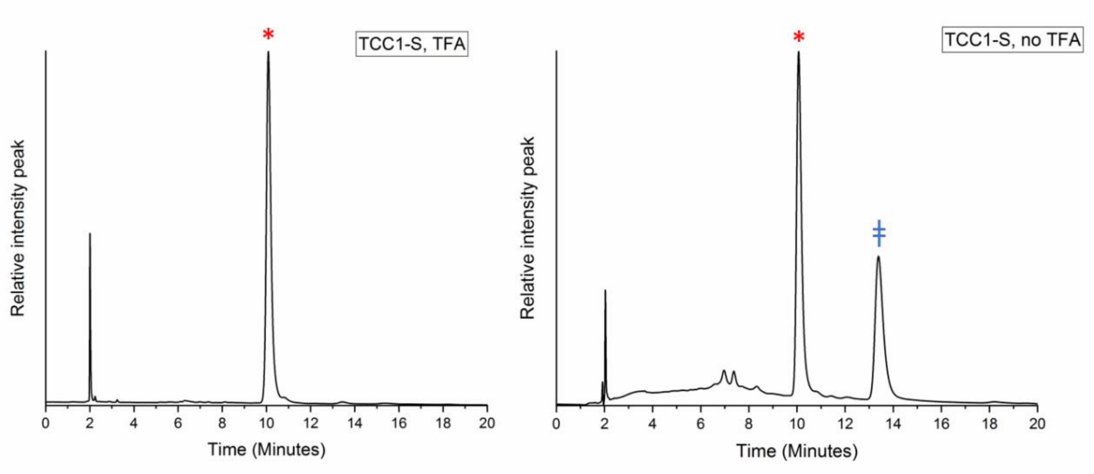

**Figure 27** Chromatographs comparing the standard reaction in DCM with TFA, and the other in DCM with no TFA. * = **TCC1**[3+6], ‡ = **TCC1**[6+12].

There are other routes to encourage the synthetic preference towards the thermodynamic or kinetic product. For preferential formation of a thermodynamic product, concentration and temperature can also influence the equilibrium of reaction. High dilution, whereby the concentration of the reactants is typically equal to or less than 1 mg/mL$^{-1}$, can encourage the formation of the thermodynamic product.[36,50] High dilution prevents the formation of kinetic oligomeric materials, as the synthesis of cages results in a loss of entropy to the system.[51] For example, Nishikawa *et. al.* demonstrated that as they increased the concentration of a macrocyclization from 1 mM to 5 mM, the yield of reaction decreased from 84 % to 19 %.[52] Thermodynamic control can also be achieved by temperature, for example, **CC1** is synthesised at low temperature encouraging the thermodynamic product.[34]

By definition, solvent templating occurs by altering the packing of a crystalline material resulting in a polymorph, or re-arrangement of a molecule into an alternative molecular structure.[29,53,54] Based on results in the Warmuth study, syntheses were performed in a number of solvent systems, attempting to form **TCC1**[6+12] through solvent templation.[29] The original **TCC1**[3+6] synthesis was carried out in DCM, however **TCC1**[6+12] was found in recrystallisations with both DCM and $CHCl_3$, therefore all syntheses were carried out in both solvents to identify any potential solvent templating.

A series of parallel reactions were performed in $CHCl_3$ (**Table 2**) and DCM (**Table 3**), at both room and high temperature 61 °C $CHCl_3$, 40 °C DCM). Solvent systems and stoichiometric equivalents were also varied, always using the halogenated solvents as the primary solvents, and introducing secondary solvents in a 1:1 volumetric ratio. Analytical HPLC was used in all cases to analyse the data, which could confirm the presence of **TCC1**$_{[6+12]}$, as well as determining the relative peak area.

### *3.2.2 Reactions in $CHCl_3$*

The optimisations were carried out in 14 mL vials on a heated carousel (for those reactions under reflux conditions) with approximately 10-11 mL of solution per reaction. Approximately half a drop of TFA was added for reactions stating an acid catalyst was used.. For the HPLC data, all measurements were taken after 5 days when the reactions were considered to be complete, based on the original literature recommended reaction time.[10]

**Table 2** Optimisation of synthetic route using $CHCl_3$ as the primary solvent.

| Reaction | Stoichiometry Aldehyde : Amine | Concentration mg/mL | Solvent(s) | Conditions[a] | Peak Area of $TCC_{[6+12]}$ (% a/a) |
|---|---|---|---|---|---|
| 1 | 3:6 | 1 | $CHCl_3$ | Standard[a] | 33.8 |
| 2 | 4:6 | 1 | $CHCl_3$ | Standard[a] | 5.20 |
| 3 | 5:6 | 1 | $CHCl_3$ | Standard[a] | 1.60 |
| 4 | 3:7 | 1 | $CHCl_3$ | Standard[a] | 28.8 |
| 5 | 3:8 | 1 | $CHCl_3$ | Standard[a] | 25.8 |
| 6 | 3:6 | 1 | $CHCl_3$ | Standard[a] | 32.3 |
| 7 | 3:6 | 2 | $CHCl_3$ | Standard[a] | 30.0 |
| 8 | 3:6 | 3 | $CHCl_3$ | Standard[a] | 31.6 |
| 9 | 3:6 | 4 | $CHCl_3$ | Standard[a] | 27.8 |
| 10 | 3:6 | 5 | $CHCl_3$ | Standard[a] | 30.1 |
| 11 | 3:6 | 1 | $CHCl_3$ | Standard[a] | 32.0 |
| 12 | 3:6 | 1 | $CHCl_3$ | Standard[a], TFA | 1.00 |
| 13 | 3:6 | 1 | $CHCl_3$ | RT, No TFA | 23.8 |
| 14 | 3:6 | 1 | $CHCl_3$ | RT, TFA | 1.80 |

| | | | | | |
|---|---|---|---|---|---|
| 15 | 3:6 | 1 | $CHCl_3$ | Standard[a], molecular sieves | 31.6 |
| 16 | 3:6 | 1 | $CHCl_3$ | Standard[a] | 34.4 |
| 17* | 3:6 | 1 | THF | Standard[a] | 22.9 |
| 18* | 3:6 | 1 | 1:1 $CHCl_3$/MeOH | Standard[a] | 29.0 |
| 19 | 3:6 | 1 | $CHCl_3$ | 100 °C, ca. 3.1 bar pressure tube, sand bath | 32.8 |
| 20 | 3:6 | 1 | $CHCl_3$ | 100 °C, ca. 3.1 bar, Parr pressure vessel, oven | 15.2 |

[a] standard conditions are 61 °C with stirring and no TFA catalyst.
* Precipitate was observed.

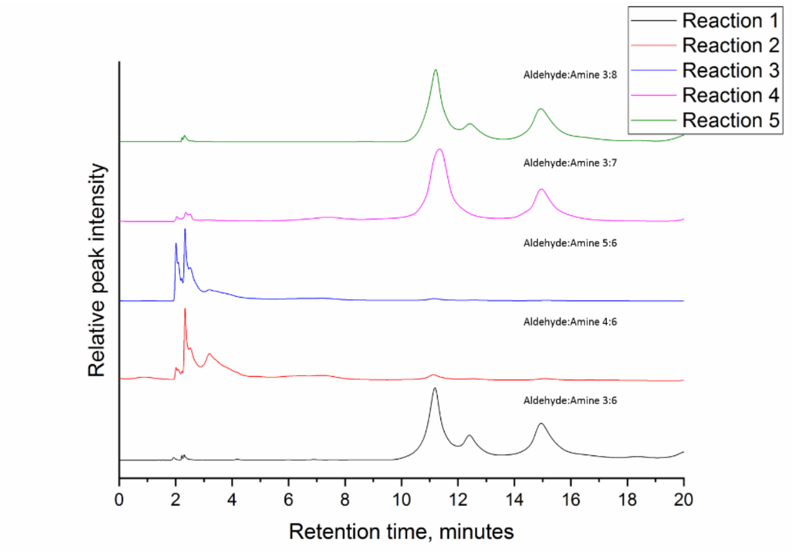

**Figure 28** HPLC Chromatographs of reactions 1–5, showing the effect of stoichiometry on the outcome of the reaction. Label shows the ration of aldehyde to amine used.

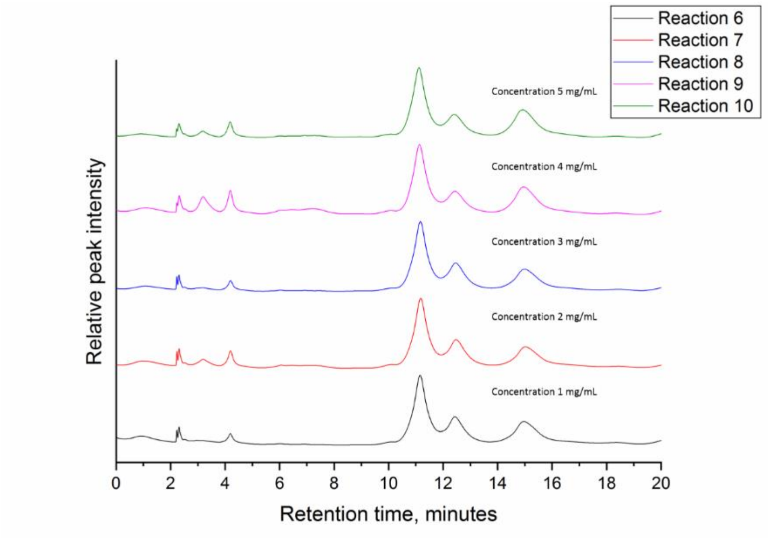

**Figure 29** HPLC Chromatographs of reactions 6–10, showing the effect of concentration on the reaction outcome.

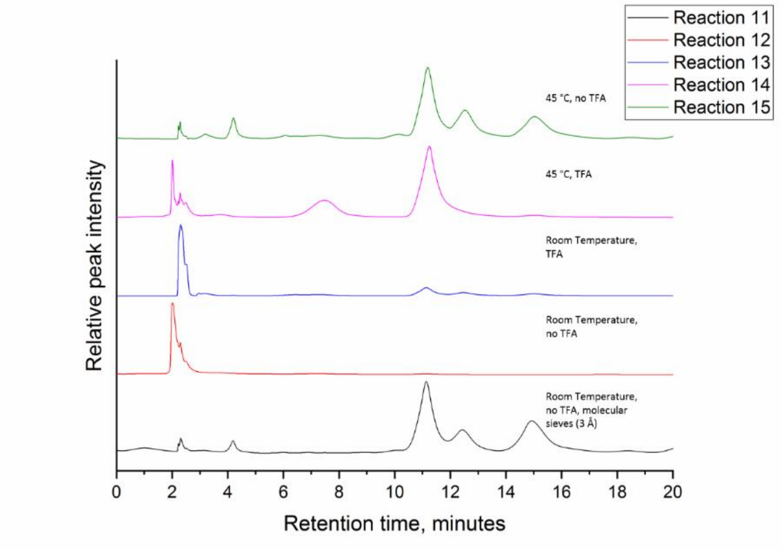

**Figure 30** HPLC Chromatographs of reactions 11–15, showing the effect of molecular sieves and TFA catalyst on the reaction outcome.

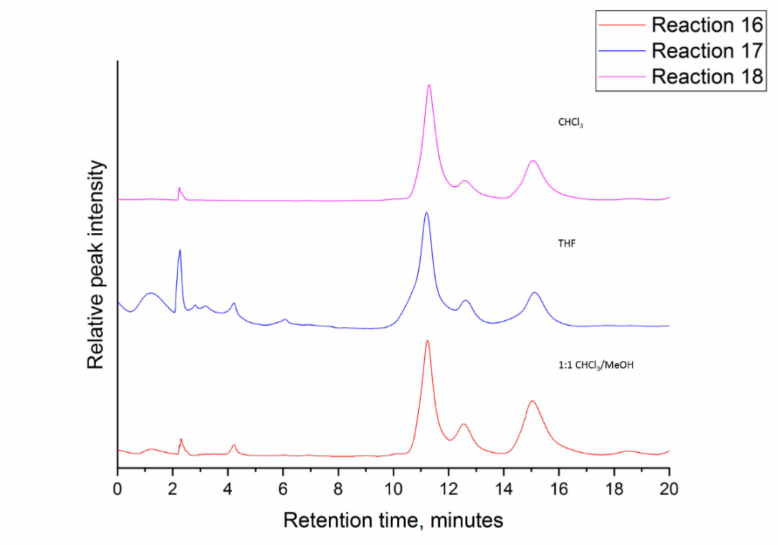

**Figure 31** HPLC Chromatographs of reactions 16–18, showing the effect of changing the solvent on the reaction outcome. It can be seen the presence of MeOH affords higher conversion to the larger **TCC1**$_{[6+12]}$.

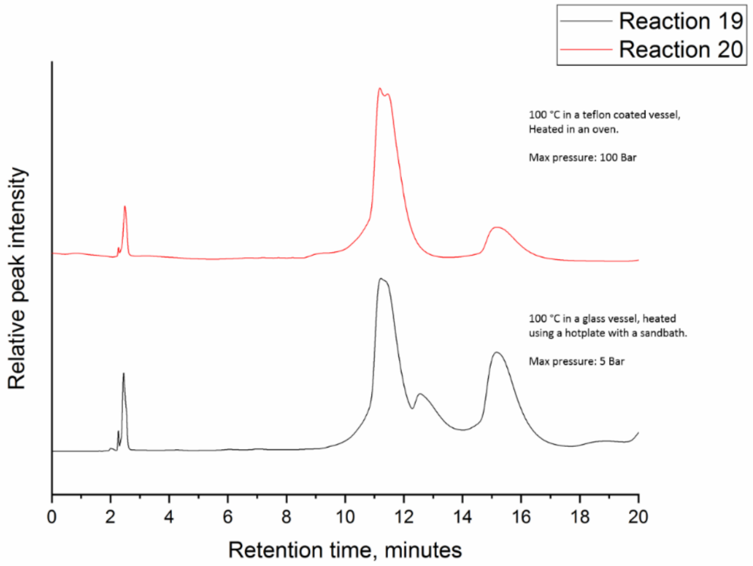

**Figure 32** HPLC Chromatographs of reactions 19 and 20, which were carried out at elevated temperatures in either a high pressure vessel placed inside an oven or in a pressure tube placed in a sand bath. Although both reactions were nominally carried out at 100 °C, the top of the pressure tube was not immersed in the sand bath so the actual reaction temperature may be lower.

### *3.2.3 Reactions in DCM*

In some of the syntheses using $CHCl_3$ as the primary solvent a third peak was observed between **TCC1**$_{[3+6]}$ and **TCC1**$_{[6+12]}$. Attempts were made to find the molecular mass of this peak using LC-MS, however the experiments were unsuccessful. Our conclusions from this led us to believe it is most likely an intermediate product between **TCC1**$_{[3+6]}$ and **TCC1**$_{[6+12]}$.

**Table 3** Optimisation of synthetic route using DCM as the primary solvent

| Reaction | Stoichiometry Aldehyde:Amine | Concentration (mg/mL) | Solvents | Conditions | Peak Area of TCC$_{[6+12]}$ (% a/a) |
|---|---|---|---|---|---|
| 21 | 3:6 | 1 | DCM | Standard[a] | 23.4 |
| 22 | 5:6 | 1 | DCM | Standard[a] | 2.10 |
| 23 | 3:8 | 1 | DCM | Standard[a] | 5.70 |
| 24 | 3:6 | 2 | DCM | Standard[a] | 59.2 |
| 25 | 3:6 | 4 | DCM | Standard[a] | 32.3 |
| 26 | 3:6 | 5 | DCM | Standard[a] | 34.7 |
| 27 | 3:6 | 1 | DCM | Standard[a] | 45.5 |
| 28 | 3:6 | 1 | DCM | 45 °C, TFA | 2.50 |
| 29 | 3:6 | 1 | DCM | Room Temperature, TFA | 0.00 |
| 30 | 3:6 | 1 | DCM | Room Temperature, no TFA | 36.2 |
| 31 | 3:6 | 1 | DCM | Standard[a], molecular sieves | 23.6 |
| 32* | 3:6 | 1 | 1:1 DCM/MeOH | Standard[a] | 71.9 |
| 33 | 3:6 | 1 | 1:1 DCM/$CHCl_3$ | Standard[a] | 39.7 |
| 34* | 3:6 | 1 | 1:1 DCM/THF | Standard[a] | 36.0 |
| 35* | 3:6 | 1 | 1:1 DCM/EtOH | Standard[a] | 51.4 |
| 36* | 3:6 | 1 | 1:1 DCM/IPA | Standard[a] | 46.7 |

[a] standard conditions are 45°C with stirring and no TFA catalyst.

* Precipitate was observed

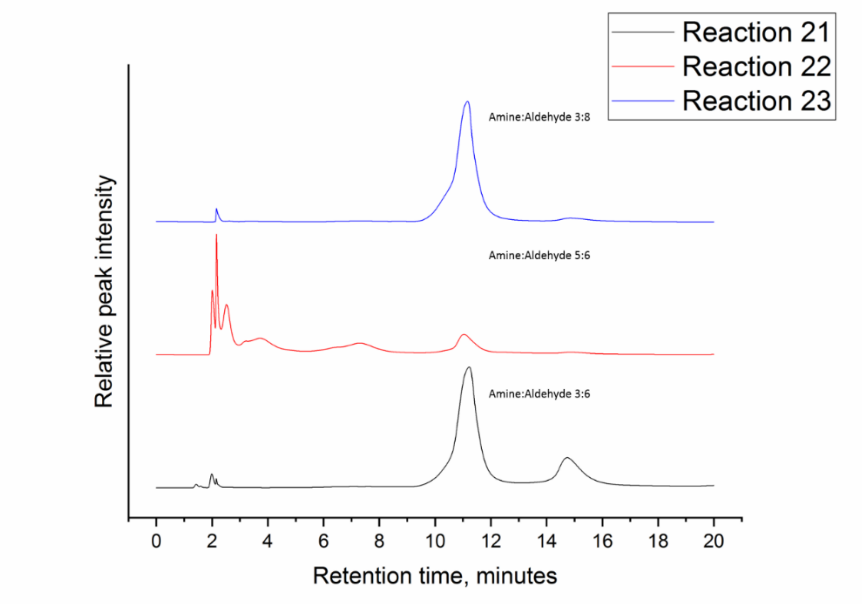

**Figure 33** HPLC Chromatographs of reactions 21–23, showing the effect of stoichiometry on the outcome of the reaction

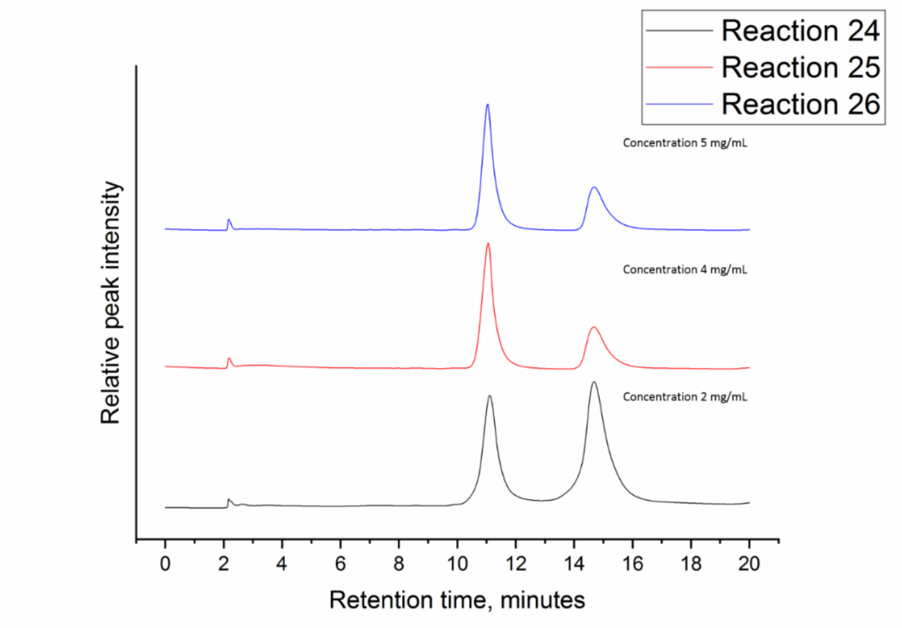

**Figure 34** HPLC Chromatographs of reactions 24–26, showing the effect of concentration on the outcome of the reaction.

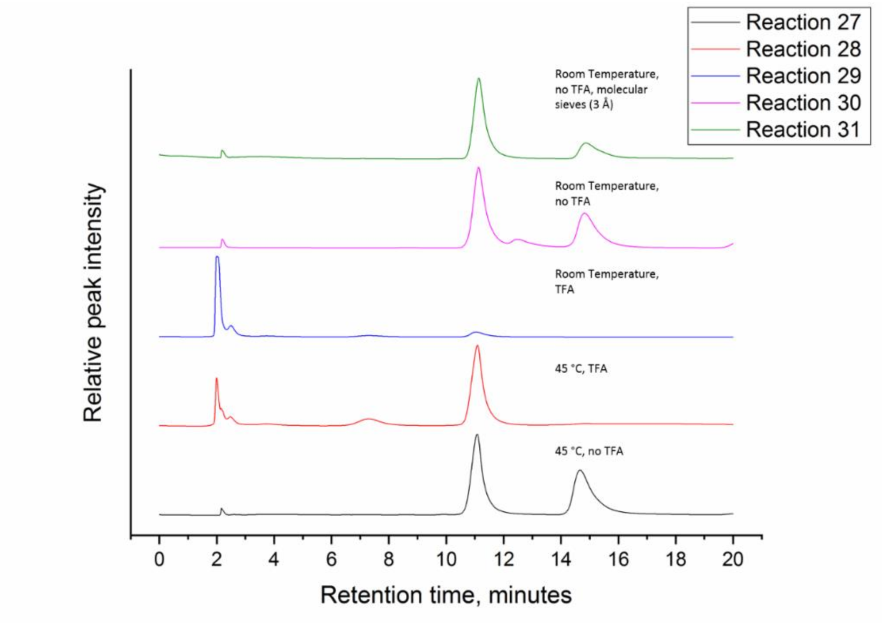

**Figure 35** HPLC Chromatographs of reactions 27 – 31 showing the effect molecular sieves, temperature and acid catalysis on the outcome of the reaction.

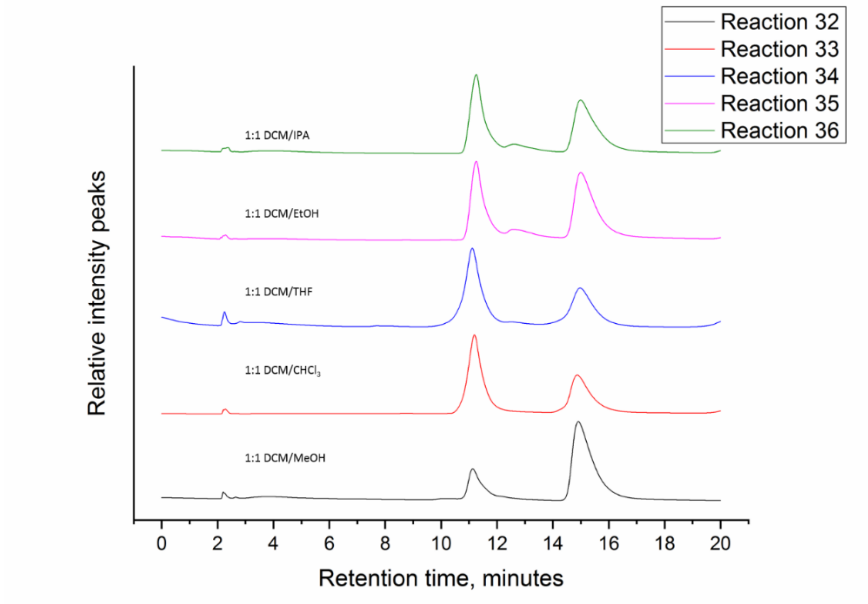

**Figure 36** HPLC Chromatographs of reactions 32–36 showing the effect of solvent composition on the outcome of the reaction.

## *3.3 HPLC Data Summary*

A third peak in the chromatographs was observed for reactions in $CHCl_3$, implying the solvent doesn't lead to clean conversion to either **TCC1**$_{[3+6]}$ or **TCC1**$_{[6+12]}$. For the stoichiometric study, when the stoichiometric ratio was ‘normal’, i.e. 3:6 aldehyde:amine both **TCC1**$_{[3+6]}$ and **TCC1**$_{[6+12]}$ were formed. When the amine was in excess neither cages were synthesised, and with excess aldehyde had no impact on the relative ratio compared with a stoichiometry of 3:6. In DCM however, excess aldehyde and excess amine reactions led to the formation of only **TCC1**$_{[3+6]}$, whereas a 3:6 reaction formed a mixture of both cages, with the dominant species present being **TCC1**$_{[3+6]}$.

As discussed in section 3.2.1, concentration can have a profound effect on the yield of reactions. Therefore concentration studies were performed from 1 mgmL$^{-1}$ to 5 mgmL$^{-1}$. Despite these conditions still being dilute, cage reactions are typically performed at 1 mgmL$^{-1}$.[2] In $CHCl_3$, there was no difference between the reactions dependent on the concentration of reactants, however in DCM the trend showed that with lower concentration, the most dilute reaction formed more **TCC1**$_{[6+12]}$ than **TCC1**$_{[3+6]}$.

Thirdly, conditions of the reactions were altered, comparing syntheses at room temperature, reflux and with and without acid catalyst. Also, molecular sieves were used for one standard[a] reaction to determine whether this had an impact on the large cage formation. In $CHCl_3$, **TCC1**$_{[6+12]}$ was only observed in reactions performed under reflux, and without the addition of an acid catalyst. The reaction performed at room temperature with TFA contained only a small amount of **TCC1**$_{[3+6]}$, and no cages were formed in the absence of TFA. Finally, the inclusion of molecular sieves yielded no change from the standard reaction. Comparatively, in DCM the reactions had similar outcomes, however when the room temperature reaction with no TFA formed two cages, and in the absence of molecule sieves under standard conditions increased the relative amount of **TCC1**$_{[6+12]}$.

Solvent had the most dramatic influence on cage ratios. In $CHCl_3$, there was very little change in the relative peak area between the three reactions ($CHCl_3$, $CHCl_3$/THF, $CHCl_3$/MeOH). DCM however showed a general increase in the relative peak areas of **TCC1**$_{[6+12]}$:**TCC1**$_{[3+6]}$, this is discussed in more detail in section 3.5.

From all 36 reactions, the optimal conditions were found to be in the 1:1 solvent system DCM/MeOH, with no acid catalyst, at 45 °C and a concentration of 1 mgmL$^{-1}$. Despite the relative amount of **TCC1**$_{[6+12]}$ being better in DCM, a higher concentration than 1 mgmL$^{-1}$ in DCM/MeOH resulted in some precipitation, preventing complete conversion from starting to materials to the cage. **Figure 37** compares some the 'optimal' conditions (blue trace) compared with other reaction conditions, showing the dramatic impact the alternative conditions have on the relative amount of **TCC1**$_{[3+6]}$ and **TCC1**$_{[6+12]}$ in solution.

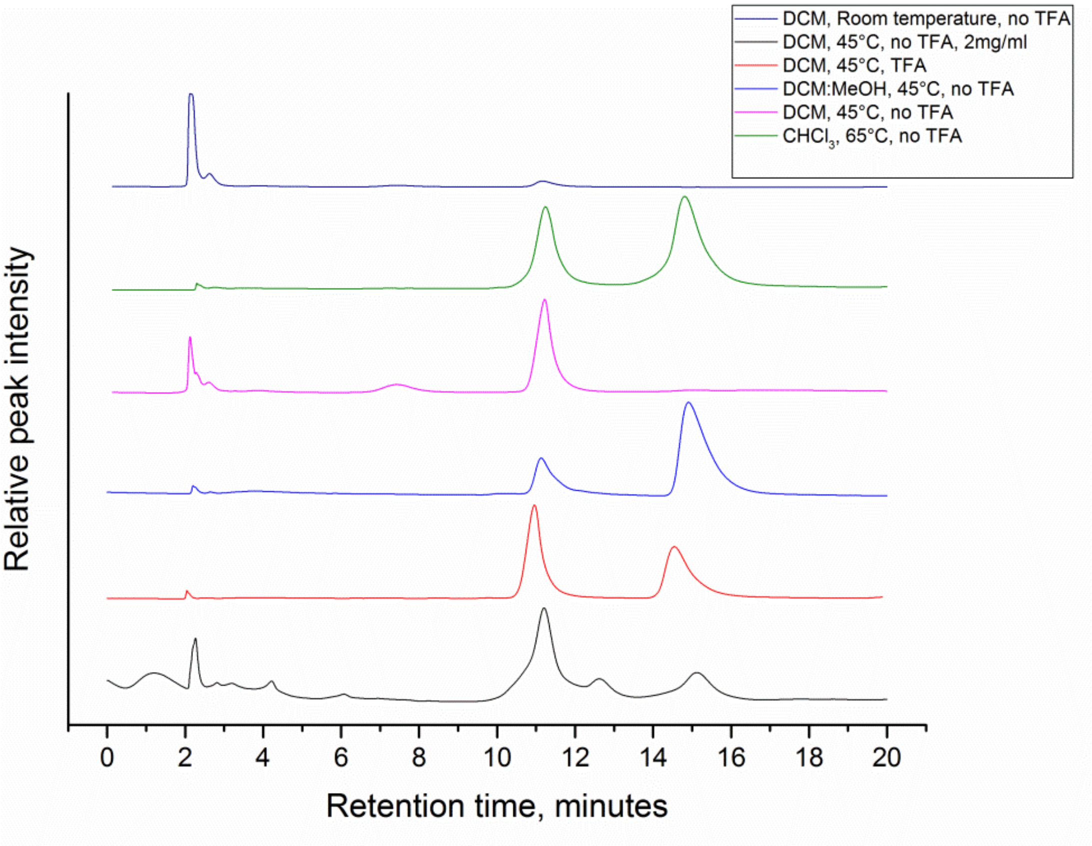

**Figure 37** Summary of the results, highlighting the findings of the synthetic variation.

## 3.4 Isolation of the materials

Prep-HPLC was attempted using a 35 mL min$^{-1}$ flow rate and 100% MeOH. The solvent from the fraction which contained **TCC1**$_{[6+12]}$ was removed under vacuum at 35 °C, leaving behind an off-white powder. The powder was then analysed using HPLC and $^1$H NMR, which revealed that it was in fact starting material. It has been shown that in some circumstances cages can collapse when desolvated, implying structural instability. However, in this case it is likely the cage is in fact chemically unstable and so upon removal of the guest solvent **TCC1**$_{[6+12]}$ breaks down into its SMs. Despite the reaction starting with a combined reagent mass of 500 mg, only 35 mg of material was recovered due to precipitation of the material in the column, likely as a result of the low solubility of **TCC1**$_{[6+12]}$. The implication being that the cage is unlikely to be stable to desolvation or isolation, and hence when in the presence of water in aqueous solvent the cage undergoes decomposition into the SMs.

Attempts were made again to isolate the material from the reaction. ‘Gentler methods’ were employed, partially removing the solvent under vacuo at lower temperatures (25 °C) until some precipitate was observed. Precipitation was encouraged using an anti-solvent, in this case hexane. After the precipitate was isolated, again there was only a small amount which was **TCC1**$_{[6+12]}$, with **TCC1**$_{[6+12]}$ remaining in solution. This ‘gentle’ method was also applied to the fraction obtained from prep-HPLC, which again showed SMs (**Figure 38** and **39**). The cage was not stable out of solution, meaning it was either unstable when desolvated, or was chemically unstable. Therefore, we were unable to isolate the material from solution and further attempts to do so were abandoned.

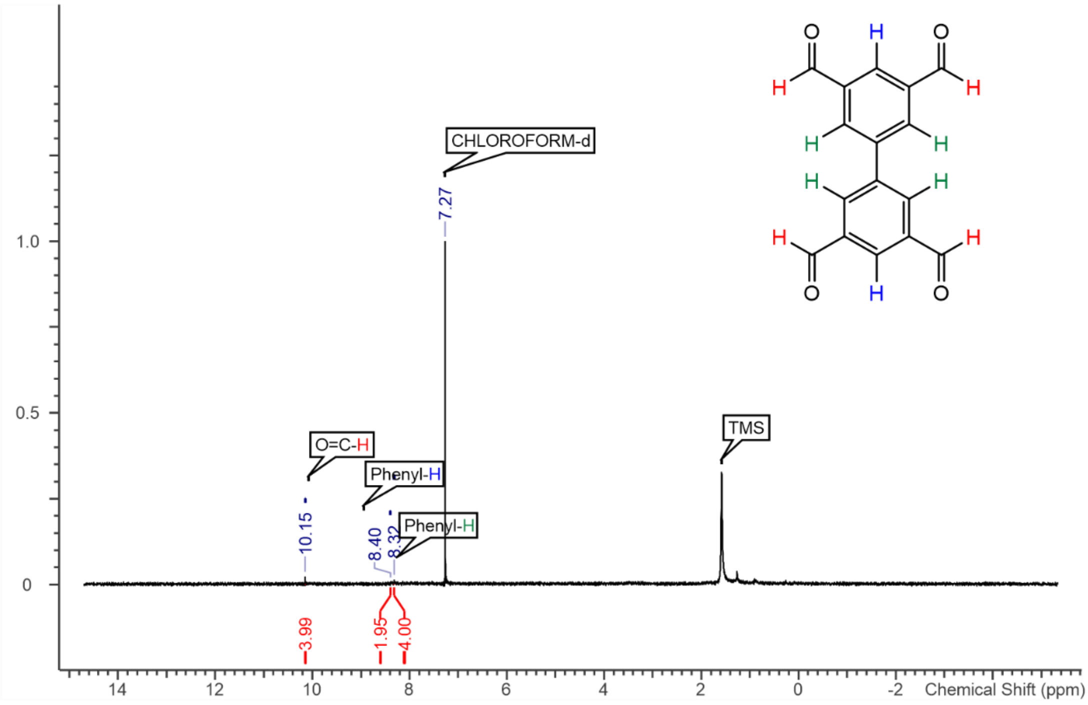

**Figure 38** NMR of the solid collected following prep-HPLC, corresponding with the starting aldehyde 5,5'-(ethyne-1,2-diyl)diisophthalaldehyde.

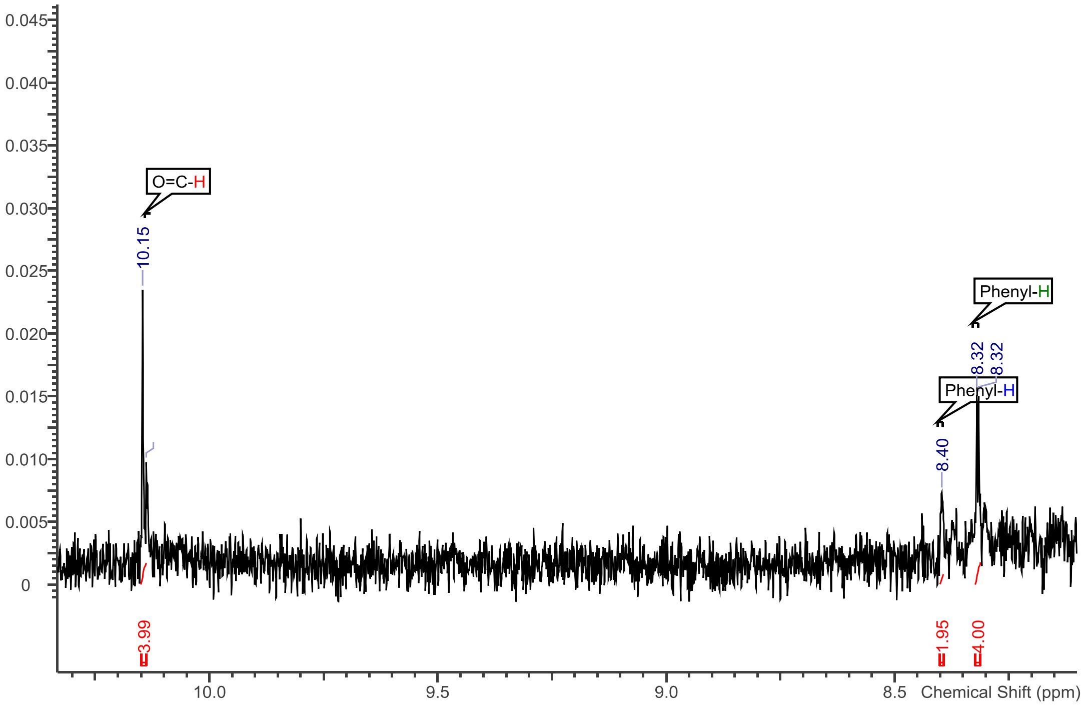

**Figure 39** NMR of the solid collected following prep-HPLC, corresponding with the starting aldehyde 5,5'-(ethyne-1,2-diyl)diisophthalaldehyde, focusing on the peaks shown in **Figure 38**.

## *3.5 Solvent effect on the reaction*

It's evident that the most influential condition is the polarity of the solvent in which the reaction takes place. It is most likely that the polar solvent impacts on the entropy of the reaction. Earlier, we discussed Liu and Wamuth discuss solvent effects on entropy in great detail, proposing that the solvent has an effect on the stability of the cages.[29] They showed that despite all the reactions containing mixtures of the three cages, there was a preference for each cage dependent on the solvent used.

**Figure 40** shows the impact of a secondary solvent on the relative amounts of **TCC1**$_{[6+12]}$ in solution for the reactions. The data shows that with increasing relative polarity, there was a correlation with the amount of **TCC1**$_{[6+12]}$ in the reaction. As it was discussed earlier, the optimal conditions for the largest proportion of **TCC1**$_{[6+12]}$ was in DCM/MeOH.

| Primary Solvent | Secondary Solvent | Relative Polarity | Peak area of TCC$_{[6+12]}$ (% a/a) |
|---|---|---|---|
| Dichloromethane | Tetrahydrofuran | 0.207 | 36.0 |
| Dichloromethane | Chloroform | 0.259 | 39.7 |
| Dichloromethane | Propan-2-ol | 0.546 | 46.7 |
| Dichloromethane | Ethanol | 0.654 | 51.4 |
| Dichloromethane | MeOH | 0.762 | 71.9 |

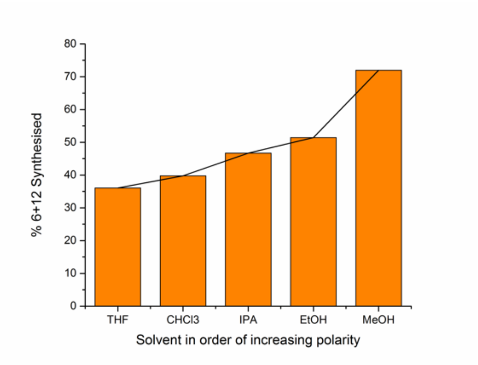

**Figure 40** Data showing the percentage of [6+12] cage formed for different solvent compositions. Higher conversion to **TCC1**$_{[6+12]}$ seemed to be proportional to the polarity of the secondary solvent used for reactions 32–36. Polarity values were determined using the relative polarity by comparison to water, the solutions were made up as an equal mixture of DCM and a secondary solvent.[55]

## 3.6 Searching for **TCC2**$_{[6+12]}$ and **TCC3**$_{[6+12]}$

Identical recrystallisation experiments with **TCC2**-*S* and **TCC3**-*S* were performed over a 7 days period, searching for any evidence of **TCC2**$_{[6+12]}$ or **TCC3**$_{[6+12]}$. The cages were dissolved to a concentration of 1 mgmL$^{-1}$, and left in incubation at 20 °C. However, after this amount of time there was no evidence of formation. Shown in **Figure 41** are the chromatographs after the materials were left in solution for 7 days, both were run using the same column (syncronosis C6) and mobile phase (MeOH) as the **TCC1**-*S* experiments, however no second peaks were observed. The chromatographs have been cut to 20 minutes for the figure, however the entire run time was 30 minutes in case the larger cages eluted later than anticipated. When TFA was added to the recrystallisation, some precipitation was observed and no peaks visible in the chromatograph. This implied the cages had undergone reversal to their SMs.

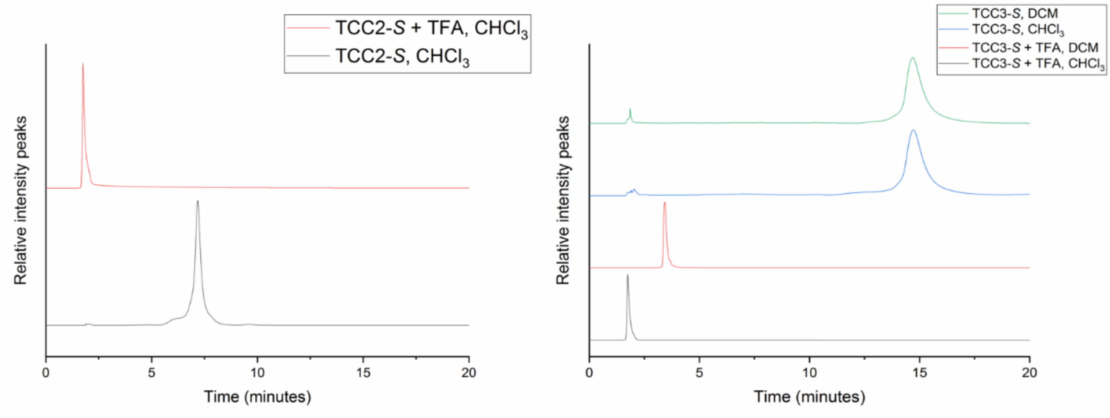

**Figure 41** Chromatographs of **TCC2**-*S* and **TCC3**-*S* in CHCl$_3$ comparing with and without TFA.

## 4 Computational Outlook

*N.B The following text has been modified from existing text by collaborator Valentina Santolini, Imperial College.*

Despite best efforts to isolate **TCC1**$_{[6+12]}$, all experiments proved unsuccessful. Therefore we wanted to rationalise **TCC1**$_{[6+12]}$ formation, and furthermore compare the formation energies of all 3 parent cages, **TCC1-3**$_{[3+6]}$ and the large, **TCC1-3**$_{[6+12]}$ cages, using computational calculations. The lowest energy conformer was calculated for each structure, with all cages analysed in the gas phase using high temperature Molecular Dynamic (MD). As expected, in agreement with experimental data, A) **TCC1**$_{[6+12]}$ partially collapses, B) **TCC2**$_{[6+12]}$ maintained an open internal cavity and exhibited shape persistence, and C) **TCC3**$_{[6+12]}$ collapsed completely, losing the internal void (**Figure 42**). Experimental data showed no evidence of **TCC2**$_{[6+12]}$ & **TCC3**$_{[6+12]}$.

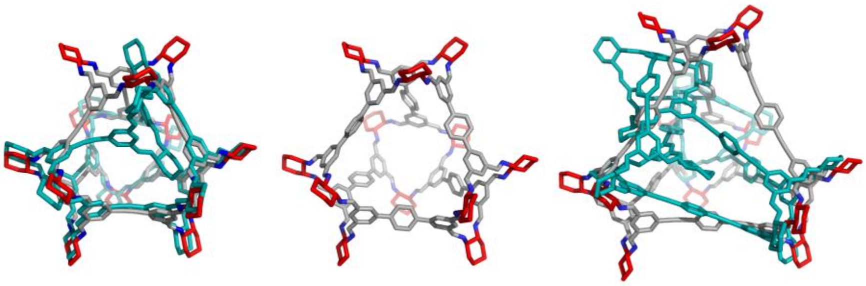

A B C

**Figure 42** A) **TCC1**[6+12], collapsed (teal) and open structures are overlaid; B) **TCC2**[6+12]; C) **TCC3**[6+12], collapsed (teal) and open structures are overlaid

**TCC1**[6+12] was around 3 kJ mol$^{-1}$ higher in energy than the partially collapsed cage. Despite such a minor energetic difference, it would be expected that this molecule would undergo collapse and loss of its internal cavity when undergoing desolvation. **CC7** was postulated to undergo a vertex-folding mechanism when collapsing, whereby each of the vertices rotated towards the internal cavity when the internal solvent is lost.[54] **TCC1**[6+12] contains 12 cyclohexanediamine vertices, causing significant collapse and resulting in disorder in the crystal structure and therefore a substantial decrease in potential porosity. The open conformer of **TCC3**[6+12] was determine to be around 96 kJ mol$^{-1}$ higher in energy than the completely collapsed conformer, therefore it was determine this cage would not be shape persistent. As all reactions are performed in solvent, the cages would most likely assemble as the open conformer. Therefore, we chose to compare the internal energies of the open [6+12] cages with those of the experimental and modelled conformers (**Figure 43**).[54]

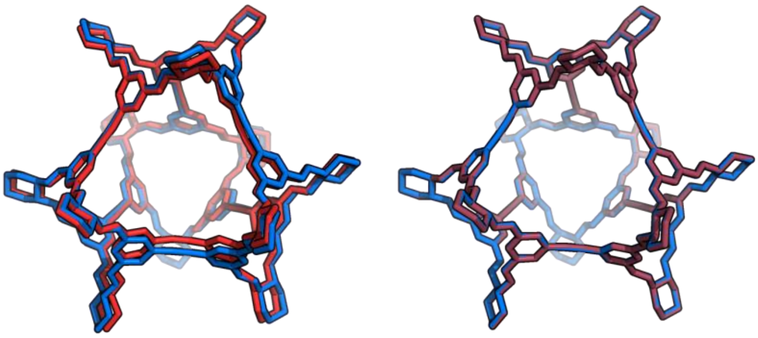

**Figure 43** Left – overlays of modelled (blue) and crystal structures for **TCC1**[6+12] (red); right – Overlays of modelled (blue) and minimised crystal structures (dark red).

Solvated and desolvated crystal structures were available for **TCC1-3**[3+6], as well as manually-constructed molecules whereby geometry optimisations were performed using DFT. For **TCC1**[3+6], between the three conformations there were few structural differences, therefore the energies were similar. Comparatively, **TCC2**[3+6] and **TCC3**[3+6] did not show the same structural similarity. Gas phase simulations do not account for solvent or crystal packing effects, therefore the 'swelling' observed experimentally in solvated crystal structures for **TCC2**$_{[3+6]}$ and **TCC3**$_{[3+6]}$ is not detected computationally (**Figure 44**).

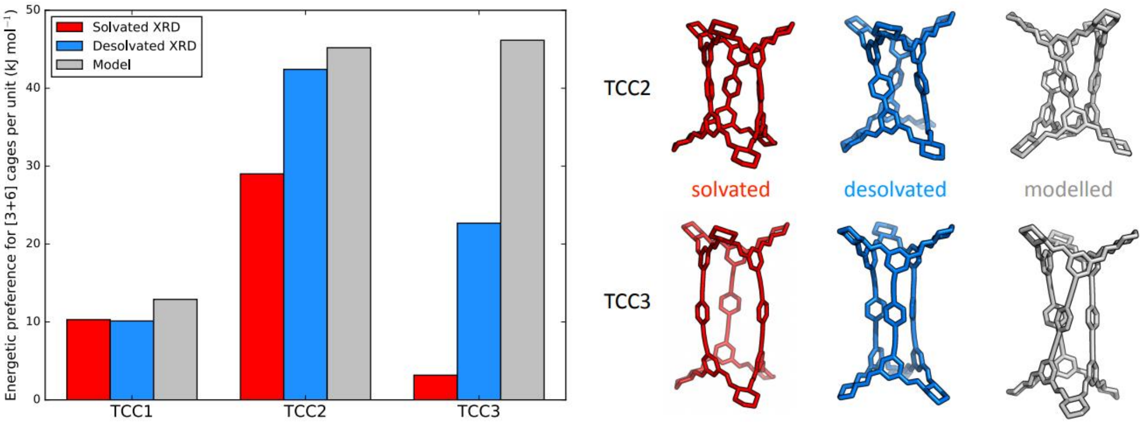

**Figure 44** DFT relative stabilities of large **TCC1–3**$_{[6+12]}$ cages with respect to smaller **TCC1–3**$_{[3+6]}$ cages normalized per [3+6] stoichiometric unit; the relative formation energies of open **TCC1–3**$_{[6+12]}$ is 0 in each case (left). The different solvated, desolvated, and modelled crystal structures for **TCC2**$_{[3+6]}$ and **TCC3**$_{[3+6]}$ are shown (right).

Subsequently, we next compared the relative energies of the open **TCC1-3**$_{[6+12]}$ and **TCC1-3**$_{[3+6]}$ (modelled, solvated and desolvated crystal structure) normalised per [3+6] stoichiometric unit, with the [6+12] cages being exactly twice the size of the [3+6] molecule (**Figure 44**). In all three systems, the calculations suggested a preference for the formation of the smaller cages.[10] Only a relatively small energetic difference between the internal relative energy of the [3+6] cages (modelled, solvated and desolvated) and the open [6+12] cages for **TCC1** was found, of around ~ 10 kJ mol$^{-1}$ per [3+6] stoichiometric unit. We hypothesise that the energy difference between the open, solvated [6+12] cage and [3+6] cage could be overcome by altering the reaction conditions, with the most significant impact likely made by solvent choice.[29]

Comparatively, **TCC2**$_{[6+12]}$, is much less energetically favourable than **TCC2**$_{[3+6]}$ somewhere between 29 and 42 kJ mol$^{-1}$, for the modelled, solvated and desolvated structures. **TCC3** is considerably more complicated, as there is a large variation in relative energies between the different conformations. If we were to only take the desolvated and simulation conformations into consideration, there is a preference for the formation of **TCC3**$_{[3+6]}$ by 23 and 45 kJ mol$^{-1}$. Conversely, the solvated SCXRD conformation is only 2 kJ mol$^{-1}$ more stable than the open [6+12] cage, most likely due to the significant strain visible in the solvated **TCC3**$_{[3+6]}$ conformation. When considering these together, we can therefore rationalise why only **TCC1**$_{[6+12]}$ was observed experimentally when in certain experimental conditions, whereas the equivalent analogues for **TCC2**$_{[6+12]}$ & **TCC3**$_{[6+12]}$ were not.

# *5 Conclusions*

We have demonstrated that it is possible for an imine organic cage to re-equilibrate in solution, transforming from **TCC1**$_{[3+6]}$ into **TCC1**$_{[6+12]}$, stoichiometrically twice as large with an alternative geometry and topology. This work has further highlighted the importance of dynamic imine chemistry towards the formation of new cage materials. We have also shown it is possible to discover new cage topologies and/or geometries through alternative reaction conditions, similarly to other cage species such as MOPs.

The reaction has been optimised to preferentially form **TCC1**$_{[6+12]}$, and furthermore computational calculations have confirmed that the **TCC1**$_{[6+12]}$ when collapsed is the thermodynamic product, but that **TCC1**$_{[3+6]}$ and **TCC1**$_{[6+12]}$ when open and solvated are close in energy and hence form simultaneously under the same experimental conditions.

We were unable to isolate **TCC1**$_{[6+12]}$, and *in silico* methods showed that this was due to the fact that the large cage is not shape persistent, and so when the solvent is no longer within the intrinsic pore, the cage is unable to remain in an ‘inflated’ state. The NMR spectra of the material collected after pre-HPLC showed that the cage was unstable when desolvated and underwent decomposition into its constituent past. Furthermore, this implied that upon desolvation the cage was not just structurally unstable and formed a collapsed species, but was also chemically unstable.

For the other cages in the series, **TCC2**[3+6] and **TCC3**[3+6], we showed that despite repeating the same experimental conditions we could not find any evidence of **TCC2**[6+12] or **TCC3**[6+12]. Computational calculations revealed that these large cages were significantly higher in energy than their smaller counterparts and so supported that they were not observed experimentally.

# 6 References

1 C. J. Pugh, V. Santolini, R. L. Greenaway, M. A. Little, M. E. Briggs, K. E. Jelfs and A. I. Cooper, *Cryst. Growth Des.*, 2018, **18**, 2759–2764.

2 T. Tozawa, J. T. A. Jones, S. I. Swamy, S. Jiang, D. J. Adams, S. Shakespeare, R. Clowes, D. Bradshaw, T. Hasell, S. Y. Chong, C. Tang, S. Thompson, J. Parker, A. Trewin, J. Bacsa, A. M. Z. Slawin, A. Steiner and A. I. Cooper, *Nat Mater*, 2009, **8**, 973–978.

3 M. A. Little, S. Y. Chong, M. Schmidtmann, T. Hasell and A. I. Cooper, *Chem. Commun.*, 2014, **50**, 9465–9648.

4 J. T. A. Jones, D. Holden, T. Mitra, T. Hasell, D. J. Adams, K. E. Jelfs, A. Trewin, D. J. Willock, G. M. Day, J. Bacsa, A. Steiner and A. I. Cooper, *Angew. Chemie*, 2011, **123**, 775–779.

5 P. S. Reiss, M. A. Little, V. Santolini, S. Y. Chong, T. Hasell, K. E. Jelfs, M. E. Briggs and A. I. Cooper, *Chem. - A Eur. J.*, 2016, **22**, 16547–16553.

6 S. Jiang, K. E. Jelfs, D. Holden, T. Hasell, S. Y. Chong, M. Haranczyk, A. Trewin and A. I. Cooper, *J. Am. Chem. Soc.*, 2013, **135**, 17818–17830.

7 J. Tian, P. K. Thallapally and B. P. McGrail, *CrystEngComm*, 2012, **14**, 1909–1919.

8 T. Hasell, M. A. Little, S. Y. Chong, M. Schmidtmann, M. E. Briggs, V. Santolini, K. E. Jelfs, A. I. Cooper, A. Trewin, F. Schiffman, F. Cora, B. Slater, A. Steiner, G. M. Day, A. I. Cooper, J. Liu, D. M. Strachan, P. K. Thallapally and A. I. Cooper, *Nanoscale*, 2017, **9**, 6783–6790.

9 T. Hasell, S. Y. Chong, M. Schmidtmann, D. J. Adams and A. I. Cooper, *Angew. Chemie Int. Ed.*, 2012, **51**, 7154–7157.

10 A. G. Slater, M. A. Little, A. Pulido, S. Y. Chong, D. Holden, L. Chen, C. Morgan, X. Wu, G. Cheng, R. Clowes, M. E. Briggs, T. Hasell, K. E. Jelfs, G. M. Day and A. I. Cooper, *Nat. Chem.*, 2016, **9**, 1, 17-25.

11 A. R. Hughes, N. J. Brownbill, R. C. Lalek, M. E. Briggs, A. G. Slater, A. I. Cooper and F. Blanc, *Chem. - A Eur. J.*, 2017, **23**, 17217–17221.

12 M. O'Keeffe, M. A. Peskov, S. J. Ramsden and O. M. Yaghi, *Acc. Chem. Res.*, 2008, **41**, 1782–1789.

13 E. V. Alexandrov, V. A. Blatov, A. V. Kochetkov and D. M. Proserpio, *CrystEngComm*, 2011, **13**, 3947-3958.

14 O. M. Yaghi, M. O'Keeffe, N. W. Ockwig, H. K. Chae, M. Eddaoudi and J. Kim, *Nature*, 2003, **423**, 705–714.

15 X. Zou, H. Ren and G. Zhu, *Chem. Commun.*, 2013, **49**, 3925-3936.

16 A. Yamamoto, S. Uehara, T. Hamada, M. Miyata, I. Hisaki and N. Tohnai, *Cryst. Growth Des.*, 2012, **12**, 4600–4606.

17 W. Guo, E. Galoppini, R. Gilardi, G. I. Rydja and Y.-H. Chen, *Cryst. Growth Des.*,

2001, **1**, 231–237.

18 A. P. Côté, A. I. Benin, N. W. Ockwig, M. O'Keeffe, A. J. Matzger and O. M. Yaghi, *Science*, 2005, **310**, 1166–70.

19 V. Santolini, M. Miklitz, E. Berardo and K. E. Jelfs, *Nanoscale*, 2017, **9**, 5280–5298.

20 Y. Liu, X. Liu and R. Warmuth, *Chem. - A Eur. J.*, 2007, **13**, 8953–8959.

21 Q. F. Sun, J. Iwasa, D. Ogawa, Y. Ishido, S. Sato, T. Ozeki, Y. Sei, K. Yamaguchi and M. Fujita, *Science*, 2010, **328**, 1144–1147.

22 R. L. Greenaway, V. Santolini, M. J. Bennison, B. M. Alston, C. J. Pugh, M. A. Little, M. Miklitz, E. G. B. Eden-Rump, R. Clowes, A. Shakil, H. J. Cuthbertson, H. Armstrong, M. E. Briggs, K. E. Jelfs and A. I. Cooper, *Nat. Commun.*, 2018, **9**, 2849-2856.

23 X.-P. Zhou, J. Liu, S.-Z. Zhan, J.-R. Yang, D. Li, K.-M. Ng, R. W.-Y. Sun and C.-M. Che, *J. Am. Chem. Soc.*, 2012, **134**, 8042–8045.

24 D. J. Tranchemontagne, Z. Ni, M. Okeeffe, O. M. Yaghi, M. O 'keeffe and O. M. Yaghi, *Angew. Chem. Int. Ed*, 1930, **47**, 5136–5147.

25 Q.-F. Sun, J. Iwasa, D. Ogawa, Y. Ishido, S. Sato, T. Ozeki, Y. Sei, K. Yamaguchi and M. Fujita, *Science (80-. ).*, 2010, **328**, 1144–1147.

26 J. D. Evans, K. E. Jelfs, G. M. Day and C. J. Doonan, *Chem. Soc. Rev.*, 2017, **46**, 3286–3301.

27 T. Hasell, X. Wu, J. T. A. Jones, J. Bacsa, A. Steiner, T. Mitra, A. Trewin, D. J. Adams and A. I. Cooper, *Nat. Chem.*, 2010, **2**, 750–755.

28 K. E. Jelfs, E. G. B. Eden, J. L. Culshaw, S. Shakespeare, E. O. Pyzer-Knapp, H. P. G. Thompson, J. Bacsa, G. M. Day, D. J. Adams and A. I. Cooper, *J. Am. Chem. Soc.*, 2013, **135**, 9307–9310.

29 X. Liu and R. Warmuth, *J. Am. Chem. Soc.*, 2006, **43**, 14120–14127.

30 X. Liu, Y. Liu, G. Li and R. Warmuth, *Angew. Chemie Int. Ed.*, 2006, **45**, 901–904.

31 S. Jiang, J. T. A. Jones, T. Hasell, C. E. Blythe, D. J. Adams, A. Trewin and A. I. Cooper, *Nat. Commun.*, 2011, **2**, 207, 1-11.

32 N. Giri, M. G. Del Pópolo, G. Melaugh, R. L. Greenaway, K. Rätzke, T. Koschine, L. Pison, M. F. C. Gomes, A. I. Cooper and S. L. James, *Nature*, 2015, **527**, 216–220.

33 T. Hasell, J. L. Culshaw, S. Y. Chong, M. Schmidtmann, M. A. Little, K. E. Jelfs, E. O. Pyzer-Knapp, H. Shepherd, D. J. Adams, G. M. Day and A. I. Cooper, *J. Am. Chem. Soc.*, 2014, **136**, 1438–1448.

34 D. P. McMahon, A. Stephenson, S. Y. Chong, M. Little, J. T. A. Jones, A. I. Cooper and G. M. Day, *Faraday Discuss.*, **211**, 383-399..

35 T. Mitra, X. Wu, R. Clowes, J. T. A. Jones, K. E. Jelfs, D. J. Adams, A. Trewin, J. Bacsa, A. Steiner and A. I. Cooper, *Chem. - A Eur. J.*, 2011, **17**, 10235–10240.

36 C. D. Meyer, C. S. Joiner and J. F. Stoddart, *Chem. Soc. Rev.*, 2007, **36**, 1705-1723.

37 M. Liu, M. A. Little, K. E. Jelfs, J. T. A. Jones, M. Schmidtmann, S. Y. Chong, T. Hasell and A. I. Cooper, 2014, **21**, 7583–7586.

38 A. L. Spek, *Acta Crystallogr. Sect. C, Struct. Chem.*, 2015, **71**, 9–18.

39 R. W. Grosse-Kunstleve and P. D. Adams, *J. Appl. Crystallogr.*, 2002, **35**, 477–480.

40 S. C. Capelli, H.-B. Bürgi, B. Dittrich, S. Grabowsky and D. Jayatilaka, *IUCrJ*, 2014, **1**, 361–379.

41 G. N. Murshudov, P. Skubák, A. A. Lebedev, N. S. Pannu, R. A. Steiner, R. A. Nicholls, M. D. Winn, F. Long and A. A. Vagin, *Acta Crystallogr. Sect. D Biol. Crystallogr.*, 2011, **67**, 355–367.

42 A. Thorn, B. Dittrich, G. M. Sheldrick and IUCr, *Acta Crystallogr. Sect. A Found. Crystallogr.*, 2012, **68**, 448–451.

43 G. M. Sheldrick, *Acta Crystallogr. A.*, 2008, **64**, 112–22.

44 V. Santolini, M. Miklitz, E. Berardo and K. E. Jelfs, *Nanoscale*, 2017, **9**, 5280–5298.

45 M. E. Belowich and J. F. Stoddart, *Chem. Soc. Rev.*, 2012, **41**, 2003-2024.

46 G. Zhu, Y. Liu, L. Flores, Z. R. Lee, C. W. Jones, D. A. Dixon, D. S. Sholl and R. P. Lively, *Chem. Mater.*, 2018, **30**, 262–272.

47 L. M. Bateman, O. A. McNamara, N. R. Buckley, P. O'Leary, F. Harrington, N. Kelly, S. O'Keeffe, A. Stack, S. O'Neill, D. G. McCarthy and A. R. Maguire, *Org. Biomol. Chem.*, 2015, **13**, 11026–11038.

48 P. Timmerman, J.-L. Weidmann, K. A. Jolliffe, L. J. Prins, D. N. Reinhoudt, S. Shinkai, L. Frish and Y. Cohen, *J. Chem. Soc. Perkin Trans. 2*, 2000, **0**, 2077–2089.

49 B. Lee, H. M. Stowe, K. H. Lee, N. H. Hur, S.-J. Hwang, E. Paek and G. S. Hwang, *Phys. Chem. Chem. Phys.*, 2017, **19**, 24067–24075.

50 V. Martí-Centelles, M. D. Pandey, M. I. Burguete and S. V. Luis, *Chem. Rev.*, 2015, **115**, 8736–8834.

51 B. L. Shaw, *J. Am. Chem. Soc.*, 1975, **97**, 3856–3857.

52 K. Nishikawa, Y. Yoshimi, K. Maeda, T. Morita, I. Takahashi, T. Itou, S. Inagaki and M. Hatanaka, *J. Org. Chem.*, 2013, **78**, 582–589.

53 S. R. Batten, *J. Solid State Chem.*, 2005, **178**, 2475–2479.

54 V. Santolini, G. A. Tribello and K. E. Jelfs, *Chem. Commun.*, 2015, **51**, 15542–15545.

55 C. Reichardt and T. Welton, *Solvents and Solvent Effects in Organic Chemistry*, Wiley-VCH, 2011, 131-132.

# Chapter 3

## The Role of Crystallography in High Throughput Discovery of Organic Molecular Cages

# 1 Introduction

*The work reported herein is part of a larger study, published in Nature Communications, 2018.*[1]

## 1.1 High-throughput Screening

High throughput methods allow scientists to perform hundreds, or even thousands of reactions, in parallel, utilising robotics to increase the rate at which successful compounds, or 'hits', are discovered. High-throughput screening (HTS) is an approach used by the pharmaceutical industry to discover drug molecules.[2,3] After 1989, when computational screening became feasible due to improved technology, libraries of compounds were generated increasing the rate of drug discovery. Prior to this, drug design was reliant on experimental work and in vivo testing, which proved to be both an expensive and lengthy process.[4,5] Since high throughput discovery and implementation in laboratories, the cumulative numbers of potential drug candidates identified from high throughput screening has increased every year.[6]

One successful use of this approach was identified in 2017, whereby high-throughput methodology was implemented to overcome a difficult synthetic procedure of a potential drug candidate.[7] Their research showed that by using simple, inexpensive tools, such as 96-well plates, overcame challenges in research and development expense; including time, number of people and the amount of material required.[8]

Since the initial combinatorial chemistry experiments for drug discovery began, the proven success of these HTS has been implemented in other areas of chemistry than the pharmaceutical industry. Chemical coating utilises substrates with different properties to the object they are applied, for example, anti-corrosives, antibacterial properties or wettability.[9–11] Using HTS, chemical coatings can be developed at a faster rate, using less reagents and have significant impacts in many areas of chemistry.[12] As well as HT formulations, HT analytical techniques can be employed *in situ*, such as infra-red (IR), NMR, PXRD and even solution based methods such as LCMS.[13,8]

The proven success of using HT methods can be applied to other areas of chemistry, for example, the formation of a functional material.[14] In 2008, the Yaghi group showed it was possible to use HTS in order to synthesised functional zeolites for $CO_2$ capture.[15] As well as materials for gas uptake, electrocatalytic materials for hydrogen evolution have been shown to be successfully synthesised based on computational density functional theory-based calculations.[16]

## *1.2 High-throughput Cage Synthesis*

Synthesising functional materials by design is a time-consuming process, for example, imine cages synthesised in the Cooper group take an average of 5 days for reaction completion.[17] HTS allows us to develop a large, combinatorial library and attempt multiple, small scale reactions at one time, rather than waiting for the results from each individual reaction, as is the usual approach for synthetic development. The traditional route can take months, or even years, to find and develop new cage materials. However, by using HTS a large screen of potential cages can be identified in a matter of weeks.

Dynamic Covalent Chemistry (DCC) has been strongly integrated into the synthesis of supramolecular systems.[18] By utilising the formation of strong, but reversible, covalent bonds, it is possible to synthesise multicomponent thermodynamic products.[19] Assessing previous successful syntheses in literature, focusing on the geometry and functionality of the precursors, combinatorial libraries of potential tectons for cages, or other materials, synthesis can be generated.

Dynamic imine bond formation has been extensively studied in supramolecular chemistry, with the reversibility of the imine bond being utilised to form an energetically stable, or potentially thermodynamic product. The decided starting materials for this study were aldehydes and amines, with alternative co-ordination numbers, to form organic molecular cages (OMCs).

OMC synthesis can be a slow process, with reaction times under traditional, high dilution methods taking days until completion.[20,21] However, the rate of reversibility of imine bond formation can be improved using an acid catalyst, such as <0.1% by volume of trifluoroacetic acid (TFA). Therefore the thermodynamic product can be synthesised in less time It has been shown that using TFA not only increases the rate of imine-bond formation, but it also overcomes the energy barrier to form the thermodynamic product more quickly, rather than kinetic products.[22]

## *1.3 High-throughput Analysis*

One of the most important considerations when performing HT experiments are which analytical methods are best to process such large volumes of data. To analyse and characterise materials which are synthesised through HT, it is important to avoid any time-consuming analysis which wouldn't reveal anything significant. Infra-red (IR) measurements can indicate the presence of a functional group, for example, formation of an imine bond. However, IR rarely provides any direct structural information, which is of paramount importance for supramolecular systems, as it is not always clear what the reaction outcome is. For example, although IR data could indicate the formation of an imine bond with a sharp C=N stretch at 1656 - 1742 $cm^{-1}$, this wouldn't be able to confirm whether the molecule synthesised was a cage or macrocycle, or whether the reaction had gone to completion.

Comparatively, nuclear magnetic resonance spectroscopy (NMR) can provide this information, and a $^1H$ NMR would only take an average of 16 minutes, but the structure of the complex would need to be inferred from the NMR spectra. Solution-based NMR can be used to elucidate some structural information, however this can be limited by highly symmetrical materials.[23] $^1H$ NMR determines proton 'environments', showing a peak at the corresponding frequency of the nucleus. Therefore, in highly symmetrical molecules, the chemical environments can be determined but the relative structure would be difficult to accurately predict. In these cases, SCXRD can be used for accurate structural determination. It has been shown that for various isomers of fullerene, $^{13}C$ NMR can be used for accurate identification however other complimentary spectroscopic techniques were required for full confirmation.[24]

Solid state NMR, using magic angle spin (MAS) can be also be employed, rather than solution based in order to determine structural information. This technique can be used to compliment X-ray data, as opposed to replacing it.[25] Published in 2017 is an example of using kinetic solid state NMR to show that tubular cages **TCC2** and **TCC3** could be used as molecular rotors.[26] Furthermore, NMR can be used to show where in a solid structure gases can occupy the cages, and henceforth preferential conditions for gas sorption.[27] The Warmuth group has also published a number of organic cages, which have all been characterised using 1D and 2D NMR, with conclusions verified by GPC and MALDI-TOF, as well as computational data.[28–30]

NMR is an incredibly useful spectroscopic tool for both crystalline and amorphous samples, particularly for kinetic or sorption studies. Nonetheless, we showed in Chapter 2 that it was not possible to determine between **TCC1**$_{[3+6]}$ and **TCC1**$_{[6+12]}$ using $^1$H NMR.[31] Mastalerz group synthesised a large organic cage, with the main information obtained from the $^1$H NMR spectra that the cage had formed the correct stoichiometry, 2:3, and the predicted symmetry of the reaction product.[32] Other cage structures have also relied heavily on crystal structures when they have the same stoichiometric ratio to determine the difference between the two different products.[33]

Interpreting NMR data can be challenging, particularly when assessing more complex structures such as interlocked cages.[34] Interlocked structures can prove challenging to analyse by NMR data, due to the interactions through space, which can cause shielding and, hence, change the frequency of the chemical shifts.[35] Previous studies into interlocked systems have used other methods for the identification of these interlocked species, predominantly crystallography, and NMR as a tool for verification.[36]

Examples of utilising NMR for structural identification include the ‘Star of David’ catenane, which relied heavily on the X-ray crystal structure, as well as comparing the NMR spectra of the starting materials and partially reacted reagents.[37] Interlocked cages are also reliant on 2D NMR, for example Heteronuclear single-quantum correlation spectroscopy (HSQC). A triply interlocked covalent cage, involving two equivalents of Covalent Cage 1 (**CC1**) utilised 2D NMR spectroscopy to provide further information of the through-space interactions between the two cages.[38] Fujita et al. also demonstrated

NMR as a useful tool to follow an interlocking reaction, however an X-ray structure was again required in order to determine the structure accurately.[39]

These limitations of NMR for determining the structure mean other approaches need to be considered. Currently, there are existing methods which can be used which involve minimal human-interactions and rely on robotics and software to solve crystal structures. Synchotrons can be used for high-throughput studies, with fast collection times and high energy X-rays, enabling better data collections for smaller crystals.[40] Current technology at Diamond Light Source (DLS) is introducing automated sample changing of crystals using robotics and single crystals cooled in $N_2$.[41–44]

In order to get a complete picture of the atomic structure for supramolecular complexes, the most efficient and accurate method is to use (SCXRD). However, crystallography can be a time-consuming process, as is requires the growth of a single crystal. Single crystal growth can take anything from days to weeks, and is dependent on two important factors in crystallisations; nucleation and crystal growth.[45] The two are independent of one another, but crystal growth is reliant on nucleation.[46,47] Nucleation is reliant on a number of conditions such as temperature, the concentration of the solution, or the presence of impurities as nucleation is a thermodynamic process.[48] Once nucleation has occurred, crystal growth can follow, as the nuclei agglomerate and form a larger crystalline structure.[49]

As the intermolecular interactions between POCs are non-covalent, they are non-directional and weaker than directional covalent organic or metal-organics used to synthesise other porous molecular materials, crystal growth can also be challenging.[50,51] A recent study has shown that crystal growth of **CC3** was dependent upon the synthesis time, as shown in **Figure 1**.[52] In this particular case, three distinct growth stages were identified; 1) rapid crystal growth stage favoured by slow synthesis times; 2) intermediate synthesis times resulted in increased amounts of crystal fragmentation and redissolution; and finally, 3) with longer synthesis times regrowth begins and larger crystals can be found again which corresponds to Ostwald ripening.[53]

This study has highlighted the impact that one variable, synthesis time, has on the crystal growth of one particular POC. However, this material, by comparison to other POCs, has a relatively short growth time (approximately 4 days), whereas some systems can take weeks or even longer. For microcrystalline materials, PXRD can be employed, however for SCXRD a larger crystal is required.[54] Therefore, the main limit to obtain a single crystal structure, is the growth of a well-ordered single crystal which is large enough for a data collection, producing an accurate model.

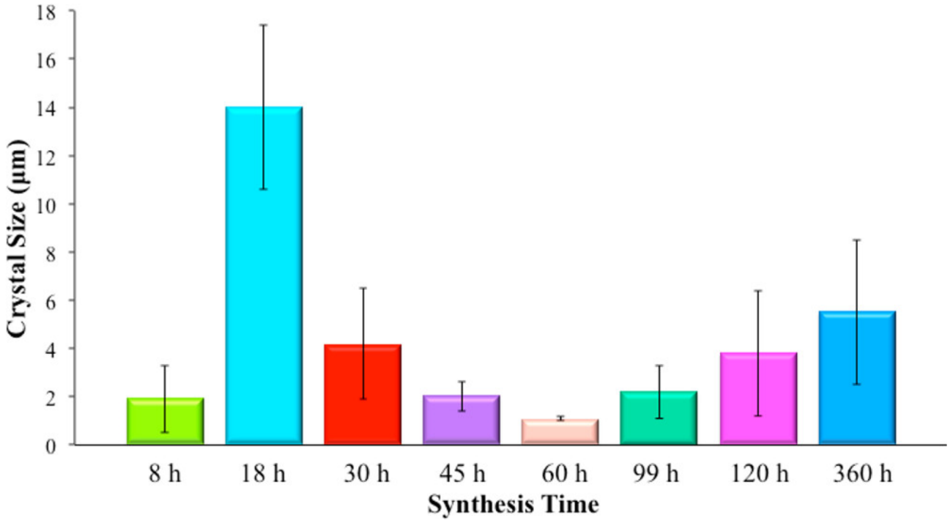

**Figure 1** Chart showing the effect synthesis time has on the crystal growth of **CC3**, indicating the optimal synthetic time for large crystals is 18 hours. Reprinted with permission from J. Lucero et al., *Cryst. Growth Des.*, 2018, **18**, 921–927. Copyright 2018 American Chemical Society.

# 2 Results and Discussion

## 2.1 High-throughput methodology

A large database was generated using aldehyde and amine precursors, which were expected to react under certain experimental conditions to form larger molecules including organic cages and macrocycles.[22,55] Since the development of HTS, it has been clear that this is an area of science which is entirely reliant on combining the expertise from multiple disciplines with one aim.[56] Therefore, this study combined synthesis, crystallography and computational work, with collaborators at Imperial College London.

As with all HTS, by utilising computational methods alongside experimental we increase the rate of potential hits. Currently, there are limited computational methodologies which allow for accurate prediction of large, self-assembled molecules due to their increasing conformational complexity.[57,58] The number of self-assembled materials being published has moved at a fairly slow rate as a result of the limits mentioned. However, this chapter discusses how recent advances in computational methodology allows us to determine the formation energy of cages and their respective topologies, increasing the rate at which we are discovering POCs.[59–62]

Using *in silico* approaches, we can calculate the formation energy of POCs, allowing us to pre-determine whether a structure is likely to form and whether it will be shape persistent.[63,64] Despite significant advancement in computational methodology, we cannot predict the effect of solvent on synthesis. Currently, calculations are typically carried out in the absence of solvent, and at zero energy, therefore negating solvent effects on the reaction. Santolini et al. discussed how solvent stabilisation energies can be calculated for crystal structure prediction, and the results correlated with the solvate structures.[65] They showed that by using known POCs, they could determine the lowest energy conformer and, hence, demonstrated that the solvent behaves as a ‘scaffold’, and the effects of this could be reproduced.

Collaborators analysed the tectons selected for the study, determining their formation energies and the most likely stoichiometric products. Low energy confirmations were searched and then the structures minimised using DFT calculations at the PBE+D3/TZVP level.[66] From this, the formation energy per imine bond was calculated and normalised. This then allows us to compare directly the energies of the cages disregarding the size or topology of the cage.[67,66]

To assess the accuracy of the computational results, they needed to be correlated with the single crystal structures. The crystal structures were over-laid with the lowest energy conformers to compare accuracies. With respect to the conformer naming system, whereby **$\mathbf{Tri^2Di^3}$** refers to two tectons with three reactive groups and three tectons with two reactive groups for the cage formation, respectively. Although computational chemistry has advanced significantly, single crystal structures can provide us with significantly more information. The materials were dissolved in dichloromethane (DCM) and chloroform ($CHCl_3$), alongside 14 common organic solvents listed in **Table 1**.

**Table 1** List of organic solvents used in the recrystallisations of the POCs in the HTS.

| ***Primary Solvents*** | ***Anti-solvents*** | |
|---|---|---|
| Dichloromethane<br>Chloroform | Acetone | *m*-xylene |
| | Hexane | *o*-xylene |
| | Pentane | *p*-xylene |
| | 2-Propanol | Ethyl Acetate |
| | Diethyl Ether | Acetonitrile |
| | Ethanol | Tetrahydrofuran |
| | Methanol | 1,4-dioxane |

Single crystal data can provide absolute structure determination without any prior knowledge of the reaction components, reaction stoichiometry and the chirality. Earlier we discussed the importance of using single crystal data, although NMR can provide us with structural information, it can be difficult to determine the stoichiometry.

A general flow chart detailing the methodology is shown in **Figure 2** detailing which sections are computational and experimental. The first step was to assemble the building block database and then assess the potential outcome based on ‘quick’ initial analyses. From the initial selection, containing 78 combinations of aldehydes and amine, the most promising based on the analysis were carried forward to the HTS, and the remaining were no longer considered. These were initially characterised using NMR and LCMS. Other considerations at play were the ease of synthesis, in terms of time scale and number of synthetic steps required.

Once assembly was confirmed from the characterisation, solutions were recrystallised and for the materials which grew single crystals the structures were obtained. Potential polymorphs or solvate structures were furthermore identified, and scale up of the materials with full analyses the final step. In this chapter we will focus on the important role crystallography plays in HT screening, focusing on the benefit of using the method alongside other analyses. We demonstrate examples whereby the computational methods did not correlate with the experimental data, and an unexpected result which was not predicted and only discovered using crystallography.

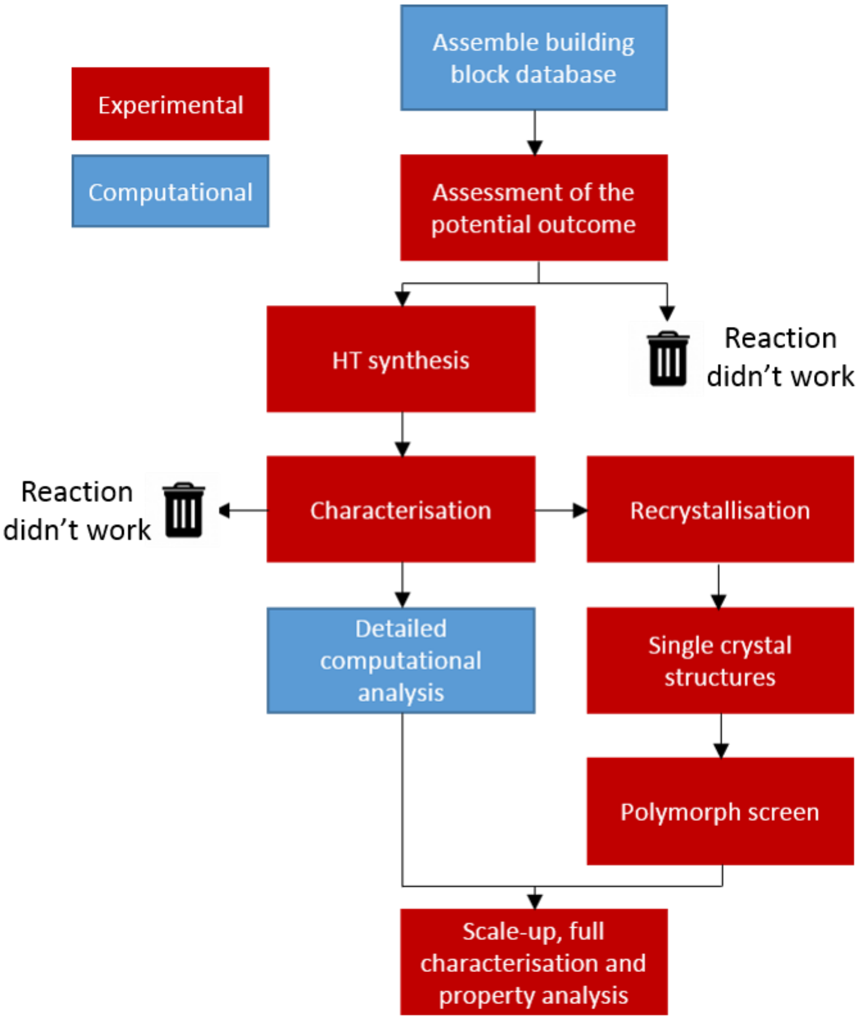

**Figure 2** Flow chart detailing the general work flow for the HTS. Blue indicates the areas which were computational, and red the experimental processes. Initial computational analyses determined the relative formation energies, whereas the more detailed and time intensive work focused on shape persistence and estimating the materials propensity for porosity.

Herein we will show the structures of these cages from the starting materials shown in **Figure 3**, and interesting results from this study. **Figure 3** shows both the calculated stoichiometric outcome, and the experimental outcome. The materials were re-crystallised using vapour diffusion methods, dissolving the cages in chloroform ($CHCl_3$) or dichloromethane (DCM), and slowly diffusing organic solvents into these solutions

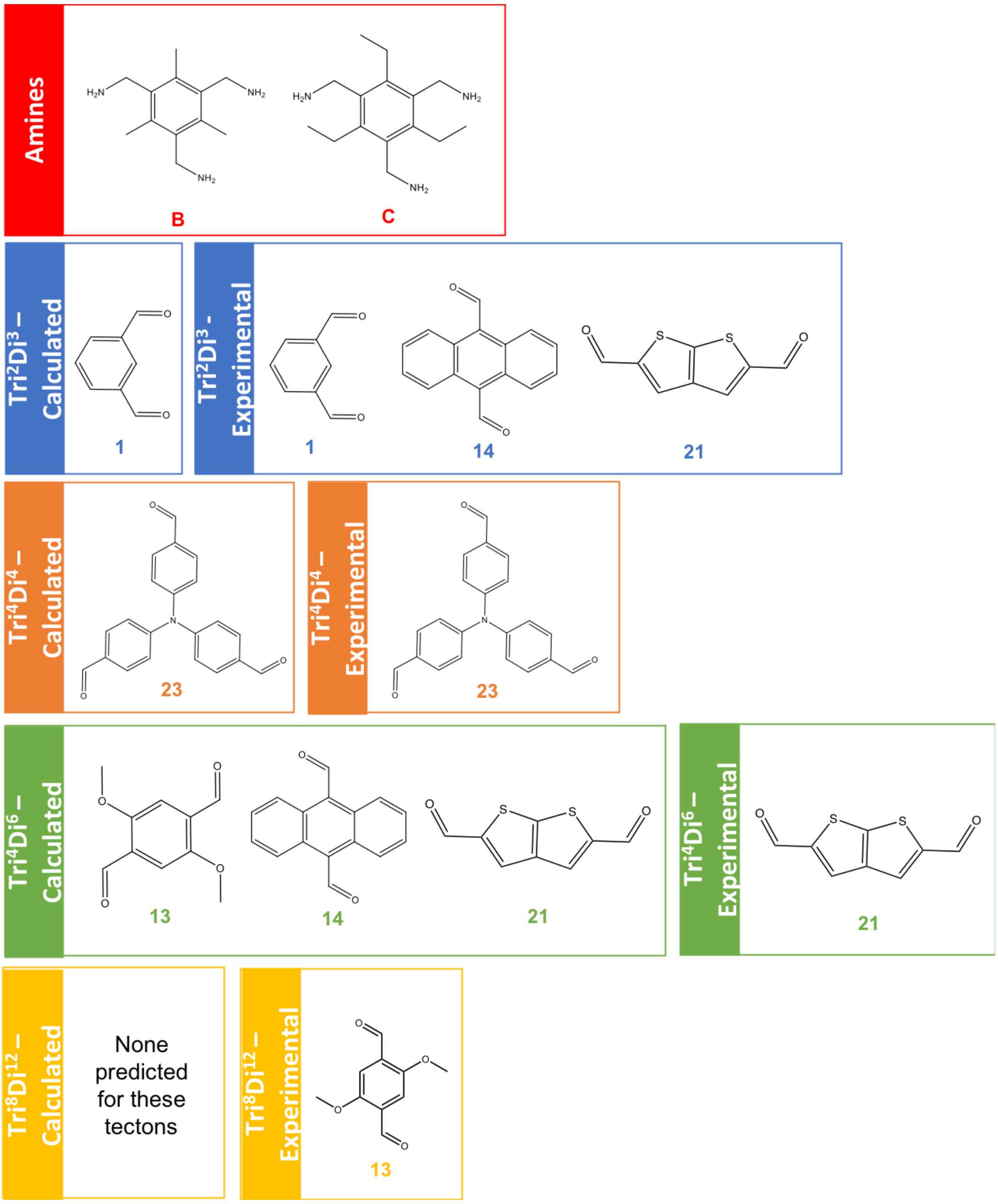

**Figure 3** Starting amine and aldehyde precursors in this study, with the calculated stoichiometries and the corresponding structures found experimentally. One exception is B13, which is discussed further in section 3.

The topologies in **Figure 4** correspond to the calculated, and experimental stoichiometric conformations shown in **Figure 3**. **Tri$^{2}$Di$^{3}$** would form a trigonal prismatic geometry, **Tri$^{4}$Di$^{4}$** a truncated tetrahedron**, Tri$^{4}$Di$^{6}$** a pyramid and **Tri$^{8}$Di$^{12}$** a cube. In the results, we will show in more detail that not only can the expected results vary, but also the topology.

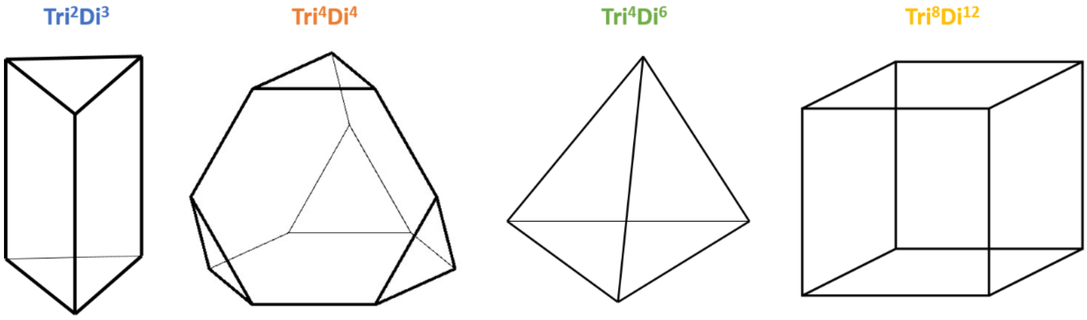

**Figure 4** Topologies of the structures based on the stoichiometry.

## *2.2. [3+2] Organic Cages*

### *2.2.1 [3+2] Organic Cage **B1***

The first [3+2] cage recrystallised was cage **B1**, synthesised from triamine (2,4,6-trimethylbenzene-1,3,5-triyl)trimethanamine and isophthalaldehyde. From the 28 crystallisation conditions one polymorph was found. The single crystal structure, **B1**·0.82($C_4H_8O_2$)·0.18($CH_2Cl_2$)·0.2($H_2O$), crystallised from a $CH_2Cl_2$/EtOAc solution in the triclinic space group $P\bar{1}$. The asymmetric unit for this phase comprises one complete **B1** cage and two disordered solvent molecules, 0.82($C_4H_8O$), and 0.18($CH_2Cl_2$), along with residual electron density modelled as water, 0.2($H_2O$).

The solvent was modelled as a mixture of EtOAc, $CH_2Cl_2$, and $H_2O$. EtOAc and $CH_2Cl_2$ were disordered over one position and site occupancies were determined using a free variable, with an occupancy of 0.82 and 0.18 respectively. For the disordered $CH_2Cl_2$, C-Cl bond distance restraints were used during refinement (DFIX in SHELX). The occupancy of the disordered $H_2O$ molecule was also determined using a free variable. For this $H_2O$ molecule it was not possible to accurately determine H atom positions. This resulted in an unlikely close intermolecular contact between one of the $H_2O$ H atoms and an aryl C-H H atom (PLAT415_ALERT_2_B checkCIF alert). For a displacement ellipsoid plot of the asymmetric unit see, **Figure 5A**.

The crystal structure **B1**·0.82($C_4H_8O_2$)·0.18($CH_2Cl_2$)·0.2($H_2O$) is shown overlaid with the calculated structure in **Figure 5B**. One of the linkers can be seen to have poor positional agreement between the crystal structure and computational model, but otherwise there appears to be good agreement between the two. The root-mean-square-differential (RMSD) was calculated to be only 0.25 Å between the calculated and predicted structure. The closer to 0, the better the agreement, therefore the RMSD in this case shows good agreement between the two.

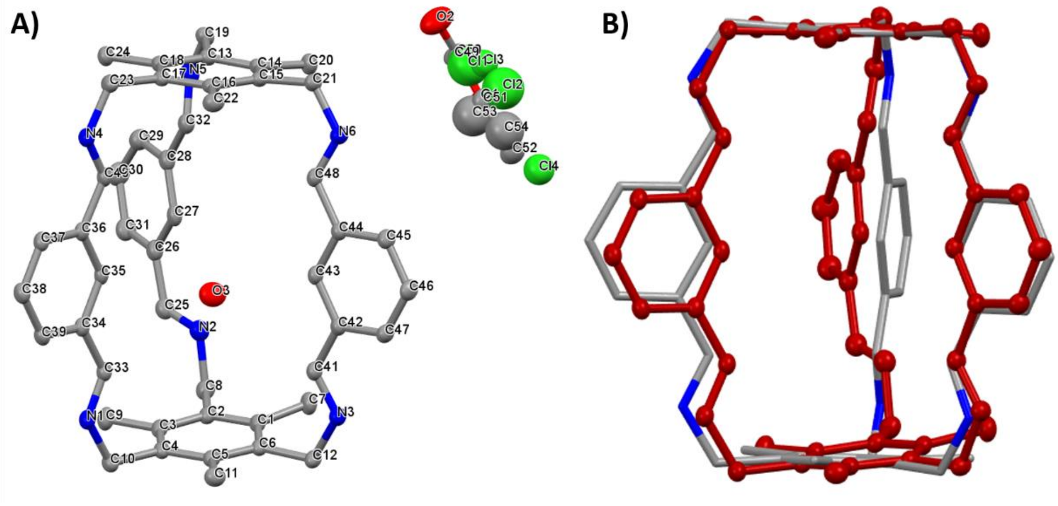

**Figure 5 A)** The displacement ellipsoid plot from the single crystal structure of **B1**·0.82($C_4H_8O_2$)·0.18($CH_2Cl_2$)·0.2($H_2O$), with ellipsoids displayed at 50% probability; **B)** Overlay of the experimental crystal structure of **B1** (red) and the calculated cage.

The cages packed window to edge (WTE), with the phenyl groups on the linkers forming both parallel and parallel-displaced $\pi$–$\pi$ stacks throughout the structure at a distance 3.89 Å and 3.47 Å respectively. In this cage, the ‘edge’ refers to the cage vertices, or linkers. No window to window (WTW) interactions were observed in the crystal structure. Parallel $\pi$–$\pi$ stacking between cages can be seen when viewed along the *b*-axis in **Figure 6**, and parallel displaced $\pi$–$\pi$ stacking and the *a*-axis.

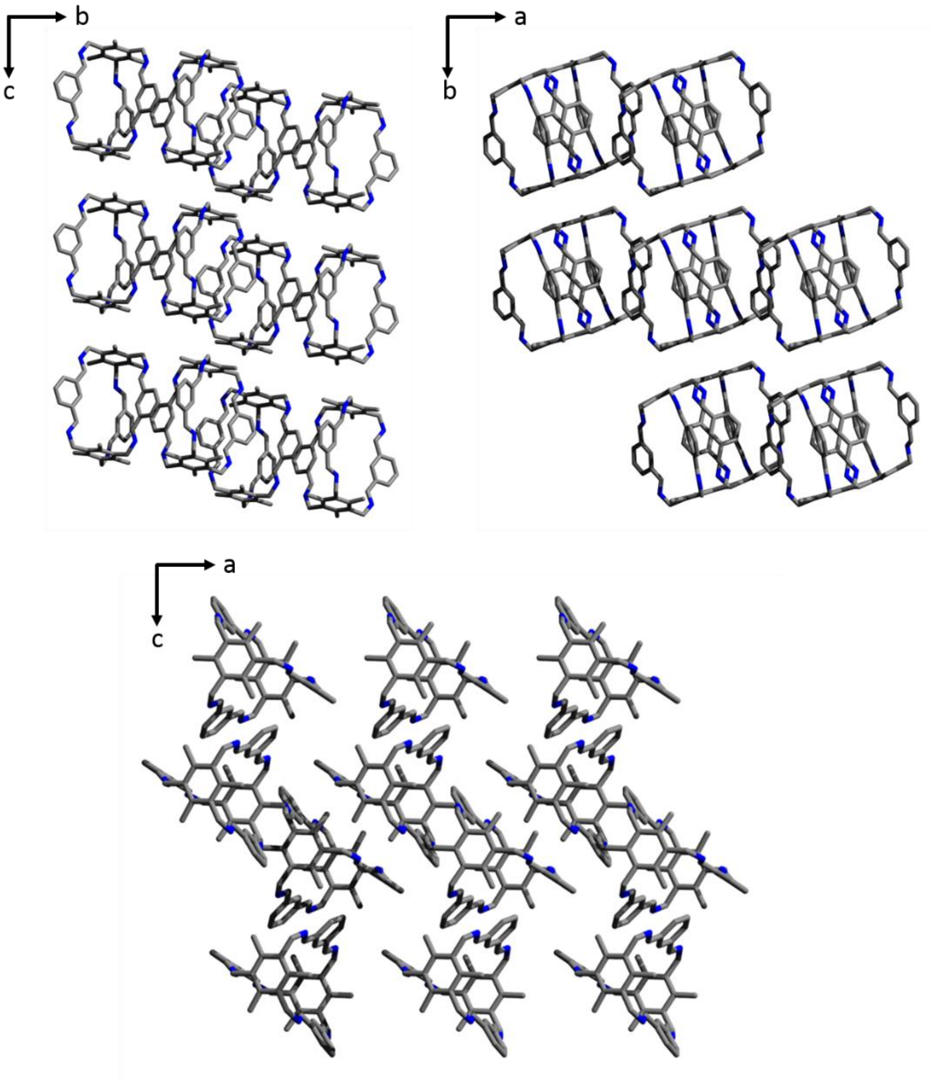

**Figure 6** **B1**$\cdot$0.82($C_4H_8O_2$)$\cdot$0.18($CH_2Cl_2$)$\cdot$0.2($H_2O$) showed both parallel and parallel-displaced π–π stacking between the cage molecules, directing the WTE packing observed.

### *<u>2.2.2 [3+2] Organic cage **C1**</u>*

**C1**, another [3+2] cage, was synthesised using the same aldehyde as **B1**, but with triamine (2,4,6-triethylbenzene-1,3,5-triyl)trimethanamine. From all 28 conditions, two polymorphs of **C1** were identified, crystallising from DCM and hexane, and the second polymorph DCM and *m*-xylene. The first structure was isostructural to **B1**, however the second crystal structure of **C1** showed hexagonal channels throughout the cage molecules.

During refinement, all non-H atoms were refined anisotropically unless stated otherwise, the H-atoms were located using the difference map and refined using the riding model. The crystal structure was solved using SHELXT[68] and refined using SHELXL[69]. All adsorption corrections were performed using SAINT[70]. For an improved model, RIGU[71] was applied to the cage molecule to improve the atomic displacement parameters (ADP), but not necessary for the disordered dichloromethane solvent which was modelled in the final structural solution. **C1.**DCM.Hexane was grown via vapour diffusion in an incubator at 15°C. Crystals were well-refined, with minimal structural disorder except for the solvent. The water which was modelled from residual electron density was refined isotropically and their combined occupancy total 70%. The disordered DCM was modelled at 50% occupancy over 2 sites. The displacement ellipsoid plot can be seen in **Figure 7A**, with solvent and hydrogen atoms removed for clarity.

The overlaid structures from the single crystal structure of **C1**$\cdot CH_2Cl_2\cdot 0.7(H_2O)$ and the calculated structures shows almost perfect agreement. The phenyl rings in the linkers are in the same positions, as well as the ethyl chains on the triamine. The RMSD between the structures is only 0.12 Å, further demonstrating the reliability between the calculated and experimental structures.

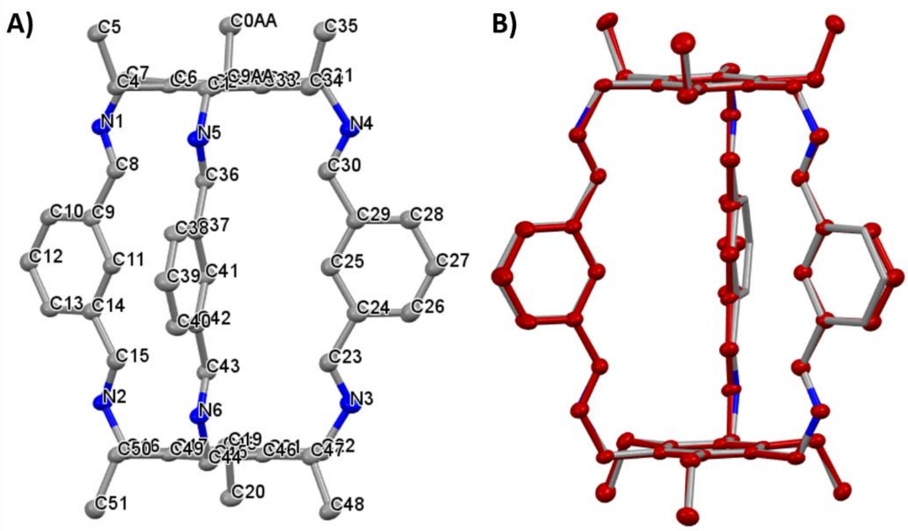

**Figure 7 A)** Displacement ellipsoid plot from the single crystal structure **C1**$\cdot CH_2Cl_2\cdot 0.7(H_2O)$. Ellipsoids are displayed at 50% probability. The water was omitted from the figure for clarity; **B)** Overlay of the calculated cage and the experimental crystal structure of **C1** (red).

The other polymorph of **C1** was recrystallised from DCM and *m*-xylene. The displacement ellipsoid plot for **C1**$\cdot CH_2Cl_2\cdot 3(C_8H_{10})$ can be seen in **Figure 8. C1**$\cdot CH_2Cl_2\cdot 0.7(H_2O)$ (left, **Figure 9**), shows WTE packing, arising from the T-shaped $\pi$–$\pi$ stacking at a distance of 3.84 Å. The anti-solvent for this crystal structure was hexane, however in the crystal structure, the solvent modelled was $CH_2Cl_2$ and water, implying that $C_6H_{14}$ had little impact on directionality in the crystal packing. Comparatively, **C1**$\cdot CH_2Cl_2\cdot 3(C_8H_{10})\cdot(H_2O)$ crystallised with hexagonal channels throughout the structure due to preferential $\pi$–$\pi$ stacking between cage and *m*-xylene solvent. The cage linkers showed parallel-displaced $\pi$–$\pi$ stacking, with one *m*-xylene per cage, at a distance of approximately 4.02 Å.

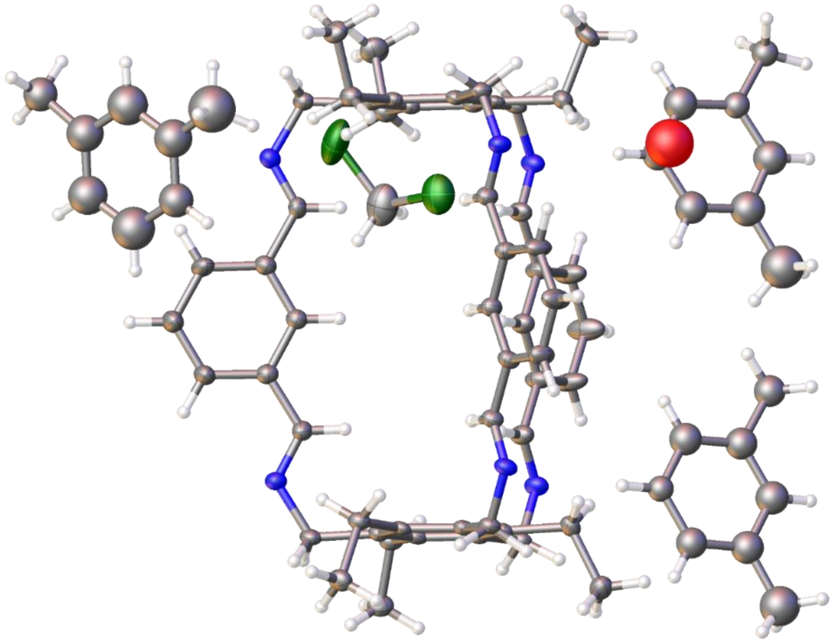

**Figure 8** Displacement ellipsoid plot from the single crystal structure of **C1**$\cdot CH_2Cl_2\cdot 3(C_8H_{10})\cdot(H_2O)$. Each *m*-xylene molecule was modelled with 33.3% occupancy. Ellipsoids are displayed at 50% probability. Labels were omitted for clarity.

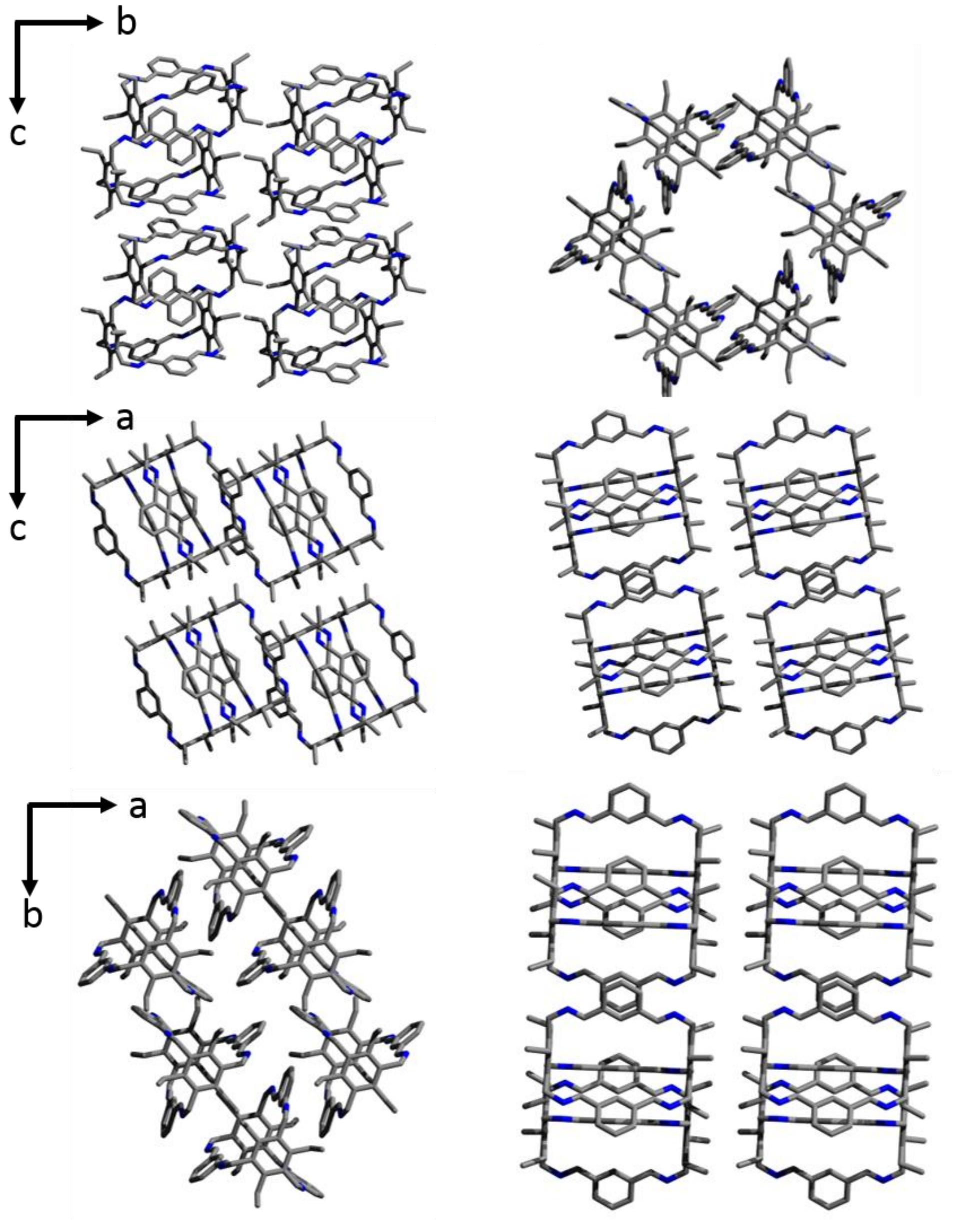

**Figure 9** Comparison between the crystal packing of **C1**·($CH_2Cl_2$)·0.7($H_2O$) on the left, and **C1**·($CH_2Cl_2$)·3($C_8H_{10}$)·($H_2$ on the right. Viewing along the *a*-, *b*- and *c*-axes (top to bottom). Recrystallisation using hexane shows edge-to-edge packing with minimal interactions between the cages, comparatively using *m*-xylene, the cage forms hexagonal channels which are directed by the $\pi-\pi$ interactions between the cages and the *m*-xylene solvent, which has been omitted for clarity.

There are currently several examples of solvent directed crystal packing, with **CC1** shown to be a solvatomorphic POC, as well as **CC3** exhibiting guest controlled directed packing.[65,72,73] Crystal packing can be directed by taking advantage of stronger interactions between the solvent and the cage.

Cages packed in the crystal structure tend to have weak, non-covalent interactions which are typically less directional compared to other porous molecular solids.[50,51,74,75] Introduction of certain solvents can either promote, or interrupt these weak, WTW interactions and directs the packing towards a porous or non-porous solid respectively.[73] Cage **C1** formed a [3+2] cage regardless of the crystallisation method, comparatively when using *m*-xylene the $\pi$–$\pi$ interactions between the solvent and the cage encourage the formation of one-dimensional channels throughout the structure, shown in **Figure 10**.

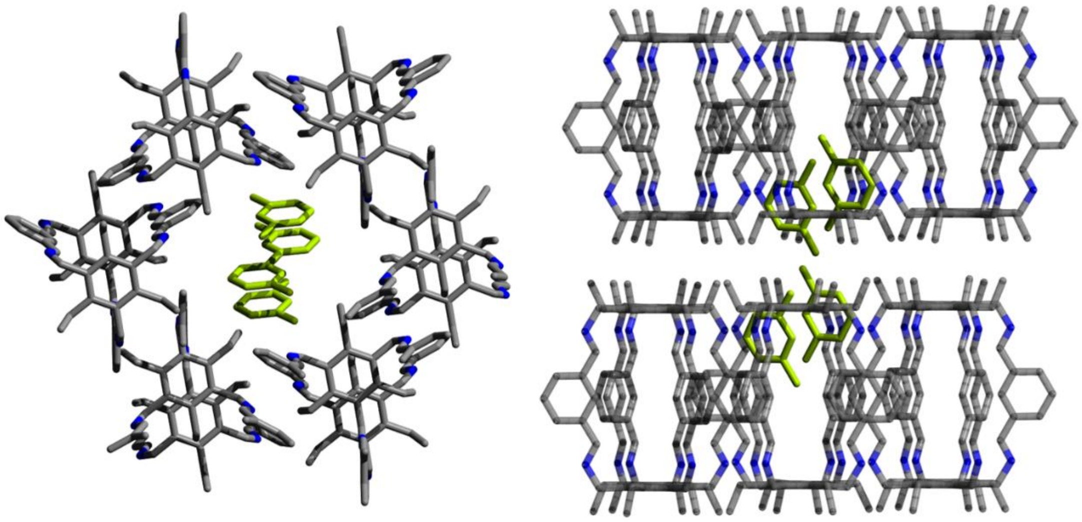

**Figure 10** Solvent *m*-xylene in the pseudo-pore of **C1**, modelled as green for clarity.

### <u>2.2.3 [3+2] Organic Cage **C14**</u>

**C14** was synthesised from (2,4,6-triethylbenzene-1,3,5-triyl)trimethanamine and anthracene-9,10-dicarboxylic acid. The single crystal was grown from DCM and THF. The calculated structure for **C14** can be seen overlaid with the single crystal structure of **C14**$\cdot$($CH_2Cl_2$)$\cdot$1.5($C_4H_8O$), showing there is some variation in the imine angles, and the position of the anthracene aldehyde linker. Calculations revealed that the [6+4] age was energetically more favourable based on formation energy per bond than the [3+2]. The [6+4] cage was around -23.5 kJ mol$^{-1}$ per bond, whereas the [3+2] cage was = 20.1 kJ mol$^{-1}$. The RMSD between the calculated and experimental structure was 1.74 Å, which is a considerable difference. The imine angle, which determine the position of the anthracene linkers differ between the two, leading to the difference in the overlaid structures.

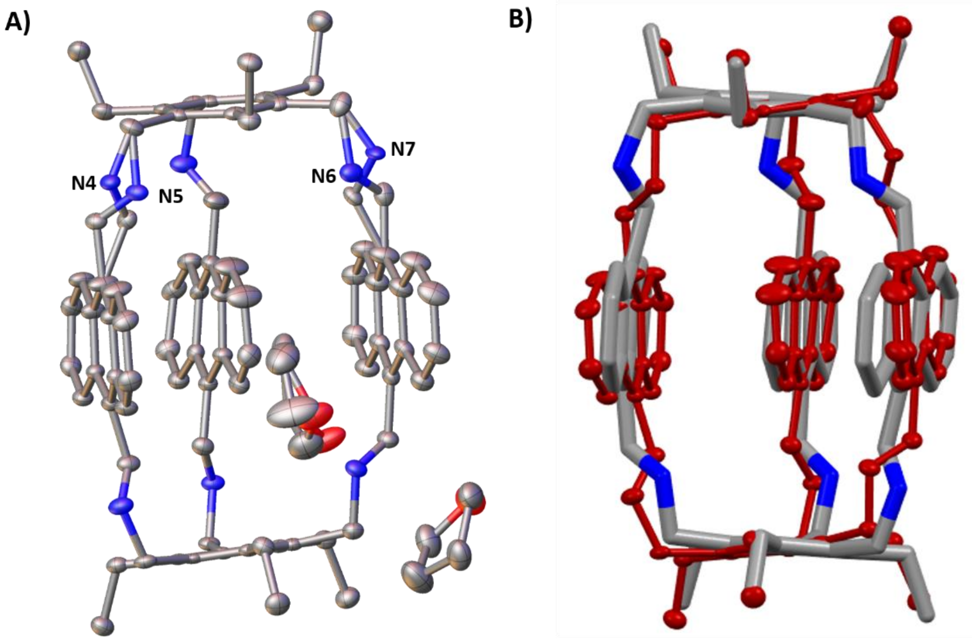

**Figure 11 A)** Displacement ellipsoid plot from the single crystal structure of **C14**$\cdot$(CH$_2$Cl$_2$)$\cdot$1.5(C$_4$H$_8$O), showing disorder on the imines of N4 and N5, and N6 and N7. Other atom labels and all hydrogen atoms are omitted for clarity. Ellipsoids are displayed with 50% probability; **B)** Overlay of the single crystal structure of **C14** (red) and the calculated structure.

The asymmetric unit comprises one complete **C14** cage and two THF molecules. Due to disorder, diffuse scatter beyond 0.85 Å was omitted during refinement (PLAT027_ALERT_3_A checkCIF alert), and two -CH$_2$=N-CH- groups were modelled over two positions. In the crystal structure two reasonably well ordered THF molecules were located between **C14** cages and modelled with 50% occupancy. Due to slight disorder, one of these THF molecules was refined with a rigid bond restraint (RIGU in SHELX), and for this molecule one -O-CH$_2$- group was modelled over two positions. N6 and N7 were modelled with 50% occupancy each, N4 40% and N5 60% occupancy.

Disordered THF was modelled with 100% occupancy for one well-ordered molecule, and 50% for the more disordered. Despite only having seen the [2+3] cages experimentally, both from synthesis and crystallisation, calculations revealed that the [4+6] cage was in fact energetically favoured by approximately 22 kJ mol$^{-1}$.

For most of the cages in this study, we have seen good agreement between computational and experimental results. However, for a few examples there were discrepancies between experimental and computational results. In this case, despite the [6+4] cage being predicted to be energetically more favourable and stable, the [3+2] cage was found experimentally. The $\pi-\pi$ stacking interactions, at a distance of 3.483 Å, direct the formation of the [3+2] cage, as seen in **Figure 12**.

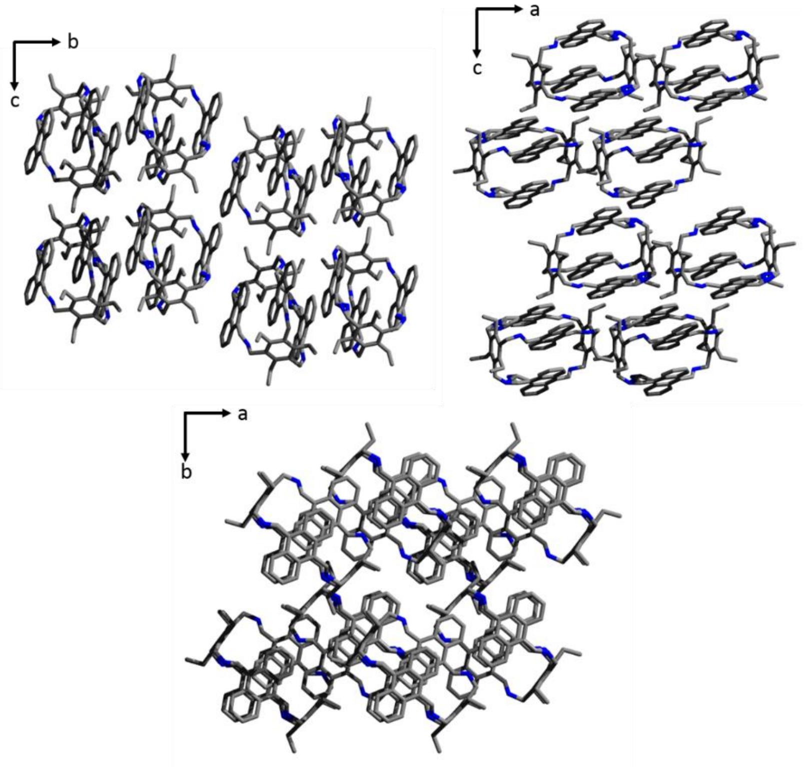

**Figure 12 C14**$\cdot$($CH_2Cl_2$)$\cdot$1.5($C_4H_8O$) viewed along the *a*-, *b*- and *c*-axes (top left clockwise).

## *2.3 [4+4] Organic Cages*

### *2.3.1 [4+4] Organic Cage **C23***

**C23** was synthesised from triamine (2,4,6-triethylbenzene-1,3,5-triyl)trimethanamine and 4,4’,4’’-nitrilotribenzenealdehyde. It was predicted that by using two tri functional groups a larger [4+4] tetrapod would be formed. The single crystal structure, **C23**·6.5($CH_2Cl_2$)·7.5($C_2H_3N$), crystallised from a DCM/MeCN solution in the monoclinic space group *P*2/*c*. The asymmetric unit (**Figure 13**) for this phase comprises with one complete **C23** cage. Due to disorder, **C23** was refined with a rigid bond restraint (RIGU in SHELX) and diffuse scatter beyond 1.05 Å was omitted during refinement (THETM01_ALERT_3_A, PLAT027_ALERT_3_A, and PLAT340_ALERT_3_B checkCIF alerts). There was good agreement between the calculated structured and the experimental structure of **C23**, shown in **Figure 13B** with an RMSD of 1.10 Å, which is good considering the size of the cage. The variation between the two arises from the rotation of the phenyl linkers, which are then constrained once the bonding occurs.

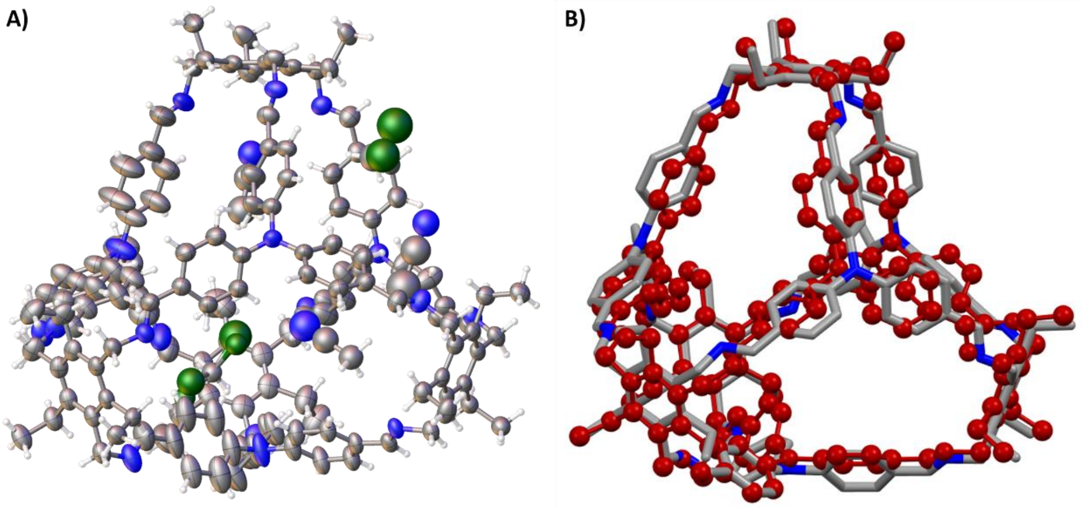

**Figure 13 A)** Displacement ellipsoid plot from the single crystal structure of **C23**·6.5($CH_2Cl_2$)·7.5($C_2H_3N$). Ellipsoids are displayed with a 50% probability, and labels are omitted for clarity; **B)** Overlay of the calculated structure, and the experimental crystal structure of **C23** (red).

In the structure, a 1,4 substituted aromatic ring was disordered over two positions, site occupancies for the disordered parts were determined using a free variable (**Figure 14 A&B**). C102 in **C14** was modelled using an EXYZ restraint, which assumes equivalent atomic coordinates of the names atoms.[76] C102 was part of the disordered phenyl linker, seen in **Figure 14**. Disordered $CH_2Cl_2$ (1 ½ per **C23**) and MeCN (2 ½ per **C23**) were located in the structure, these were refined isotropically with bond distance restraints (DFIX in SHELX). Additional solvent molecules were too disordered to be accurately modelled in the large pores (PLAT602_ALERT_2_A and PLAT049_ALERT_1_B checkCIF alerts). Hence, the SQUEEZE in PLATON was used during the final refinement cycles.[35, 36]

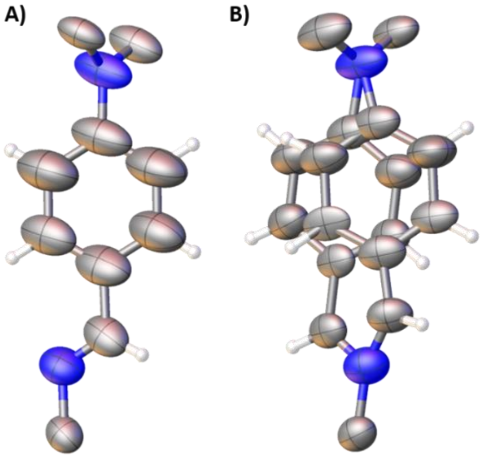

**Figure 14 A)** Prior to modelling of the disordered imine; **B)** After the disordered imine was modelled across two positions with 50% occupancy for each. Ellipsoid probability is displayed at 50%.

SQUEEZE found a 4915 Å$^3$ void with disordered electron counts of 1298 (e-). As a result, 20 $CH_2Cl_2$ and 20 MeCN solvent molecules were assigned arbitrarily, based on the electron count. In the structure, the solvent accessible surface was modelled using a Connolly surface interfaced through Mercury, and determined this to be 1691.64 Å$^3$ based on a 1.55 Å probe radius (**Figure 15**).[77]

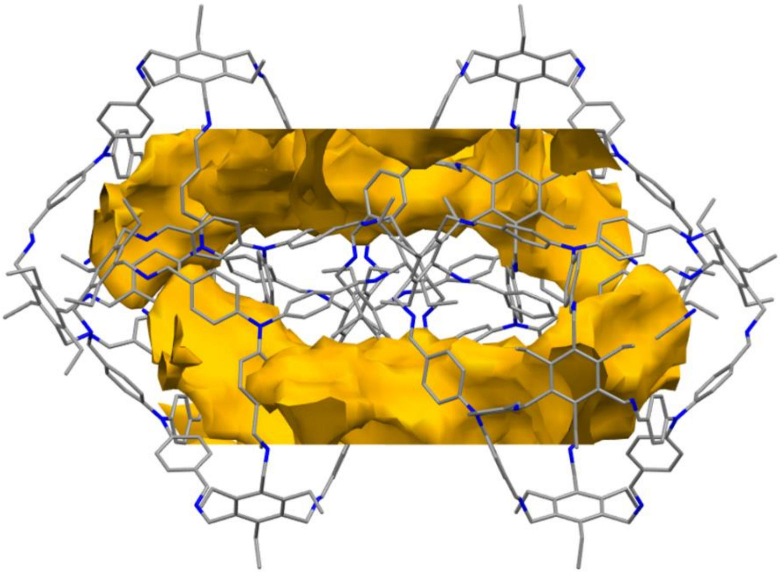

**Figure 15** Solvent accessible volume in showing the window-to-window interactions in **C23**, viewed along the *c** axis. A probe radius of 1.55 Å was used, the Van der Waals radius of $N_2$. The solvent accessible volume of 1691.64 $Å^3$ corresponds to 9.3% of the unit cell volume.

# 3 New Topology – Triply Interlocked Bridged Catenane

## 3.1 Mechanically Interlocked Molecules

Interlocked species were first reported in 1964 by Schill and Lüttringhaus, where they showed these interlocked materials could be directly synthesised.[78] They showed that a [2] catenane, with a similar topology to the structure in **Figure 16** could be synthesised using copper directed synthesis. These interlocked molecules form as a direct result of the reversibility of the imine bonds, or through templation using metal ions. When interlocked, they will typically be more thermodynamically stable than the molecule independently, therefore the reaction can continually 'self-correct' and form the interlocked material.[79] Since this important discovery, interlocked molecular species have since been studied in more detail and there are a plethora of structures, including complex structures such as Borromean rings, pentaknots and rotaxanes.[80–83]

A catenane is not limited to two cyclic materials which interlock as shown in the example in **Figure 16**, but as the definition implies it is a molecule which interlocks, and can consist of many rings. **Figure 16** shows one of the earliest examples of a catenane, published in 1985, showing the ‘traditional’ catenane consisting of two interlocked rings.[84,85] This description also covers molecules which are covalently linked, as well as interlocking.

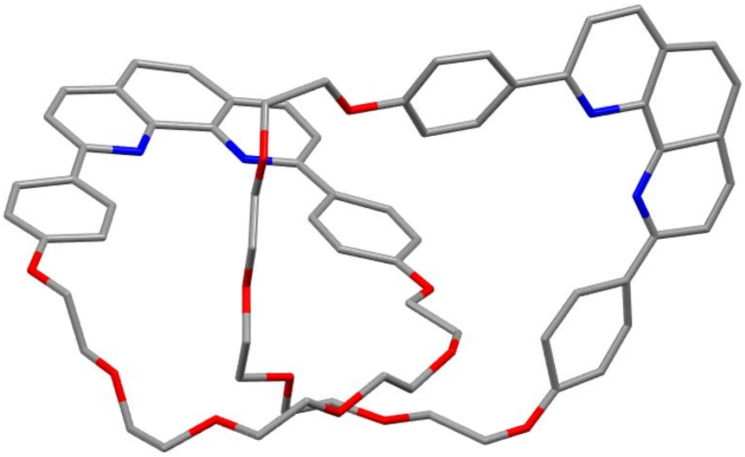

**Figure 16** [2] catenane published by Jean-Pierre Sauvage and co-workers.[84]

One example of this behaviour is the covalently bridged catenane, or pretzelane, where the molecule interlocks, and the interlocked parts are covalently attached. The first example of a pretzelane[86] was reported in 1996, which consisted of the familiar interlocking system of the catenane, seen previously, however the covalent link transformed this from a typical catenane into a more complex topology.[87] These materials are formed by intramolecular reactions which encourage the interlocking of the materials such as $\pi$–$\pi$ stacking.[88,89] Pretzelanes can exhibit similar functionality to a catenane. We can take advantage of their molecular topology, leading to their application in molecular machinery for sensors.[89] Currently, the literature shows only around 59 published pretzelane or pretzelane-type structures.

OMCs have also been shown to form interlocked structures, in 2010 a triply-interlocked catenane of the organic molecular cage, **CC1**, was reported.[90,38] The original reported structure was the independent OMC, however when recrystallized from DCM and *o*-xylene, an [6+4] interlocked cage structure was formed. Computational calculations revealed that **CC1** is a kinetic product, whereas the triply interlocked [8+12] species is the thermodynamic reaction product.

## *3.2 [8+12] Bridged Catenane Cage*

When in solution, the $^1$H NMR and $^{13}$C NMR indicated that **B13** was a [6+4] cage, and computational calculations also indicated the [6+4] cage would be energetically stable. However when crystallised, this formed the interlocked species. The single crystal structure, **B13**$\cdot$2(CHCl$_3$)$\cdot$2(C$_4$H$_8$O)$\cdot$18.5(H$_2$O), was recrystallised from a solution of **B13** in CHCl$_3$, with THF diffused into the solution. The displacement ellipsoid plot for **B13**$\cdot$2(CHCl$_3$)$\cdot$2(C$_4$H$_8$O)$\cdot$18.5(H$_2$O) is shown in **Figure 17**. The asymmetric unit for this phase comprises ½ of the interlocked covalently attached cage (**Figure 17**); the complete cage is related by inversion symmetry. **Figure 18** shows the calculated cage structure, which was predicted to form a [6+4] cage.

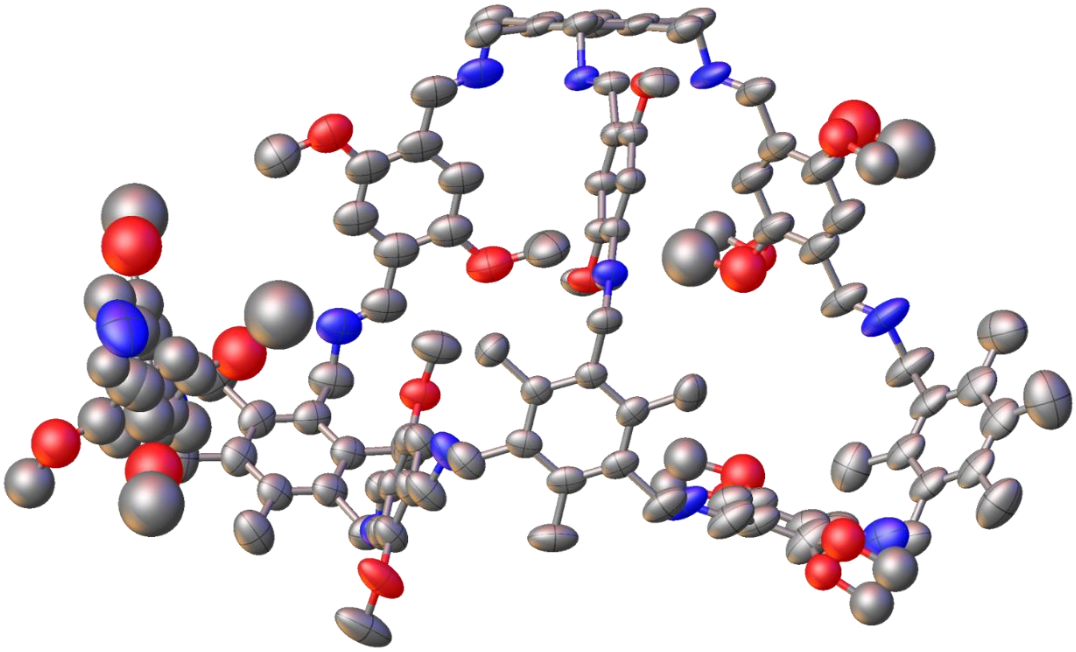

**Figure 17** Displacement ellipsoid plot from single crystal structure of **B13**$\cdot$2(CHCl$_3$)$\cdot$2(C$_4$H$_8$O)$\cdot$18.5(H$_2$O). Ellipsoids are displayed with 50% probability. Hydrogen atoms and labels are omitted from the figure for clarity.

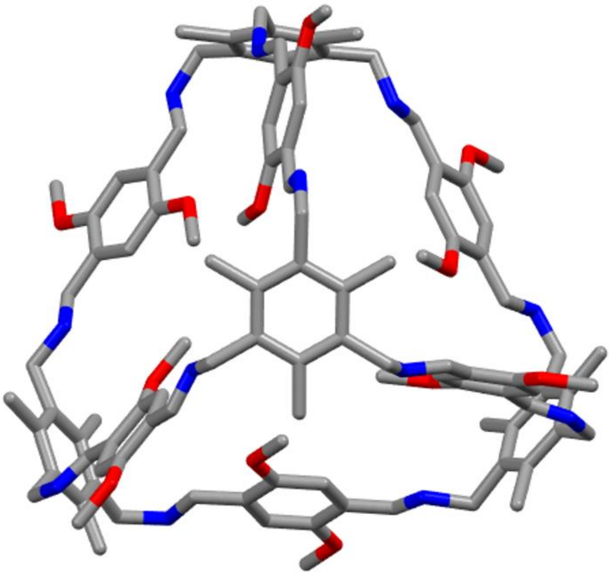

**Figure 18** Calculated [6+4] cage structure. The structure was predicted to be a [6+4] cage in solution, however the structure re-equilibrated in solution forming the interlocked species.

Due to disorder, a suitable resolution limit of 0.95 Å was applied during refinement (THETM01_ALERT_3_B and PLAT340_ALERT_3_B checkCIF alerts) and the final refinement statistics were poor (PLAT082_ALERT_2_B, PLAT084_ALERT_3_B checkCIF alerts), in part, this was due to the severely disordered solvent. Diffuse electron density, found in voids in the crystal structure, was modelled as a mixture of $CHCl_3$, THF, and tentatively assigned $H_2O$. In the crystal structure, the **B13$_{\mathbf{[8+12]}}$** cage was disordered and refined with 1,2 and 1,3 bond distance restraints (DFIX, SADI and DANG in SHELX), and a group rigid bond restraint (RIGU in SHELX). In addition, six aromatic rings were refined with constrained geometries (AFIX 66 in SHELX). Two of these were used to model a dimethoxybenzene unit which is disordered over two positions

Pretzelanes typically form due to strong intramolecular interactions. The most common interactions observed are hydrogen bonding, or $\pi$–$\pi$ stacking. These dominant features lead to this unusual interlocking behaviour.[,91] **Figure 19** shows the cage pretzelane, unlike other published pretzelanes, the cage shows two covalent bridges, and two links, whereas other published structures contain only one covalent bridge. Further recrystallisations showed that single crystals of the pretzelane can be grown using a variety of anti-solvents, including THF, hexane and diethyl ether.

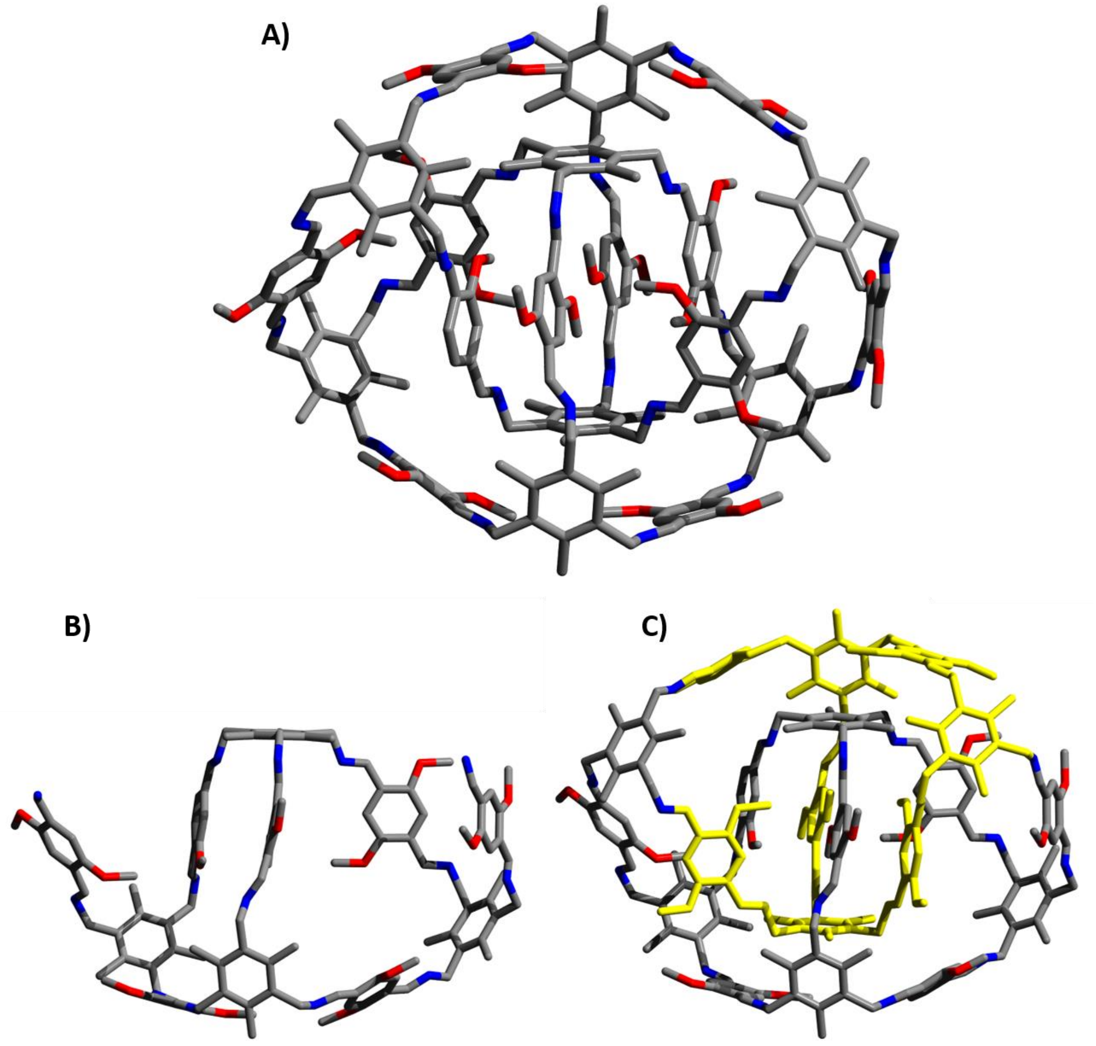

**Figure 19 A)** The interlocked and covalently linked pretzelane structure; **B)** Asymmetric unit of the pretzelane; **C)** Highlighting visually how the two asymmetric units form a covalent link and interlocking structure.

The crystal structure showed significant disorder on the covalently bonded linkers, whereas the central part of the structure showed $\pi$–$\pi$ stacking, which was well-ordered. **Figure 20A** & **20B** show the disordered sections in the bridged catenane. **21A** shows the covalent bridge which links the two cages together forming the interlocked structure, both parts are modelled with 50% occupancy. **21B** shows the two methoxy groups which were modelled across two positions, also with 50% occupancy.

These dimethoxy benzene units were refined isotropically and, due to severe disorder, one of these dimethoxy benzene units was refined with constrained displacement parameters (EADP in SHELX). Due to the limited resolution of the diffraction data, it was not possible to determine H atom positions. H atoms were therefore placed in estimated positions and refined using the riding model. The estimated positions of the disordered H atoms are unlikely to be correct resulting in close intramolecular H-H contact between a disordered $-CH_3$ group and disordered aryl$-CH_2$ group (PLAT412_ALERT_2_B checkCIF alert). Solvent was extremely disordered in the crystal structure and solvent molecules that were located was refined with 1,2 and 1,3 bond distance restraints (DFIX and DANG in SHELX) and only the $CHCl_3$ molecules were refined anisotropically. Also, occupancies are tentative and diffuse electron density was modelled as $H_2O$ molecules, which were refined without H atoms.

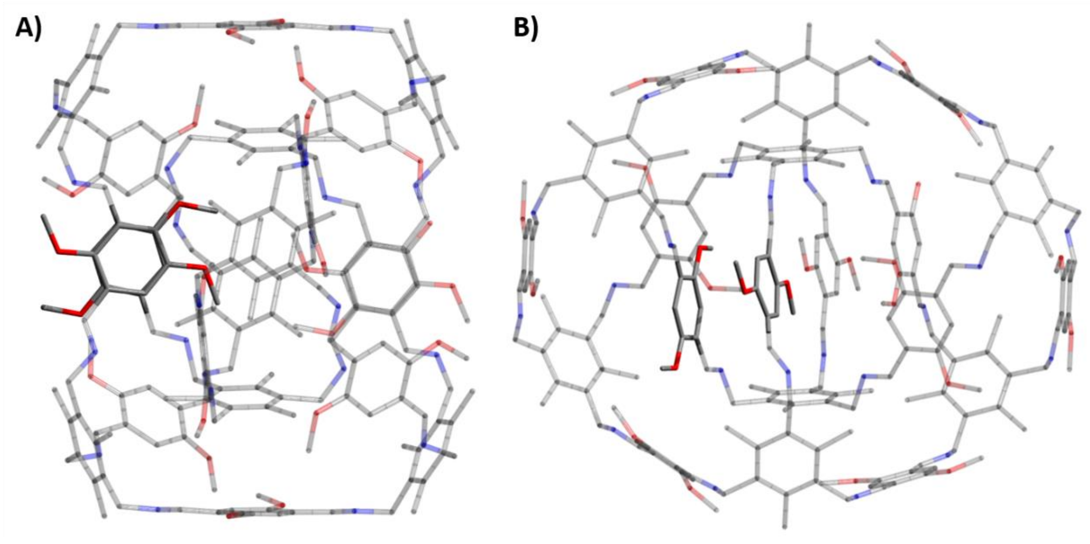

**Figure 20 A)** A side view showing the aromatic (**B** from **Figure 21**) with a 60 ° rotation with respect to one another; **B)** Looking alongside the offset $\pi-\pi$ stacking, showing the four aromatic groups which are responsible for the interlocking of the structure.

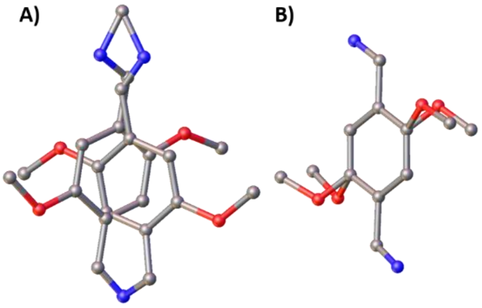

**Figure 21** Disorder in the triply interlocked bridged catenane, of the dimethoxy unit which did not form the $\pi$–$\pi$ stacking seen in the structure.

To gain further understanding into the intramolecular interactions which promote the formation of the interlocked species, the software Spartan was used to perform calculations. Shown in **Figure 22** are the electrostatic potential maps of molecules ranging from the basic benzene, to the imine building block which is found in the cage structure. The electron density potential revealed that although the 1,4-methoxybenzene has a more negative energy, which would lead to repulsive forces when $\pi$–$\pi$ stacking, the imine addition of the imine building block reduces this negativity. Hence, these strong, favourable intermolecular interactions lead to the formation of the interlocked cage.

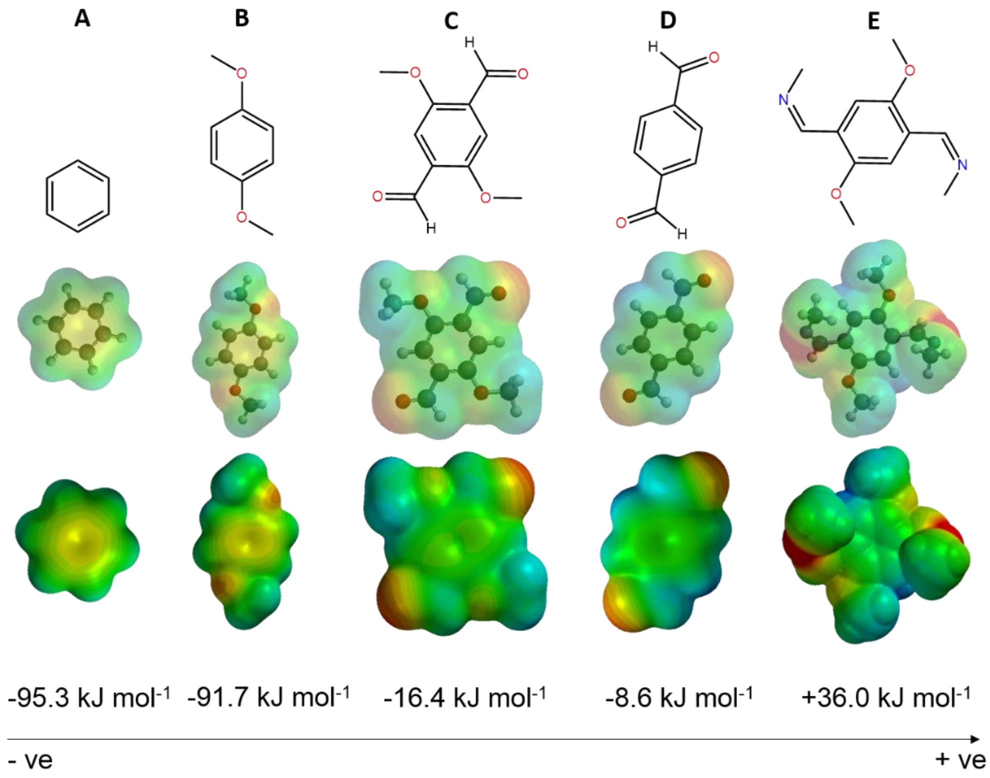

**Figure 22** Electron Density Potential calculations of compounds **A**-**E**. The electron density potential values are listed below, which were calculated from the centre of the phenyl ring.

## *4 Re-equilibration: Cage doubling*

In Chapter 2 we discussed the re-equilibration of a [3+6] imine-based organic cage into a larger, [6+12] species. As a dynamic, reversible system, it is not too surprising therefore to see this same behaviour from other starting materials. In this study, I found that **C21** underwent re-equilibration as in solution, forming **C21Tri$^{2}$Di$^{3}$** (**Figure 23A**), and the larger equivalent **C21Tri$^{4}$Di$^{6}$** (**Figure 23B**).

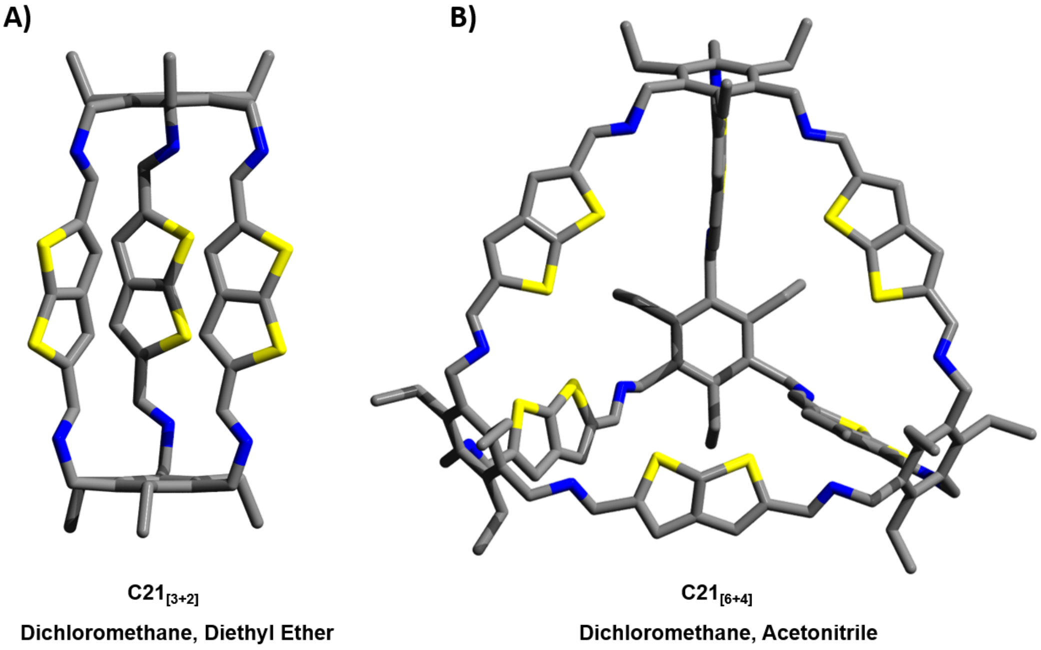

**Figure 23 A)** Organic cages **C21**[3+2]; **B) C21**[6+4].

The single crystal structure, **C21Tri²Di³**·0.5($CH_2Cl_2$)·0.25($C_4H_{10}O$), crystallised from a $CH_2Cl_2$/$Et_2O$ solution in the triclinic space group $P\bar{1}$.

Due to slight disorder of the cage structure, the C-S bond distances were restrained during refinement (DFIX in SHELX), and one methyl group was modelled over two positions. In the structure, the solvent was disordered and modelled as a mixture of partially occupied $CH_2Cl_2$ and $Et_2O$. The $CH_2Cl_2$ molecule was refined with C-Cl bond distance restraints (DFIX in SHELX). During refinement, all H-atoms were placed in estimated positions and refined using the riding model. For the disordered $Et_2O$ molecules the −$CH_3$ H-atoms are unlikely to be in the correct position, resulting in there being close intermolecular contacts in the final structure (PLAT413_ALERT_2_A alert). For a displacement ellipsoid plot, see **Figure 24A**.

**C21Tri⁴Di⁶**·7.12($CH_2Cl_2$)·5.12($C_2H_3N$)·0.25($H_2O$), crystallised from a $CH_2Cl_2$/MeCN solution in the monoclinic space group $P2_1/n$. The asymmetric unit for this phase comprises one complete **C21** cage. The crystal data quality was poor and a resolution limit of 1 Å was applied during refinement (THETM01_ALERT_3_A and PLAT027_ALERT_3_A checkCIF alert). In the crystal structure **C21** is disordered; one thiophene group was modelled over two positions, and one thiophene group was modelled over three positions. For the disordered parts site occupancies were determined using free variables and one severely disordered part was refined with constrained displacement parameters (EADP in SHELX). The displacement ellipsoid plot for **C21** seen in **Figure 25B**.

Due to disorder, **C21** was refined with a rigid bond restraint (RIGU in SHELX), and C-C, C-N, S-C 1,2 and 1,3 of bond distance restraints were used during refinement (DFIX and DANG in SHELX), in addition to planarity restraints (FLAT in SHELX). Atoms that shared similar coordinates were refined with constrained displacement parameters (EADP in SHELX). It is likely that additional disorder of **C21** could not be resolved. Two $CH_2Cl_2$ molecules were located in the crystal structure, these were refined with C-Cl bond distance restraints (DFIX in SHELX). Solvent was poorly resolved in the large lattice voids, hence, it was necessary to use the SQUEEZE routine in Platon during the final refinement cycles (PLAT602_ALERT_2_A and PLAT049_ALERT_1_B checkCIF alert).[92,93] SQUEEZE found a 5825 $Å^3$ void with disordered electron count of 1575 (e-). As a result, 20.5 $CH_2Cl_2$ and 20.5 MeCN solvent molecules were tentatively added to the unit cell atom count (CHEMW03_ALERT_2_A, PLAT043_ALERT_1_A, and PLAT051_ALERT_1_A checkCIF alert).

Calculations can provide us with more insight, helping us to form conclusions regarding the mechanisms taking place. We have already seen that the reversibility of the imine bond can lend itself to the formation of new cage species from the same starting materials. Calculations revealed that the smaller cage is energetically more favourable when considering the relative energy per [2+3] unit. However, the formation energy per bond was -10.8 kJ $mol^{-1}$ for the [2+3] cage, and -14.1 kJ $mol^{-1}$ for the [4+6] cage.

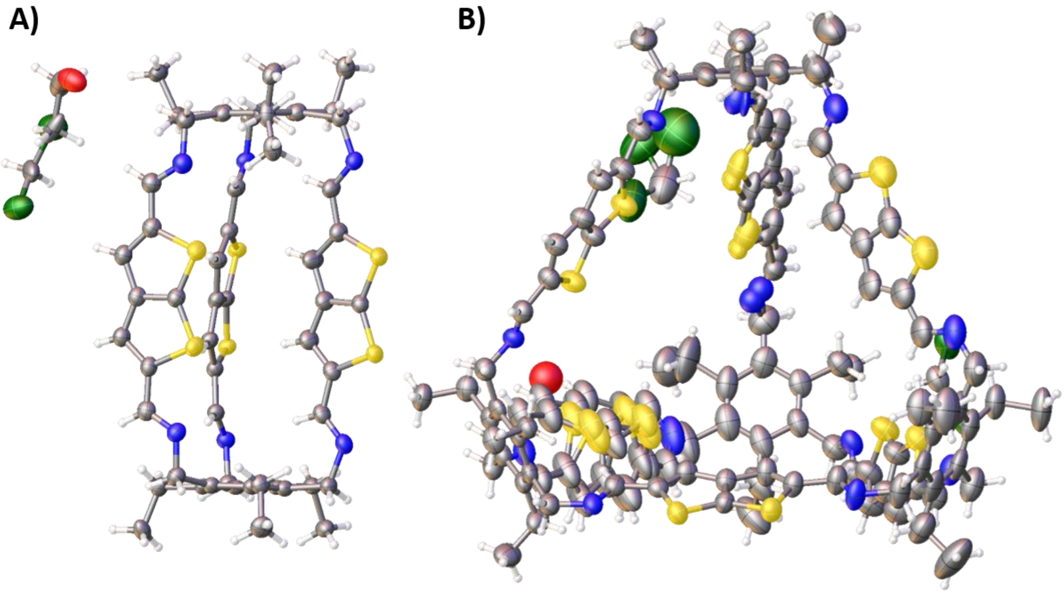

**Figure 24** Displacement ellipsoid plots for **A) C21Tri$^2$Di$^3$**; **B) C21Tri$^4$Di$^6$**.

In addition, due to disorder, and the limited resolution of the diffraction data, it was not possible to accurately determine H atom positions. H atoms were therefore placed in estimated positions and refined using the riding model. The estimated positions of the disordered H atoms are unlikely to be correct resulting in close inter- and intramolecular H-H contacts (PLAT410_ALERT_2_A, PLAT413_ALERT_2_A, and PLAT411_ALERT_2_B checkCIF alerts).

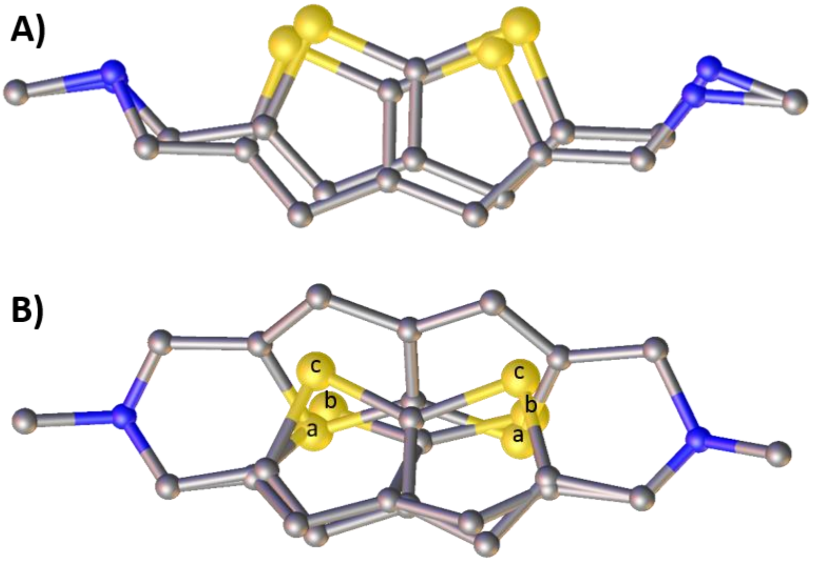

**Figure 25** Disorder in the thiophene linkers in the single crystal structure **C21Tri⁴Di⁶**. **A)** Both positions were modelled with 50% site occupancies; **B)** For one of the groups sulfur a, b and c were refined with occupancies of 18.4, 35.3 and 41.6%, respectively.

The calculated structures for both **C21Tri²Di³** and **C21Tri⁴Di⁶** are shown in **Figure 26A** and **Figure 26B** respectively. The RMSD for **C21Tri²Di³** was only 0.75 Å, and **C21Tri⁴Di⁶** 0.91 Å. The thiophene linkers cause the discrepancies in both structures, however there are more significant variations for **C21Tri⁴Di⁶**, as there are twice the number of thiophene linkers present.

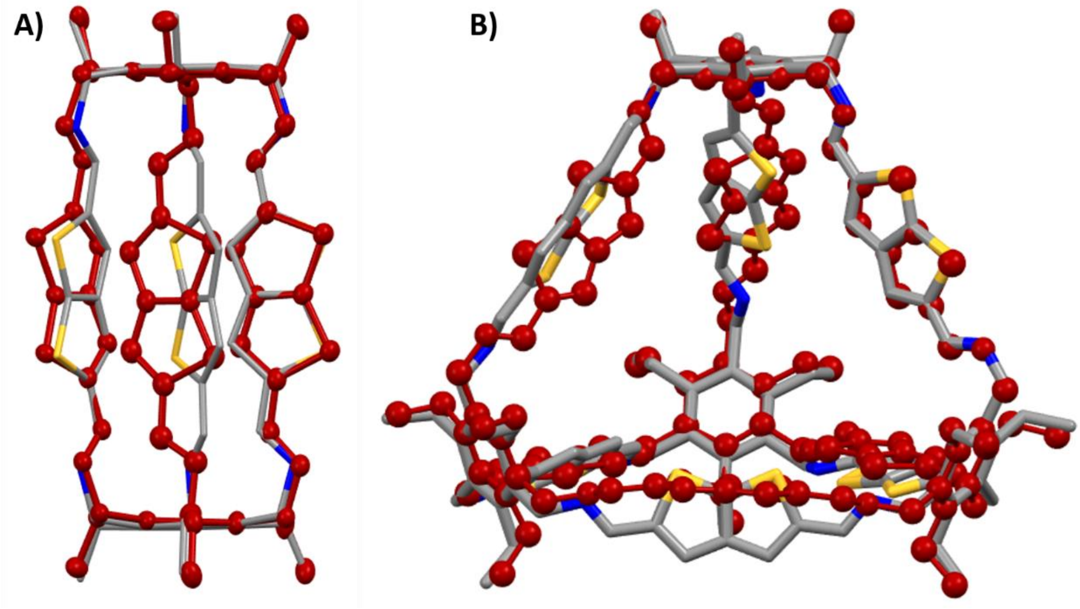

**Figure 26 A)** Overlay of the experimental crystal structure of **C21Tri²Di³** (red) and the calculated cage structure; **B)** Overlay of the experimental crystal structure of **C21Tri⁴Di⁶** (red) and the calculated cage structure.

# *5 Conclusions*

This project has been a combinatorial study involving high throughput synthesis and extensive analysis. In this study, I have shown that the use of crystallographic structural determination has led to discoveries which would otherwise not have been found (**Figure 25**). For all structures predicted accurately, excluding **B13**, the RMSD values showed there was good agreement between the calculated structures and the experimental structures, however in some cases the predicted and experimental structures varied more significantly.

Both **B1** and **C1** formed [3+2] cages with a trigonal prismatic topology as predicted by the computational analyses, however through recrystallisation studies two polymorphs of **C1** were identified. The first, a close packed, window to edge structure, and the second which was directed by solvent to form hexagonal channels throughout the structure.

When in solution, initial analysis indicated that **B13** was a [6+4] cage and initially computational calculations predicted that this would be the most probable outcome. The NMR data showed the cage to be following this trend. I showed, however, that when the cage was recrystallised it transformed into the interlocked [12+8] cage species reported here. Without using crystallography, the interlocked cage would not have been identified, further demonstrating the importance of using solid state analysis such as SCXRD. The interlocked cage, which was templated through intramolecular $\pi$–$\pi$ stacking, was found to be the thermodynamically stable species.

Compared to **TCC1** in Chapter 2, **C21** was able to be synthesised selectively dependent on the solvent used. When using $CHCl_3$ at reflux during the HT screen, it was determined that the [2+3] cage was the dominant product. However, under the same conditions but in DCM there was a mixture of both the small and large cages.[1] The two crystal structures used were both from the synthesis in DCM.

# 6 References

1 R. L. Greenaway, V. Santolini, M. J. Bennison, B. M. Alston, C. J. Pugh, M. A. Little, M. Miklitz, E. G. B. Eden-Rump, R. Clowes, A. Shakil, H. J. Cuthbertson, H. Armstrong, M. E. Briggs, K. E. Jelfs and A. I. Cooper, *Nat. Commun.*, 2018, **9**, 2849.

2 J. Inglese, D. S. Auld, J. Inglese and D. S. Auld, in *Wiley Encyclopedia of Chemical Biology*, John Wiley & Sons, Inc., Hoboken, NJ, USA, 2008.

3 R. Macarron, M. N. Banks, D. Bojanic, D. J. Burns, D. A. Cirovic, T. Garyantes, D. V. S. Green, R. P. Hertzberg, W. P. Janzen, J. W. Paslay, U. Schopfer and G. S. Sittampalam, *Nat. Rev. Drug Discov.*, 2011, **10**, 188–195.

4 K. H. Bleicher, H.-J. Böhm, K. Müller and A. I. Alanine, *Nat. Rev. Drug Discov.*, 2003, **2**, 369–378.

5 D. B. Kitchen, H. Decornez, J. R. Furr and J. Bajorath, *Nat. Rev. Drug Discov.*, 2004, **3**, 935–949.

6 R. Mullin, *Chem. Eng. News*, 2004, **82**, 22–32.

7 M. Shevlin, *ACS Med. Chem. Lett.*, 2017, **8**, 601–607.

8 R. P. Hertzberg and A. J. Pope, *Curr. Opin. Chem. Biol.*, 2000, **4**, 445–451.

9 D. Fix, D. V. Andreeva, Y. M. Lvov, D. G. Shchukin and H. Möhwald, *Adv. Funct. Mater.*, 2009, **19**, 1720–1727.

10 I. Perelshtein, G. Applerot, N. Perkas, G. Guibert, S. Mikhailov and A. Gedanken, *Nanotechnology*, 2008, **19**, 245705.

11 J. Rafiee, X. Mi, H. Gullapalli, A. V. Thomas, F. Yavari, Y. Shi, P. M. Ajayan and N. A. Koratkar, *Nat. Mater.*, 2012, **11**, 217–222.

12 B. Chisholm, R. Potyrailo, J. Cawse, R. Shaffer, M. Brennan, C. Molaison, D. Whisenhunt, B. Flanagan, D. Olson, J. Akhave, D. Saunders, A. Mehrabi and M. Licon, *Prog. Org. Coatings*, 2002, **45**, 313–321.

13 A. P. Watt, D. Morrison, K. L. Locker and D. C. Evans, *Anal. Chem.*, 2000, **72**, 979–984.

14 R. Macarron, M. N. Banks, D. Bojanic, D. J. Burns, D. A. Cirovic, T. Garyantes, D. V. S. Green, R. P. Hertzberg, W. P. Janzen, J. W. Paslay, U. Schopfer and G. S. Sittampalam, *Nat. Rev. Drug Discov.*, 2011, **10**, 188–195.

15 R. Banerjee, A. Phan, B. Wang, C. Knobler, H. Furukawa, M. O'Keeffe and O. M. Yaghi, *Science (80-. ).*, 2008, **319**, 939–43.

16 J. Greeley, T. F. Jaramillo, J. Bonde, I. Chorkendorff and J. K. Nørskov, *Nat. Mater.*, 2006, **5**, 909–913.

17 M. E. Briggs and A. I. Cooper, *Chem. Mater.*, 2017, **29**, 149–157.

18 Y. Jin, Q. Wang, P. Taynton and W. Zhang, *Acc. Chem. Res.*, 2014, **47**, 1575–1586.

19 Y. Jin, C. Yu, R. J. Denman and W. Zhang, *Chem. Soc. Rev.*, 2013, **42**, 6634.

20 Y. Jin, Q. Wang, P. Taynton and W. Zhang, *Acc. Chem. Res.*, 2014, **47**, 1575–1586.

21 M. E. Briggs, A. G. Slater, N. Lunt, S. Jiang, M. A. Little, R. L. Greenaway, T. Hasell, C. Battilocchio, S. V. Ley and A. I. Cooper, *Chem. Commun.*, 2015, **51**, 17390–17393.

22 M. E. Belowich and J. F. Stoddart, *Chem. Soc. Rev.*, 2012, **41**, 2003.

23 F. N. Tebbe, R. L. Harlow, D. B. Chase, D. L. Thorn, G. C. Campbell, J. C. Calabrese, N. Herron, R. J. Young and E. Wasserman, *Science (80-. ).*, 1992, **256**, 822–825.

24 K. Kikuchi, N. Nakahara, T. Wakabayashi, S. Suzuki, H. Shiromaru, Y. Miyake, K. Saito, I. Ikemoto, M. Kainosho and Y. Achiba, *Nature*, 1992, **357**, 142–145.

25 R. K. Harris, *Solid State Sci.*, 2004, **6**, 1025–1037.

26 A. R. Hughes, N. J. Brownbill, R. C. Lalek, M. E. Briggs, A. G. Slater, A. I. Cooper and F. Blanc, *Chem. - A Eur. J.*, 2017, **23**, 17217–17221.

27 S. Komulainen, J. Roukala, V. V. Zhivonitko, M. A. Javed, L. Chen, D. Holden, T. Hasell, A. Cooper, P. Lantto and V.-V. Telkki, *Chem. Sci.*, 2017, **8**, 5721–5727.

28 X. Liu, Y. Liu, G. Li and R. Warmuth, *Angew. Chemie Int. Ed.*, 2006, **45**, 901–904.

29 X. Liu and R. Warmuth, *J. Am. Chem. Soc.*, 2006, **43**, 14120–14127.

30 C. Givelet, J. Sun, D. Xu, T. J. Emge, A. Dhokte and R. Warmuth, *Chem. Commun.*, 2011, **47**, 4511.

31 C. J. Pugh, V. Santolini, R. L. Greenaway, M. A. Little, M. E. Briggs, K. E. Jelfs and A. I. Cooper, *Cryst. Growth Des.*, 2018, acs.cgd.7b01422.

32 G. Zhang, O. Presly, F. White, I. M. Oppel and M. Mastalerz, *Angew. Chemie Int. Ed.*, 2014, **53**, 1516–1520.

33 V. Spetzler, R. Kiebach, C. Nather and W. Bensch, *Zeitschrift fur Anorg. und Allg. Chemie*, 2004, **630**, 2398–2404.

34 C. A. Hunter, *J. Am. Chem. Soc.*, 1992, **114**, 5303–5311.

35 M. Pellecchia, *Chem. Biol.*, 2005, **12**, 961–971.

36 K. Kim, *Chem. Soc. Rev.*, 2002, **31**, 96–107.

37 D. A. Leigh, R. G. Pritchard and A. J. Stephens, *Nat. Chem.*, 2014, **6**, 978–982.

38 T. Hasell, X. Wu, J. T. A. Jones, J. Bacsa, A. Steiner, T. Mitra, A. Trewin, D. J. Adams and A. I. Cooper, *Nat. Chem.*, 2010, **2**, 750–755.

39 M. Fujita, N. Fujita, K. Ogura and K. Yamaguchi, *Nature*, 1999, **400**, 52–55.

40 H. Nowell, S. A. Barnett, K. E. Christensen, S. J. Teat and D. R. Allan, *J. Synchrotron Radiat.*, 2012, **19**, 435–441.

41 F. Cipriani, F. Felisaz, L. Launer, J.-S. Aksoy, H. Caserotto, S. Cusack, M. Dallery, F. di-Chiaro, M. Guijarro, J. Huet, S. Larsen, M. Lentini, J. McCarthy, S. McSweeney, R. Ravelli, M. Renier, C. Taffut, A. Thompson, G. A. Leonard and M. A. Walsh, *Acta Crystallogr. Sect. D Biol. Crystallogr.*, 2006, **62**, 1251–1259.

42 G. Ueno, R. Hirose, K. Ida, T. Kumasaka, M. Yamamoto and IUCr, *J. Appl. Crystallogr.*, 2004, **37**, 867–873.

43 A. E. Cohen, P. J. Ellis, M. D. Miller, A. M. Deacon and R. P. Phizackerley, *J. Appl. Crystallogr.*, 2002, **35**, 720–726.

44 N. Johnson, P. Waddell, W. Clegg and M. Probert, *Crystals*, 2017, **7**, 360.

45 R. D. Doherty, D. A. Hughes, F. J. Humphreys, J. J. Jonas, D. J. Jensen, M. E. Kassner, W. E. King, T. R. McNelley, H. J. McQueen and A. D. Rollett, *Mater. Sci. Eng. A*, 1997, **238**, 219–274.

46 R. D. Doherty, R. W. Cahn and P. Haasen, *Diffusive Phase Transitions in Physical Metallurgy, 4th Edition*, Elsevier, Amsterdam, 1996.

47 D. W. Oxtoby, *J. Phys. Condens. Matter*, 1992, **4**, 7627–7650.

48 D. Erdemir, A. Y. Lee and A. S. Myerson, *Acc. Chem. Res.*, 2009, **42**, 621–629.

49 R. J. Davey, K. Allen, N. Blagden, W. I. Cross, H. F. Lieberman, M. J. Quayle, S. Righini, L. Seton and G. J. T. Tiddy, *CrystEngComm*, 2002, **4**, 257–264.

50 J. Tian, P. K. Thallapally and B. P. McGrail, *CrystEngComm*, 2012, **14**, 1909.

51 L. J. Barbour, *Chem. Commun.*, 2006, **0**, 1163.

52 J. Lucero, S. K. Elsaidi, R. Anderson, T. Wu, D. A. Gómez-Gualdrón, P. K. Thallapally and M. A. Carreon, *Cryst. Growth Des.*, 2018, **18**, 921–927.

53 Z. Zhang, Z. Wang, S. He, C. Wang, M. Jin and Y. Yin, *Chem. Sci.*, 2015, **6**, 5197–5203.

54 H. N. Chapman, P. Fromme, A. Barty, T. A. White, R. A. Kirian, A. Aquila, M. S. Hunter, J. Schulz, D. P. DePonte, U. Weierstall, R. B. Doak, F. R. N. C. Maia, A. V. Martin, I. Schlichting, L. Lomb, N. Coppola, R. L. Shoeman, S. W. Epp, R. Hartmann, D. Rolles, A. Rudenko, L. Foucar, N. Kimmel, G. Weidenspointner, P. Holl, M. Liang, M. Barthelmess, C. Caleman, S. Boutet, M. J. Bogan, J. Krzywinski, C. Bostedt, S.

Bajt, L. Gumprecht, B. Rudek, B. Erk, C. Schmidt, A. Hömke, C. Reich, D. Pietschner, L. Strüder, G. Hauser, H. Gorke, J. Ullrich, S. Herrmann, G. Schaller, F. Schopper, H. Soltau, K.-U. Kühnel, M. Messerschmidt, J. D. Bozek, S. P. Hau-Riege, M. Frank, C. Y. Hampton, R. G. Sierra, D. Starodub, G. J. Williams, J. Hajdu, N. Timneanu, M. M. Seibert, J. Andreasson, A. Rocker, O. Jönsson, M. Svenda, S. Stern, K. Nass, R. Andritschke, C.-D. Schröter, F. Krasniqi, M. Bott, K. E. Schmidt, X. Wang, I. Grotjohann, J. M. Holton, T. R. M. Barends, R. Neutze, S. Marchesini, R. Fromme, S. Schorb, D. Rupp, M. Adolph, T. Gorkhover, I. Andersson, H. Hirsemann, G. Potdevin, H. Graafsma, B. Nilsson and J. C. H. Spence, *Nature*, 2011, **470**, 73–77.

55 Y. Jin, Q. Wang, P. Taynton and W. Zhang, *Acc. Chem. Res.*, 2014, **47**, 1575–1586.

56 J. L. Dahlin and M. A. Walters, *Future Med. Chem.*, 2014, **6**, 1265–90.

57 T. Hasell, S. Y. Chong, K. E. Jelfs, D. J. Adams and A. I. Cooper, *J. Am. Chem. Soc.*, 2012, **134**, 588–598.

58 D. Fujita, Y. Ueda, S. Sato, N. Mizuno, T. Kumasaka and M. Fujita, *Nature*, 2016, **540**, 563–566.

59 I. G. Garcia, M. Bernabei, R. P. Soto and M. Haranczyk, *Cryst. Growth Des.*, 2017, **17**, 5614–5619.

60 D. Nazarian, J. S. Camp, Y. G. Chung, R. Q. Snurr and D. S. Sholl, *Chem. Mater.*, 2017, **29**, 2521–2528.

61 G. Fraux and F.-X. Coudert, *Chem. Commun.*, 2017, **53**, 7211–7221.

62 S. Li, Y. G. Chung and R. Q. Snurr, *Langmuir*, 2016, **32**, 10368–10376.

63 G. Zhu, Y. Liu, L. Flores, Z. R. Lee, C. W. Jones, D. A. Dixon, D. S. Sholl and R. P. Lively, *Chem. Mater.*, 2018, **30**, 262–272.

64 V. Santolini, M. Miklitz, E. Berardo and K. E. Jelfs, *Nanoscale*, 2017, **9**, 5280–5298.

65 D. P. McMahon, A. Stephenson, S. Y. Chong, M. Little, J. T. A. Jones, A. I. Cooper and G. M. Day, *Faraday Discuss.*, , DOI:10.1039/C8FD00031J.

66 S. Grimme, J. Antony, S. Ehrlich and H. Krieg, *J. Chem. Phys.*, 2010, **132**, 154104.

67 E. O. Pyzer-Knapp, H. P. G. Thompson, F. Schiffmann, K. E. Jelfs, S. Y. Chong, M. A. Little, A. I. Cooper and G. M. Day, *Chem. Sci.*, 2014, **5**, 2235.

68 G. M. Sheldrick, *Acta Crystallogr. Sect. A, Found. Adv.*, 2015, **71**, 3–8.

69 D. Kratzert, J. J. Holstein and I. Krossing, *J. Appl. Crystallogr.*, 2015, **48**, 933–938.

70 Bruker, Apex 2, Bruker AXS Inc., Madison, 2012.

71 A. Thorn, B. Dittrich and G. M. Sheldrick, *Acta Crystallogr. Sect. A Found. Crystallogr.*, 2012, **68**, 448–451.

72 V. Santolini, G. A. Tribello and K. E. Jelfs, *Chem. Commun.*, 2015, **51**, 15542–15545.

73 M. A. Little, S. Y. Chong, M. Schmidtmann, T. Hasell and A. I. Cooper, *Chem. Comm.*, 2014, **50**, 9465–8.

74 C. S. Cundy and P. A. Cox, *Chem. Rev.*, 2003, **103**, 663–702.

75 M. Mastalerz, *Angew. Chemie Int. Ed.*, 2010, **49**, 5042–5053.

76 O. V. Dolomanov, L. J. Bourhis, R. J. Gildea, J. A. K. Howard and H. Puschmann, *J. Appl. Crystallogr.*, 2009, **42**, 339–341.

77 M. F. Sanner, A. J. Olson and J.-C. Spehner, *Biopolymers*, 1996, **38**, 305–320.

78 G. Schill and A. Lüttringhaus, *Angew. Chemie Int. Ed. English*, 1964, **3**, 546–547.

79 F. Aricó, T. Chang, S. J. Cantrill, S. I. Khan and J. F. Stoddart, *Chem. - A Eur. J.*, 2005, **11**, 4655–4666.

80 L. Carlucci, G. Ciani and D. M. Proserpio, *CrystEngComm*, 2003, **5**, 269–279.

81 M. J. Hardie, *Nat. Chem.*, 2011, **4**, 7–8.

82 V. N. Vukotic, K. J. Harris, K. Zhu, R. W. Schurko and S. J. Loeb, *Nat. Chem.*, 2012, **4**, 456–460.

83 G. Gil-Ramírez, D. A. Leigh and A. J. Stephens, *Angew. Chem. Int. Ed. Engl.*, 2015, **54**, 6110–50.

84 M. Cesario, C. O. Dietrich-Buchecker, J. Guilhem, C. Pascard and J. P. Sauvage, *J. Chem. Soc. Chem. Commun.*, 1985, **0**, 244.

85 M. Cesario, C. O. Dietrich-Buchecker, J. Guilhem, C. Pascard and J. P. Sauvage, *J. Chem. Soc. Chem. Commun.*, 1985, 244.

86 F. V. Ralf Jäger, Thomas Schmidt, Detlef Karbach, *Synth. Lett.*, 1996, **8**, 723–725.

87 Y. Liu, S. A. Vignon, X. Zhang, P. A. Bonvallet, S. I. Khan, K. N. Houk and Stoddart J. F., *J. Org. Chem.*, 2005, **70**, 9224–9344.

88 C. Reuter, A. Mohry, A. Sobanski and F. Vögtle, *Chem. - A Eur. J.*, 2000, **6**, 1674–1682.

89 Y.-L. Zhao, A. Trabolsi and J. F. Stoddart, *Chem. Commun.*, 2009, **0**, 4844–4846.

90 J. T. A. Jones, T. Hasell, X. Wu, J. Bacsa, K. E. Jelfs, M. Schmidtmann, S. Y. Chong, D. J. Adams, A. Trewin, F. Schiffman, F. Cora, B. Slater, A. Steiner, G. M. Day and A. I. Cooper, *Nature*, 2011, **474**, 367–371.

91 M. Han, H.-Y. Zhang, L.-Z. Yang, Z.-J. Ding, R.-J. Zhuang and Y. Liu, *European J. Org. Chem.*, 2011, 7271–7277.

92 A. L. Spek, *Acta Crystallogr. Sect. C, Struct. Chem.*, 2015, **71**, 9–18.

93 A. L. Spek and IUCr, *Acta Crystallogr. Sect. A Found. Crystallogr.*, 1990, 46, 34.

# Chapter 4

## Functional Material Discovery: By Strategic Design and High Throughput Screening

# 1 Introduction

*The work discussed herein can be found in the Nature paper by Pulido et al. My role focused on the crystal structure determination of **T1** and **T2**, as well as the further work dicussed surrounding the desolvation and further studies of **T1**.*[1]

Hydrogen-bonded organic frameworks (HOFs) have been known for decades, however only recently has their functionality as porous materials been studied.[2,3] They exhibit microporosity, and the ability to uptake and separate gases.[4–6] In Chapter 1, we introduced important properties of HOFs, such as thermal stability, and solubility which provides routes towards crystal growth, easing structural elucidation.[6,7] In this chapter we explore the benefits of HOFs, factors that separate them from other types of microporous framework materials, and what makes these materials particularly interesting.

HOFs have improved solubility compared with other organic framework materials, such as covalent organic frameworks (COFs). In the seminal work by Yaghi et al. they discovered that the limited solubility of COFs could be overcome by using reversible condensation conditions during synthesis.[7] Currently, there are only a handful of COFs with reported single crystal structures, due to their poor solubility in organic solvents and limited reversibility during reaction.[8,9] Therefore, structural data is traditionally obtained using powder diffraction, and geometrical principles from reticular chemistry, as discussed in section 1.2 in Chapter 2.[10]

HOFs are prepared using discrete molecules which are soluble in common organic solvents, however, they are formed through the reversible formation of weaker hydrogen bonding (H-bonding) interactions. This enables error correction during crystallisation and provides easier access to conditions which enable single crystal growth and structural data.[2,11,12] Despite non-covalent bonds HOFs can have impressive thermal stability.[13] One microporous HOF structure published by Chen et al. was stable up to 250 °C, and exhibited impressive affinity for chlorofluorocarbons (CFCs), a potent greenhouse species.[14]

If the interactions between the guests in the framework and the host HOF, the activation and reactivation of HOFs is a low energy consuming process.[15] Typically, activation will take place in a vacuum oven at lower temperatures, around 40–50 °C for 24 hours.[17] By comparison, covalent organic frameworks (COFs) have been shown to be thermally stable up to 600 °C.[1819] Imine bonds, which are commonly seen in COFs have a much higher bond energy than the hydrogen bonds seen in HOFs. For example, the C=N bond has a bond energy of 645 kJmol$^{-1}$. Comparatively, H-bonding varies greatly on the bond angle and length, however **Table 1** details the relative energies, hence the significant difference in stability to increased temperatures.[7,16,17]

**Table 1** Hydrogen-bond types and their relative energies of vaporisation.

| ***Bond-type*** | ***Relative energies (kJ mol$^{-1}$)*** |
|---|---|
| O-H---N | 29 |
| O-H---O | 21 |
| N-H---N | 13 |
| N-H---O | 8 |

## *1.1 Microporous HOFs*

### *1.1.1 Hydrogen Bonding Motifs*

In 1990, Margaret Etter introduced empirical hydrogen-bonding rules which describe the nature of the bonding, e.g., dimer vs. intramolecular, and the number of donor and acceptor atoms involved.[18] These bonding rules can be simplified by the notation $N_y^x$(n), where N represents the H-bonding motif and whether it is infinite or finite. This can be represented by C (Chain), D (Dimer), R (Ring), or S (intramolecular). $N^x$ and $N_y$ are the number of acceptors and donors, respectively, and (n) is the number of atoms involved in the repeat unit.

In **Figure 1** are two examples of H-bonding motifs, $R_2^2$(8) and S(6). Following from the development of these empirical rules, hydrogen bonded assemblies have been studied in great detail and these interactions are an important driving force in supramolecular self-assembly.[19] For example, in 2008 Mu et al. demonstrated that Aryl-F---H H-bonding drove the formation of a self-assembled chiral network. The spontaneous formation of these rigid molecular structures was attributed to the H-bonding motif present.[20] Supramolecular aggregates have also been shown to form as a result of H-bonding interactions, which promote molecular recognition and self-organisation.[21]

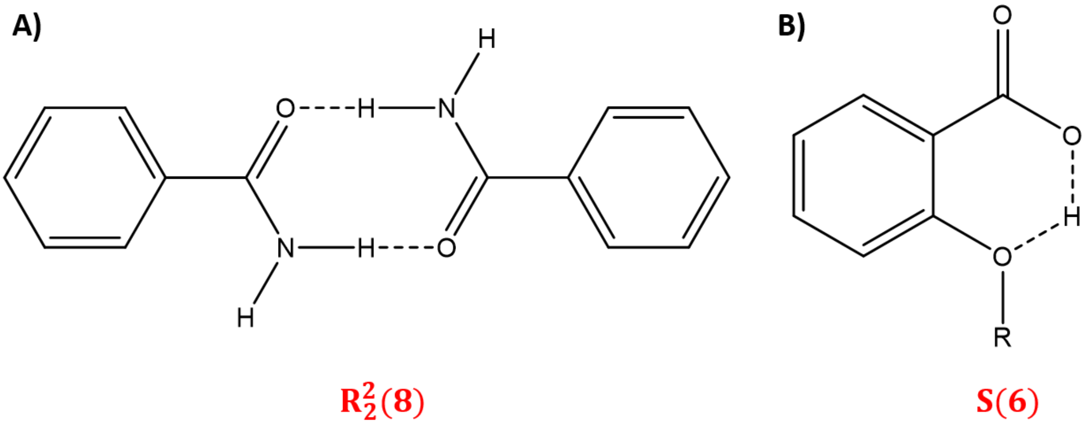

**Figure 1 A)** A ring H-bonding motif with 2 acceptors and donors and 8 atoms involved; **B)** Intramolecular H-bonding motif with 6 atoms involved.

### *1.1.2 Microporous Hydrogen-bonded Organic Frameworks*

Desiraju introduced the concept of hydrogen-bonded frameworks in 1995, by taking advantage of H-bonding tectons for crystal engineering in supramolecular materials.[22] Conceptually, this opened up the possibility of a new method to design of supramolecular assemblies, and with so many potential tectons for H-bonding a new field emerged.[23–25]

HOFs are formed using hydrogen-bonding building blocks, described here as tectons, which can be recrystallised from solvents forming 1-, 2-, or 3-dimensions networks. These networks can be designed by considering the bond angles, bond distances, and strength of the hydrogen bond interactions between the tectons.[26,25] Although a material may contain voids or pores, the framework structures need to be energetically stable so they are maintained after desolvation. In some cases, guest removal will result in the collapse of the framework which has been seen in a number of reported HOFs.[27–30] This can arise from limited rigidity or weaker h-bonding interactions, hence, although the material may contain guest accessible channels or voids within the material, the HOF would not behave as a porous material.

One of the first microporous solids, which was structurally held together with hydrogen bonds, was reported in 1994 (**Figure 2**).[31] The macrocycle had six hydroxy groups and a calculated density of 1.29 g $cm^{-3}$. The HOF was crystallised by slow diffusion of methanol into a solution of the macrocycle in **Figure 2** and ethanol. These H-bonding solvents interacted with the macrocycle and interrupted bonding between the macrocycles. The crystal structure formed stacks, arising from both Van der Waals (VdW) and $\pi$–$\pi$ interactions, generating channels throughout the material.

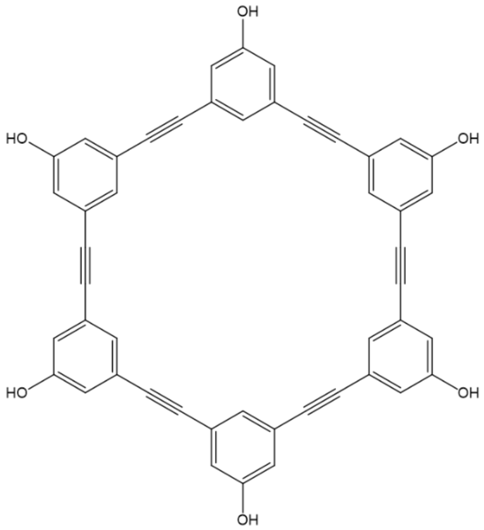

**Figure 2** The macrocyclic hydrogen-bonding tecton used for the first potentially microporous HOF in 1994 by Venkataraman et al.

In 1997, HOF-1 was reported by Brunet et al., which they quoted as showing unprecedented structural integrity, with the monomer shown in **Figure 3**.[32] The crystal structure formed an $R_2^2(8)$ hydrogen bonding motif, resulting in hexagonal channels throughout the structure. The largest channel in the resulting structure was 11.8 Å at its widest, however they never fully removed guests from the pores. They did however show that when 63% of the guests were removed, the network most likely remained intact which was determined through NMR studies. It wasn't until 2011 that HOF-1 was reported to be permanently porous, and furthermore showed selective separations for $C_2H_2/C_2H_4$.[5] The selectivity arises from the favourable adsorption enthalpy for $C_2H_2$ (58.1 $kJmol^{-1}$) compared with $C_2H_4$ (31.9 $kJmol^{-1}$), which is higher than MOFs which exhibit the same selective separation.[33,34]

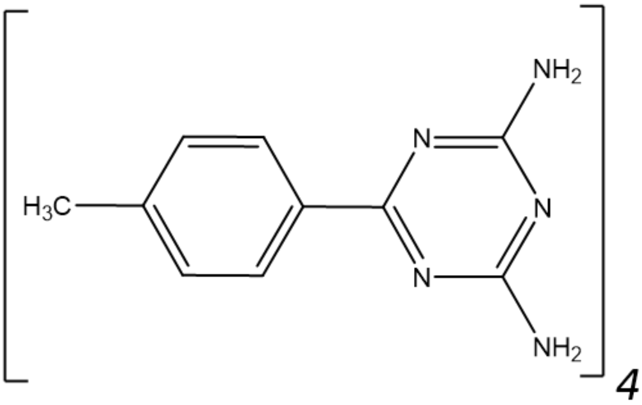

**Figure 3** H-bonding tecton used for HOF-1, first reported in 1997, and further used for selective $C_2H_2$ and $C_2H_4$ separations.

Proton conduction has been hailed as one of the most promising technologies for clean and efficient power generation, prompting the discovery of more materials with this functionality.[35] MOFs have been shown to exhibit proton conduction through cooperative H-bonding, leading to the theoretical application of HOFs in proton conduction.[36,37] [3839]

In 2012, Mastalerz et al. published a HOF which had an exceptionally high Brunauer Emmett Teller Surface Area ($SA_{BET}$) of 2796 $m^2 g^{-1}$. The tecton used to form the microporous network was a triptycene derivative with H-bonding benzimidazolone functionality. Triptycentrisbenzimidazolone (referred to here as **T2**). Shown in **Figure 4** is the crystal structure of **T2**, which has two H-bonding motifs, forming two distinctive pores in the structure. The $R_2^2(8)$ motif forms ribbons throughout the crystal structure and is responsible for the larger pore A, with a diameter of 14.5 Å at its widest. The N-H---O bond angle was 169 °, and the bond length 2.88 Å. The linear hydrogen bonds result in pore B, with an N-H---O bond length of 2.739 Å and angle 139.28 °. The slits forming pore B have diameters of 3.8 Å at its shortest point, and 5.8 Å at its widest. The self-assembled cooperative H-bonding contributes to the strength of the framework, with the result being a permanently microporous HOF.[40]

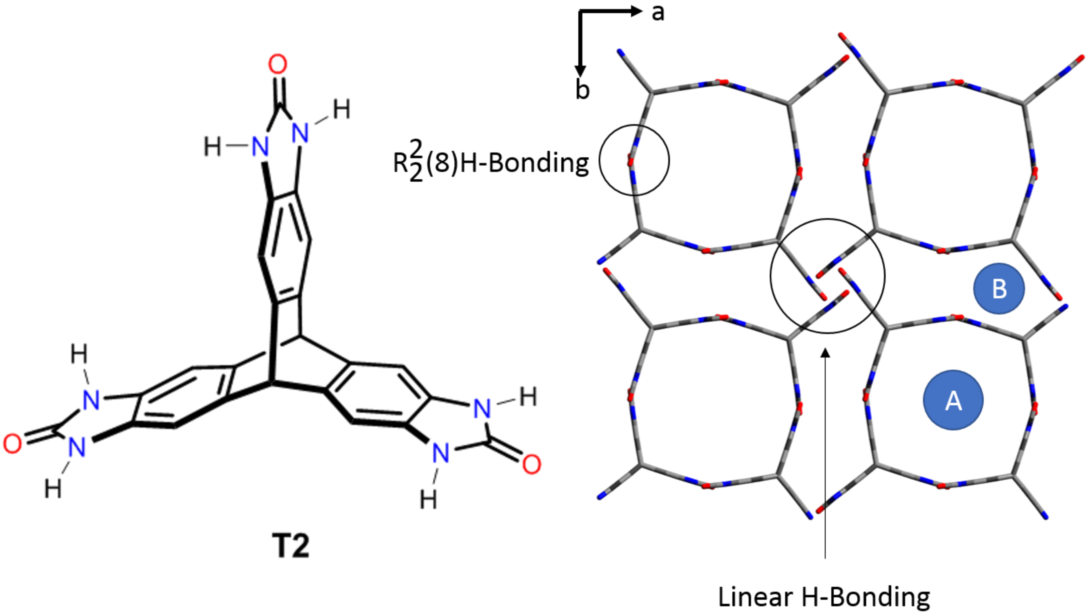

**Figure 4** The left-hand side shows the molecular structure of **TTBI**, and the right-hand side shows the way in which these pack together in a single crystal.

Multiple research groups are now starting to take advantage of these triptycene derivatives.[41–43] Triptycene is a large and bulky building block with trigonal geometry and a rigid core. These derivatives are not only being used in crystalline materials, such as COFs and HOFs, but also in polymeric materials for adsorption, separations and even water treatment.[44–49] In 2014, the Mastalerz group also published porous molecular cube, further illustrating the rigidity of triptycene building blocks in porous material synthesis.[50]

## *1.2 Crystal Structure Prediction*

Crystal structure prediction (CSP) is the application of complex and time-expensive computational software to predict the most likely crystal structure of molecules or materials using the most commonly reported space groups in the Cambridge Crystallographic Data Centre. Still in its infancy, CSP is seen as a potential solution for the increased rate of discovery of new, functional materials.,[51] CSP is a fairly routine method in drug discovery in the pharmaceutical industry.[52] Polymorphism can present significant issues when commercialising drugs, as each individual polymorph requires a patent, therefore CSP presents an effective solution towards polymorph screening that isn't experimentally demanding and time consuming.[53–55]

Computational design and structure prediction has been applied for hybrid organic-inorganic frameworks, such as MOFs.[56] Controlled synthesis of materials containing large pores is challenging, therefore the development of computational methods to predict the framework architecture and dimensionality are essential, especially when considering polymorphism.[57] Férey et al*.* discussed crystal structure prediction with respect to the application of limits, as with frameworks a size limit to the pore needs to be applied according to rational design.[58] However, the application of these limits could potentially deter from the discovery of materials with 'giant pores'. Despite these limitations, they were able to accurately predict a number of structure and polymorphs of experimental MOF crystal structures.

Despite the technology behind CSP, which has undergone significant improvements in the last few decades, there are still limitations making it a highly complex method for the discovery of functional molecules or materials.[59] CSP is limited due to the number of variables within a crystal structure; including cell dimensions, space group, the number of molecules within the asymmetric unit, the conformation of the molecule if it contains any degrees of freedom and finally the arrangement of the molecules, which may or may not contain directionality, such as halogen bonding, $\pi$–$\pi$ stacking or H-bonding.[60–62]

In this study, CSP calculations were performed using a quasi-random sampling procedure, interfaced through Global Lattice Energy software.[63] The molecules were sketched in ChemDraw, and then an initial molecular-geometry optimization performed in Materials Studio software.[64] Density functional theory (DFT) was then used to further refine the molecular geometries, using a M06-2X exchange correlation functional and 6-311G** basis set, interfaced through Gaussian09 software.[65] Crystal structures were generated with Z' = 1, with all 89 space groups reported in the Cambridge Structural Database for all non-polymeric organic molecular crystals.

## *1.3 Energy-Structure-Function Maps*

While CSP is making leaps and bounds in development, the next significant development would be to combine accurate prediction with the development and design of new functional molecules or materials.[66] Applying CSP to both structure prediction and properties has been seen, in zeolites, cathode materials for batteries and porous solids.[67–69] However, despite these advances the non-hypothetical design of functional molecules or materials still requires significant developments. For molecular crystals polymorphism is particularly problematic, as the structures are held together by weaker interactions, small changes can lead to a high number of crystal structures.[70] Therefore, structure-function predictions are more difficult than other analogues such as MOFs or COFs containing strong ionic or covalent bonds respectively.[71,7]

A structure's stability relates to its lattice energy, the lower the lattice energy, the more stable the structure.[72] Therefore, from the predicted structure we can determine the structures relative stability from this predicted energy. Porous materials must contain guest accessible voids, which are able to be accessed via selective diffusion. Therefore, by also considering the density of the material alongside the lattice energy, porous materials by *de novo* design could be identified through the use of energy-structure-function maps (ESF maps).

# 2 HOFs by Strategic Design

## 2.1 Molecular Porous Material Tectons

When considering molecular materials and HOFs by design, the initial considerations were to use bulky tectons such as triptycene (**T0**), and bulky materials which possess directional H-bonding; triptycene-2,3,6,7,14,15-hexacarboxytriimide (**T1**) and Triptycentrisbenzimidazolone (**T2**). CSP calculations were performed to determine the number of potential polymorphs for the three tectons, and henceforth ESFs were produced, plotting the density (g cm$^{-3}$) as a function of relative lattice energy (kJ mol$^{-1}$). As the structure becomes less dense, it would be expected that the crystal lattice energy would become less stable. However, a stable porous material would have a low density and an energetically stable crystal lattice energy.

**Figure 5** shows the ESFs for **T0**, **T1**, and **T2**, with each individual spot on the graph representing a predicted crystal structure, and the colour depicting the dimensionality (grey corresponds to 0D, yellow 1D, blue 2D and red 3D). **T0** shows that with an increase in density (*x*-axis), the relative lattice energy (*y*-axis) increases. Without any directional bonding, this narrow spread of data would be anticipated, as a low density structure is unlikely to be achieved. Comparatively, **T1** and **T2** show a much broader trend, with more energetically stable structures present with lower densities. Most significantly, **T2** shows 'spikes' in the ESF, which indicate materials which exceptionally low density (< 0.5 gcm$^{-3}$), but with promise of structural stability.

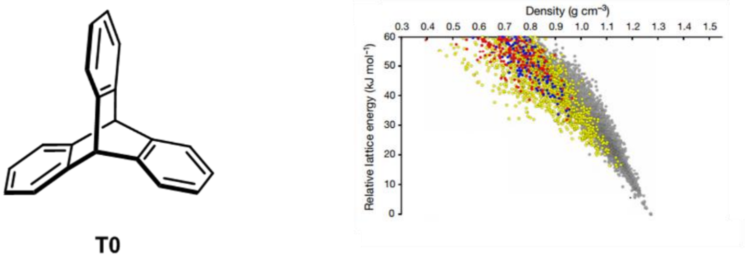

**T0**

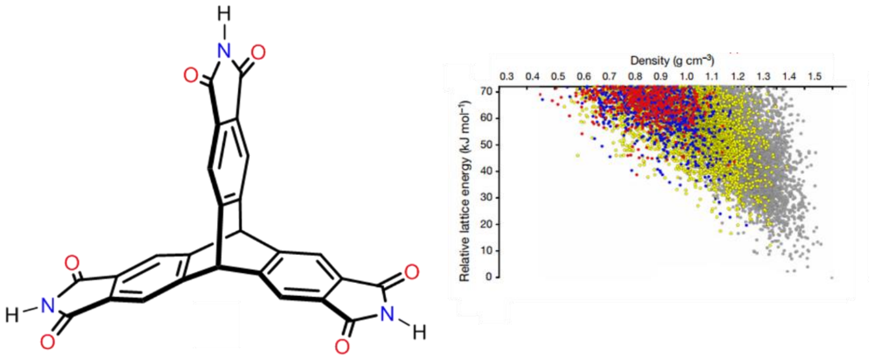

**T1**

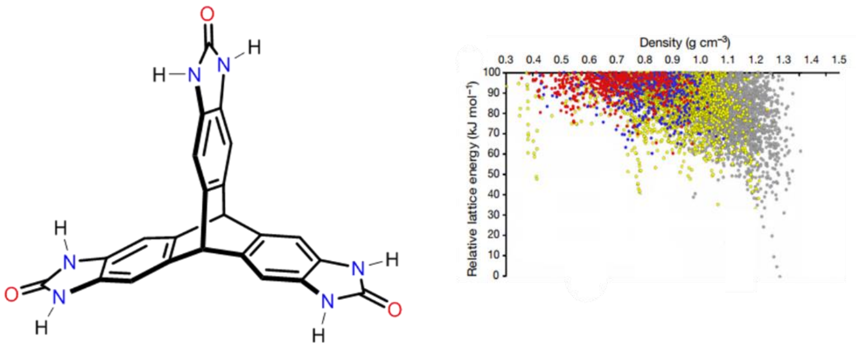

**T2**

**Figure 5** ESF Maps for **T0**, **T1** and **T2**.

Crystal structures and syntheses of **T0**, **T1**, and **T2** had been reported previously, **T2** being discussed earlier in the chapter.[73] The original work by Zonta et al. which discussed the synthesis and crystal structure of **T1** was based on the theory of utilising the bulky building block triptycene (**T0**) and adding H-bonding functionality to generate a HOF with hexagonal channels.[74] The reported structure did not have the predicted hexagonal pores when recrystallised by slow diffusion of methanol (MeOH) into a solution of **T1** in dimethylformamide (DMF). However, the resulting close-packed structure crystallised showed strong H-bonding interactions between **T1** and DMF, hence, interrupting the ideal H-bonding between the tectons preventing formation of channels in the structure.

In section 1.3, we discussed that ESFs can be used to predict the probability tecton to form a porous material. ESFs for **T1** showed no potential 'hits', *i.e.*, any materials with a low density and stable lattice energy. To confirm the prediction, recrystallisations were performed with **T1** as the tecton. Comparatively, the ESF for **T2** showed the potential for a framework material with an incredibly low density of $< 0.5$ gcm$^{-3}$, therefore recrystallisations were also investigated for this tecton.[75]

## *2.2 Hydrogen Bonded Organic Framework **T1***

In order to access an alternative polymorph and henceforth generate a porous framework, recrystallisations of **T1** in organic solvents were performed. Solutions were made with a concentration of 10 mgmL$^{-1}$ in THF, and anti-solvents were slowly diffused into the solutions. The anti-solvents discussed here are dimethylacetamide (DMA) and chloroform ($CHCl_3$).

Powder patterns revealed that from reaction, **T1** was the same close-packed phase as **T1**$\cdot CH_3OH$. **Figure 6** shows the powder patterns of **T1**$\cdot CH_3OH$ and **T1**$\cdot$reaction. The powder pattern was obtained by recrystallisation of **T1** in $C_4H_8O$ (THF) with $CH_3OH$ diffused into the solution, the solvent was decanted and the solid left to dry overnight under ambient conditions.

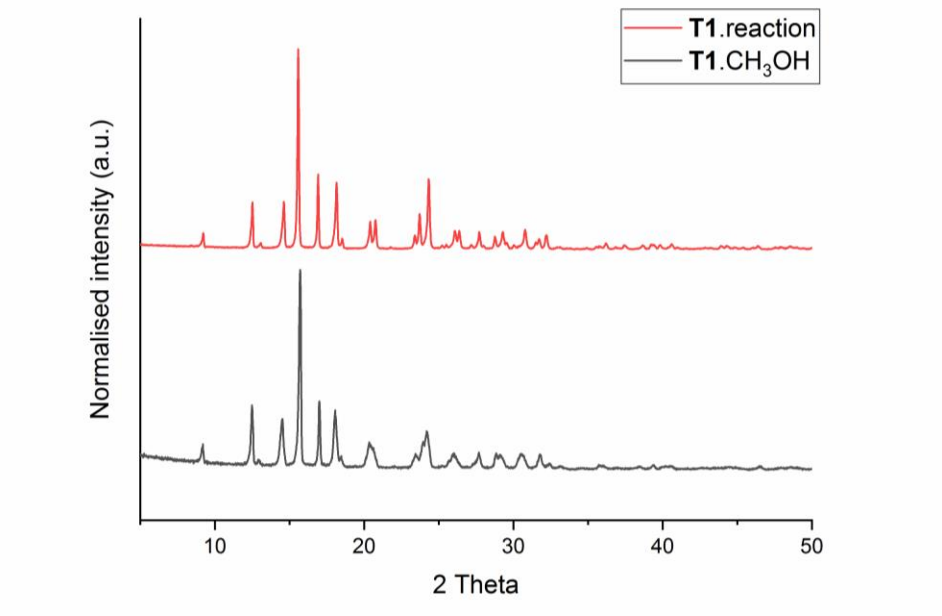

**Figure 6** Powder diffraction patterns comparing **T1**·CH$_3$OH and **T1** as obtained from the reaction, showing they are the same polymorph.[74]

Earlier we discussed the reported crystal structure, which showed H-bonding between **T1** and DMF, shown in **Figure 7**. This interaction is seen with all the functional groups and dominates the crystal packing. Similarly, **T1**·CH$_3$OH exhibited a close-packed structure with an absence of channels due to non-cooperative H-bonding, therefore attempts were made to recrystallise **T1** with alternative solvent systems which could direct the packing towards a porous structure.[76,77] **Figure 8** shows **T1**.C$_3$H$_7$NO.MeOH viewed along the c-axis, with the residual solvent coloured green for clarity. The structure showed strong H-bonding between **T1** and DMF, with a 1:1 ratio.

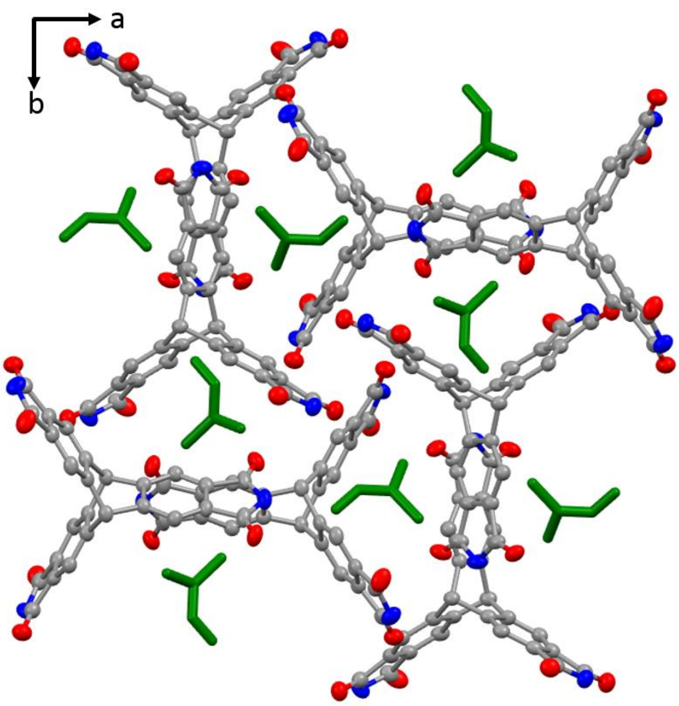

**Figure 7** **T1** from the literature, with the DMF represented as green, and the hydrogen atoms were omitted from the figure for clarity.[74]

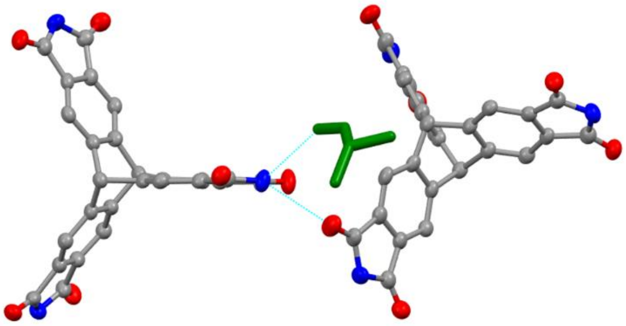

**Figure 8** **T1**$\cdot C_3H_7NO\cdot CH_3OH$, H-bonding between **T1** and DMF (green).

### *2.2.1 **T1**$\cdot C_9OH_{12}$*

The first recrystallisation was using dimethylanisole (DMA), which could potentially promote π–π stacking with the **T1** host and generate a framework crystal structure. **T1**$\cdot(C_9H_{12}O)\cdot 1.25(H_2O)$: Formula $C_{35}H_{25}N_3O_{8.75}$; $M$ = 570.16 g mol$^{-1}$, monoclinic $P2_1/n$, colourless block crystals; $a$ = 14.3994(5) Å, $b$ = 22.1420(8) Å, $c$ = 11.5625(4) Å, $\beta$ = 100.262(3)°, $V$ = 3687.4(2) Å$^3$; $\rho$ = 1.027 g cm$^{-3}$ (solvated); $\mu$(Mo-Kα) = 0.105 mm$^{-3}$; $F$ (000) = 1191; $T$ = 100 K; 27410 reflections measured ($4.642 < 2\theta < 49.366$ °), 5572 unique ($R_{int}$ = 0.0838), 3902 ($I > 2\sigma(I)$); $R_1$ = 0.0832 for observed and $R_1$ = 0.2283 for all reflections; $wR_2$ = 0.2364 for all reflections; max/min difference electron density = 0.747 and -0.357 e·Å$^{-3}$; data/restraints/parameters = 3902/11/380; GOF = 1.146. The displacement ellipsoid plot for **T1**·($C_9H_{12}O$)·($H_2O$) is shown in **Figure 9**.

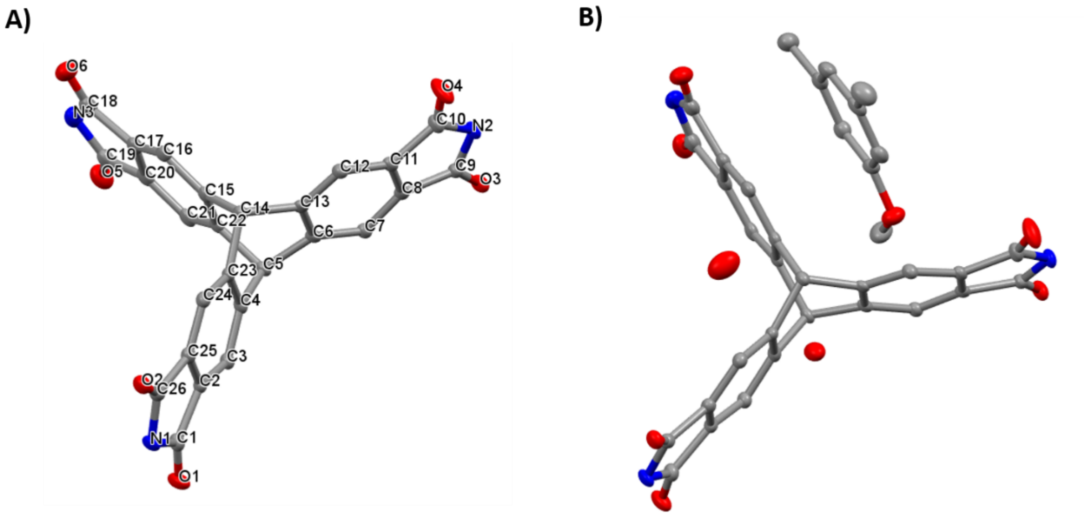

**Figure 9 A)** Labelled displacement ellipsoid plot excluding solvent and water for **T1**·$C_9H_{12}$·O·2($H_2O$). Ellipsoids are displayed at 50% probability level. **B)** Displacement ellipsoid plot including the solvent and disordered water. Hydrogen atoms were omitted for clarity.

The asymmetric unit for **T1**·($C_9H_{12}O$)·($H_2O$) is comprised of one complete **T1** molecule, one ordered DMA guest, and 1.25 molecules of water. Residual electron density was arbitrarily modelled as water, which is most likely present from the aqueous solution. The water showed hydrogen bonding to **T1**.

Crystal packing in **Figure 10** shows an $R_2^2(8)$ for **T1-T1** interactions from only two out of three of the hydrogen-bonding functional groups. The third H-bonding group of **T1** was to water in the structure. The N-H---O between **T1** had a bond angle of 161.189°, and the length 2.915 Å (C in **Figure 10**). The N-H---O between **T1** and $H_2O$ bond angle was 174.782° (B in **Figure 10**), and length 2.851 Å. The O-H---O angle, A in **Figure 10** was 145.389 ° and bond length 3.017 Å.

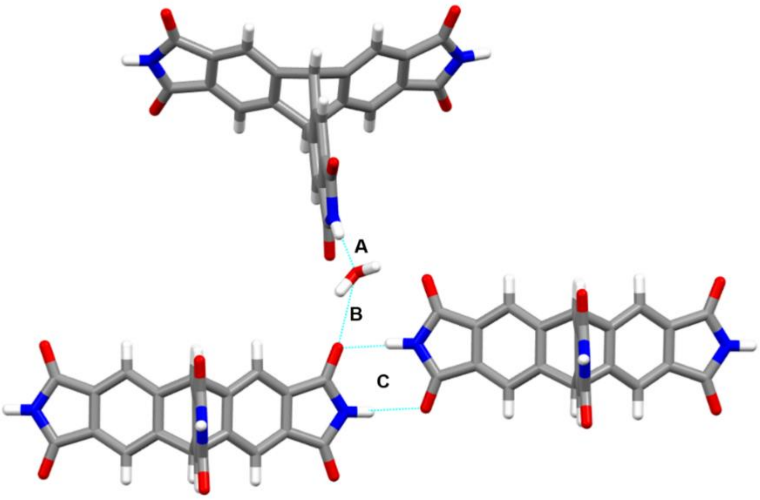

**Figure 10** H-bonding in **T1**·$C_9H_{12}O$ : A) N-H---O between **T1** and $H_2O$; B) O-H-OOO between $H_2O$ and **T1**; C) N-H---O between **T1**.

No H-bonding was observed between the DMA and **T1**, but only π–π stacking. The combination of H-bonding between the **T1** molecules and π–π stacking dominates the crystal packing, leading to the formation of the close-packed structure (**Figure 11**). As well as a lack of voids in the structure, guest removal was not possible due to strong interactions, therefore **T1**.$C_3H_7NO.CH_3OH$ was not a porous polymorph.

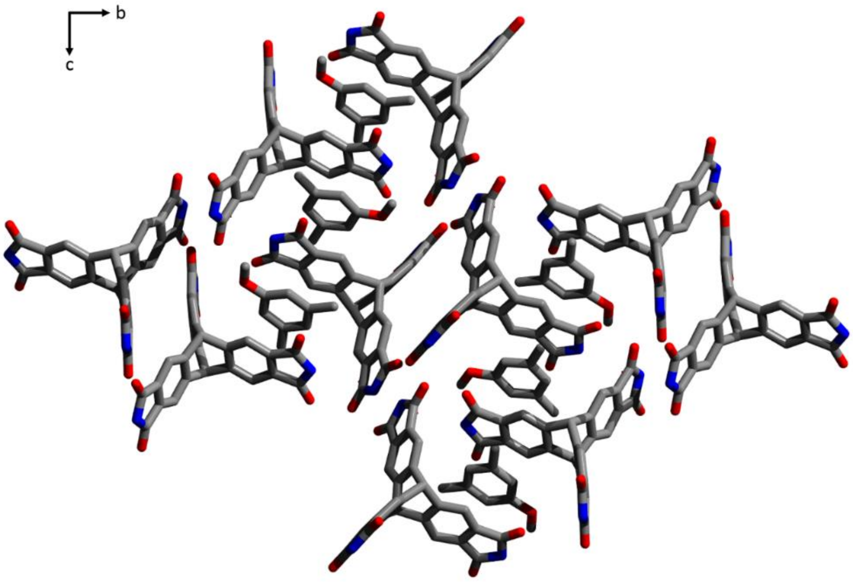

**Figure 11** Crystal packing in **T1**·$C_9H_{12}O$, viewed along the a-axis. The solvent can be seen between two molecules of **T1**, generating the close-packed structure.

### *2.2.2 **T1**·Toluene·THF*

The first potentially porous polymorph found was **T1**·$C_7H_8$·$C_4H_8O$, which showed hexagonal pores which, templated by a co-crystallisation with toluene. **T1** was dissolved in THF, with toluene layered onto the solution and the crystal left to grow under ambient conditions for approximately 3 days. A displacement ellipsoid plot is shown in **Figure 12**. 21 restraints were used in the refinement, including a rigid body restraint for C14, 15, 16 and 17, which is the ½ toluene in the displacement ellipsoid plot. The hydrogen positions for both solvent molecules were also refined using the riding model.

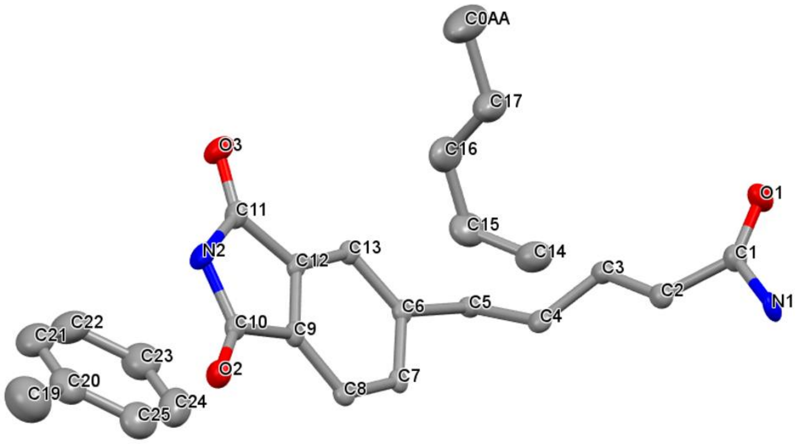

**Figure 12** Labelled displacement ellipsoid plot showing the asymmetric unit of **T1**·$C_7H_8$, with 1.5 toluene molecules, ellipsoid displayed at 50% probability.

**T1**·$C_7H_8$ crystallised with 3 toluene molecules per **T1**, and in the asymmetric unit 1.5 toluene molecules. The H-bonding motif is $R_2^2(8)$, with the N-H---O bond angle of 165.963° and length 2.841 (**Figure 13**).

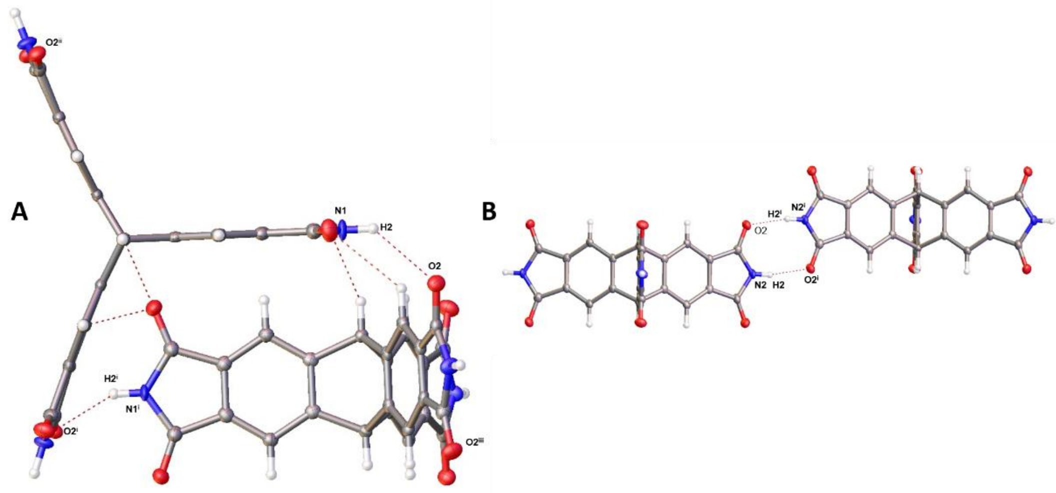

**Figure 13 A)** H-bonding at 100 K which occurs in the corners of the channels of **T1**·Toluene. i: (5/2-X, ½+Y, ½-Z), ii: (5/2-X, 2-Y, -1+Z), iii: (1+X, 3/2-Y, 1/2-Z); **B)** H-bonding at 100 K, i: (3/2-X, 1-Y, +Z )

The crystal structure showed hexagonal channels which were directed through π–π stacking from the co-crystallised toluene. **T1**·$C_7H_8$ stacks edge-to-face with the average π-π stacking distance of 3.64 Å. Shown in **Figure 14** are the hexagonal channels in **T1**·$C_7H_8$, which have a diameter of 14.4 Å at the widest point, measured using atom O1 inside of the wall channels.

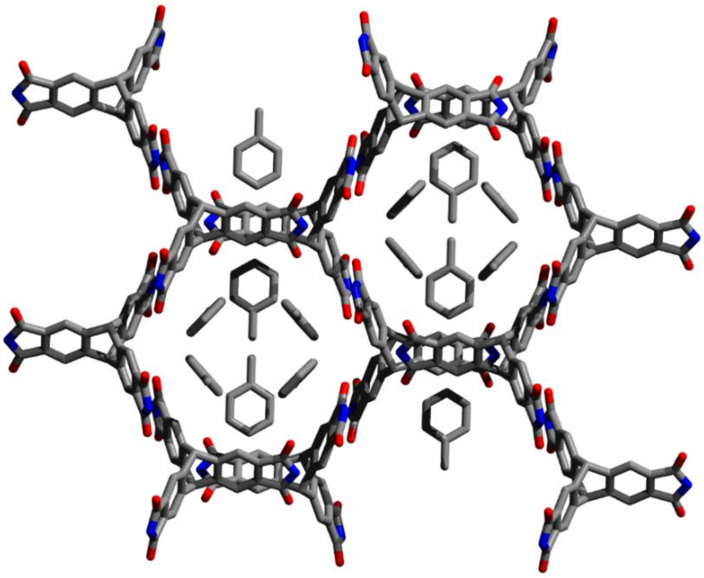

**Figure 14** Crystal packing in **T1**·$C_7H_8$, showing the π–π stacking directing the channels.

### 2.2.3 **T1**·$CHCl_3$·THF

Activating the materials requires full desolvation, and based on the strong π–π interactions between toluene and **T1** it was found that guest removal was not a possibility. Therefore, a solvent system which formed an isostructural framework needed to be identified. **T1**·$CHCl_3$·$C_4OH_8$ was found to be isostructural to **T1**·$C_6H_8$. However, in **T1**·$CHCl_3$·$C_4OH_8$, the solvent was diffusely scattered throughout the hexagonal channels, compared with the well-ordered toluene in **T1**·$C_6H_8$. A displacement ellipsoid plot is shown in **Figure 15**. 717.8 electrons were removed during the squeeze algorithm, which were attributed to be the equivalent of 9 $C_4H_8O$ molecules, and 6 $CHCl_3$ molecules.

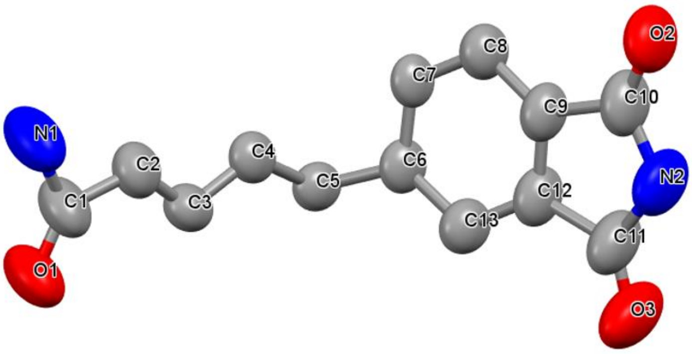

**Figure 15** Displacement ellipsoid plot, ellipsoids displayed at 50% probability. Asymmetric unit of **T1**·$CHCl_3$·THF at 350 K, z' = 0.5, no solvent is modelled as it was too diffuse and therefore is omitted from the figure.

The hexagonal channels in **T1**·$CHCl_3$·THF, shown in **Figure 16**, contained residual electron density, which is typical for materials containing significant voids with no interaction between the solvent and crystal pores. Therefore, attempts were made to desolvate the structure *in situ*, whilst collecting single crystal X-ray data to determine if the crystal structure was retained after thermally removing the solvent from the crystal pores. During this study, it was found that the **T1** structure was retained at 350 K, but that solvent had not been completely removed from the pores, based on the maximum residual electron density peak of 1.9 e·Å$^3$. The isostructural framework had an N-H---O bond angle of 167 ° and length 2.90 Å. The channel diameter measured 13.536 Å.

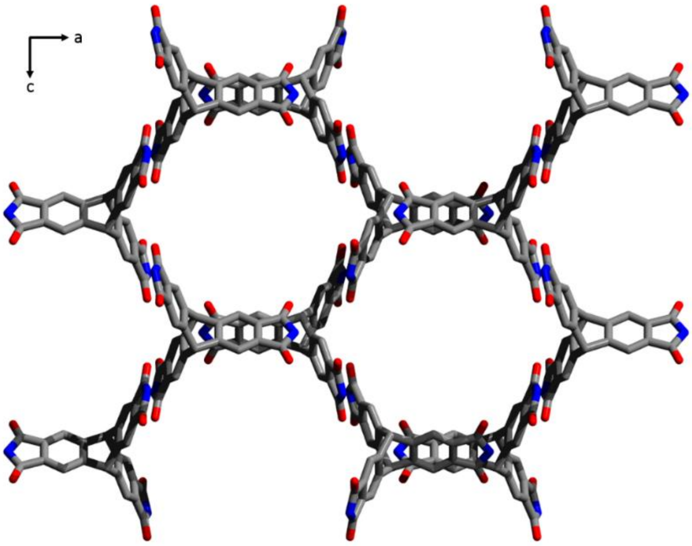

**Figure 16** Hexagonal channels in **T1**·$CHCl_3$·$C_4H_8O$, with the modelled disordered solvent not shown in the channels.

In order to generate a porous material from the **T1**·$CHCl_3$·$C_4H_8O$ solvate, it was necessary to fully evacuate the solvent guests from the crystal pores whilst maintaining the inefficient packing of **T1**·$CHCl_3$·$C_4H_8O$. To evaluate the thermal desolvation of **T1**·$CHCl_3$·$C_4H_8O$, thermogravimetric analysis (TGA) was employed. TGA measures the loss of mass as a function of the temperature increase. By measuring loss of mass, the temperature at which solvent loss occurs can be traced, and therefore temperature of desolvation identified at atmospheric pressure. Solvent loss can be identified by a steady decrease, whereas decomposition can be identified by the mass plummeting signiciantly towards 0%. Simulated powder patterns from the single crystals structures were generated, and compared with the powder patterns from the material. From the single crystal structure, it was calculated that the solvent was 42.5% by mass of **T1**·$CHCl_3$·$C_4H_8O$, however this should be considered an approximation as the single crystal structure is not representative of the bulk material.

The TGA scan shown in **Figure 17** show a mass loss of 15.59% between 25 °C and 203.80 °C, and 18.35% between 203.80 °C and 232.46

°C, a combined loss of 33.94%. The boiling point of THF is 66 °C, and $CHCl_3$ 61.2 °C, therefore it would be expected to evacuate the structure at a lower temperature, unless there is a strong interaction between the solvents and **T1**. Between 315.58 °C and 337.24 °C, 0.78% of mass is lost, which potentially corresponds to thermal decomposition of the imide in **T1**.[78] Finally, between 337.24 – 479.60 °C there is a final loss of 1.42%, which is also likely further imide decomposition.

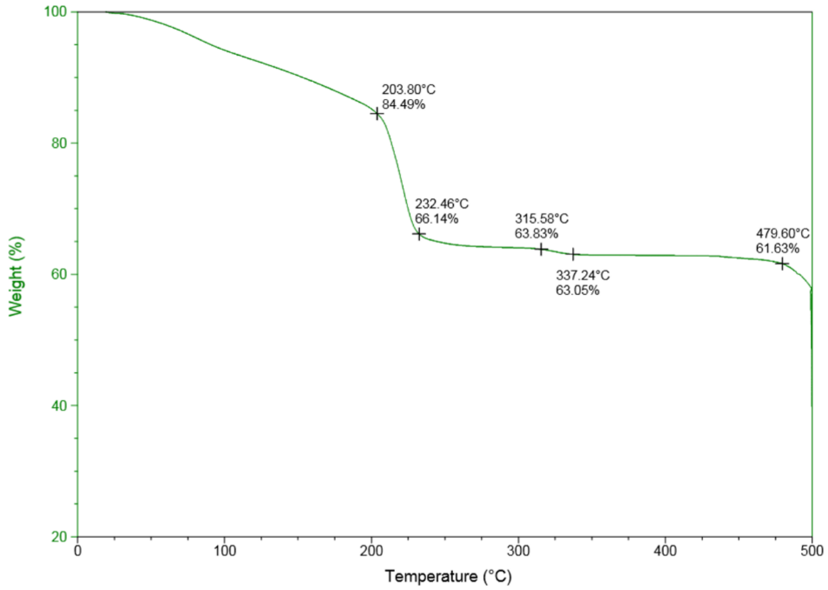

**Figure 17** TGA trace for **T1**$\cdot CHCl_3 \cdot C_4H_8O$.

As well as using TGA to follow the desolvation, phase changes were also monitored using differential scanning calorimetry (DSC). DSC can be used to measure the relative stability of macromolecular materials, and furthermore we can use this in conjunction with the TGA data to get a more complete picture. DSC is performed by placing the sample into a closed pan, unlike TGA which is open, therefore variations can arise in the temperature values between TGA and DSC measurements.

**Figure 18** shows the DSC of **T1**$\cdot CHCl_3 \cdot C_4H_8O$. The endotherm at 234 °C corresponds to the mass loss seen in **Figure 17** between 203.8 – 232.46 °C, and the exotherm at 319 °C corresponds to a small mass loss at 315.58 – 337.24 °C. There is a significant endotherm at 538.90 °C, which most likely indicates decomposition of the material.

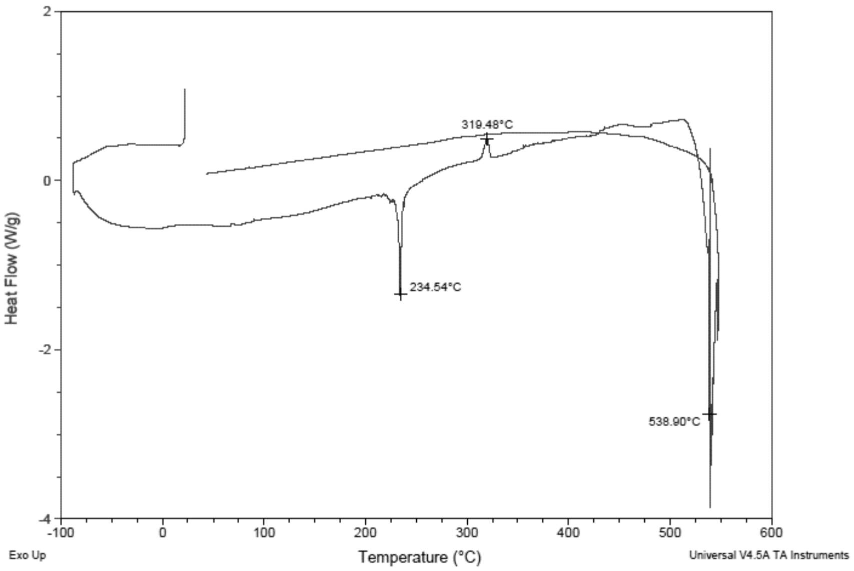

**Figure 18** DSC trace for **T1**·$CHCl_3$·$C_4H_8O$

Powder patterns were collected for **T1** after desolvation, but prior to decomposition. The simulated PXRD pattern from the single crystal structure of **T1**.$CHCl_3$.$C_4H_8O$ (blue) showed one large peak at low angle, which is fairly typical for organic framework materials.[7] The powder patterns in **Figure 19** compared the simulated powder pattern from the single crystal structure of **T1**·$CHCl_3$·$C_4H_8O$ (blue), the experimental powder structure (black) and the structure after confirmed desolvation post-TGA (red). There is a clear difference in crystal structure pre- and post- TGA, therefore we have shown that despite proven loss of solvent, the framework structure was not maintained. Therefore, solvent swaps were attempted using a more volatile solvent, which in this case was pentane, $C_5H_{12}$.

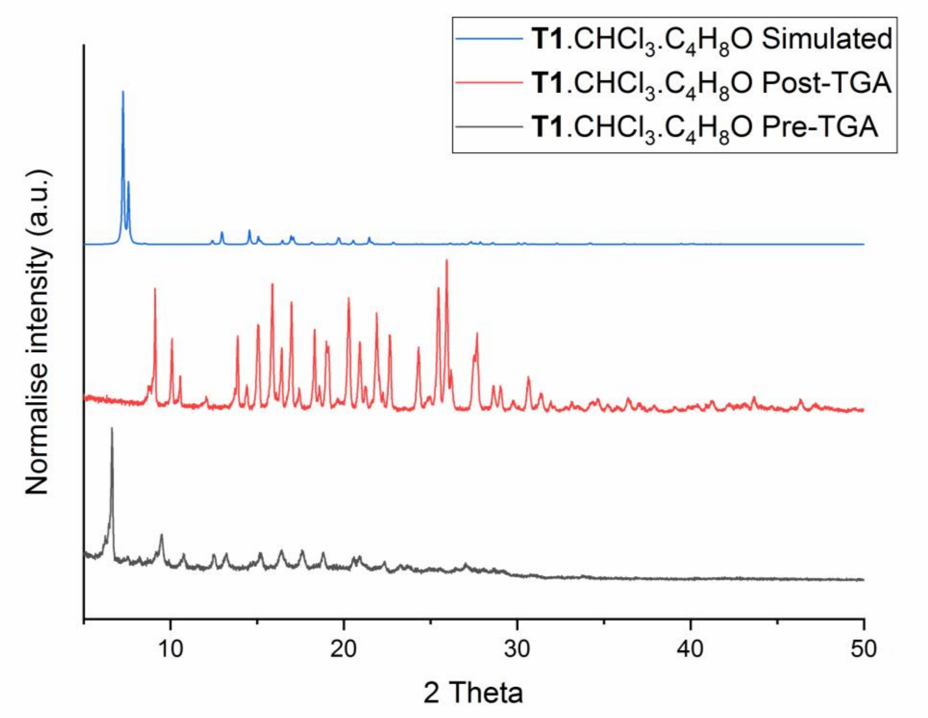

**Figure 19** Powder diffraction patterns: **T1**·$CHCl_3$·THF; Blue: Simulated powder pattern of **T1**·$CHCl_3$·THF; Red: Material post-TGA measurements prior to decomposition; Black: Solvated crystal structure pre-TGA.

### *2.2.4 Solvent Exchanges: **T1**·Pentane*

For **T1**·$C_7H_8$ we saw strong interactions between the solvent and **T1**, therefore guest removal would prove to be too difficult. We found the structure **T1**·$CHCl_3$·THF was structurally stable to partial guest removal, however upon full guest removal the powder pattern showed an alternative pattern, implying a loss of the channel structure. Therefore, it was necessary to find a solvent which would have minimal, weak interactions with the **T1** structure, and a low enough volatility for removal at lower temperatures.

Solvent swaps were performed by setting up recrystallisations of **T1**·$CHCl_3$·$C_4H_8O$ using the same conditions as mentioned previously. Once crystals had grown after around 5 days, half the recrystallisation solvent was decanted and replaced with the equivalent volume of pentane. This was repeated every day for one week until the crystals were in pentane only. The single crystal structure collected to confirm loss of $CHCl_3$, $C_4H_8O$, and presence of pentane in the structure. A displacement ellipsoid plot shown in

**Figure 20**. Residual electron density was modelled as water (O8 and O9), as the solvents used were aqueous.

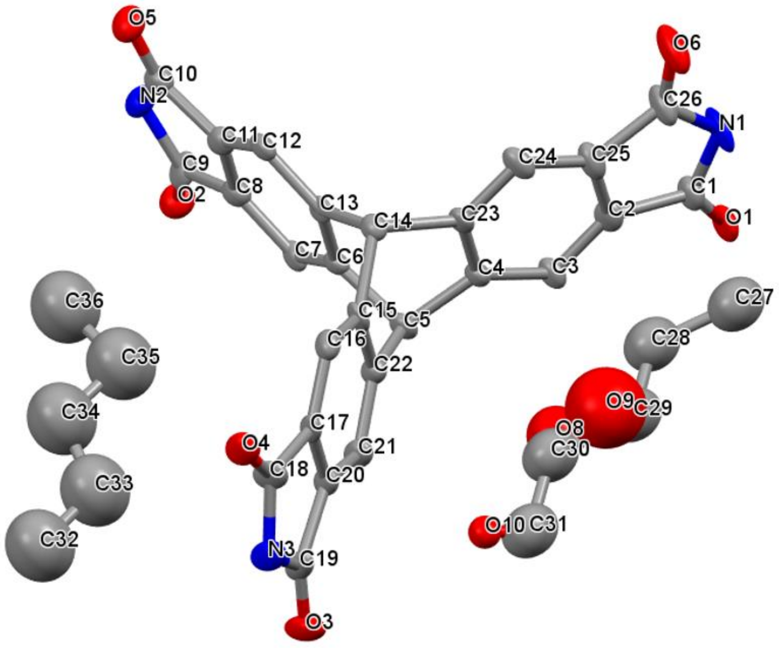

**Figure 20** Asymmetric unit of **T1**$\cdot$1.25($C_5H_{12}$)$\cdot$0.64($H_2O$) with atom labels. H-atoms have been omitted for clarity. Ellipsoids are displayed at 50% probability.

The crystal packing observed was similar to both **T1**.$C_7H_8$ and **T1**$\cdot$$CHCl_3$$\cdot$$C_4H_8O$, however there was a distinct difference between the channels in the structure. The channels were occupied with disordered solvent, similar to **T1**$\cdot$$CHCl_3$.$C_4H_8O$ and **T1**$\cdot$$C_7H_8$, however there was a slight 'twist' to the structure as shown in **Figure 23**.

The crystal packed in the space group *P*na2$_1$, with the same $R_2^2(8)$ H-bonding motif seen in all the channel structures. The N(1)-H---O(2) bond angles in the ring were 161.83° with bond length 2.90 Å, and 152.27° with bond length 2.88 Å (**Figure 21 B** & **D**). For both the **T1**$\cdot$$C_7H_8$ and **T1**$\cdot$$CHCl_3$$\cdot$$C_4H_8O$ structures the bond hydrogen bond angles and lengths were the same. Comparatively, **T1**.$C_5H_{12}$ exhibited a significant difference (**Figure 21**). H-bonding in **T1**$\cdot$$C_5H_{12}$ did not exhibit the same linearity as **T1**$\cdot$$CHCl_3$$\cdot$$C_4H_8O$, leading to weaker H-bonds, and henceforth a less stable structure. This resulted in the twist in the structure shown in **Figure 23**.

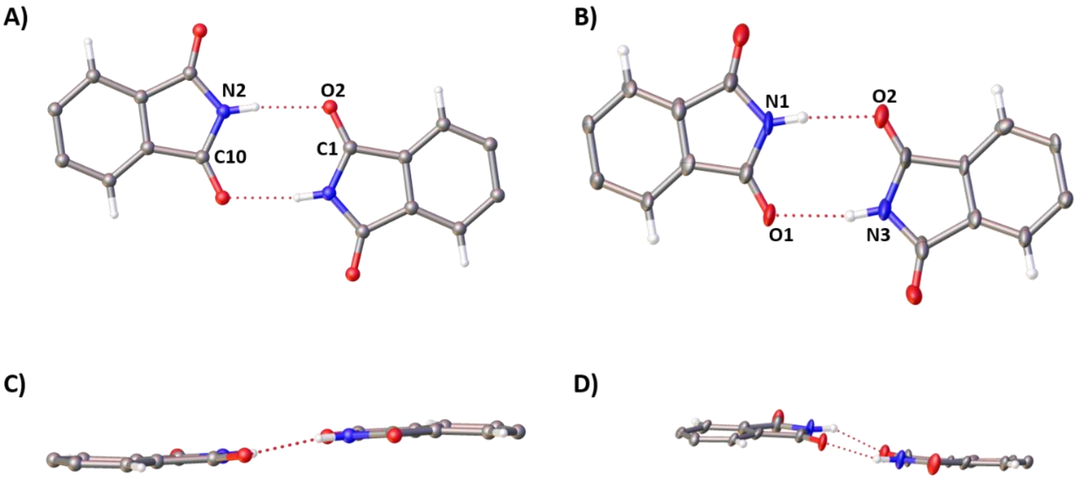

**Figure 21** Comparison of intermolecular H-bonding interactions in **T1**·$CHCl_3$·$C_4H_8O$ (**A** + **C**) versus **T1**·pentane (**B** + **D**) **A)** viewed along the ring motif, showing the N-H---O; **B)** H-bonding in **T1**·$C_5H_{10}$ viewed along the ring motif; **C) T1**.$CHCl_3$.THF viewed along the side showing some linearity but veering away from the 'ideal' 180° for strong H-bonding; **D) T1**·$C_5H_{12}$ showing a significant twist, veering significantly away from a linear structure.

The $2_1$ screw axis in **T1**·$C_5H_{12}$·$H_2O$, which led to the 'twist' in the channels can be more clearly seen in **Figure 22**. The disordered pentane was modelled using an EADP restraint. The two alkane chains were modelled with 75% and 50% occupancy. All H-atoms were refined using the riding model.

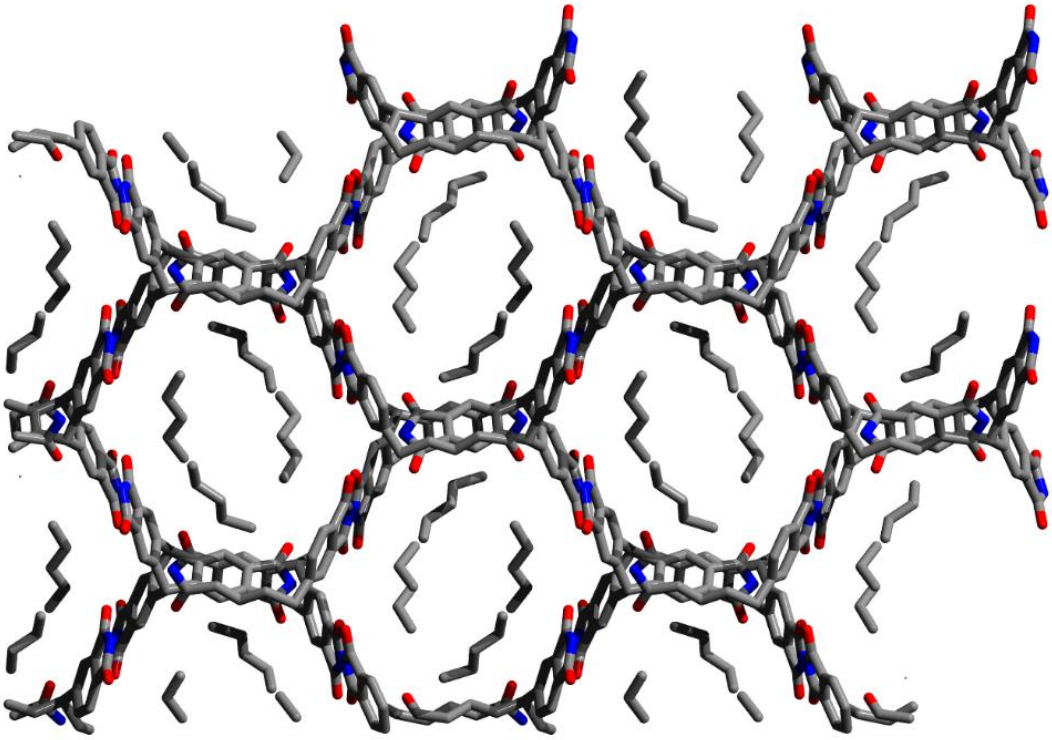

**Figure 22** Crystal packing of **T1**·1.25($C_5H_{12}$)·0.64($H_2O$) shown along the *b*-axis. Water and hydrogens were omitted from the figure for clarity.

After determining the crystal structure of **T1**·$C_5H_{12}$·$H_2O$ at 100 K, attempts were made to desolvate the crystal *in situ* using SCXRD. To investigate this, **T1**.$C_5H_{12}$.$H_2O$ was collected at higher temperatures as with **T1**·$CHCl_3$·$C_4H_8O$. At 350 K, the structure still contained residual electron density in the channels. Another option for desolvation at low temperatures to avoid decomposition is by using a vacuum oven as discussed previously. The solid was placed in the oven at 45 °C, to prevent decomposition, and left for 12 hours to ensure full guest removal from the channels. The resulting solid however appeared cloudy and discoloured, and the resulting material was found to be amorphous (**Figure 23**). Therefore despite best efforts, we were unsuccessful in complete guest removal of solvent from **T1** to generate a porous material.

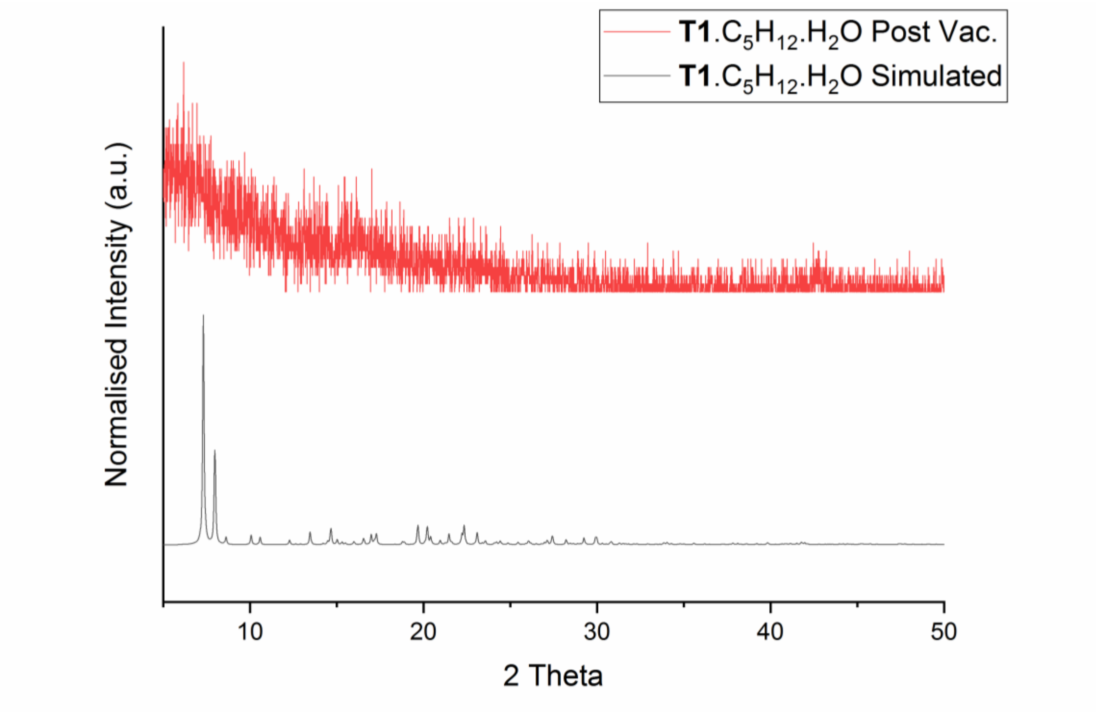

**Figure 23** Powder patterns for **T1**·$C_5H_{12}$·$H_2O$; Simulated powder pattern from the single crystal structure (black), and the amorphous powder pattern after exposure to the vacuum oven.

## *3 Hydrogen Bonded Organic Framework **T2***

Earlier we introduced another H-bonding tecton, **T2**, which was published by the Mastalerz research group in 2014.[73] They showed it had exceptionally high porosity due to the cooperative H-bonding between the tectons forming two individual pores. The tetragonal structure reported was grown through slow diffusion of acetone into a saturated solution of **T2** in dimethylsulfoxide (DMSO). Herein we discuss the recrystallisation and discovery of a new, low density polymorph of **T2**, as well as a sulfur analogue and its crystal structure.

### *3.1 **T2**·$C_3H_9NO$·$C_3H_4O$*

*N.B Structural data for **T2**·DMAC.Acetone was collected by Dr Marc Little.*

**T2** was recrystallised through diffusion of acetone into a solution of **T2** in dimethylacetamide (DMAC), growing large, yellow and needle-shaped crystals. The crystal were fairly weakly diffracting, therefore synchotron radiation was used and a resolution limit set to 0.9 Å. The collection temperature was set to 240 K, as opposed to the typical collection temperature of 100 K. Data collection was attempted at 100 K however the diffraction was poor, when the temperature was increased it improved indicating a likely phase transaction to the crystalline framework observed.[79]

One hydrogen bonding motif was identified, $R_2^2(8)$, with bond angle 170.085° and length 2.821 Å (**Figure 24**). Evidence shows that the closer to 180° a hydrogen bond is, the shorter the bond length and therefore strengthening the hydrogen bond.[79] The new polymorph of **T2** was named **T2-**$\gamma$, with cooperative H-bonding forming the hexagonal crystal structure shown in **Figure 25**. The diameter of these pores were 19.9 Å, or 1.99 nm, placing it into the mesoporous category.

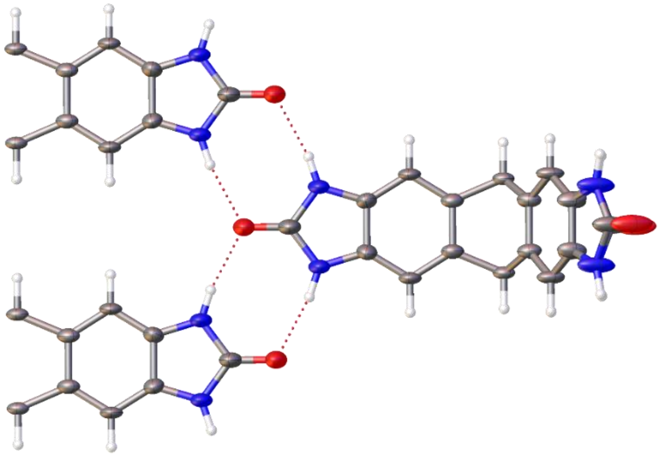

**Figure 24** $R_2^2(8)$ H-bonding in **T2** between three molecules of **T2**.

The structure shown in **Figure 26** is the solvated structure, with DMAC visible in the channels. No H-bonding was observed between **T2** and DMAC, showing a strong affinity for **T2** to form hydrogen bonds with itself.

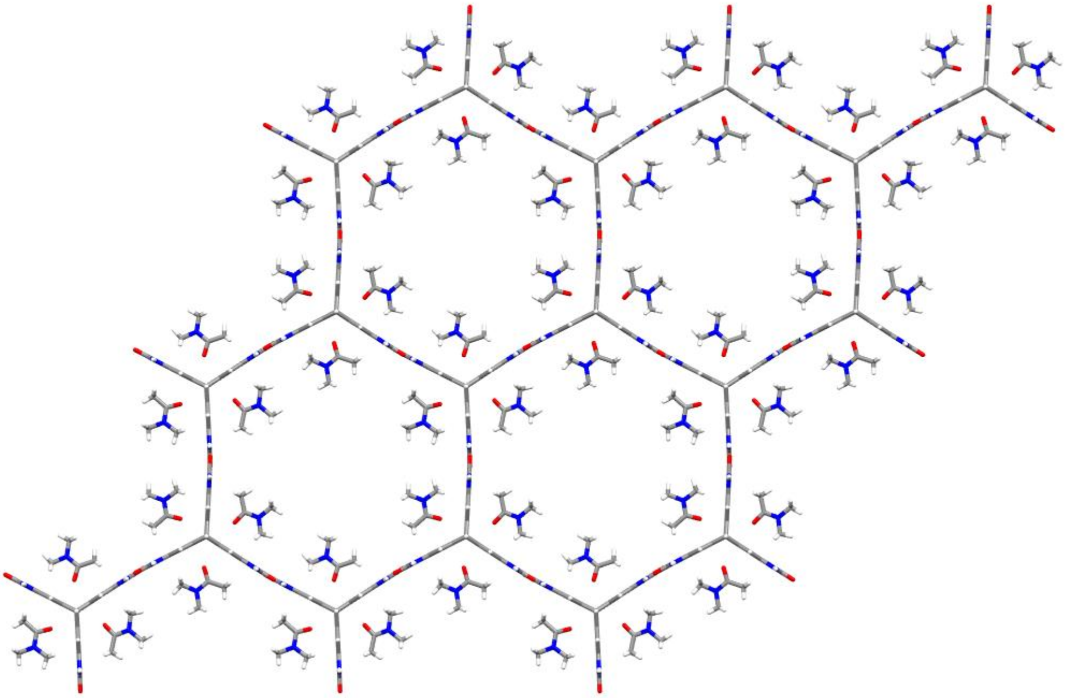

**Figure 25** **T2** when viewed along the c-axis showing large, hexagonal channels.

### *3.2 **T2**-S$\cdot C_3H_9NO\cdot C_3H_4O$*

Following on from the synthesis of **T2,** an alternative tecton with the alternative functional group imidazolidone-2-thiol was investigated. Despite sulfur being known for forming Hydrogen bonds, particularly in biological systems, the strength of these bonds is dependent upon whether the sulfur behaves as a donor or acceptor, with sulfur behaving as a donor typically increasing the strength of the bond.[80] S-H---S is a fairly weak hydrogen bond, with a strength of 4.18 kJ mol$^{-1}$, however the incorporation of a hetero atom, for example O-H---S, increases the strength to around -22.85 kJ mol$^{-1}$.[8182] Therefore, when incorporating a thiol functional group, it is assumed the structure would form strong cooperative H-bonding in the form of N-H---S.

**T2**-S was recrystallised by dissolving the material in DMAC to a concentration of 10 mgmL$^{-1}$, followed by diffusion of acetone into the solution. The crystallisations were left at room temperature for a few days, which eventually yielded a number of large, needle-shaped yellow crystals. The crystal structure was then collected, and 169 electrons were removed during the solvent mask algorithm, which was attributed to 2($C_3H_4O$) and 2 ($C_3H_9NO$). A displacement ellipsoid plot for **T2**-S.2($C_3H_9NO$).2($C_3H_4O$) is shown in **Figure 26**.

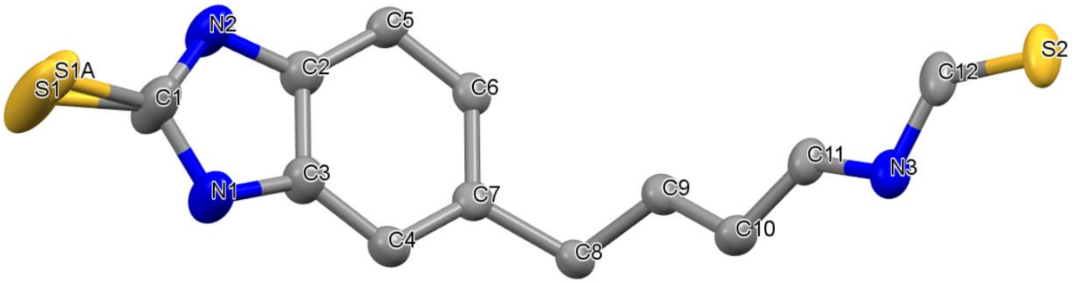

**Figure 26** Labelled displacement ellipsoid plot of **T2**-S.2($C_3H_9NO$).2($C_3H_4O$); ellipsoids displayed at 50% occupancy level. H-atoms have been omitted for clarity.

As anticipated, the H-bonding in **T2**-S was directed by the stronger N-H---S bonds, with an $R_2^2(8)$ motif. The **T2**S – **T2**S N-H---S interactions had bond angles of 170.48° of 3.41 Å for S1, and an angle of 171.44° and length 3.20 Å for S1A. There were also $R_4^2(12)$ C-H---S and N-H---S H-bonding, with weak C-H---S bonding, with part 1 having a bond angle of 135.73° and length 3.44 Å, and part 2 an angle of 145.29° and length 3.39 Å. The 'secondary' N-H---S interactions had the same angles and lengths as the $R_2^2(8)$ motif. N2 didn't have any involvement in H-bonding, shown in **Figure 27**.

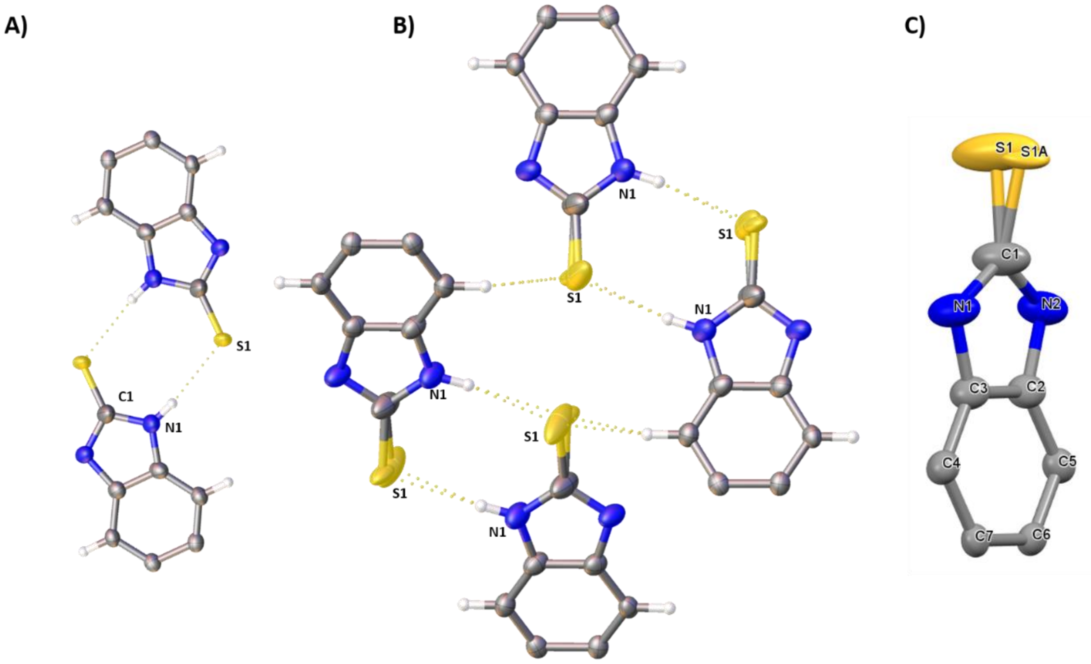

**Figure 27 A)** $R^{2}_{2}(8)$ motif between N1 and S1; **B)** $R^{2}_{4}(12)$ motif between N1, S1 and C1, showing both the N-H---S and C-H---S hydrogen bonds; **C)** Disordered S: S1 and S1A which were split across two positions.

Unlike **T2**-γ, **T2**-S did not form a hexagonal structure when recrystallised under the same conditions. **Figure 28** shows the crystal structure along the *a*, *b*-, and *c*-axes. The solvent was significantly disordered, therefore a solvent mask was applied during the refinement through Olex 2.[83] S1 was modelled across two positions due to structural disorder, with S1 at 66.6% occupancy, and S1A at 33.3% occupancy. Pores can be seen along the a-axis in **T2**-S, which had a distance of approximately 11.745 Å.

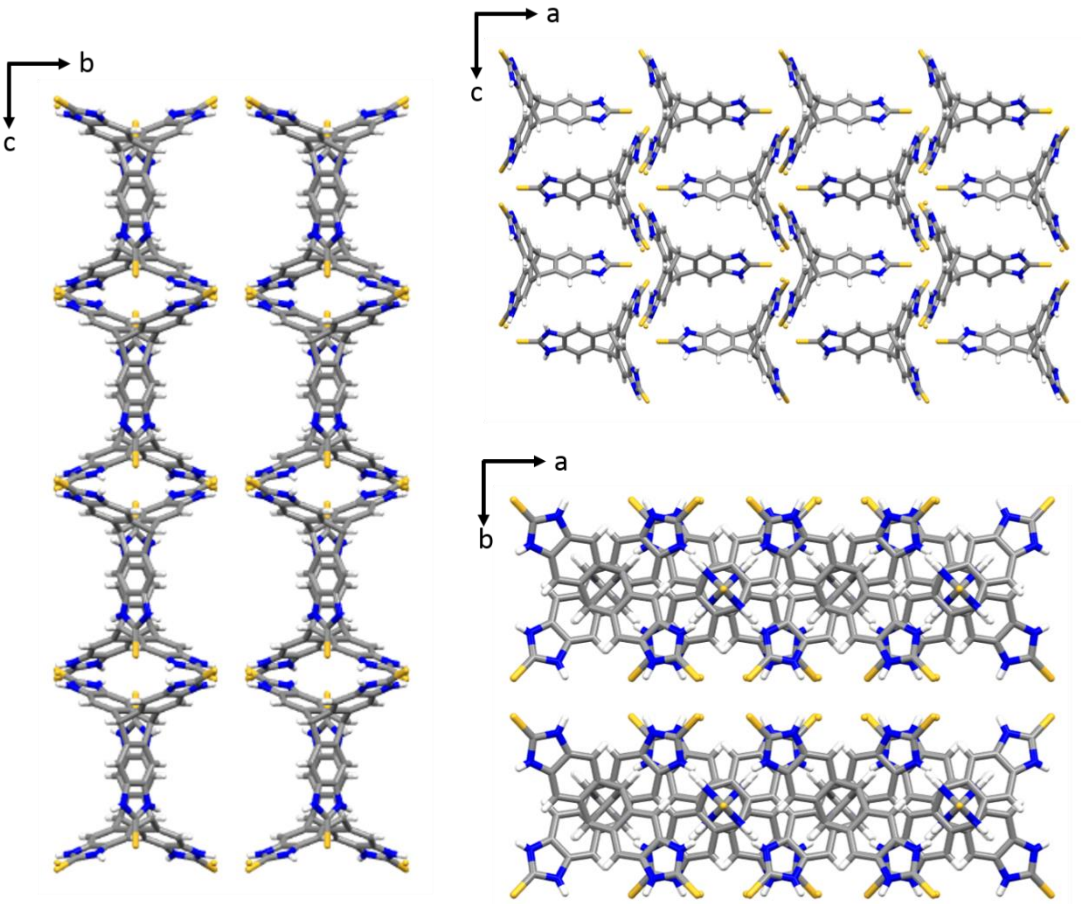

**Figure 28** Crystal packing of **T2**-S along the *a*-, *b*-, and *c*-axis, showing the close packed nature. Solvent was omitted from the figure to show the potential voids in **T2**-S.

**T2**-S crystallised with a fairly close packed structure, and when viewed along the *a*-axis there is evidence of potential for guest uptake in the voids. Connolly surfaces accessed through Mercury showed a potential solvent accessible void, with a probe radius of 1.55 Å, of 616.58 Å$^3$ (**Figure 29**). Neither *in situ* or *ex situ* experiments were performed on **T2**-S to determine if it was porous, however we have shown that under the same recrystallisation conditions the analogous structure did not exhibit the same hydrogen bonding as **T2**·DMAC, indicating that despite the ability of sulfur to H-bond, there is a significant change to the H-bonding motif, and hence the crystal packing.

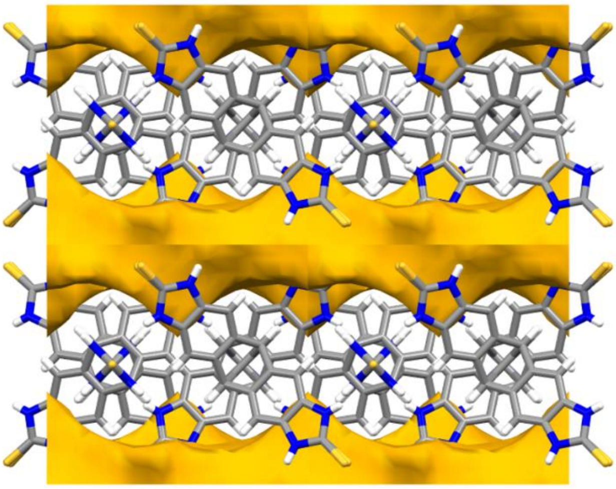

**Figure 29** Solvent accessible voids in **T2**-S, with a probe radius of 1.55 Å, equivalent to the VdW radii of $N_2$.

## *4 Comparing **T1** and **T2***

The ESFs for **T1** showed computationally the formation of a porous network wasn't likely to arise, as the resulting crystal structure would have been energetically unfavourable. Recrystallisations, TGA and DSC data demonstrated experimentally that **T1** does not form the same stable, porous framework as **T2**. In the original **T2** crystal structure from Mastalerz et al. there were two H-bonding regions in the crystal structure, further stabilising the framework. Comparatively, for **T1** for the channel structures, only one H-bonding region was identified, similarly to the more porous **T2** structure. **Table 2** and **Figures 30–32** illustrate in the hexagonal channel structure of **T2** that the hydrogen bonds are at 170°, whereas the closest angle to linear in **T1** was 165°.

**Table 2** H-bonding, comparing **T1** and **T2** from **Figures 30**, **31** and **32**.

| *D-H…* | *d(D-H) (Å)* | *d(H---A) (Å)* | *d(D---A) (Å)* | *<(DHA) (°)* |
|---|---|---|---|---|
| T1 N(1)-H(1)---O(2) | 0.88 | 2.47 | 3.119 | 130.7 |
| T1 N(2)-H(2)---N(2) | 0.88 | 1.98 | 2.838 | 165.8 |

| | | | | |
|---|---|---|---|---|
| T1 N(2)-H(2)---N(2) | 0.88 | 3.03 | 3.566 | 121.2 |
| T2 N(1)-H(1)---O(2) | 0.87 | 1.960 | 2.821 | 170.085 |

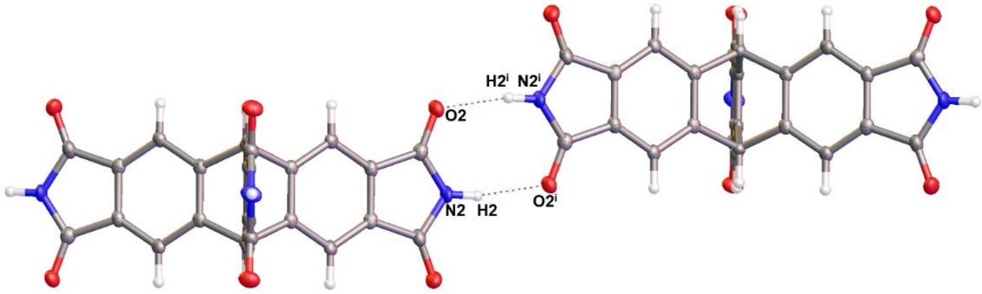

**Figure 30** H-bonding at 100 K, i: (3/2-X, 1-Y, +Z).

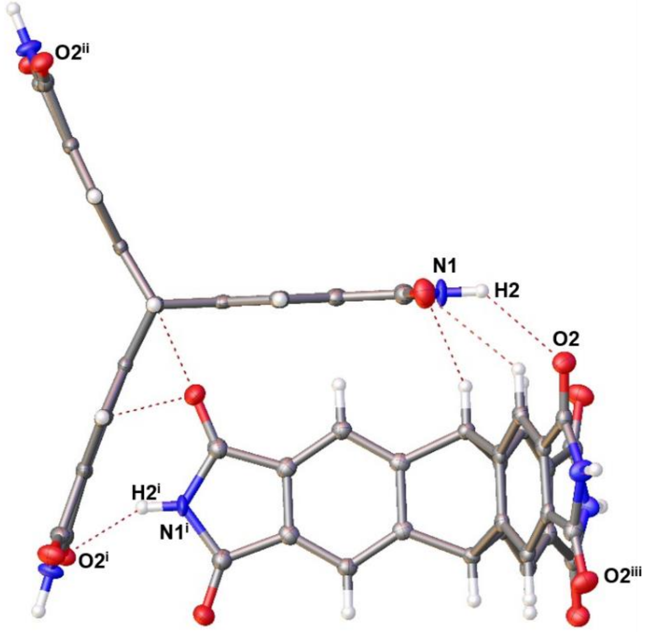

**Figure 31** H-bonding at 100 K which occurs in the corners of the channels of **T1**.Toluene. i: (5/2-X, ½+Y, ½-Z), ii: (5/2-X, 2-Y, -1+Z), iii: (1+X, 3/2-Y, 1/2-Z)

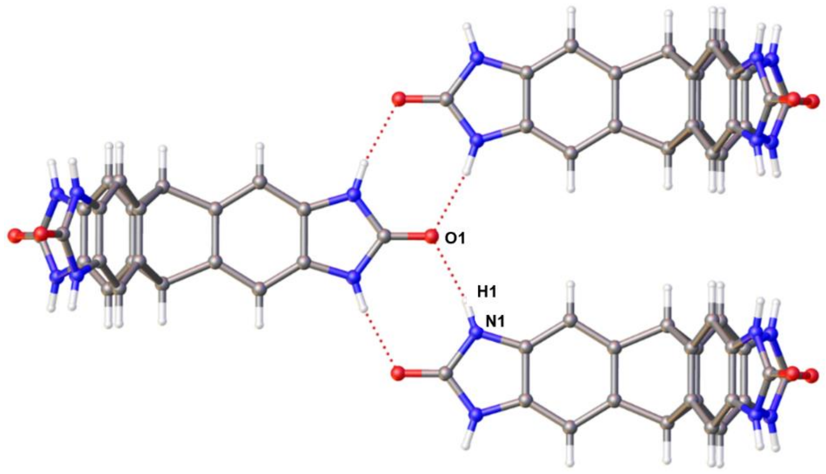

**Figure 32** H-bonding in **T2**. H1 (+X, +Y, ½-Z), N1 (+X, +Y, ½-Z), O1 (+Y, +X, -Z).

Evidence in literature shows that the strength of a hydrogen bond is dependent on both the distance and the bond angle.[84–86] The closer to 180 ° and shorter the bond, the stronger the bonding interaction. The H-bonding in **T2**-γ all have the same angle and length, 170° and 2.821 Å, respectively. Comparatively in **T1** there are three H-bonding environments, none of which are conducive to a strong H-bonding framework. This further rationalises the difficulty experienced obtaining a permanently porous framework, and further demonstrates the importance of bong length and angles in a hydrogen bonded material.

# *5 Porous Materials by High Throughput Screening*

## *5.1 High Throughput Screening for Porous Materials*

So far in this chapter, we focused on the development of HOFs through strategic design, taking advantage of both CSP and the rigidity of triptycene. In Chapter 3, we discussed the benefits of HT screening, from its application in the pharmaceutical industry, and the benefits in materials chemistry for the increased rate of functional molecule or material discovery.[87–91] In this section of we will discuss using commercially available amines, carboxylic acids and sulfonic acids in an attempt to generate new, porous materials through the means of either a salt or HOF.

For all the cages in Chapter 3, **T1** and **T2**, computational analyses were used to identify functional materials or molecules, and experimental work was performed to confirm the results.[1] In Chapter 3, there were multiple examples, including the bridged catenane structure, which was not computationally predicted.[91] This further highlighted the importance of experimental work, and furthermore experimental work alone can be responsible for serendipitous results.

Earlier in the chapter, HOFs were discussed in great detail, focusing in particular on their role as impressive microporous materials for both gas uptake and selective separations, for example $C_2H_4$ from $C_2H_6$.[92,1] Porous materials are reliant on the formation of cooperative, non-covalent interactions generating structures containing voids large enough for guest access. However, rational design of these materials can be time-consuming, computationally and experimentally expensive, and the end result may not yield the ideal results. Alternatively, high throughput screening with starting materials which are capable of either H-bonding, or forming an organic salt can increase the chances of finding porous materials capable of gas uptake.

### *5.1.1 Porous Salts*

Currently, there are limited examples of porous organic salts due to the challenge presented by the synthesis and design of such materials.[6,93,94] In 2018, Xing et al*.* developed a series of Crystalline Porous Organic Salts (CPOS) which exhibited the highest surface area and gas uptake of any CPOS to date.[95] **Table 3** shows the acids and bases used, with bulky tetrahedral sulfonic and carboxylic acids, and linear diamines. Their research showed that by using small molecules they were able to develop salts which co-crystallised forming clusters, generating voids throughout the crystal structure capable of guest access. The crystals grown formed helical 1D chains, with one CPOS exhibit $CO_2$ uptake of 40 $cm^3g^{-1}$.

**Table 3** Porous salt reagents used by Xing et al., showing the successful recrystallisations and their respective $SA_{BET}$.[95]

| |  | 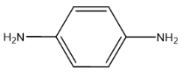 | 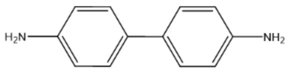 |
|---|---|---|---|
| 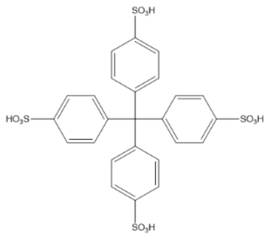 | Organic Salt<br>$SA_{BET} = 216\ m^2g^{-1}$ | Organic Salt<br>$SA_{BET} = 129\ m^2g^{-1}$ | Organic Salt<br>$SA_{BET} = 12\ m^2g^{-1}$ |
| 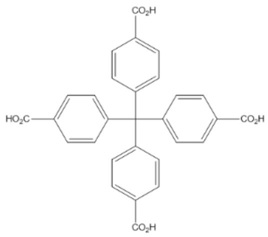 | Organic Salt<br>$SA_{BET} = 29\ m^2g^{-1}$ | No Salt Formed | No Salt Formed |

## 5.2 Method Development

Based on the structures synthesised by Xing et al.[95], as well as the HOFs discussed previously, a selection of sulfonic acids and amines were co-crystallised, as well as carboxylic acids and amines in an effort to synthesise organic salts and HOFs respectively. Detailed in **Figure 33** is the general workflow used for the study. Initially a combinatorial library was produced of commercially available materials, according to functionality, toxicity and precursor availability. Precursors were chosen based on their functional groups, carboxylic acids, sulfonic acids, and amines were chosen for their hydrogen bonding abilities or potential to form organic salts based on their compatible $pK_a$ values.

After generating a library of suitable tectons, a list of suitable solvent were identified, which could be used to solubilise the materials for the crystallisation screen. These solvents were chosen based on their miscibility and volatility; for effective co-crystallisation the two solutions required suitable miscibility, and as the methodology required evaporation of the solvent, relatively high volatility was necessary. For non-miscible solvents a layering technique was applied, and for miscible solvents the solutions were mixed together. In some cases, the layered crystallisations resulted in single crystal growth. The miscible mixtures were left to evaporate, leaving behind either microcrystalline or amorphous powders.

A bespoke high throughput infra-red imaging instrument (HTIR) was used to identify any potentially porous materials using $CO_2$ as the probe gas. This HTIR instrument works by measuring the temperature change (and hence the isosteric heat of adsorption) of the material when it is exposed to both vacuum and the probe gas and can be used to rapidly screen 96 samples.

Isosteric enthalpy of adsorption states that when an adsorbate is adsorbed onto a surface, heat is evolved.[96] The heat generated is an indication of the strength of interaction between the adsorbate and adsorbant.[97] Therefore, the higher the temperature change when the adsorbate is exposed, the stronger the interaction.[98] Isotherms can measure the amount of adsorbate capacity, whereas the heat generated upon adsorption indicates the strength of this interaction. Traditionally, the heat of adsorption could be measured by recording isotherms at different temperatures.[97] However, the bespoke HTIR kit uses an IR camera to measure the temperature of molecules when exposed to a probe gas, in this case $CO_2$. If a material is porous and adsorbs the probe gas the physical response on the HTIR kit is the sample will appear to glow, due to the increase in temperature with adsorption. $CO_2$ is the chosen probe gas due to measurements being conducted at room temperature.

Samples which underwent a significant temperature change (> 1 °C), they were then scaled up to scales of 200 mg and BET isotherms for both $CO_2$ and $N_2$ were performed. PXRD data was collected pre- and post-$CO_2$ exposure to assess any changes to the structure. This technique enabled assessment of any changes to the structure during $CO_2$ measurements.

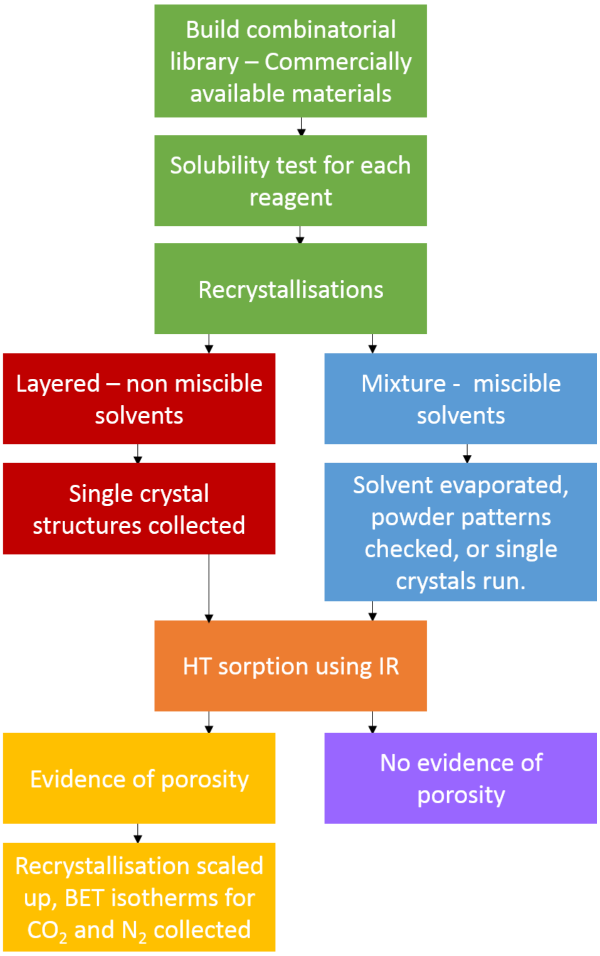

**Figure 33** General method for the discovery of new porous materials.

### *5.2.1 Co-Former Choices*

All the purchased materials used are shown in **Figures 34**, **35** and **36**, the corresponding letter for each material is below the structure. The labels were applied by 'order of use', and correspond with all data provided in *Materials and Methods*. A PXRD of **IO** would be a co-crystallisation of the disulfonic acid **SA-I**, and the triamine **AM-O**. The amines were co-crystallised with both the sulfonic acids and carboxylic acids.

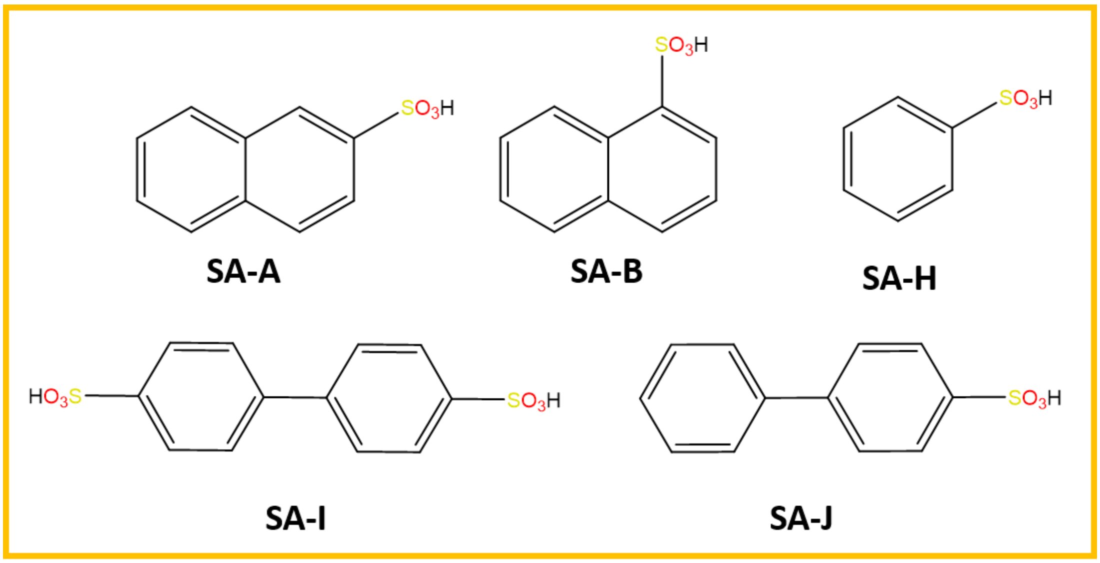

**Figure 34** Sulfonic acids **SA–A**, **SA–B**, **SA–H**, **SA-I** and **SA–J.**

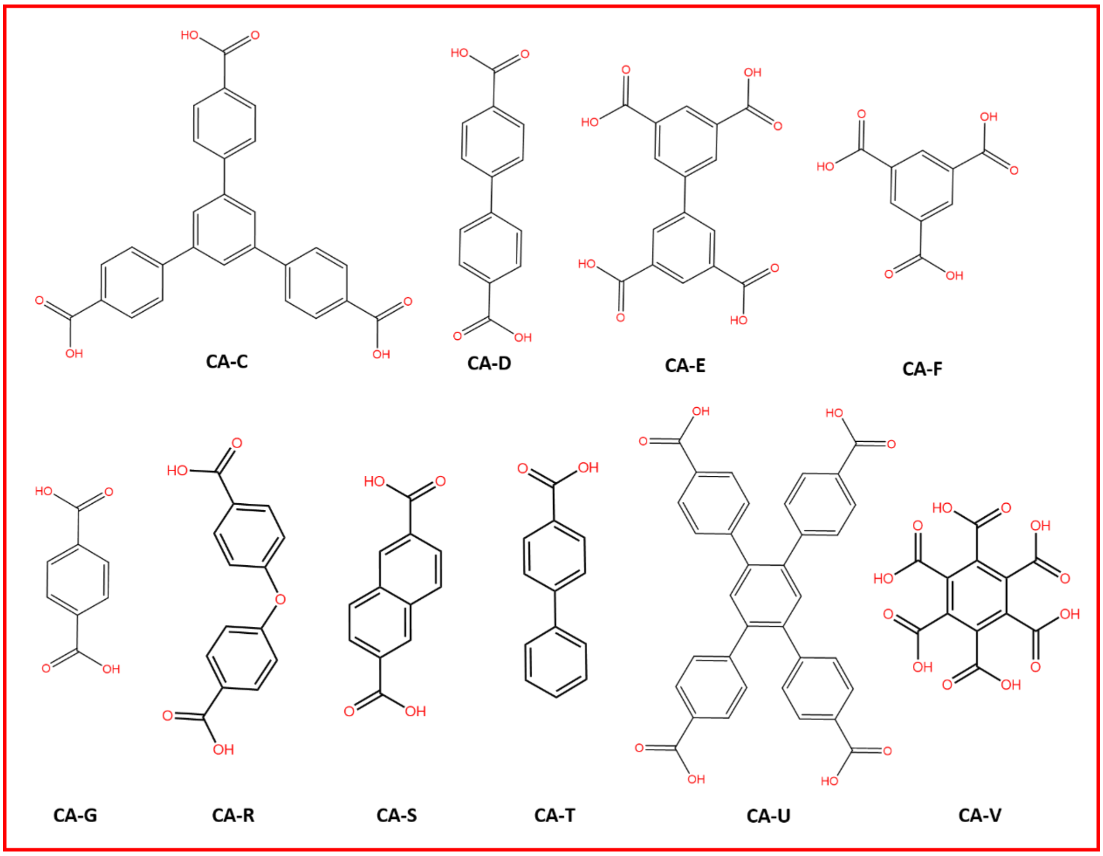

**Figure 35** Carboxylic acids **CA-C**, **CA-D**, **CA-E**, **CA-F**, **CA-G**, **CA-R**, **CA-S**, **CA-T**, **CA-U** and **CA-V**.

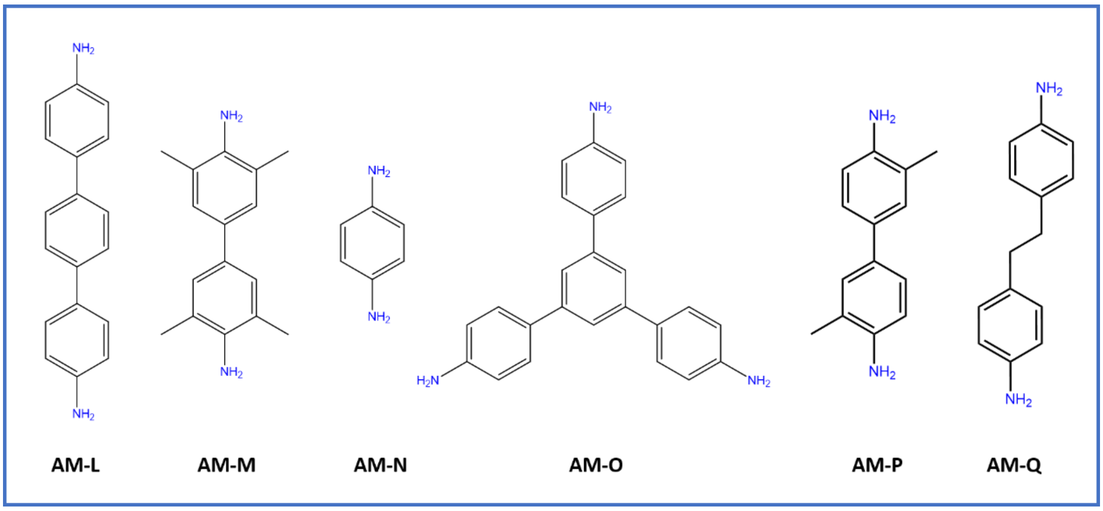

**Figure 36** Amines **AM-L**, **AM-M**, **AM-N**, **AM-O**, **AM-P** and **AM-Q**.

Crystallisations were set up using sulfonic acids **SA-H SA-I** and **SA-J**, and amines **AM-L**, **AM-M**, **AM-N** and **AM-O**. 7 solutions were prepared with a concentration of 5 mgmL$^{-1}$ of each co-formers, with the sulfonic acids dissolved in water, and the amines in ethyl acetate. The ethyl acetate solutions were layered onto the water and left for a period of 5 days at room temperature to grow crystals.

Single crystal structures were obtained for SA-J/AM-M and SA-J/AM-O from these crystallisations, which proved the formation of salts between the co-formers. Following on, the materials were then co-crystallised on a larger scale, incorporating all the co-formers and using a fast evaporation method. Solutions of the precursors in appropriate solvents were prepared at a concentration of 10 mg mL$^{-1}$, and the solutions mixed together. In some cases, this resulted in precipitation, however in others the mixtures remained solubilised.

## *5.3 HTIR: Comparing ΔT for Samples*

Earlier, HTIR was introduced as one of the most important steps in the methodology behind HT screening for porous materials. After all the materials were co-crystallised the remaining powder-like material was collected and placed into a 96-well plate, to record the powder patterns and then place directly onto the HTIR kit. The only potential issue from this method is the use of the proxiplates used for diffraction as theyproduce peaks in the background

(**Figure 37**). However, the results show that for crystalline materials, this doesn’t present any major issues, as the powder patterns are used for reference, and not taken forward for analysis or structural elucidation.

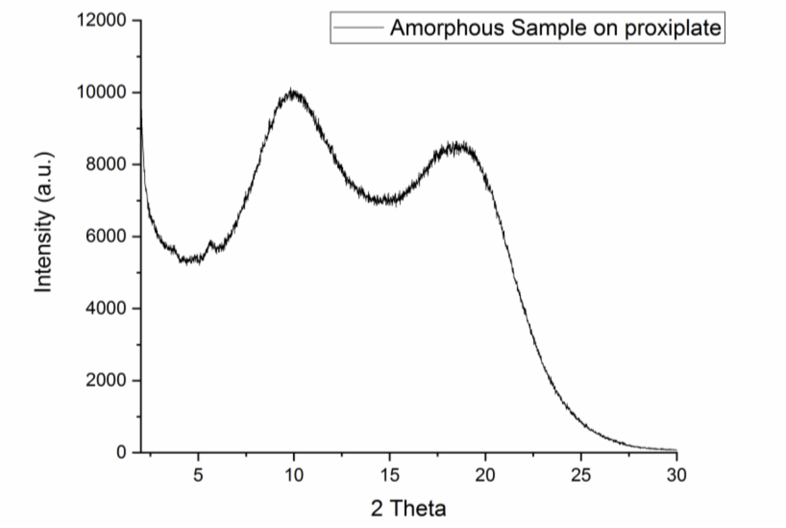

**Figure 37** Powder pattern collected on the proxiplate of an amorphous sample, showing the background peaks which result from the 96-well plate.

Prior to diffraction, the plates are placed in a vacuum oven at 60 °C to ensure any residual solvent is removed from the sample, as well as any water. Following this step, powder diffraction checks whether the samples are amorphous or crystalline. Amines are known for being particularly hygroscopic, therefore the samples on the plate are placed under vacuum for 24 hours on the HTIR kit. Samples which show evidence of gas uptake can be identified visually, as shown in **Figure 38**, as they appear to ‘light up’.

**Figure 38** The sample plate as seen on the HTIR kit, showing glowing samples which indicate uptake of $CO_2$.

A complete run on the HTIR takes around 10 minutes, with the aim of the experiment to collect a large number of results quickly, identify potential hits and run complete isotherms. The samples are identified visually, then after the data has been collected and the change in temperature calculated any hits are determined. **CC3** which has been discussed in other chapters was used as one of many test materials for the equipment and showed a ∆T of ~ 2.4 °C.

110 recrystallisations were set-up, including recrystallisation of the co-formers in the same solvent to identify any false hits. From those 110, 50 co-crystallisations showed a significant enough ∆T to indicate a potential hit, along with 5 co-formers. The data shows that 11 out of the 12 co-crystallisations involving co-former **Q** had a $\Delta T > 1.5$ °C, and for some > 6 °C. However, we can also see that when recrystallised on its own, it showed a ∆T close to 7 °C. The structure of **Q** does not look suitable to build a framework or other porous structure, and potentially the $CO_2$ is strongly binding to the amines, a common observation.[99]

**Figure 39** and **40** show the temperature responses of the co-crystals after exposure. The materials marked with an asterisk were the materials which were chosen to be scaled up for detailed adsorption measurements using both $N_2$ and $CO_2$ probe gases. Although a high number of the co-crystals showed promise as porous materials, the choice of which mixtures to carry forward was based on a number of factors: 1) if the co-former showed any potential of has uptake independently; 2) the solubility of the two co-formers when the solutions were mixed together; 3) collections of previous single crystal structure, allowing us to further understand the salt formation.

**Figure 39** shows the potential organic salts, which showed a response which would correspond to a strong interaction between the material and $CO_2$. It was observed that with nearly all the co-crystallisations, both carboxylic acids and sulfonic acids involving **AM-P** and **AM-Q** there was the same large ∆T. **AM-P** independently however did not show the same response, whereas **AM-Q** did. **Figure 40** shows the potential co-crystals of the amines with the carboxylic acids, with the same impressive results when using **AM-P** and **AM-Q**.

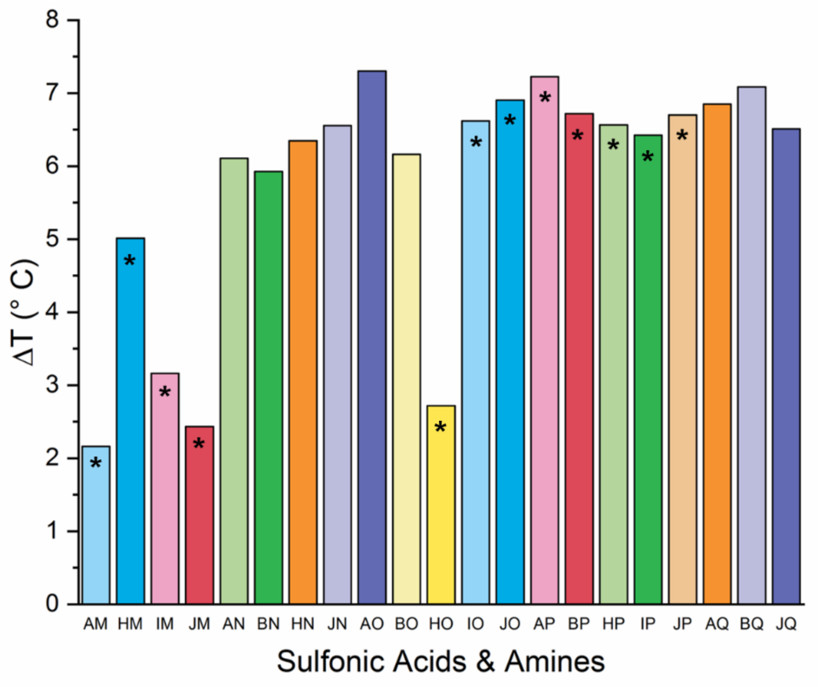

**Figure 39** Combine data for the SA and amine mixtures, showing ΔT after exposure to $CO_2$.

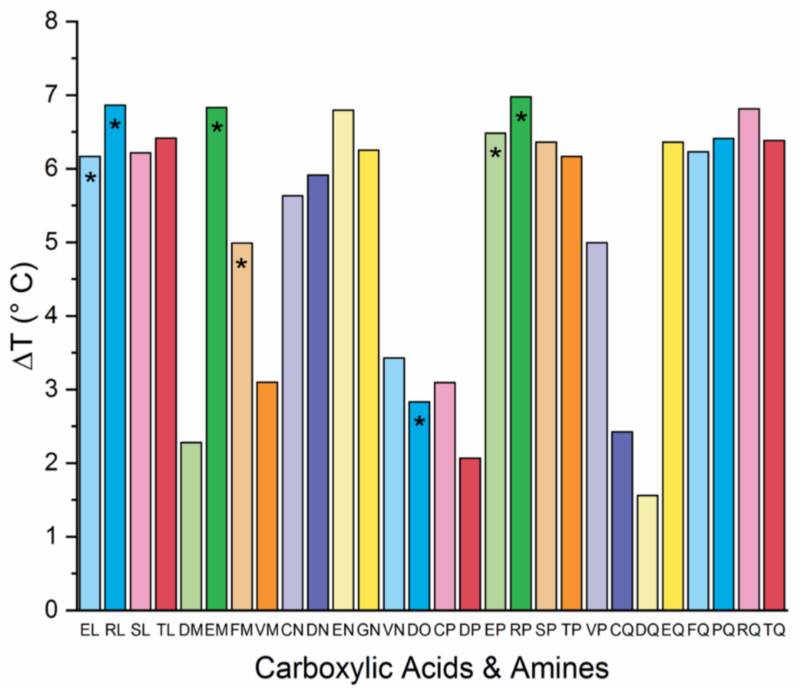

**Figure 40** Combined data for the CA and amine mixtures, showing ΔT after exposure to $CO_2$.

## 5.4 'Hit' Summary

Of the 17 materials which were scaled up for $N_2$ and $CO_2$ uptake measurements, 5 are discussed here in more detail as they either showed promise as porous materials, or a single crystal structure were obtained. **CA-R**/**AM-L**, **CA-E**/**AM-M**, **SA-J**/**AMO** and **SA-B**/**AM-P** all showed either a high $SA_{BET}$, or an impressive uptake of $CO_2$ (**Table 4**). **SA-J**/**AM-O** and **SA-J**/**AM-M** also had a single crystal structures, which provides more information with respect to structure-property relationships observed. The isotherms collected from the other chosen hits can be found in Chapter 5.

**Table 4** $SA_{BET}$ and $CO_2$ uptake for 5 selected co-crystals.

| *Precursors* | *$SA_{BET}$, $N_2$ ($m^2\ g^{-1}$)* | *$N_2$ Uptake (mmol $g^{-1}$)* | *$N_2$ Uptake ($cm^3\ g^{-1}$)* | *$CO_2$ Uptake (mmol $g^{-1}$)* | *$CO_2$ Uptake ($cm^3\ g^{-1}$)* |
|---|---|---|---|---|---|
| **CA-R**/**AM-L** | 40.69 | 1.30705 | 31.3692 | 0.08379 | 2.01 |
| **CA-E**/**AM-M** | 4.54 | 0.41524 | 9.96576 | 0.11791 | 24.70 |
| **CA-J**/**AM-M** | 3.36 | 0.14848 | 3.56352 | 0.08875 | 2.13 |
| **SA-J**/**AM-O** | 10.16 | 0.71338 | 17.12112 | 0.52693 | 12.65 |
| **SA-B/AM-P** | 73.49 | 1.77752 | 42.66048 | 0.10146 | 2.43 |

### 5.4.1 Co-crystal **CA-R/AM-L**

**CA-R/AM-L** was identified from the initial screen as being potentially porous, with a ΔT of 6.86197 °C. Single crystals of **CA-R/AM-L** did not grow, however the powder diffraction patterns implied that it was a semi-crystalline powder, with the pattern varying significantly from the starting materials. In **Figure 39**, the isotherm shows a linear trend, however at higher pressure the gas uptake of **CA-R/AM-L** increases.

If assuming that isotherm corresponds to BET adsorption, which assume a multi-layer coverage, the isotherm shape would imply a macroporous solid. However, this is highly unlikely, therefore the isotherm can be better described by a Langmuir-Freundlich adsorption, which assumes there is only mono-layer coverage.[100] A linear trend implies there is weak adsorption by the co-crystal **CA-R/AM-L**.

**CA-R/AM-L** showed a maximum gas uptake of 1.308 mmol $g^{-1}$ (31.37 $cm^3$ $g^{-1}$) $N_2$ at 1 bar, and the $SA_{BET}$ of **CA-R/AM-L** was determined to be 40.6941 $m^2g^{-1}$, although this is not as high as the SA of the CPOS by Xing et al., this still shows promise for the HT methodology. $CO_2$ uptake was low for **CA-R**/**AM-L**, implying that the material did show porosity, but the VdW radii for $CO_2$ is 2.32 Å at its widest, whereas $N_2$ is only 1.55 Å, leading to the conclusion that there are likely to be pores within the system, however these may be too small for $CO_2$ to access (**Figure 41**).

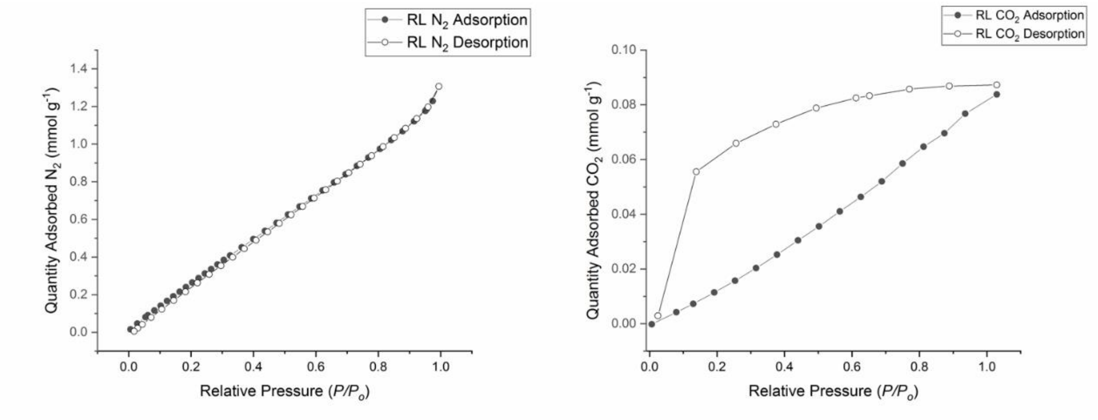

**Figure 41** Linear adsorption isotherm of $N_2$ for **CA-R/AM-L**, and the isotherm of $CO_2$.

**Figure 42** compares the powder patterns for the co-formers and potential co-crystal. It is evident there is a different, less crystalline phase formed with no resemblance to the co-formers **CA-R** and **AM-L**.

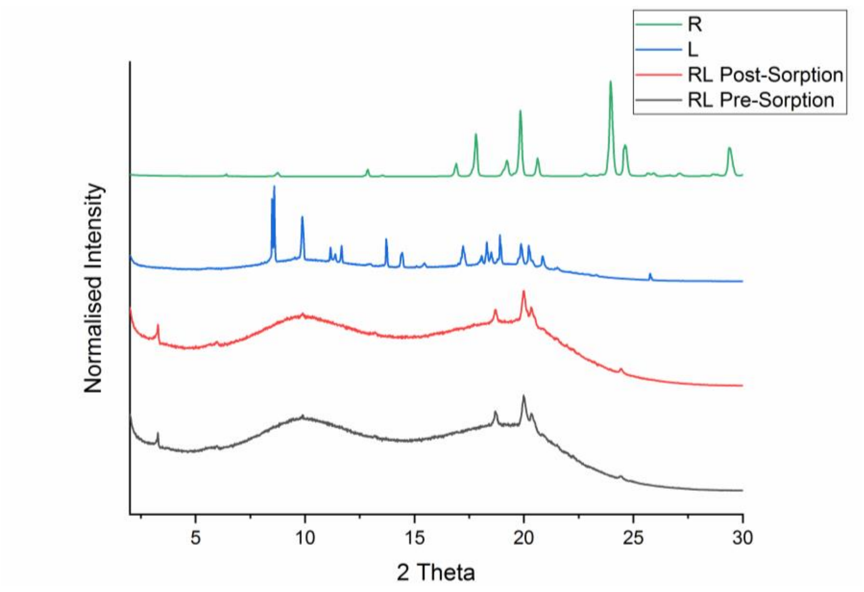

**Figure 42** Powder patterns of **CA-R/AM-L**, **CA-R** and **AM-L**.

### *5.4.2 Co-crystal* ***CA-E/AM-M***

**CA-E/AM-M** showed the best $CO_2$ uptake of all the materials which were measured, with a maximum uptake of 24.696 $cm^3g^{-1}$, despite the $SA_{BET}$ only measuring at 4.5391 $m^2g^{-1}$ (**Figure 43**). It is unlikely that the $CO_2$ uptake arises from pores in the structure, but rather interactions with the diamine **AM-M**.[101] Other materials have been shown to undergo improved $CO_2$ uptake when functionalised with amines. For example, Long et al. showed that incorporating *N*,*N'*-dimethylethylenediamine into a MOF resulted in increased $CO_2$ uptake, making it one of the best MOFs for $CO_2$ uptake and selectivity.[102] Amine scrubbing has been used since the 1930s for the effective separation of $CO_2$ from other natural gases and hydrogen.[103] This process uses amines to bind $CO_2$, and selectively remove them in low concentrations from a mixture of gases. This process of binding is the most likely explanation for the exceptional $CO_2$ uptake in **CA-E/AM-M**.

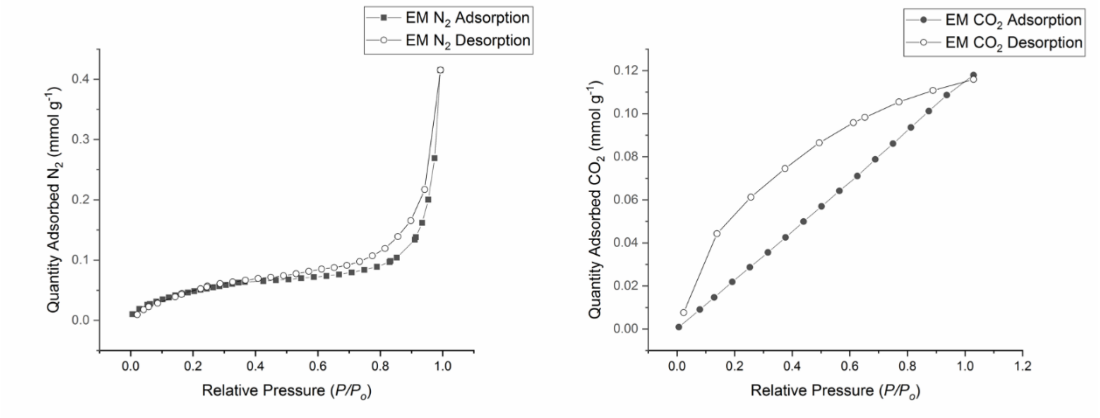

**Figure 43** Type II isotherm for $N_2$, showing a non-porous material, and the gas uptake for $CO_2$ in **CA-E/AM-M**.

**Figure 44** shows the powder patterns for **CA-E/AM-M** and its co-formers. The powder patterns shown for **CA-E/AM-M** both pre- and post-sorption are very similar to **AM-M**, implying there was no co-crystallisation between the two starting materials. The HTIR screen didn't show any potential for $CO_2$ uptake when testing using just **AM-M**, however we see impressive $CO_2$ uptake for **CA-E/AM-M**.

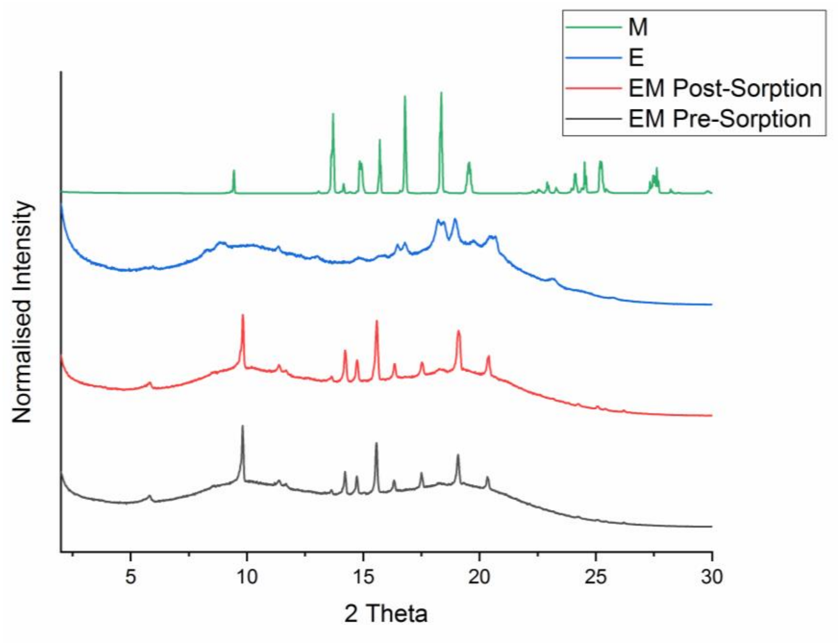

**Figure 44** Powder patterns for **CA-E/AM-M**, **CA-E** and **AM-M**, both pre- and post-sorption.

### *5.4.3 Co-crystal* ***SA-J/AM-M***

Co-crystals of **SA-J**/**AM-M** were grown through a layered crystallisation, with the crystallisation occurring at the interface between the two immiscible solvents, EtOAc for the diamine **AM-M**, and water for the sulfonic acid **SA-J**. The displacement ellipsoid plot is shown in **Figure 45**.

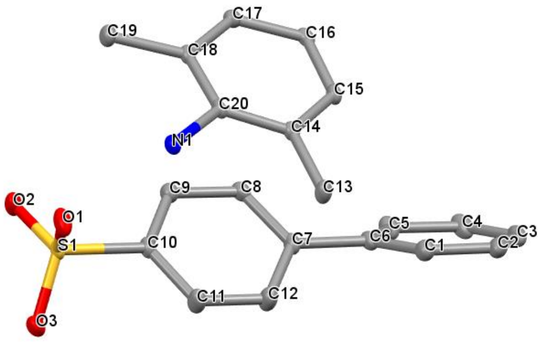

**Figure 45** Displacement ellipsoid plot for the asymmetric unit of **SA-J**/**AM-M**, ellipsoids shown at 50 % probability.

The co-crystals had a 2:1 ratio of the sulfonic acid:diamine. The crystals grew forming a close-packed crystal structure, with both the diamines forming an ammonium ion. Disordered solvent was found in the structure, which was bound to the sulfonic acid, however it was removed from the image in **Figure 46**.

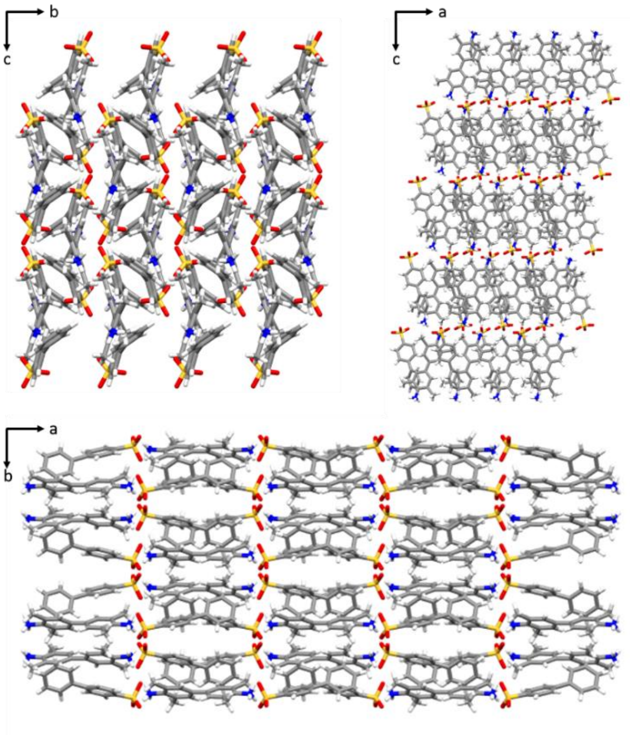

**Figure 46** Crystal packing along the *a*-, *b*- and *c*-axes, showing the close-packed crystal structure.

The isotherms shown in **Figure 47** shows that despite a $\Delta T$ of 2.43 °C, the structure was non-porous to either $N_2$ or $CO_2$. The $N_2$ type II isotherm is typical for either macroporous or non-porous materials.[104] The maximum uptake for $CO_2$ at 1 bar was 0.08875 mmol $g^{-1}$, which is particularly low.

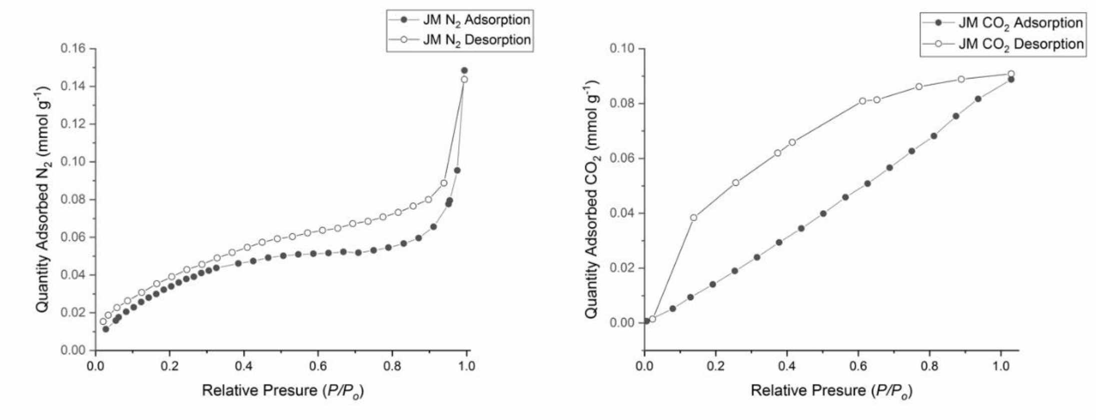

**Figure 47** $N_2$ isotherm for the gas uptake from 0 – 1 bar of **SA-J/AM-M**, showing no evidence of porosity.

Powder patterns, shown in **Figure 48**, were collected comparing the precursors, the co-crystals both pre- and post- sorption, and the simulated powder pattern from the single crystal structure. There seems to be good agreement between the simulated powder pattern and the diffraction after the HT sorption measurements, with a shift in the value of 2θ most likely corresponding to the solvent in the structure. The lack of any evidence of porosity, alongside the close packed structure implies the fast recrystallisation had the same results as single crystal growth, and is the same phase.

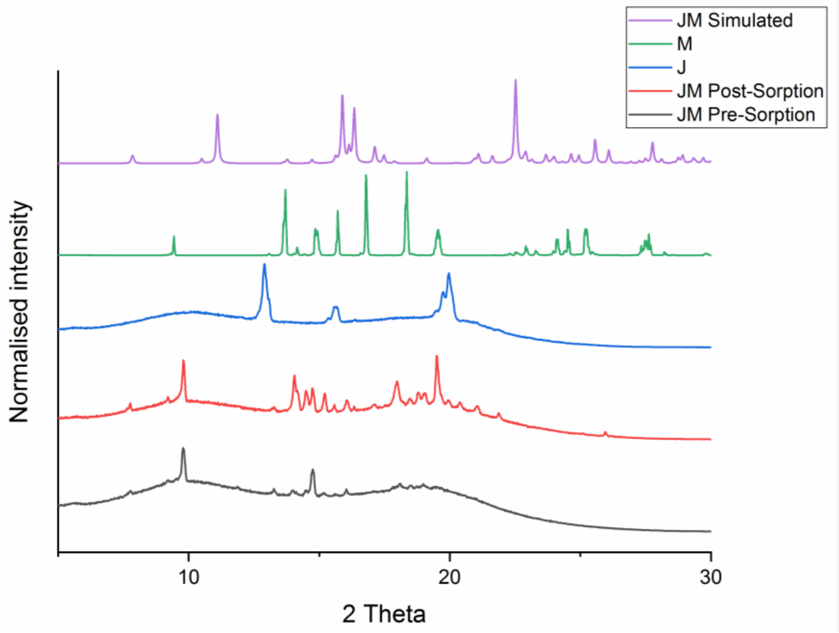

**Figure 48** Powder patterns for **SA-J**/**AM-M**, **SA-J** and **AM-M**, both pre- and post-sorption.

### *5.4.4 Co-crystal **SA-J/AM-O***

Co-crystals of **SA-J**/**AM-O** were grown through a layered recrystallisation, **SA-J** was dissolved in water, and the triamine **AM-O** in ethyl acetate. At the immiscible solvent interface, needle crystals were grew over a period of one week. The displacement ellipsoid plot is displayed in **Figure 49**. The disordered EtOAc was modelled using an EADP restraint, with a 50% occupancy for all except for O5 and O5A which were modelled with a 25% occupancy.

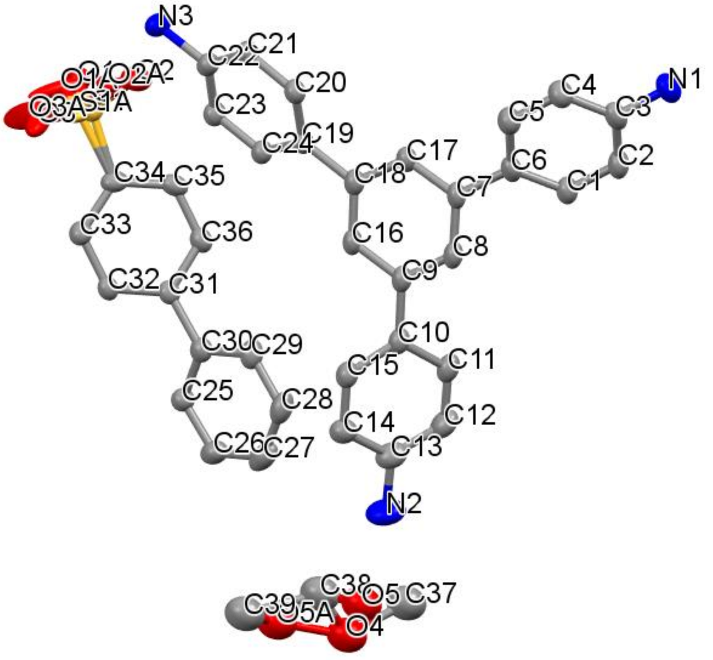

**Figure 49** Displacement ellipsoid plot of **SA-J/AM-O**, with disordered EtOAc. Ellipsoids displayed at 50% probability.

**Figure 50** shows the crystal packing of **SA-J/AM-O** along the *a*-, *b*- and *c*-axes, with the solvent removed from the figures. When viewed along the *c*-axis, the solvent occupied the void space and **SA-J/AM-O** had a $\Delta$T of 6.90 °C in the HTIR kit, implying the material was potentially porous. However, when recording complete isotherms the material was shown to in fact be non-porous. The sulfonic acid was disordered and modelled across two positions, with $SO_3$ split across two positions. S1 was modelled with 44.1% occupancy, and S1A 55.9%. The oxygen atoms were also disordered and modelled with varying occupancies, O1 65.7%, O2 80.9% and O3 49.3%.

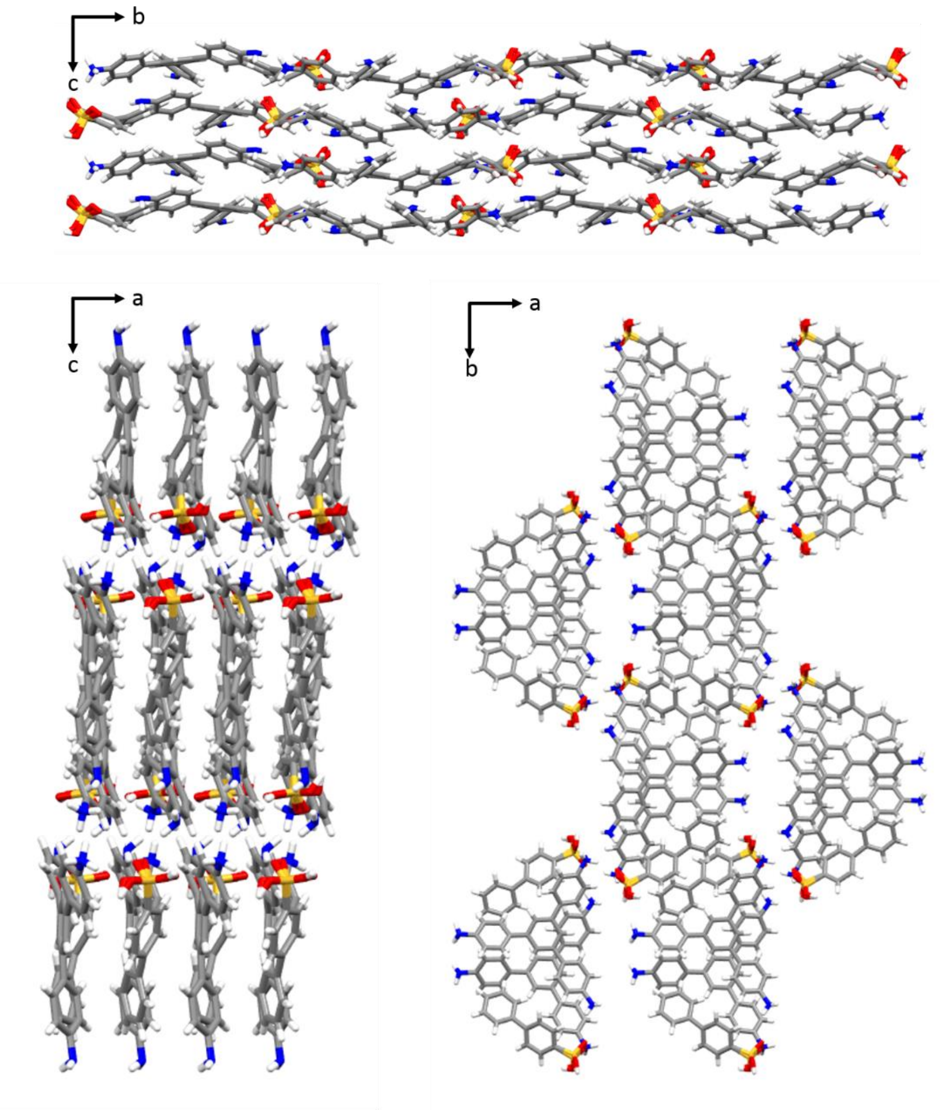

**Figure 50** Crystal packing of **SA-J/AM-O**, along the *a*-, *b*- and *c*-axes.

The crystal showed a salt had formed between the triamine and sulfonic acid, proven by the formation of an ammonium salts in one position of the triamine. Prior to all gas uptake measurements, the crystals were placed under vacuum for 24 hours, both at 50 °C and at room temperature, ensuring full removal of solvent from the void space. Despite the formation of the salt, the resulting structure was non-porous, with a type II isotherm for $N_2$ adsorption. The $CO_2$ uptake by **SA-J/AM-O** was 0.52693 mmolg$^{-1}$, which converts to 12.65 cm$^3$ g$^{-1}$ (**Figure 51**).

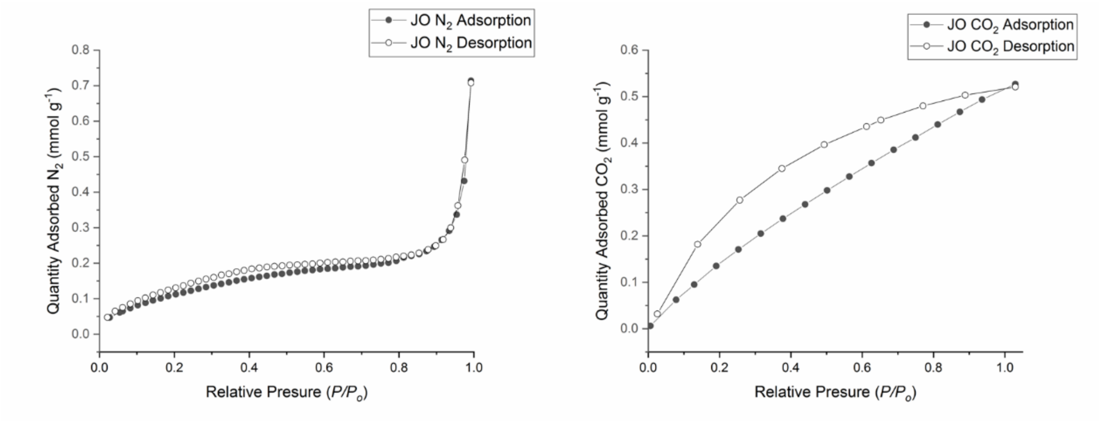

**Figure 51** Type II isotherm for **SA-J/AM-O**, showing limited $N_2$ uptake at 1 bar, and the $CO_2$ uptake for **SA-J/AM-O**.

The powder diffraction patterns shown in **Figure 52** compares the two co-formers, **SA-J** and **AM-O**, the co-crystal **SA-J/AM-O** post before and after HT sorption and the simulated powder pattern from the single crystal structure. Powder patterns for the co-crystals are slightly different to the simulated pattern, with a shift in 2θ which could correspond to the solvent in the structure. The co-crystals show some similarities, however don't appear to be highly crystalline. This difference could arise from either exposure to the higher temperatures in the vacuum oven, or the faster recrystallisation method being less effective.

The $SA_{BET}$ of **SA-J/AM-O** was only 10.16 $m^2g^{-1}$ using $N_2$ as the probe gas, however the $CO_2$ uptake was 12.65 $cm^3g^{-1}$, which is comparable to a [3+2] propeller cage synthesised by Zhang et al., which had a selective $CO_2$ uptake of ~ 9 $cm^3$ $g^{-1}$.[105] This cage however, had a diameter of 10.4 Å at it's largest and a higher $SA_{BET}$, therefore the $CO_2$ uptake could potentially also be a result of both the amine binding effect.

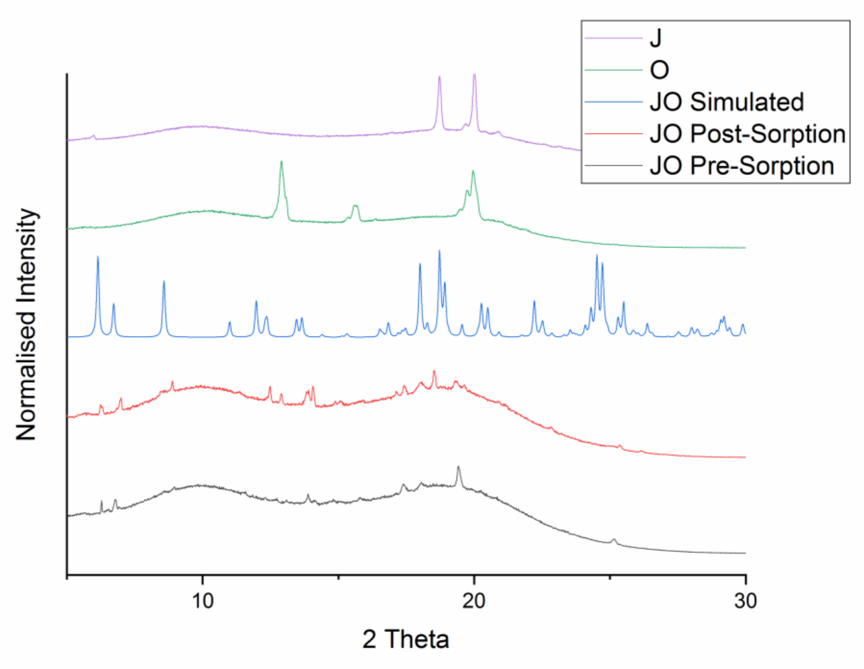

**Figure 52** Powder diffraction patterns for **SA-J**/**AM-O**, **SA-J** and **AM-O**, showing no change between the structure after HT sorption, and also indicating an alternative co-crystal has been obtained.

### *5.4.5 Co-crystal **SA-B/AM-P***

**SA-B**/**AM-P** was identified as a hit in the initial HT screening process, with a ∆T of 6.72 °C. This is a significant change in temperature, with **CC3**, a known porous material showing a ∆T of < 2.4 °C. Such a significant change in temperature could arise from two things, either a significant uptake of $CO_2$, or binding to the amines in **AM-P**. Powder patterns were assessed both prior to and following the HT gas sorption, which showed no change, implying if the structure has formed a porous network or framework this has been maintained after exposure to both vacuum and gas . Co-crystals were grown on a larger scale for effective gas adsorption, using both $CO_2$ and $N_2$ (**Figure 53**).

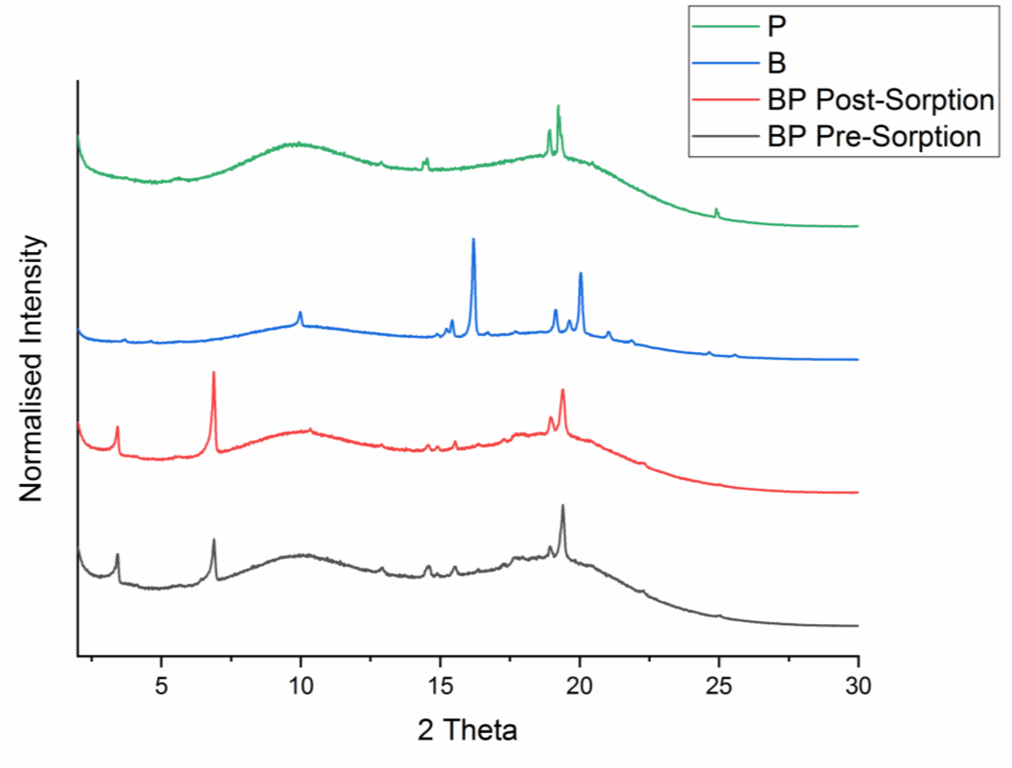

**Figure 53** Powder diffraction patterns for **SA-B**/**AM-P**, **SA-B** and **AM-P**, showing no structural change after gas sorption, and indicating the formation of a new material based on the starting materials.

The $SA_{BET}$ when using $N_2$ was found to be 73.49 $m^2g^{-1}$, and $N_2$ uptake of 1.78 $mmolg^{-1}$ (31.37 $cm^3$ $g^{-1}$). The isotherm for **SA-B**/**AM-P** was a Langmuir-type isotherm, whereby the isotherm has a linear correlation. The gas uptake continually increases with the uptake of $N_2$.This isotherm type is typical of a material where all sites have equal energy at all sorbent concentrations. Compared with the $N_2$ uptake, the $CO_2$ uptake was very low, only 2.44 $cm^3g^{-1}$, which shows selectivity for $N_2$, or pores which are not wide enough for the diffusion of $CO_2$ (**Figure 55**).

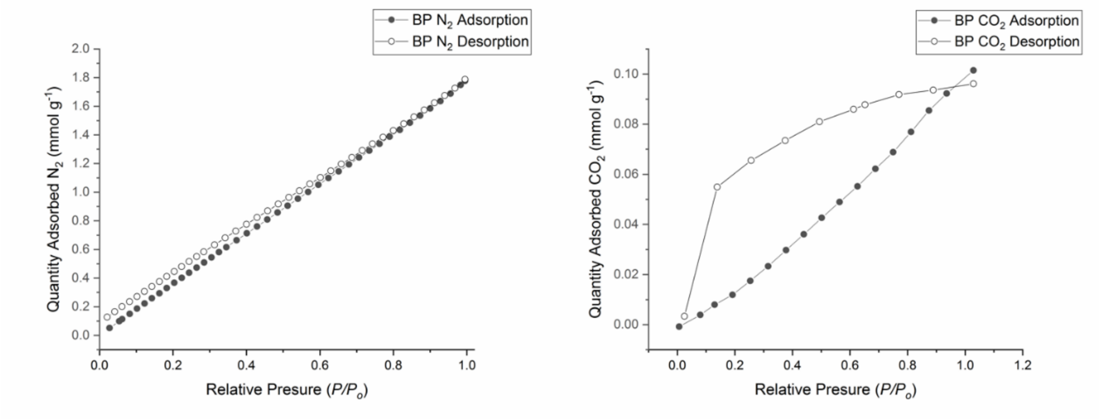

**Figure 55** Adsorption isotherms for $N_2$ and $CO_2$ sorption for **SA-B/AM-P**.

## 5.5 Starting Material Hits

We have discussed in detail the effect of amine scrubbing, i.e. the impact of $CO_2$ binding in the presence of amines. We have seen that certain co-formers were responsive to the HT $CO_2$ sorption, however the most responsive are shown in **Figure 56**. The fact these co-formers showed potential porosity meant some were excluded from being carried forward. Despite the low $SA_{BET}$ some of the co-crystals showed, there was impressive $CO_2$ uptake. This could be a result of this binding, however it is unlikely it was the amines alone responsible, otherwise this would have been identified earlier during the screening process.

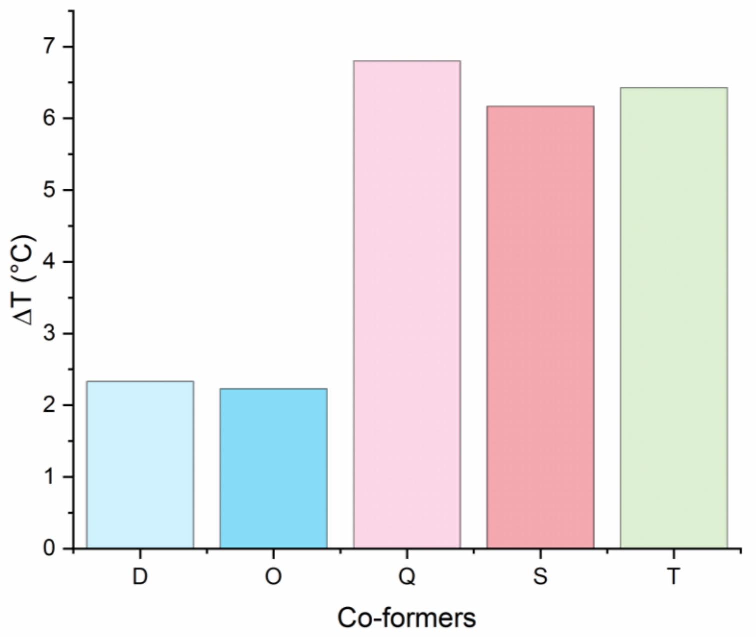

**Figure 56** Co-formers which responded to the HTIR measurements, prompting their exclusion from the co-crystals hits identified during screening.

Co-formers **CA-D**, **AM-O**, **AM-Q**, **CA-S** and **CA-T** showed a significant ΔT upon exposure to $CO_2$. The single crystal structure of **AM-O** showed channels throughout the structure, and is likely to behave as a porous material when recrystallised (**Figure 58**). The displacement ellipsoid plot is shown in **Figure 57**.

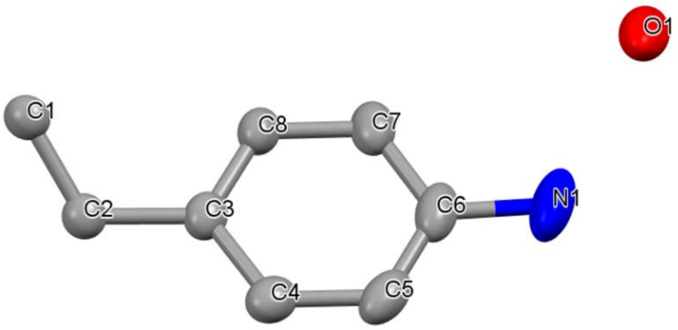

**Figure 57** The displacement ellipsoid plot for **AM-O**$\cdot$3($H_2O$), recrystallised from ethyl acetate. The hydrogens have been omitted for clarity, ellipsoid were displayed at 50 % probability.

**AM-O** showed hexagonal channels (**Figure 58**) throughout the crystal structure, with water hydrogen bonding to the amines. All materials were activated prior to measurements, through solvent removal in the vacuum oven at 60 °C, followed by the proxy-plate being left under vacuum again for another 24 hours to ensure full desolvation. No *in situ* experiments were attempted using SCXRD, however it is likely that the triamine **AM-O** is porous.

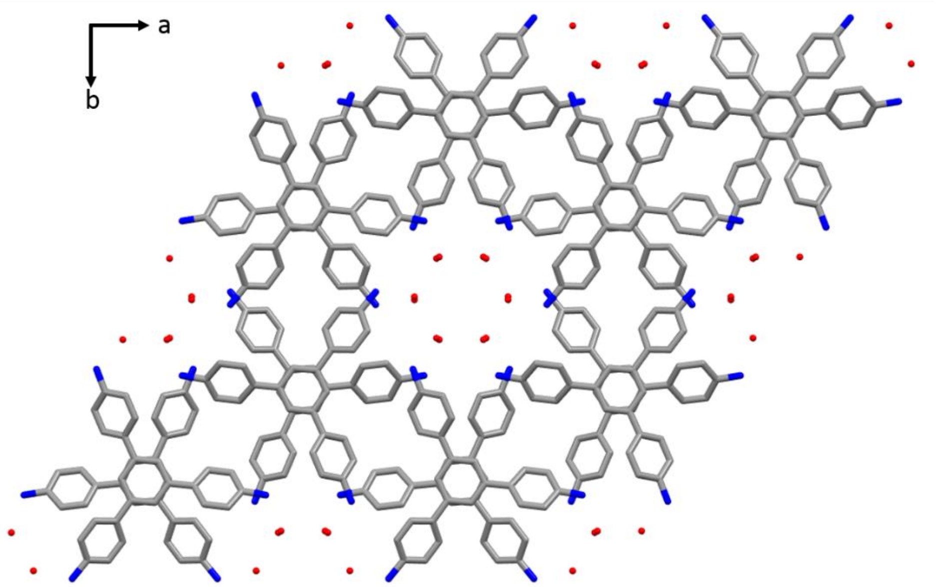

**Figure 58** Crystal packing from the single crystal structure of **AM-O**$\cdot 3(H_2O)$, viewed along the *c*-axis.

A crystal structure of **AM-Q** was not found, and none are currently present in the CCDC structural database, therefore the $CO_2$ uptake observed is most likely a result of the amine scrubbing, which was discussed in *section 5.4.2*.

# *6 Conclusions*

In this chapter we have approached the discovery of new porous materials in two very different ways, one by strategic design and utilising computational analyses, and the second approach by random ‘trial and error’ of commercially available materials.

**T1** had hydrogen bond directionality, as well as the well-known H-bonding motif $R_2^2(8)$, known to stabilise framework structures. This potential to form cooperative hydrogen bonding throughout the system should provide the potential for the formation of a microporous HOF. However, despite the framework forming the desired channels throughout the system we were unable to successfully desolvate the material. Multiple methods were attempted, none of which proved to provide a permanently porous HOF.

**T2** however showed incredible porosity, and had an incredibly low density of 0.417 gcm$^{-3}$ and was permanently porous, with the framework structure remaining stable with guest removal. This can be justified by the difference in the bond length and angles between **T1** and **T2**, when we veer closer to a linear hydrogen bond, the bond length decreases and henceforth increases the strength. Therefore, despite **T1** and **T2** showing the same, stable H-bonding motif, the bond lengths in **T2** were shorter and so provided a stronger framework material capable of guest removal and significant gas uptake.

The second, high throughput method took advantage of the HT equipment available to quickly determine the isosteric enthalpy of adsorption, and hence potential gas uptake in a series of co-crystallisations between sulfonic acids and carboxylic acids with amines. Using the 96-well plate increased the speed of collection for powder patterns both pre- and post-sorption of $CO_2$ in the high throughput method, as well as reducing collection time for initial scanning of potentially porous materials.

From the 110 co-crystallisations, 17 hits were carried forward which showed the largest $\Delta T$, and from those 2 co-crystals were identified as having a $SA_{BET}$ of a microporous material. Despite the gas uptake being much lower than other molecular materials, the method has shown that in less than one week we can effectively find porous materials through trial and error. However, despite the benefits of the HTIR kit, using $CO_2$ as a probe gas showed biased results due to the amines ability at binding $CO_2$. Despite this, two potentially porous materials were identified and furthermore shows the methodology can be used to identify porous co-crystals.

# 7 References

1 A. Pulido, L. Chen, T. Kaczorowski, D. Holden, M. A. Little, S. Y. Chong, B. J. Slater, D. P. McMahon, B. Bonillo, C. J. Stackhouse, A. Stephenson, C. M. Kane, R. Clowes, T. Hasell, A. I. Cooper and G. M. Day, *Nature*, 2017, **543**, 657–664.

2 J. Luo, J.-W. Wang, J.-H. Zhang, S. Lai and D.-C. Zhong, *CrystEngComm*, , DOI:10.1039/C8CE00655E.

3 Y.-F. Han, Y.-X. Yuan and H.-B. Wang, *Molecules*, 2017, **22**, 266.

4 X.-Z. Luo, X.-J. Jia, J.-H. Deng, J.-L. Zhong, H.-J. Liu, K.-J. Wang and D.-C. Zhong, *J. Am. Chem. Soc.*, 2013, **135**, 11684–11687.

5 Y. He, S. Xiang and B. Chen, *J. Am. Chem. Soc.*, 2011, **133**, 14570–14573.

6 A. Karmakar, R. Illathvalappil, B. Anothumakkool, A. Sen, P. Samanta, A. V. Desai, S. Kurungot and S. K. Ghosh, *Angew. Chemie Int. Ed.*, 2016, **55**, 10667–10671.

7 A. P. Côté, A. I. Benin, N. W. Ockwig, M. O'Keeffe, A. J. Matzger and O. M. Yaghi, *Science (80-. ).*, 2005, **310**, 1166–70.

8 Y.-B. Zhang, J. Su, H. Furukawa, Y. Yun, F. Gándara, A. Duong, X. Zou and O. M. Yaghi, *J. Am. Chem. Soc.*, 2013, **135**, 16336–16339.

9 D. Beaudoin, T. Maris and J. D. Wuest, *Nat. Chem.*, 2013, **5**, 830–834.

10 M. O'Keeffe, M. A. Peskov, S. J. Ramsden and O. M. Yaghi, *Acc. Chem. Res.*, 2008, **41**, 1782–1789.

11 Y. Liu, C. Hu, A. Comotti and M. D. Ward, *Science (80-. ).*, 2011, **333**, 436–440.

12 Y. He, S. Xiang and B. Chen, *J. Am. Chem. Soc.*, 2011, **133**, 14570–14573.

13 X.-Z. Luo, X.-J. Jia, J.-H. Deng, J.-L. Zhong, H.-J. Liu, K.-J. Wang and D.-C. Zhong, *J. Am. Chem. Soc.*, 2013, **135**, 11684–11687.

14 T.-H. Chen, I. Popov, W. Kaveevivitchai, Y.-C. Chuang, Y.-S. Chen, O. Daugulis, A. J. Jacobson and O. Š. Miljanić, *Nat. Commun.*, 2014, **5**, 5131.

15 H. J. Park, D.-W. Lim, W. S. Yang, T.-R. Oh and M. P. Suh, *Chem. - A Eur. J.*, 2011, **17**, 7251–7260.

16 J. W. Larson and T. B. McMahon, *Inorg. Chem.*, 1984, **23**, 2029–2033.

17 J. Emsley, *Chem. Soc. Rev.*, 1980, **9**, 91.

18 M. C. Etter, *Acc. Chem. Res.*, 1990, **23**, 120–126.

19 F. Meng, Y. Li, X. Liu, B. Li and L. Wang, *Cryst. Growth Des.*, 2015, **15**, 4518–4525.

20 Z. Mu, L. Shu, H. Fuchs, M. Mayor and L. Chi, *J. Am. Chem. Soc.*, 2008, **130**, 10840–10841.

21 Z. Wang, L. Wang, X. Zhang, J. Shen, S. Denzinger and H. Ringsdorf, *Macromol. Chem. Phys.*, 1997, **198**, 573–579.

22 G. R. Desiraju, *Angew. Chemie Int. Ed. English*, 1995, **34**, 2311–2327.

23 M. W. Hosseini, *Acc. Chem. Res.*, 2005, **38**, 313–323.

24 C. B. Aakeröy, P. D. Chopade, C. Ganser and J. Desper, *Chem. Commun.*, 2011, **47**, 4688.

25 C. B. Aakeröy, A. M. Beatty and B. A. Helfrich, *Angew. Chemie Int. Ed.*, 2001, **40**, 3240–3242.

26 G. R. Desiraju, *J. Am. Chem. Soc.*, 2013, **135**, 9952–9967.

27 J.-H. Fournier, T. Maris, J. D. Wuest, W. Guo and E. Galoppini, *J. Am. Chem. Soc.*, 2003, **125**, 1002–1006.

28 O. Lebel, T. Maris, M.-È. Perron, E. Demers and J. D. Wuest, *J. Am. Chem. Soc.*, 2006, **128**, 10372–10373.

29 Kobayashi, Shirasaka, Sato, Horn and Furukawa, *Angew. Chem. Int. Ed. Engl.*, 1999, **38**, 3483–3486.

30 K. Kobayashi, S. Azumi, S. Sakamoto and K. Yamaguchi, *J. Am. Chem. Soc.*, 2003, **125**, 3035–3045.

31 D. Venkataraman, S. Lee, J. Zhang and J. S. Moore, *Nature*, 1994, **371**, 591–593.

32 Philippe Brunet, 1 and Michel Simard and J. D. Wuest*, , DOI:10.1021/JA963905E.

33 Z. Guo, H. Wu, G. Srinivas, Y. Zhou, S. Xiang, Z. Chen, Y. Yang, W. Zhou, M. O'Keeffe and B. Chen, *Angew. Chemie Int. Ed.*, 2011, **50**, 3178–3181.

34 S. Xiang, W. Zhou, J. M. Gallegos, Y. Liu and B. Chen, *J. Am. Chem. Soc.*, 2009, **131**, 12415–12419.

35 S. J. Peighambardoust, S. Rowshanzamir and M. Amjadi, *Int. J. Hydrogen Energy*, 2010, **35**, 9349–9384.

36 M. Sadakiyo, T. Yamada, K. Honda, H. Matsui and H. Kitagawa, *J. Am. Chem. Soc.*, 2014, **136**, 7701–7707.

37 S. B. Tayade, S. S. Bhat, R. Illathvalappil, V. M. Dhavale, V. A. Kawade, A. S. Kumbhar, S. Kurungot and C. Näther, *CrystEngComm*, 2018, **20**, 1094–1100.

38 Q. Tang, Y. Liu, S. Liu, D. He, J. Miao, X. Wang, G. Yang, Z. Shi and Z. Zheng, *J. Am. Chem. Soc.*, 2014, **136**, 12444–12449.

39 M. Sadakiyo, T. Yamada, K. Honda, H. Matsui and H. Kitagawa, *J. Am. Chem. Soc.*, 2014, **136**, 7701–7707.

40 M. Mastalerz and I. M. Oppel, *Angew. Chemie Int. Ed.*, 2012, **51**, 5252–5255.

41 B. S. Ghanem, K. J. Msayib, N. B. McKeown, K. D. M. Harris, Z. Pan, P. M. Budd, A. Butler, J. Selbie, D. Book and A. Walton, *Chem. Commun.*, 2007, 67–69.

42 B. S. Ghanem, M. Hashem, K. D. M. Harris, K. J. Msayib, M. Xu, P. M. Budd, N. Chaukura, D. Book, S. Tedds, A. Walton and N. B. McKeown, *Macromolecules*, 2010, **43**, 5287–5294.

43 M. G. Rabbani, T. E. Reich, R. M. Kassab, K. T. Jackson and H. M. El-Kaderi, *Chem. Commun.*, 2012, **48**, 1141–1143.

44 J. H. Chong and M. J. MacLachlan, *Chem. Soc. Rev.*, 2009, **38**, 3301.

45 Z. Kahveci, T. Islamoglu, G. A. Shar, R. Ding and H. M. El-Kaderi, *CrystEngComm*, 2013, **15**, 1524–1527.

46 C. Zhang, P.-C. Zhu, L. Tan, J.-M. Liu, B. Tan, X.-L. Yang and H.-B. Xu, *Macromolecules*, 2015, **48**, 8509–8514.

47 M. G. Rabbani, T. E. Reich, R. M. Kassab, K. T. Jackson and H. M. El-Kaderi, *Chem. Commun.*, 2012, **48**, 1141–1143.

48 R. Bera, S. Mondal and N. Das, *Microporous Mesoporous Mater.*, 2018, **257**, 253–261.

49 R. G. D. Taylor, M. Carta, C. G. Bezzu, J. Walker, K. J. Msayib, B. M. Kariuki and N. B. McKeown, *Org. Lett.*, 2014, **16**, 1848–1851.

50 S. M. Elbert, F. Rominger and M. Mastalerz, *Chem. - A Eur. J.*, 2014, **20**, 16707–16720.

51 S. M. Woodley and R. Catlow, *Nat. Mater.*, 2008, **7**, 937–946.

52 S. L. Price, *Adv. Drug Deliv. Rev.*, 2004, **56**, 301–319.

53 M. A. Neumann, J. van de Streek, F. P. A. Fabbiani, P. Hidber and O. Grassmann, *Nat. Commun.*, 2015, **6**, 7793.

54 J. Nyman and S. M. Reutzel-Edens, *Faraday Discuss.*, , DOI:10.1039/C8FD00033F.

55 M. Vasileiadis, C. C. Pantelides and C. S. Adjiman, *Chem. Eng. Sci.*, 2015, **121**, 60–76.

56 C. Mellot-Draznieks, J. Dutour and G. Férey, *Angew. Chemie Int. Ed.*, 2004, **43**, 6290–6296.

57 B. Moulton and M. J. Zaworotko, *Chem. Rev.*, 2001, **101**, 1629–58.

58 *,‡ Gérard Férey, † Caroline Mellot-Draznieks, † and Christian Serre and F. Millange†, , DOI:10.1021/AR040163I.

59 M. A. Neumann, F. J. J. Leusen and J. Kendrick, *Angew. Chemie Int. Ed.*, 2008, **47**, 2427–2430.

60 † Panagiotis G. Karamertzanis, ‡ Parathy R. Anandamanoharan, ∥ Phillipe Fernandes, § Peter W. Cains, † Martin Vickers, † Derek A. Tocher, ∥ and Alastair J. Florence and † Sarah L. Price*, , DOI:10.1021/JP068530Q.

61 P. G. Karamertzanis, G. M. Day, G. W. A. Welch, J. Kendrick, F. J. J. Leusen, M. A. Neumann and S. L. Price, *J. Chem. Phys.*, 2008, **128**, 244708.

62 A. Gavezzotti, , DOI:10.1021/JP022288F.

63 D. H. Case, J. E. Campbell, P. J. Bygrave and G. M. Day, *J. Chem. Theory Comput.*, 2016, **12**, 910–924.

64 2012.

65 M. J. Frisch and G. W. Trucks, 2013.

66 S. Datta and D. J. W. Grant, *Nat. Rev. Drug Discov.*, 2004, **3**, 42–57.

67 D. W. Lewis, D. J. Willock, C. R. A. Catlow, J. M. Thomas and G. J. Hutchings, *Nature*, 1996, **382**, 604–606.

68 G. Ceder, Y.-M. Chiang, D. R. Sadoway, M. K. Aydinol, Y.-I. Jang and B. Huang, *Nature*, 1998, **392**, 694–696.

69 C. M. Simon, J. Kim, D. A. Gomez-Gualdron, J. S. Camp, Y. G. Chung, R. L. Martin, R. Mercado, M. W. Deem, D. Gunter, M. Haranczyk, D. S. Sholl, R. Q. Snurr and B. Smit, *Energy Environ. Sci.*, 2015, **8**, 1190–1199.

70 A. J. Cruz-Cabeza, S. M. Reutzel-Edens and J. Bernstein, *Chem. Soc. Rev.*, 2015, **44**, 8619–8635.

71 M. Eddaoudi, *Science (80-. ).*, 2002, **295**, 469–472.

72 A. F. Kapustinskii, *Q. Rev. Chem. Soc.*, 1956, **10**, 283.

73 M. Mastalerz and I. M. Oppel, *Angew. Chem. Int. Ed. Engl.*, 2012, **51**, 5252–5.

74 C. Zonta, O. De Lucchi, A. Linden and M. Lutz, *Molecules*, 2010, 226–232.

75 C. Zonta, O. De Lucchi, A. Linden and M. Lutz, *Molecules*, 2010, **15**, 226–32.

76 E. O. Pyzer-Knapp, H. P. G. Thompson, F. Schiffmann, K. E. Jelfs, S. Y. Chong, M. A. Little, A. I. Cooper and G. M. Day, *Chem. Sci.*, 2014, **5**, 2235.

77 M. A. Little, S. Y. Chong, M. Schmidtmann, T. Hasell and A. I. Cooper, *Chem. Commun.*, 2014, **50**, 9465–8.

78 L. Huang, Y. Shi, L. Chen, X. Jin, R. Liu, M. A. Winnik and D. Mitchell, *J. Polym. Sci. Part A Polym. Chem.*, 2000, **38**, 730–740.

79 T. Steiner, *Angew. Chem. Int. Ed.*, 2002, **41**, 49–76.

80 P. Zhou, F. Tian, F. Lv and Z. Shang, *Proteins Struct. Funct. Bioinforma.*, 2009, **76**, 151–163.

81 J. R. Sabin, *J. Am. Chem. Soc.*, 1971, **93**, 3613–3620.

82 J. R. Sabin, *J. Chem. Phys.*, 1971, **54**, 4675–4680.

83 O. V. Dolomanov, L. J. Bourhis, R. J. Gildea, J. A. K. Howard and H. Puschmann, *J. Appl. Crystallogr.*, 2009, **42**, 339–341.

84 G. R. Desiraju, *Acc. Chem. Res.*, 2002, **35**, 565–573.

85 A. Cavezzotti ' and C. Filippini, *J. Phys. Chem*, 1994, **98**, 4831–4837.

86 C. L. Perrin and J. B. Nielson, *Annu. Rev. Phys. Chem.*, 1997, **48**, 511–544.

87 T. L. Blundell, H. Jhoti and C. Abell, *Nat. Rev. Drug Discov.*, 2002, **1**, 45–54.

88 R. Banerjee, A. Phan, B. Wang, C. Knobler, H. Furukawa, M. O'Keeffe and O. M. Yaghi, *Science (80-. ).*, 2008, **319**, 939–43.

89 A. P. Watt, D. Morrison, K. L. Locker and D. C. Evans, *Anal. Chem.*, 2000, **72**, 979–984.

90 K. H. Bleicher, H.-J. Böhm, K. Müller and A. I. Alanine, *Nat. Rev. Drug Discov.*, 2003, **2**, 369–378.

91 R. L. Greenaway, V. Santolini, M. J. Bennison, B. M. Alston, C. J. Pugh, M. A. Little, M. Miklitz, E. G. B. Eden-Rump, R. Clowes, A. Shakil, H. J. Cuthbertson, H. Armstrong, M. E. Briggs, K. E. Jelfs and A. I. Cooper, *Nat. Commun.*, 2018, **9**, 2849.

92 Y. He, S. Xiang and B. Chen, *J. Am. Chem. Soc.*, 2011, **133**, 14570–14573.

93 M. Yoon, K. Suh, H. Kim, Y. Kim, N. Selvapalam and K. Kim, *Angew. Chemie Int. Ed.*, 2011, **50**, 7870–7873.

94 L. Jiménez-García, A. Kaltbeitzel, V. Enkelmann, J. S. Gutmann, M. Klapper and K. Müllen, *Adv. Funct. Mater.*, 2011, **21**, 2216–2224.

95 G. Xing, T. Yan, S. Das, T. Ben and S. Qiu, *Angew. Chemie Int. Ed.*, 2018, **57**, 5345–5349.

96 S. Sircar, R. Mohr, C. Ristic and M. B. Rao, *J. Phys. Chem. B*, 1999, **103**, 6539–6546.

97 S. Builes, S. I. Sandler and R. Xiong, *Langmuir*, 2013, **29**, 10416–10422.

98 W. Zhou, H. Wu and T. Yildirim, *J. Am. Chem. Soc.*, 2008, **130**, 15268–15269.

99 R. Vaidhyanathan, S. S. Iremonger, G. K. H. Shimizu, P. G. Boyd, S. Alavi and T. K. Woo, *Science (80-. ).*, 2010, **330**, 650–653.

100 I. Langmuir, *J. Am. Chem. Soc.*, 1918, **40**, 1361–1403.

101 R. Vaidhyanathan, S. S. Iremonger, G. K. H. Shimizu, P. G. Boyd, S. Alavi and T. K. Woo, *Science (80-. ).*, 2010, **330**, 650–653.

102 T. M. McDonald, D. M. D'Alessandro, R. Krishna and J. R. Long, *Chem. Sci.*, 2011, **2**, 2022.

103 G. Nonhebel, *Trans. Faraday Soc.*, 1936, **32**, 1291.

104 Z. ALOthman, ALOthman and Z. A., *Materials (Basel).*, 2012, **5**, 2874–2902.

105 Y. Jin, B. A. Voss, R. D. Noble and W. Zhang, *Angew. Chemie Int. Ed.*, 2010, **49**, 6348–6351.

# Chapter 5

## Materials and Methods

# 1 General Synthetic and Analytical Methods

**1.1 Materials:** Chemicals were purchased from TCI UK, Fluorochem, or Sigma-Aldrich and used as received. Solvents were reagent or HPLC grade and purchased from Fisher Scientific. All chemicals and solvents were used as received unless specified.

**1.2 Synthesis:** All reactions requiring anhydrous or inert conditions were performed in oven-dried apparatus under an atmosphere of dry nitrogen, anhydrous solvents were introduced into the flask via a cannula. All reactions were stirred magnetically using Teflon-coated stirring bars. Where heating was required, the reactions were warmed using a stirrer hotplate with heating blocks with the stated temperature being measured externally to the reaction flask using an attached probe. Removal of solvents was done using a rotary evaporator.

**1.3 Single Crystal X-Ray Diffraction (SCXRD):** SC-XRD was measured on a Rigaku MicroMax-007 HF rotating anode diffractometer (Mo-Kα radiation, λ = 0.71073 Å, Kappa 4-circle goniometer, Rigaku Saturn724+ detector. Rigaku frames were converted to Bruker compatible frames using the programme ECLIPSE.[241] Empirical absorption corrections, using the multi-scan method, were performed with the program SADABS.[242] The crystal structure was solved with SHELXD,[1] and refined by full-matrix least squares on $|F|^2$ by SHELXL,[243] interfaced through the programme OLEX2[244]; Some structures reported were collected at beamline I19, Diamond Light Source, Didcot, UK using silicon double crystal monochromated synchrotron radiation (λ = 0.6889 Å, Rigaku Saturn724+).

A supplementary CIF, that includes structure factors and responses to checkCIF alerts, is available free of charge from the Cambridge Crystallographic Data Centre (CCDC) via www.ccdc.cam.ac.uk/data_request/cif.

**1.4 Analytical High Performance Liquid Chromatography (HPLC):** HPLC data was obtained using a Dionex UltiMate 3000 system. The column used for the analysis of OMCs was a Thermo Scientific Syncronis C8, 150 x 4.6 mm, 3 μm (97203-154630, 12475). The mobile phase was isocratic methanol at a flow rate of 1 mL/min. The column oven temperature was set to 30 °C. Detection for HPLC analysis was conducted at 254 nm.

**1.5 Thermogravimetric Analysis (TGA):** TGA analysis measures the loss of mass over time with temperature changes. The method can provide information on phase transitions, absorption, desorption as well as thermal decomposition.[245] TGA analysis was carried out using a TA Q5000IR analyser with an automated vertical overhead thermobalance. Samples were heated at a rate of 10 °C/min unless otherwise stated.

**1.6 Differential Scanning Calorimetry (DSC):** DSC is commonly used to determine the change in temperature of a sample when undergoing a phase transition, determining whether a process in endo- or exothermic.[246] This is particularly useful when studying crystalline materials which exhibit polymorphism, allowing us to determine temperature at which a transformation occurs. DSC measurements were conducted on a TA Q2000 (instrument with a Refrigerated Cooling System 90 and an autosampler) at 10 °C/min under an $N_2$ atmosphere.

**1.7 High-Resolution Liquid Chromatography Mass Spectrometry (HR-LCMS):** High resolution LCMS was carried out using an Agilent Technologies 6530B system using a Thermo-Scientific Syncronis C8 column, 100 x 3 mm, 1.7 μm (SN 0714448X7, Lot 11232), with mass detection using an accurate-mass QTOF Dual ESI mass spectrometer (capillary voltage 4000 V, fragmentor 225 V) in positive-ion detection mode. The mobile phase was isocratic MeOH containing 0.1% formic acid at a flow rate of 0.25 mL/min for a 10 minute run time.

**1.8 NMR Spectra:** Solution $^1$H and spectra were recorded at 400.13 MHz and 100.6 MHz respectively using a Bruker Avance 400 NMR or a Bruker DRX500 (500 MHz) spectrometer. Chemical shifts are reported in ppm ($\delta$) with reference to the internal residual protonated species of the deuterated solvent used for $^1$H and $^{13}$C analysis.

**1.9 Langmuir Surface Area:** $SA_{Langmuir}$ assumes that adsorbates follow the laws of ideal gases at isothermal conditions, the theory first proposed by Irving Langmuir in 1918.[247] The main assumptions of the model are that;[248]

1) The surface is homogeneous, i.e. no corrugations or defects.
2) The gas adsorps into an immobile state.
3) All the sites on the surfaces are equivalent.
4) Mono-layer coverage, i.e. each site holds one molecule at most.
5) Adjacent adsorbate molecules have no interactions.

**1.10 Brunauer-Emmett-Teller Surface Area:** BET theory explains the adsorption of gas onto a surface, the theory, derived in 1938, makes the assumption that the adsorption occurs in a random distribution of multiple layers. The general theory states that sites can be occupied by multiple adsorbates.[249] There are five major assumptions made in BET theory;[250]

1) Adsorption can only take place on a well-defined site, i.e. one per molecule
2) Only one molecular interaction is considered; a molecule acts as single adsorption site
3) The top layered molecule is in equilibrium with the gas phase
4) Desorption is a kinetically-limited process, therefore heat of adsorption must be available.
5) When at saturation pressure, the molecule layer tends to infinity.

This method is most commonly applied when using a gas such as $N_2$, therefore the method is typically conducted at its boiling point of 77 K.

# 2 Synthesis

## 2.1 Chapter 2

### 2.1.1 5,5'-(Ethyne-1,2-diyl)diisophthalaldehyde

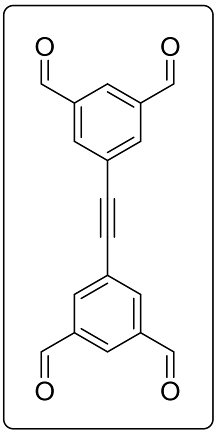

A modification of the procedure of Slater *et al*. was used for this reaction.[2] To an oven dried rbf, equipped with stirrer bar, was added 5-bromoisophthaladehyde (8.49 g, 39.87 mmol, 2.1 eq.) and the flask evacuated and backfilled with $N_2$ (x3) before the addition of anhydrous 1,4-dioxane (200 mL). The solution was degassed ($N_2$ bubbling, 30 min) before the addition of bis(tri-*n*-butylstannyl)acetylene (10 mL, 18.98 mmol, 1.0 eq.) and $Pd(PPh_3)_4$ (1.1 g, 0.95 mmol, 0.05 eq.). The resulting solution was heated at 100 °C for 18 hours under $N_2$ before being allowed to cool to room temperature and filtered through Whatman glass microfiber filter paper. To the filtrate was added water (300 mL), and the product extracted with $CHCl_3$ (2 x 500 mL). To the combined organic layer was added hexane (500 mL) and the resulting precipitate collected by filtration, washed with hexane (200 mL) and dried *in-vacuo* to afford the desired product which was used without further purification (4.25 g, 14.64 mmol, 77%).

**$^1$H NMR** (400.13 MHz, $CDCl_3$) $\delta_H$ 10.14 (4H, s), 8.39 (2H, t, *J* = 1.3 Hz), 8.31 (4H, d, *J* = 1.4 Hz). Data in accordance with literature values.[2]

### 2.1.2 **TCC1**$_{[3+6]}$[2]

To a stirred suspension of 5,5'-(ethyne-1,2-diyl)diisophthalaldehyde (2.0 g, 5.84 mmol) and trifluoroacetic acid (TFA) (5 drops) in DCM (20 mL) was added a solution of *R*,*R*-(-)-(1,2)-cyclohexanediamine (1.34 g, 11.7 mmol) in DCM (28 mL). The mixture was stirred overnight at room temperature, during which time the solution turned yellow and the tetraaldehyde compound was observed to dissolve. After 5 days the reaction mixture was diluted with DCM and the mixture was filtered to remove any insoluble bi-products. The filtrate was concentrated to ~20 mL at 25 °C under recued pressure, hexane (20 mL) was charged with stirring and the resulting white precipitate was collected via vacuum filtration to yield pure product (2.54 g, 0.7464 mmol, 87%).

1H NMR (400.13 MHz, CDCl3) δ 8.19 (s, 6 H), 8.13 (s, 6 H), 7.90 (s, 6 H), 7.83 (s, 6 H), 7.36 (s, 6 H), 3.45 - 3.53 (m, 6 H), 3.22 - 3.32 (m, 6 H), 1.96 - 1.58 (m, 48 H). MS(MALDI-TOF)$^+$: calculated for C90H91N12 [M+H]$^+$: 1339.7490; found: 1340 (M+H)$^+$; MS(ESI, TCC1-R)$^+$: calculated for C90H91N12 [M+H]$^+$: 1339.7490; found: 1339.7460, 670.3790 [M+2H]$^{2+}$

Data agrees with literature values.

### *2.1.3* ***TCC1**$_{[6+12]}$*

The following method generated a ratio of 7:1 large cage:small cage (by % a/a, HPLC, 254 nm), based on a modification of the already published method.[2]

A solution of 5,5'-(ethyne-1,2-diyl)diisophthalaldehyde (0.520 g, 1.791 mmol) and *S,S*-(+)-1,2-diaminocyclohexane (0.468 g, 4.098 mmol) in a mixed solvent system of 1:1 DCM/MeOH (1000 mL) was heated under reflux for 5 days with stirring. After cooling, the solution was concentrated to ~500 mL at 25 °C under reduced pressure. A small amount of precipitate formed in the solution (< 20 mg) which was filtered post evaporation, and the remaining solution was filtered with a syringe filter to ensure clarity. Analysis of the filtrate showed a 7:1 mixture of large cage to small cage.

### *2.1.4* ***CC1***

A solution of 1,3,5-triformylbenzene (3.75 g, 23.13 mmol) in DCM (1000 mL) was added dropwise over 24 hours (approx. 0.5 mL/min) *via* pressure – equalizing dropping funnel to a solution of ethylenediamine (2.08 g, 34.69 mmol) in DCM (500 mL) in a 2-L, three-necked round bottomed flask. This reaction took place in a cooled ice bath using isopropyl alcohol. The solution was continually stirred during addition, then left stirring for 3 days. The solvent was then removed under vacuo, maintaining water temperature below 20 °C, and the crude product re-dissolved in $CHCl_3$ (100 mL) and the solution filtered. The residual solid was washed in $CHCl_3$ (50 mL), and then the solvent removed under vacuo, and the temperature maintained below 20 °C. The product was obtained as a fine, white powder.

1 H NMR (400.13 MHz, $CDCl_3$) δ 8.19 (12 H), 7.93 (12 H), 4.03 (24 H)

### *2.1.5 **CC3**-R*

1,3,5-Triformylbenzene (5.19 g, 32.0 mmol) was laid on the bottom of a round bottomed flask, DCM (80 mL) was added, avoiding disturbance of the solid layer. 1,2-Diaminecyclohexane (4.7 g, 41.16 mmol) was dissolved in DCM (80 mL) and the solution added dropwise into the reaction. One drop of TFA was added. The reaction was left for 7 days at room temperature. The solvent was decanted, DCM (80 mL) was added and quickly decanted. The solid was then extracted with more DCM, then collected by filtration.

1 H NMR (400.13 MHz, CDCl3) δ 8.16 (s, CH=N, 12H), 7.90 (s, ArH, 12H), 3.33 (m, CHN, 12H), 1.8 – 1.6 (m, CH2, 48H) ppm. Accurate mass calculated for $C_{72}H_{85}N_{12}$: 1117.7020. Found: 1117.7065.

### *2.1.6 **RCC3**-R*

**CC3**-*R* (1 g, 0.8947 mmol) was placed in a flask with $CHCl_3$ (75 mL) and stirred until the solid began to dissolve. MeOH (75 mL) was added and stirred until the solid had fully dissolved. Sodium borohydride (1 g, 26.43 mmol) was slowly added in batches and left stirring for 12 hours. The reaction was quenched with a few drops of water and left for 12 hours. The solvent was removed under vacuum, the solid was then removed using $CHCl_3$ (3 x 50 mL) and washed with water (2 x 100 mL). The organic phase was retained and the solid extracted under vacuo. The product was then dried in a vacuum oven for 12 hours at 30 °C.

1 H NMR (CDCl3, 400 MHz) δ 7.09 (s, 12H, -ArH), 3.81 (d, 12H, -ArCH2), 3.59 (d, 12H, -ArCH2), 2.18 (m, 12H, CH on cyclohexane), 0.95 - 1.98 (m, 48H, CH2 on cyclohexane) ppm.

Data agrees with literature values.

### *2.1.6 FT-**RCC3**-R*

Paraformaldehyde (1 g, 33.30 mmol) was dissolved in MeOH (50 mL) with water (5 mL) and refluxed at 70 °C for 1 hour. A solution of **RCC3-*R*** (1 g, 0.8757 mmol) in MeOH (50 mL) was added to the solution. The reaction was left under reflux for an hour, forming a white precipitate. The solution was then filtered under gravity and the white solid washed with MeOH. The material was then dried in a vacuum oven for 12 hours at 70 °C.[26]

1 H NMR (400.13MHz, CDCl3) δ 7.12 (s, 12H, -ArH), 4.00 (d, 12H, -ArCH2 ), 3.24 (s, 12 H, -NCH2N-), 2.30 (d, 12H, -ArCH2 ), 2.29 (d, 12H, CH on cyclohexane), 1.95 (d, 12H, CH2 on cyclohexane ), 1.83 (d, 12H, CH2 on cyclohexane ), 1.29 (m, 24H, CH2 on cyclohexane) ppm.

Data agrees with literature values.

# 3 Crystallography Information Files

## 3.1 Chapter 2

| | **TCC1**$_{[6+12]}$.18($CH_2Cl_2$)·18($C_2H_8O$) |
|---|---|
| Crystallisation Solvent | DCM, EtOH |
| Wavelength [Å] | 0.71073 |
| Collection Temperature | 100 |
| Formula | $C_{234}H_{180}N_{24}Cl_{154}O_{18}$ |
| *Mr* | 5963.60 |
| Crystal Size (mm) | 0.626 x 0.1 x 0.1 |
| Crystal System | Trigonal |
| Space Group | *R*3 |
| *a* [Å] | 38.524(7) |
| *b* [Å] | 38.524(7) |
| *c* [Å] | 18.607(4) |
| *α* [°] | 90 |
| *β* [°] | 90 |
| *γ* [°] | 120 |
| *V* [$Å^3$] | 23915(10) |
| *Z* | 3 |
| $D_{calcd}$ [g $cm^{-3}$] | 1.186 |
| *μ* [$mm^{-1}$] | 0.509 |
| F(000) | 8928 |
| 2θ range [°] | 2.114 – 46.576 |
| Reflections collected | 49700 |
| Independent reflections, $R_{int}$ | 12268, 0.0791 |
| Obs. Data [$I > 2\sigma$] | 7563 |
| Data /<br>restraints /<br>parameters | 12268<br>584<br>565 |

| | |
|---|---|
| Final R1 values ($I > 2\sigma(I)$) | 0.0687 |
| Final R1 values (all data) | 0.1027 |
| Final wR($F^2$) values (all data) | 0.1641 |
| Goodness-of-fit on $F^2$ | 0.928 |
| Largest difference peak and hole [e.A$^{-3}$] | 0.210, -0.156 |
| CCDC | 1578448 |

## 3.2 Chapter 3

| | **B1·0.82($C_4H_8O_2$)·0.18($CH_2Cl_2$)·0.2($H_2O$)** | **B13[8+12]·2($CHCl_3$)·2($C_4H_8O$)·18.5($H_2O$)** |
|---|---|---|
| Crystallisation Solvent | $CH_2Cl_2$, EtOAc | $CHCl_3$, THF |
| Wavelength [Å] | 0.71073 | 0.71073 |
| Collection Temperature | 100 K | 100 K |
| Formula | $C_{51.48}H_{55.33}Cl_{0.35}N_6O_{1.84}$ | $C_{226}H_{295}Cl_6N_{24}O_{44.5}$ |
| *Mr* | 799.98 | 4272.54 |
| Crystal Size (mm) | 0.153 x 0.148 x 0.058 | 0.25 x 0.25 x 0.10 |
| Crystal System | Triclinic | Triclinic |
| Space Group | $\boldsymbol{P\bar{1}}$ | $\boldsymbol{P\bar{1}}$ |
| *a* [Å] | 11.9249(4) | 17.524(2) |
| *b* [Å] | 14.1652(5) | 19.681(3) |
| *c* [Å] | 14.5526(5) | 21.948(4) |
| $\alpha$ [°] | 73.9550(10) | 112.027(4) |
| $\beta$ [°] | 70.5990(10) | 112.920(3) |
| $\gamma$ [°] | 88.0330(13) | 95.170(4) |
| $V$ [Å$^3$] | 2223.81(13) | 6210.9(16) |
| $Z$ | 2 | 1 |
| $D_{calcd}$ [g cm$^{-3}$] | 1.195 | 1.142 |
| $\mu$ [mm$^{-1}$] | 0.094 | 0.141 |
| F(000) | 854 | 2277 |
| 2θ range [°] | 2.998-58.268 | 2.252 – 43.452 |
| Reflections collected | 29925 | 69169 |
| Independent reflections, $R_{int}$ | 11975, 0.0463 | 14703, 0.0506 |
| Obs. Data [$I > 2\sigma$] | 11975 | 8881 |
| Data /<br>restraints /<br>parameters | 11975<br>4<br>587 | 14703<br>1023<br>1398 |
| Final R1 values ($I > 2\sigma(I)$) | 0.0572 | 0.1596 |
| Final R1 values (all data) | 0.0819 | 0.2159 |
| Final wR($F^2$) values (all data) | 0.1578 | 0.4292 |
| Goodness-of-fit on $F^2$ | 1.027 | 2.755 |
| Largest difference peak and hole [e.A$^{-3}$] | 0.348 / -0.389 | 1.116 / -0.530 |

| CCDC | 1827867 | 1827870 |
|---|---|---|

| | **C1·($C_8H_{10}$)·0.25($CH_2Cl_2$)·0.25 ($H_2O$)** | **C1·($CH_2Cl_2$)·($H_2O$)0.9** |
|---|---|---|
| Crystallisation Solvent | $CH_2Cl_2$, *m*-xylene | $CH_2Cl_2$ |
| Wavelength [Å] | 0.71073 | 0.71073 |
| Collection Temperature | 100 K | 100 K |
| Formula | $C_{51.48}H_{55.33}Cl_{0.35}N_6O_{1.84}$ | $C_{55}H_{62.50}Cl_2N_6O_{0.7}$ |
| *Mr* | 925.48 | 889.71 |
| Crystal Size (mm) | 0.167 x 0.202 x 0.221 | 0.255 x 0.218 x 0.181 |
| Crystal System | Triclinic | Triclinic |
| Space Group | $P\bar{1}$ | $P\bar{1}$ |
| *a* [Å] | 15.0024(6) | 11.8919(11) |
| *b* [Å] | 15.2730(7) | 14.7301(14) |
| *c* [Å] | 15.2779(6) | 14.9935(12) |
| *α* [°] | 60.8167(16) | 83.461(2) |
| *β* [°] | 81.7670(16) | 74.190(2) |
| *γ* [°] | 76.8256(17) | 75.258(2) |
| *V* [Å$^3$] | 2973.7(17) | 2441.1(4) |
| *Z* | 2 | 2 |
| $D_{calcd}$ [g cm$^{-3}$] | 1.034 | 1.210 |
| *μ* [mm$^{-1}$] | 0.082 | 0.178 |
| F(000) | 995 | 948 |
| 2θ range [°] | 2.790 – 52.798 | 2.826 – 52.740 |
| Reflections collected | 33904 | 37817 |
| Independent reflections, $R_{int}$ | 12184, 0.0559 | 9978, 0.0573 |
| Obs. Data [$I > 2\sigma$] | 7014 | 7354 |
| Data / | 12184 | 9978 |
| restraints / | 29 | 11 |
| parameters | 644 | 621 |
| Final R1 values ($I > 2\sigma(I)$) | 0.0977 | 0.0676 |
| Final R1 values (all data) | 0.1586 | 0.0888 |
| Final wR($F^2$) values (all data) | 0.3292 | 0.2098 |
| Goodness-of-fit on $F^2$ | 1.047 | 1.060 |
| Largest difference peak and hole [e.A$^{-3}$] | 1.179 / -0.341 | 0.665 / -0.807 |
| CCDC | 1827878 | N/A |

| | **C21Tri$^4$Di$^6$·7.12($CH_2Cl2$)·5.12($C_2H_3N$) ·0.25($H_2O$)** | **C21Tri$^2$Di$^3$·0.5($CH_2Cl_2$)· 0.25($C_2H_{10}O$)** |
|---|---|---|
| Crystallisation Solvent | $CH_2Cl_2$, MeCN | $CH_2Cl_2$ |
| Wavelength [Å] | 0.71073 | 0.6889 |
| Collection Temperature | 100 K | 100 K |
| Formula | $C_{125.38}H_{138.12}Cl_{14.25}N_{17.12}O_{0.25}S_{12}$ | $C_{55.5}H_{57.5}ClN_6O_{0.25}S_6$ |
| *Mr* | 2778.78 | 1040.38 |

| | | |
|---|---|---|
| Crystal Size (mm) | N/A | 0.091 x 0.087 x 0.049 |
| Crystal System | Monoclinic | Triclinic |
| Space Group | $P2_1/n$ | $P\bar{1}$ |
| *a* [Å] | 18.776(9) | 12.900010(10) |
| *b* [Å] | 31.091(14) | 12.99880(10) |
| *c* [Å] | 26.235(11) | 17.19660(10) |
| *α* [°] | | 87.07510(10) |
| *β* [°] | 95.934(12) | 68.5880(10) |
| *γ* [°] | | 82.3650(10) |
| *V* [Å$^3$] | 15233(12) | 2660.79(4) |
| *Z* | 4 | 2 |
| $D_{calcd}$ [g cm$^{-3}$] | 1.212 | 1.299 |
| *μ* [mm$^{-1}$] | 0.470 | 0.342 |
| F(000) | 5786 | 1095 |
| 2θ range [°] | 2.038 – 41.632 | 2.466 – 51.004 |
| Reflections collected | 100268 | 35616 |
| Independent reflections, $R_{int}$ | 15945, 0.0599 | 10768, 0.0534 |
| Obs. Data [$I > 2\sigma$] | 10496 | 9080 |
| Data / | 15945 | 10768 |
| restraints / | 1544 | 14 |
| parameters | 1421 | 683 |
| Final R1 values ($I > 2\sigma(I)$) | 0.0827 | 0.0626 |
| Final R1 values (all data) | 0.1104 | 0.0693 |
| Final wR($F^2$) values (all data) | 0.2385 | 0.1960 |
| Goodness-of-fit on $F^2$ | 1.483 | 1.080 |
| Largest difference peak and hole [e.A$^{-3}$] | 0.566 / 0.556 | 1.259 / -0.389 |
| CCDC | 1827883 | 1827882 |

| | **C14·2($C_4H_8O$)** | **C23·6.5($CH_2Cl_2$)·7.5($C_2H_3N$)** |
|---|---|---|
| Crystallisation Solvent | $CH_2Cl_2$, THF | $CH_2Cl_2$, MeCN |
| Wavelength [Å] | 0.71073 | 0.71073 |
| Collection Temperature | 100 K | 100 K |
| Formula | $C_{86}H_{88}N_6O_2$ | $C_{165.50}H_{179.50}Cl_{13}N_{23.50}$ |
| *Mr* | 1237.62 | 2958.67 |
| Crystal Size (mm) | | 0.257 x 0.170 x 0.123 |
| Crystal System | Triclinic | Monoclinic |
| Space Group | $P\bar{1}$ | $P2/c$ |
| *a* [Å] | 13.2233(10) | 26.591(2) |
| *b* [Å] | 13.3938(10) | 16.3674(14) |
| *c* [Å] | 19.8291(16) | 39.525(4) |
| *α* [°] | 75.682(3) | |
| *β* [°] | 81.032(3) | 98.7932(18) |

| | | |
|---|---|---|
| $\gamma$ [°] | 72.388(3) | |
| $V$ [Å$^3$] | 3230.8(4) | 17000(3) |
| $Z$ | 2 | 4 |
| $D_{calcd}$ [g cm$^{-3}$] | 1.272 | 1.156 |
| $\mu$ [mm$^{-1}$] | 0.076 | 0.266 |
| F(000) | 1324 | 6232 |
| 2θ range [°] | 4.782 – 49.424 | 1.550 – 39.564 |
| Reflections collected | 48180 | 67739 |
| Independent reflections, $R_{int}$ | 11000, 0.0597 | 15390, 0.0698 |
| Obs. Data [$I > 2\sigma$] | 7997 | 8603 |
| Data / | 11000 | 15390 |
| restraints / | 51 | 1393 |
| parameters | 907 | 1524 |
| Final R1 values ($I > 2\sigma(I)$) | 0.0790 | 0.1126 |
| Final R1 values (all data) | 0.1088 | 0.1572 |
| Final wR($F^2$) values (all data) | 0.2176 | 0.3121 |
| Goodness-of-fit on $F^2$ | 1.069 | 1.666 |
| Largest difference peak and hole [e.A$^{-3}$] | 0.739 / -0.393 | 0.619 / -0.586 |
| CCDC | 1827880 | 1827884 |

## 3.3 Chapter 4

| | **T1($C_7H_8$)$_2$** | **T1($CHCl_3$)$_{3.25}$** |
|---|---|---|
| Crystallisation Solvent | Toluene | $CHCl_3$ |
| Wavelength [Å] | 0.70173 | 0.71073 |
| Collection Temperature | 100 K | 350 K |
| Formula | $C_{26}H_{11}N_3O_6$ | $C_{26}H_{11}N_3O_6$ |
| $Mr$ | 737.36 | 461.38 |
| Crystal Size (mm) | 0.02 x 0.03 x 0.2 | 0.3 x 0.2 x 0.02 |
| Crystal System | Orthorhombic | Orthorhombic |
| Space Group | *P*nna | *P*nna |
| $a$ [Å] | 14.4085 | 14.425 |
| $b$ [Å] | 11.4943 | 11.576 |
| $c$ [Å] | 22.9268 | 23.291 |
| $\alpha$ [°] | 90 | 90 |
| $\beta$ [°] | 90 | 90 |
| $\gamma$ [°] | 90 | 90 |
| $V$ [Å$^3$] | 3797.0 | 3840.6 |
| $Z$ | 4 | 4 |
| $D_{calcd}$ [g cm$^{-3}$] | 1.290 (w/solvent) | 1.469 (w/ solvent) |
| | 0.8071 (w/o solvent) | 0.7980 (w/o solvent) |

| | | |
|---|---|---|
| $\mu$ [mm$^{-1}$] | 0.086 | 0.058 |
| F(000) | 1543 | 944 |
| 2θ range [°] | 3.338 – 51.63 | 3.352 – 49.45 |
| Reflections collected | 32197 | 36590 |
| Independent reflections, $R_{int}$ | 3660, 0.0838 | 3285, 0.1584 |
| Obs. Data [$I > 2\sigma$] | 2716 | 1406 |
| Data / | 2716 | 1406 |
| restraints / | 27 | 0 |
| parameters | 280 | 159 |
| Final R1 values ($I > 2\sigma(I)$) | 0.0665 | 0.0783 |
| Final R1 values (all data) | 0.0925 | 0.1674 |
| Final wR($F^2$) values (all data) | 0.1636 | 0.2878 |
| Goodness-of-fit on $F^2$ | 1.089 | 1.051 |
| Largest difference peak and hole [e.A$^{-3}$] | 0.306 / -0.246 | 0.190 / -0.127 |
| CCDC | 1478357 | 1478355 |

| | **T1($C_5H_{12}$)($H_2O$)** | **T1($C_9OH_{12}$)($H_2O$)** |
|---|---|---|
| Crystallisation Solvent | Pentane | Dimethylanisole |
| Wavelength [Å] | 0.71073 | 0.71073 |
| Collection Temperature | 100 K | 100 K |
| Formula | $C_{35}H_{25.5}N_3O_{8.25}$ | $C_{32.25}H_{26}N_3O_{7.16}$ |
| *Mr* | 620.0825 | 570.16 |
| Crystal Size (mm) | N/A | N/A |
| Crystal System | Orthorhombic | Monoclinic |
| Space Group | $Pna2_1$ | $P2_1/n$ |
| *a* [Å] | 9.6634(7) | 14.3994(5) |
| *b* [Å] | 25.5546(18) | 22.1420(8) |
| *c* [Å] | 11.7346(8) | 11.5625(4) |
| $\alpha$ [°] | 90 | 90 |
| $\beta$ [°] | 90 | 100.262(3) |
| $\gamma$ [°] | 90 | 90 |
| *V* [Å$^3$] | 2851.4(3) | 3687.4(2) |
| *Z* | 4 | 4 |
| $D_{calcd}$ [g cm$^{-3}$] | 1.444 (w/ solvent) | 1.027 (w/ solvent) |
| | 1.074 (w/o solvent) | 0.8311 (w/o solvent) |
| $\mu$ [mm$^{-1}$] | 0.072 | 0.105 |
| F(000) | 1290 | 1191 |
| 2θ range [°] | 4.754 – 51.838 | 4.642 – 49.366 |
| Reflections collected | 29885 | 27410 |
| Independent reflections, $R_{int}$ | 5317, 0.0509 | 5572, 0.0838 |
| Obs. Data [$I > 2\sigma$] | 4727 | 3902 |
| Data / | 4727 | 3902 |

| | | |
|---|---|---|
| restraints / | 11 | 11 |
| parameters | 527 | 380 |
| Final R1 values ($I > 2\sigma(I)$) | 0.0509 | 0.0832 |
| Final R1 values (all data) | 0.1056 | 0.2283 |
| Final wR($F^2$) values (all data) | 0.120 | 0.2365 |
| Goodness-of-fit on $F^2$ | 1.009 | 1.146 |
| Largest difference peak and hole [e.A$^{-3}$] | 0.284 / -0.254 | 0.747 / -0.357 |
| CCDC | 1478365 | N/A |

| | **T2-S(DMAC)(Acetone)** | **JO(EtOAc)($H_2O$)** |
|---|---|---|
| Crystallisation Solvent | DMAC, Acetone | $H_2O$, EtOAc |
| Wavelength [Å] | 0.71073 | 0.700173 |
| Collection Temperature | 150 K | 100 K |
| Formula | $C_{23}H_{14}N_6S_3$ | $C_{24}H_{22}N_3.C_{12}H_{11}SO_3$ |
| *Mr* | 470.58 | 617.87 |
| Crystal Size (mm) | 0.15 x 0.20 x 0.20 | 0.10 x 0.12 x 0.30 |
| Crystal System | Orthorhombic | Monoclinic |
| Space Group | *P*cca | *P*2$_1$/c |
| *a* [Å] | 12.7748(11) | 14.8249(6) |
| *b* [Å] | 11.7452(10) | 28.7521(9) |
| *c* [Å] | 23.3106(16) | 7.2841(2) |
| *α* [°] | 90 | 90 |
| *β* [°] | 90 | 95.106(3) |
| *γ* [°] | 90 | 90 |
| *V* [Å$^3$] | 3497.6(5) | 3092.51(18) |
| *Z* | 4 | 5 |
| D$_{c0alcd}$ [g cm$^{-3}$] | 0.894 | 1.327 |
| | | 0.151 |
| *μ* [mm$^{-1}$] | 0.227 | 1299 |
| F(000) | 968 | 1299 |
| 2θ range [°] | 5.02 – 52.74 | 3.10 – 50.848 |
| Reflections collected | 17805 | 83733 |
| Independent reflections, $R_{int}$ | 3561 , 0.0499 | 10808, 0.0733 |
| Obs. Data [$I > 2\sigma$] | 2824 | 7634 |
| Data / | 3561 | 10808 |
| restraints / | 0 | 15 |
| parameters | 160 | 457 |
| Final R1 values ($I > 2\sigma(I)$) | 0.0694 | 0.1276 |
| Final R1 values (all data) | 0.0817 | 0.1596 |
| Final wR($F^2$) values (all data) | 0.2274 | 0.3785 |
| Goodness-of-fit on $F^2$ | 1.065 | 1.089 |
| Largest difference peak and hole [e.A$^{-3}$] | 0.424 / -0.477 | 0.117/0.1611 |

| | | |
|---|---|---|
| CCDC | N/A | N/A |

| | **JM(EtOAc)($H_2O$)** | **AM-O** |
|---|---|---|
| Crystallisation Solvent | $H_2O$, EtOAc | $H_2O$ |
| Wavelength [Å] | 0.70173 | 0.71073 |
| Collection Temperature | 100 K | 100 K |
| Formula | $2(C_{12}H_9O_3S).C_{16}H_{22}N_2$ | $C_{24}H_{21}N_3{\cdot}3(H_2O)$ |
| *Mr* | 708.86 | 405.48 |
| Crystal Size (mm) | 0.171 x 0.274 x 0.417 | 0.1212 x 0.031 x 0.033 |
| Crystal System | Monoclinic | Hexagonal |
| Space Group | *C*2/c | *P*6cc |
| *a* [Å] | 22.673(10) | 18.5426(5) |
| *b* [Å] | 12.8459(6) | 18.5426(5) |
| *c* [Å] | 12.0988(5) | 7.2391(2) |
| *α* [°] | 90 | 90 |
| *β* [°] | 96.485(4) | 120 |
| *γ* [°] | 90 | 90 |
| *V* [Å$^3$] | 3500.4(3) | 2155.54(13) |
| *Z* | 4 | 4 |
| $D_{c0alcd}$ [g cm$^{-3}$] | 1.345 | 1.250 |
| *μ* [mm$^{-1}$] | 0.204 | 0.083 |
| F(000) | 1496 | 864 |
| 2θ range [°] | 3.616 – 56.56 | 4.394 – 50.484 |
| Reflections collected | 17989 | 27120 |
| Independent reflections, $R_{int}$ | 4345, 0.1876 | 1468, 0.1584 |
| Obs. Data [*I* > 2*σ*] | 3861 | 1410 |
| Data / | 3861 | 1410 |
| restraints / | 0 | 1 |
| parameters | 229 | 95 |
| Final R1 values (*I* > 2*σ*(*I*)) | 0.0555 | 0.0530 |
| Final R1 values (all data) | 0.0612 | 0.0549 |
| Final wR($F^2$) values (all data) | 0.1611 | 0.1532 |
| Goodness-of-fit on $F^2$ | 1.026 | 1.036 |
| Largest difference peak and hole [e.A$^{-3}$] | 0.530 / -0.571 | 0.420 / -0.314 |
| CCDC | N/A | N/A |

# 4 Crystal Data

## 4.1 Chapter 2

**TCC1**$_{[6+12]}$

A crystal of TCC1$_{6+12}$ was removed from a solvent mixture of chloroform ($CHCl_3$) and ethanol (EtOH), then quickly mounted on a MiTiGen loop, and flash cooled to 100 K under a dry nitrogen flow to prevent desolvation. All non-H atoms were refined anisotropically. **TCC1**$_{[6+12]}$·18($CHCl_3$)·18(EtOH): Formula $C_{234}H_{342}Cl_{54}N_{24}O_{18}$; $M$ = 5693.60 g mol$^{-1}$, trigonal $R3$, colourless needle shaped crystals; $a$ = 38.524(7) Å, $c$ = 18.607(4) Å, $V$ = 23915(10) Å$^3$; $\rho$ = 1.186 g cm$^{-3}$ (solvated), 0.558 g cm$^{-3}$ (desolvated); $\mu$(Mo-Kα) = 0.509 mm$^{-3}$; $F$ (000) = 8928; crystal size = 0.100 x 0.100 x 0.626 mm; $T$ = 100 K; 49700 reflections measured ($1.057 < \theta < 23.288°$), 12268 unique ($R_{int}$ = 0.0791), 7563 ($I > 2\sigma(I)$); $R_1$ = 0.0687 for observed and $R_1$ = 0.1027 for all reflections; $wR_2$ = 0.1641 for all reflections; max/min difference electron density after solvent mask had been applied = 0.210 and -0.156 e·Å$^{-3}$; data/restraints/parameters = 12268/584/565; GOF = 0.928.

## 4.2 Chapter 3

Crystal data for **B1**·0.82($C_4H_8O_2$)·0.18($CH_2Cl_2$)·0.2($H_2O$): Formula $C_{54}H_{60}N_6$·0.82($C_4H_8O_2$)·0.18$CH_2Cl_2$)·0.2($H_2O$); $M$ = 799.87 gmol$^{-1}$, triclinic $P\bar{1}$, colourless block shaped crystals; crystal size 0.153 x 0.148 x 0.058; $a$ = 11.9249(4) Å, $b$ = 14.1652(5) Å, $c$ = 14.5526(5) Å, $\alpha$ = 73.9550(10) °, $\beta$ = 70.5990(10) °, $\gamma$ = 88.0330(13) °, $V$ = 2223.81(13) Å$^3$; $\rho$ = 1.195 gcm$^{-3}$; $\mu$(rotating anode Mo-kα $\lambda$ = 0.71073 Å); $\mu$ = 0.094 mm$^{-1}$; $F$ (000) = 854; $T$ = 100 K; 29925 reflections measured ($2.998 < \theta < 58.268$ °), 11975 unique ($R_{int}$ = 0.0463), 11975 ($I > 2\sigma(I)$); $R_1$ = 0.0572 for observed and $R_1$ = 0.0819 for all reflections; $wR_2$ = 0.1578 for all reflections; max/min difference electron density = 0.348 and -0.389 e·Å$^{-3}$; data/restraints/parameters = 11975/4/587; GOF = 1.027.

Crystal data for **C1**·($CH_2Cl_2$)·0.7($H_2O$): Formula $C_{54}H_{60}N_6$·$CH_2Cl_2$·0.7($H_2O$); $M$ = 889.71 gmol$^{-1}$, triclinic $P\bar{1}$, colourless block shaped crystals; crystal size = 0.181 x 0.218 x 0.255 mm$^3$; $a$ = 11.8919(11) Å,

$b$ = 14.7301(14) Å, $c$ = 14.9935(12) Å, $\alpha$ = 83.461(2)°, $\beta$ = 74.190(2)°, $\gamma$ = 75.258(2)°, $V$ = 2441.1(4) Å$^3$; $\rho$ = 1.210 gcm$^{-3}$; $\mu$(rotating anode Mo-k$\alpha$ $\lambda$ = 0.71073 Å) = 0.178 mm$^{-3}$; $F$ (000) = 948; $T$ = 100 K; 37817 reflections measured (2.826 < 2$\theta$ < 52.740 °), 9978 unique ($R_{\text{int}}$ = 0.0573), 7354 ($I > 2\sigma(I)$); $R_1$ = 0.0967 for observed and $R_1$ = 0.0843 for all reflections; $wR_2$ = 0.1941 for all reflections; max/min difference electron density = 0.062 and -0.560 e·Å$^{-3}$; data/restraints/parameters = 9978/0/607; GOF = 1.093.

Crystal data for **C1**.$(CH_2Cl_2)$.$3(C_8H_{10})$: Formula $C_{54}H_{62}N_6\cdot(CH_2Cl_2)\cdot3(C_8H_{10})$; $M$ = 925.48 g mol$^{-1}$, triclinic $P\bar{1}$, colourless block shaped crystals; $a$ =15.0024(6) Å, $b$ = 15.2730(7) Å, $c$ = 15.2779(6) Å, $\alpha$ = 60.8167(16) °, $\beta$ = 81.7670(16) °, $\gamma$ = 76.8256(17) °, $V$ = 2973.7(17) Å$^3$; $\rho$ = 1.034 gcm$^{-3}$; $\mu$(rotating anode Mo-k$\alpha$ $\lambda$ = 0.71073 Å) = 0.072 mm$^{-3}$; $F$ (000) = 995.0; crystal size = 0.167 x 0.202 x 0.221 mm$^3$; $T$ = 100 K; 33904 reflections measured (2.790 < 2$\theta$ < 52.798 °), 12184 unique ($R_{\text{int}}$ = 0.0509), 7014 ($I > 2\sigma(I)$); $R_1$ = 0.0977 for observed and $R_1$ = 0.1586 for all reflections; $wR_2$ = 0.3292 for all reflections; max/min difference electron density = 1.179 and -0.341 e·Å$^{-3}$; data/restraints/parameters = 26588/0/547; GOF = 1.047.

Crystal data for **C14**$\cdot(CH_2Cl_2)\cdot1.5(C_4H_8O)$: Formula $C_{86}H_{88}N_6O_2$; $M$ = 1237.62 g mol$^{-1}$, triclinic $P\bar{1}$, colourless block shaped crystals; $a$ = 13.2233(10) Å, $b$ = 13.3938(10) Å, $c$ = 19.8291(16) Å, $\alpha$ = 75.682(3)°, $\beta$ = 81.032(3)°, $\gamma$ = 72.388(3)°, $V$ = 3230.8(4) Å$^3$; $\rho$ = 1.272 gcm$^{-3}$; $\mu$(rotating anode Mo-k$\alpha$ $\lambda$ = 0.71073 Å) = 0.076 mm$^{-3}$; $F$ (000) = 1324; $T$ = 100 K; 48180 reflections measured (4.782 < 2$\theta$ < 49.424 °), 11000 unique ($R_{\text{int}}$ = 0.0597), 7997 ($I > 2\sigma(I)$); $R_1$ = 0.0790 for observed and $R_1$ = 0.1088 for all reflections; $wR_2$ = 0.2176 for all reflections; max/min difference electron density = 0.739 and -0.393 e·Å$^{-3}$; data/restraints/parameters = 11000/51/907; GOF = 1.069.

Crystal data for **C23**.$(CH_2Cl_2)$.$(C_2H_3N)_{7.5}$: Formula $C_{165.50}H_{179.50}Cl_{13}N_{23.5}$; $M$ = 2958.67 gmol$^{-1}$, monoclinic $P2/c$, colourless block shaped crystals; $a$ = 26.591(2) Å, $b$ = 16.3674(14) Å, $c$ = 39.525(4) Å, $\beta$ = 98.7932(18)°, $V$ = 17000(3) Å$^3$; $\rho$ = 1.156 gcm$^{-3}$; $\mu$(rotating anode $\lambda$ = 0.71073 Å) = 0.266 mm$^{-3}$; $F$ (000) = 6232; $T$ = 100 K; 67739 reflections measured (1.550 < 2$\theta$ < 39.564

°), 15390 unique ($R_{\mathrm{int}}$ = 0.0698), 8603 ($I > 2\sigma(I)$); $R_1$ = 0.1126 for observed and $R_1$ = 0.1572 for all reflections; $wR_2$ = 0.3121 for all reflections; max/min difference electron density = 0.619 and -0.568 e·Å$^{-3}$; data/restraints/parameters = 15390/1393/1524; GOF = 1.666.

Crystal data for **B13**$\cdot$2($CHCl_3$)·2($C_4H_8O$)·18.5($H_2O$): Formula; $C_{216}H_{240}N_{24}O_{24}\cdot 2(CHCl_3)\cdot 2(C_4H_8O)\cdot 18.5(H_2O)$ $M$ = 4272.54 g mol$^{-1}$, triclinic $P\bar{1}$, light yellow block shaped crystals; $a$ = 17.524(2) Å, $b$ = 19.671(3) Å, $c$ = 21.948(4) Å, $\alpha$ = 112.027(4) ° $\beta$ = 112.920(3) °, $\gamma$ = 95.170 (4) $V$ = 6210.9(16) Å$^3$; $\rho$ = 1.142 g cm$^{-3}$; $\mu$(rotating anode $\lambda$ = 0.71073 Å) = 0.141 mm$^{-3}$; $F$ (000) = 2277; $T$ = 100 K; 69169 reflections measured (2.252 < 2θ < 43.452 °), 14703 unique ($R_{\mathrm{int}}$ = 0.0506), 8881 ($I > 2\sigma(I)$); $R_1$ = 0.1596 for observed and $R_1$ = 0.2159 for all reflections; $wR_2$ = 0.4292 for all reflections; max/min difference electron density = 1.116 and -0.530 e·Å$^{-3}$; data/restraints/parameters = 14703/1023/1398; GOF = 2.755.

Crystal data for **C21Tri$^{2}$Di$^{3}$**·0.5($CH_2Cl_2$)·0.25($C_4H_{10}O$): Formula $C_{54}H_{54}N_6S_6\cdot 0.5(CH_2Cl_2)\cdot 5.12(C_2H_3N)\cdot 0.25(C_4H_{10}O)$; $M$ = 1040.38 g mol$^{-1}$, monoclinic $P\bar{1}$, yellow block shaped crystals; crystal size = 0.191 x 0.087 x 0.049 $a$ = 12.900010(10) Å, $b$ = 12.99880(10) Å, $c$ = 17.19660(10) Å, $\alpha$ = 87.0750(10) °, $\beta$ = 68.5880(10) °, $\gamma$ = 82.3650(10) °; $V$ = 2660.79(4) Å$^3$; $\rho$ = 1.299 g cm$^{-3}$; $\mu$(synchotron $\lambda$ = 0.6889 Å) = 0.342 mm$^{-3}$; $F$ (000) = 1095; $T$ = 100 K; reflections measured (2.466 < 2θ < 51.004 °) 35616, unique 10768 ($R_{\mathrm{int}}$ = 0.0534), 9080 ($I > 2\sigma(I)$); $R_1$ = 0.0626 for observed and $R_1$ = 0.0693 for all reflections; $wR_2$ = 0.1960 for all reflections; max/min difference electron density = 1.259 and -0.389 e·Å$^{-3}$; data/restraints/parameters = 10768/14/683; GOF = 1.080.

Crystal data for **C21**$\cdot$7.12($CH_2Cl_2$)$\cdot$5.13($C_2H_3N$)$\cdot$0.25($H_2O$): Formula $C_{108}H_{108}N_{12}S_{12}\cdot 7.12$ $(CH_2Cl_2)\cdot 5.12(C_2H_3N)\cdot 0.25(H_2O)$; $M$ = 2778.78 g mol$^{-1}$, monoclinic $P2_1$/n, yellow block shaped crystals; $a$ = 18.776(9) Å, $b$ = 31.091(14) Å, $c$ = 26.235(11) Å, $\beta$ = 95.934(12) °, $V$ = 15233(12) Å$^3$; $\rho$ = 1.212 g cm$^{-3}$; $\mu$(rotating anode $\lambda$ = 0.71073 Å) = 0.470 mm$^{-3}$; $F$ (000) = 5786; $T$ = 100 K; 100268 reflections measured (2.038 < 2θ < 41.632 °), 15945 unique ($R_{\mathrm{int}}$ = 0.0599), 10496 ($I > 2\sigma(I)$); $R_1$ = 0.0827 for observed and $R_1$ = 0.1104 for all reflections; $wR_2$ = 0.2385 for all reflections; max/min difference electron density = 0.566 and -0.556 e·Å$^{-3}$; data/restraints/parameters = 15945/1544/1421; GOF = 1.483.

## 4.3 Chapter 4

**T1**·2($C_7H_8$): Formula $C_{47}H_{35}N_3O_6$; $M$ = 737.78 g mol$^{-1}$, orthorhombic *P*nna, colourless block crystals; $a$ = 14.4085(7) Å, $b$ = 11.4943(6) Å, $c$ = 22.9268(12) Å, $V$ = 3797.0(3) Å$^3$; $\rho$ = 1.290 g cm$^{-3}$ (solvated); $\mu$(Mo-Kα) = 0.086 mm$^{-3}$; $F$ (000) = 1543; crystal size = 0.194 x 0.17 x 0.114 mm; $T$ = 100 K; 32197 reflections measured (3.338 < 2θ < 51.63 °), 3660 unique ($R_{\text{int}}$ = 0.0838), 2716 ($I > 2\sigma(I)$); $R_1$ = 0.0665 for observed and $R_1$ = 0.0925 for all reflections; $wR_2$ = 1636 for all reflections; max/min difference electron density = 0.306 and -0.246 e·Å$^{-3}$; data/restraints/parameters = 3660/21/279; GOF = 1.089.

**T1**·3.25($CHCl_3$): Formula $C_{26}H_{11}N_3O_6$; $M$ = 461.38 g mol$^{-1}$, orthorhombic *P*nna, colourless block crystals; (350 K) $a$ = 14.2257(12) Å, $b$ = 23.1375(19) Å, $c$ = 11.5625(10) Å, $V$ = 3840.6 Å$^3$; 100 K $a$ = 11.5502 (4) $b$ = 14.1303(9) $c$ = 22.5000(18) $V$ = 3672.2(4); $\rho$ = 1.469 g cm$^{-3}$ (solvated); $\mu$(Mo-Kα) = 0.086 mm$^{-3}$; $F$ (000) = 944; crystal size = 0.3 x 0.2 x 0.02 mm; $T$ = 350 K; 36590 reflections measured (3.352 < 2θ < 49.45 °), 3285 unique ($R_{\text{int}}$ = 0.1584), 2716 ($I > 2\sigma(I)$); $R_1$ (post-SQ) = 0.0783, $R_1$ (pre-SQ) = 0.2504 for observed and $R_1$ = 0.1674 for all reflections; $wR_2$ = 0.2878 for all reflections; max/min difference electron density = 0.190 and -0.127 e·Å$^{-3}$; data/restraints/parameters = 7799/96/514; GOF = 1.051.

**T1**·1.25($C_5H_{12}$)·0.64($H_2O$): Formula $C_{35}H_{25.5}N_3O_{8.25}$; $M$ = 620.0825 g mol$^{-1}$, orthorhombic *P*na2$_1$, colourless block crystals; $a$ = 9.6634(7) Å, $b$ = 25.5546(18), $c$ = 11.7346(8) Å, $V$ = 2851.4(3) Å$^3$; $\rho$ = 1.444 g cm$^{-3}$ (solvated); $\mu$(Mo-Kα) = 0.072 mm$^{-3}$; $F$ (000) = 1290; $T$ = 100 K; 29885 reflections measured (4.754 < 2θ < 51.838 °), 5317 unique ($R_{\text{int}}$ = 0.0509), 4727 ($I > 2\sigma(I)$); $R_1$ = 0.0509 for observed and $R_1$ = 0.1056 for all reflections; $wR_2$ = 0.120 for all reflections; max/min difference electron density = 0.284 and -0.254 e·Å$^{-3}$; data/restraints/parameters = 4727/11/527; GOF = 1.009.

Crystal data for **T2-S**·DMAC: Formula $C_{23}H_{14}N_6S_3$; $M$ = 470.58 g mol$^{-1}$, Orthorhombic *P*cca, yellow block crystals; $a$ = 12.7748(11) Å, $b$ = 11.7452(10), $c$ = 23.3106(16) Å, $V$ = 3497.6(5) Å$^3$; $\rho$ = 0.894 g cm$^{-3}$ (desolvated); $\mu$ = 0.227 mm$^{-3}$; $\lambda$ = 0.71073 Å; $F$ (000) = 968; crystal size = 0.15 x 0.20 x 0.20 mm; $T$ = 150 K; reflections measured (5.02 < 2θ < 52.74 °), 3561 unique ($R_{\text{int}}$ = 0.0499), 2824 ($I > 2\sigma(I)$); $R_1$ = 0.0694 for observed and $R_1$ = 0.0817 for all reflections; $wR_2$ = 0.2274 for all reflections; max/min difference electron density = 0.424 and -0.477 e·Å$^{-3}$ after solvent masked applied; data/restraints/parameters = 3561/0/160; GOF = 1.065.

Crystal data for **SA-J**/**AM-M**: Formula $2(C_{12}H_9O_3S)\cdot C_{16}H_{22}N_2$; $M$ = 708.86 g mol$^{-1}$, Monoclinic *C*2/c, colourless block crystals; $a$ = 22.6673(10) Å, $b$ = 12.8459(6), $c$ = 12.0988(8) Å, $V$ = 3500.4(3) Å$^3$; $\rho$ = cm$^{-3}$; $\mu$ = 0.204 mm$^{-3}$; $\lambda$ = 0.71073 Å; $F$ (000) = 1496; crystal size = 0.171 x 0.274 x 0.417 mm; $T$ = 100 K; 17989 reflections measured (3.616 < 2θ < 50.484 °), 4345 unique ($R_{\text{int}}$ = 0.1876), 3861 ($I > 2\sigma(I)$); $R_1$ = 0.0555 for observed and $R_1$ = 0.0612 for all reflections; $wR_2$ = 0.1611 for all reflections; max/min difference electron density = 0.530 and -0.572 e·Å$^{-3}$ after solvent masked applied; data/restraints/parameters = 4345/0/229; GOF = 1.026.

Crystal data for **JO**(EtOAc): Formula $C_{24}H_{22}N_3\cdot C_{12}H_{11}SO_3$; $M$ = 617.87 g mol$^{-1}$, Monoclinic *P*2$_1$/c, colourless block crystals; $a$ = 14.8249(6) Å, $b$ = 28.7521(9), $c$ = 7.2841(2) Å, $V$ = 3092.51(18) Å$^3$; $\rho$ = 1.327 g cm$^{-3}$; $\mu$ = 0.151 mm$^{-3}$; $\lambda$ = 0.71073 Å; $F$ (000) = 1299; crystal size = 0.10 x 0.12 x 0.30 mm; $T$ = 100 K; 83733 reflections measured (3.10 < 2θ < 50.848 °), 10808 unique ($R_{\text{int}}$ = 0.0773), 7634 ($I > 2\sigma(I)$); $R_1$ = 0.1276 for observed and $R_1$ = 0.1596 for all reflections; $wR_2$ = 0.3785 for all reflections; max/min difference electron density = 0.117 and -1.611 e·Å$^{-3}$ after solvent masked applied; data/restraints/parameters = 10808/15/457; GOF = 1.089.

Crystal data for **AM-O**: **AM-O**·3($H_2O$): Formula $C_{24}H_{21}N_3\cdot 3(H_2O)$; $M$ = 405.48 g mol$^{-1}$, Hexagonal *P*6cc, colourless needle crystals; crystal size = 0.212 x 0.031 x 0.033 mm; $a$ = 18.5426(5) Å, $b$ = 18.5426(5) Å, $c$ = 7.2391(2) Å, $V$ = 2155.54(13) Å$^3$; $\rho$ = 1.250 g cm$^{-3}$; $\mu$(Mo-Kα) = 0.083 mm$^{-3}$; $F$ (000) = 864; 27120 reflections measured (4.394 < 2θ < 50.484 °), 1468 unique ($R_{\text{int}}$ =

0.1584), 1410 ($I > 2\sigma(I)$); $R_1$ = 0.0530 for observed and $R_1$ = 0.0549 for all reflections; $wR_2$ = 0.1532 for all reflections; max/min difference electron density = 0.420 and -0.314 e·Å$^{-3}$; data/restraints/parameters = 1468/1/95; GOF = 1.036.

# *5 NMR*

## *5.1 Chapter 2*

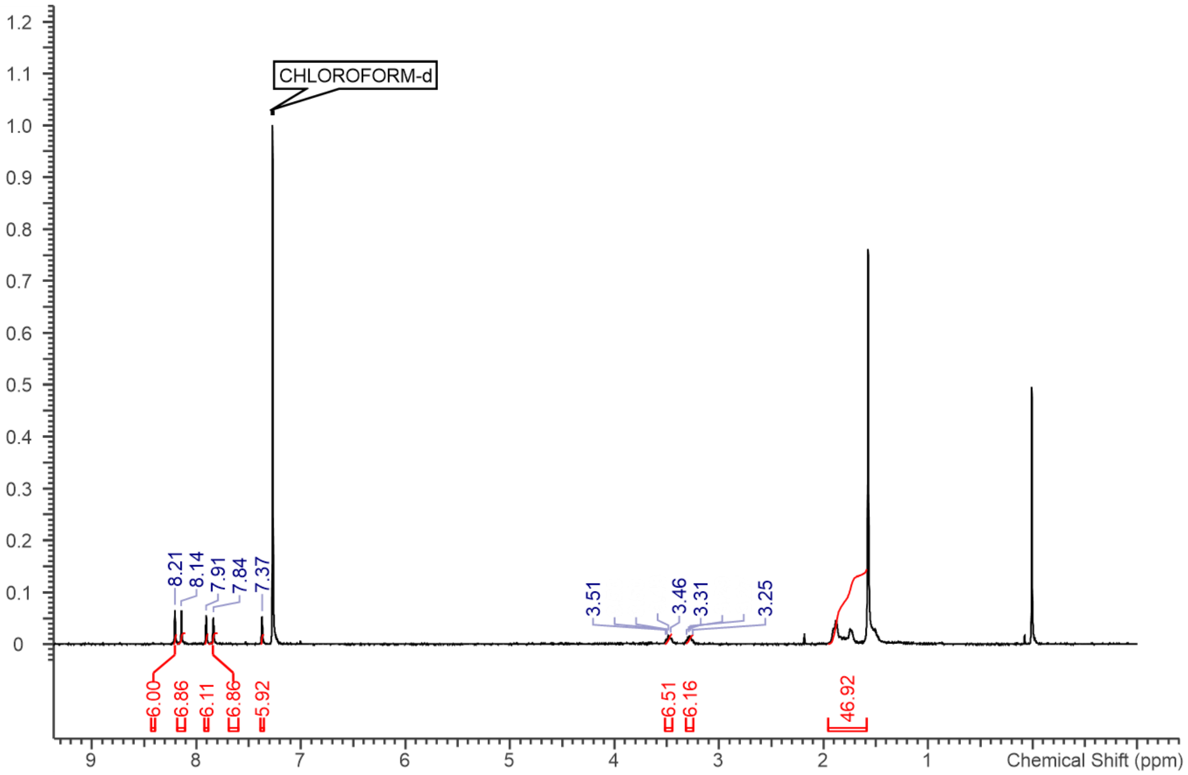

**Figure 1 TCC1-*S*:** $^1$H NMR (400 MHz, CDCl3) $\delta$ 8.21 (s, 6 H), 8.14 (s, 6 H), 7.91 (s, 6 H), 7.84 (s, 6 H), 7.37 (s, 6 H), 3.45 - 3.53 (m, 6 H), 3.22 - 3.32 (m, 6 H), 1.96 - 1.58 (m, 48 H).

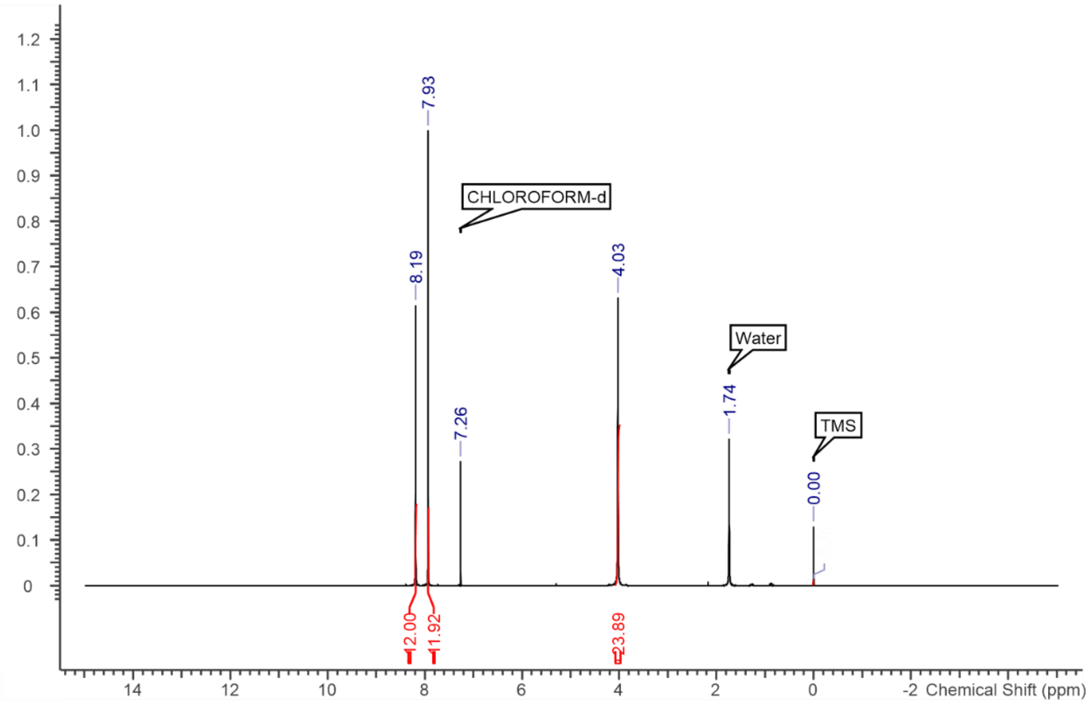

**Figure 2 CC1** $^1$H NMR ($CDCl_3$) δ 8.19 (12 H), 7.93 (12 H), 4.03 (24 H)

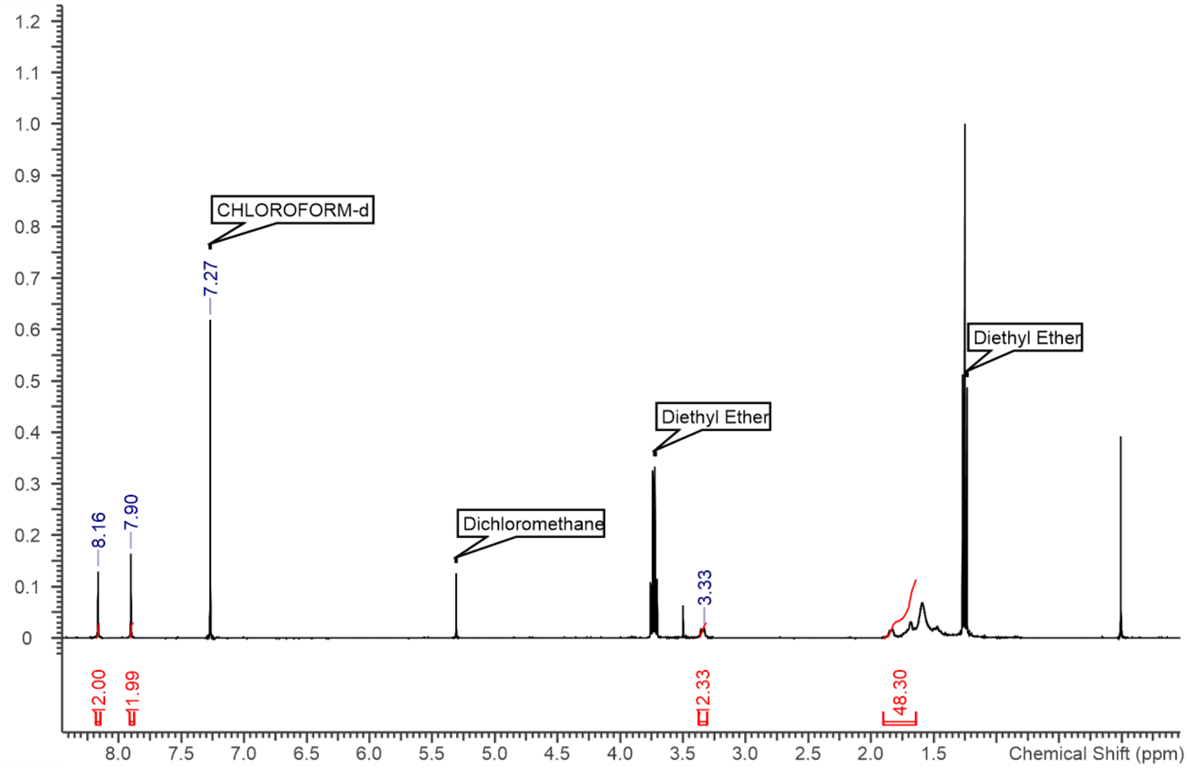

**Figure 3 CC3**-*R*: δ 8.16 (s, CH=N, 12H), 7.90 (s, ArH, 12H), 3.33 (m, CHN, 12H), 1.8 – 1.6 (m, CH2, 48H) ppm

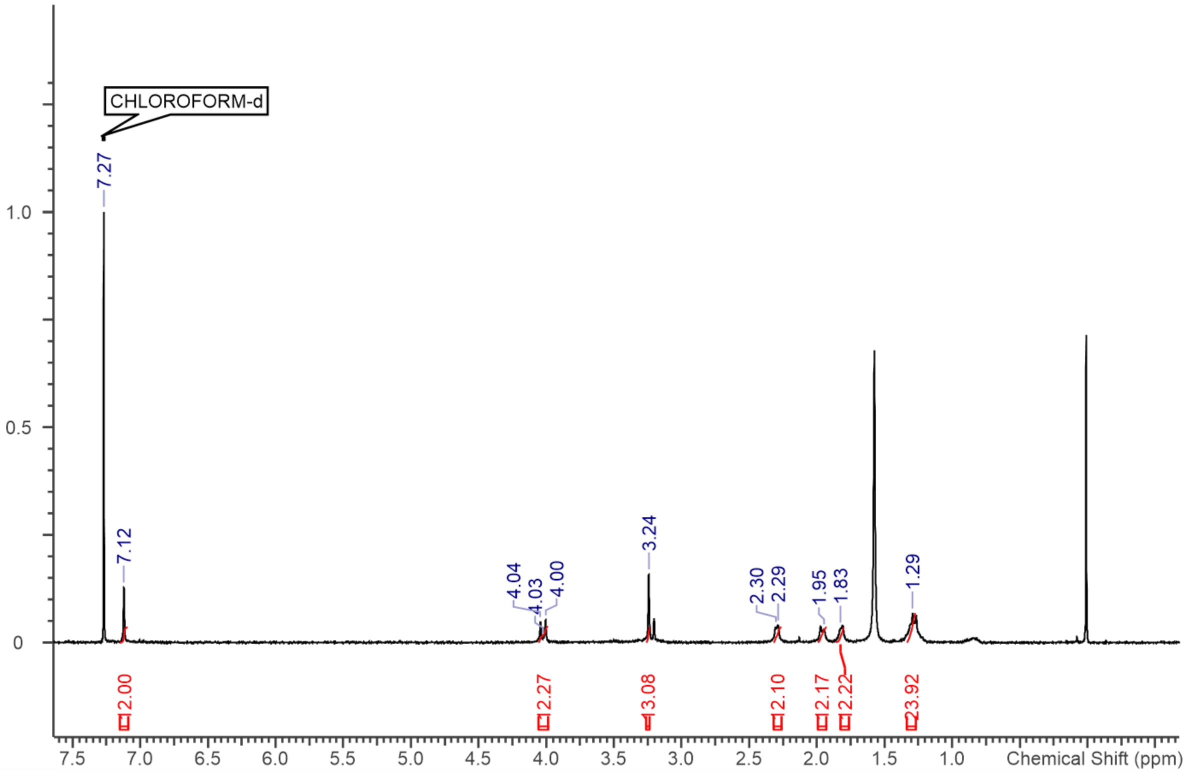

**Figure 4 FT-RCC3**-*R*: $^1$H NMR (CDCl3, 400 MHz) δ 7.12 (s, 12H, -ArH), 4.00 (d, 12H, -ArCH2 ), 3.24 (s, 12 H, -NCH2N-), 2.30 (d, 12H, -ArCH2 ), 2.29 (d, 12H, CH on cyclohexane), 1.95 (d, 12H, CH2 on cyclohexane ), 1.83 (d, 12H, CH2 on cyclohexane ), 1.29 (m, 24H, CH2 on cyclohexane) ppm.

## 6 Sorption Data

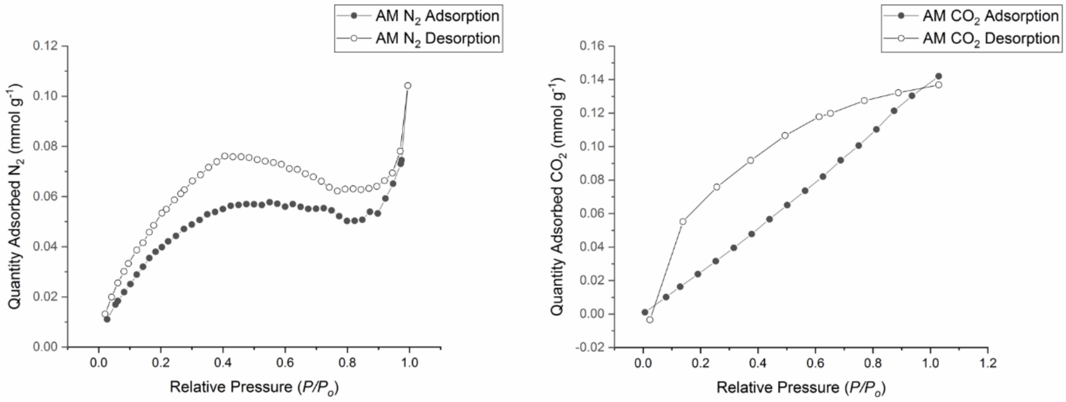

**Figure 5 AM** $N_2$ and $CO_2$ sorption.

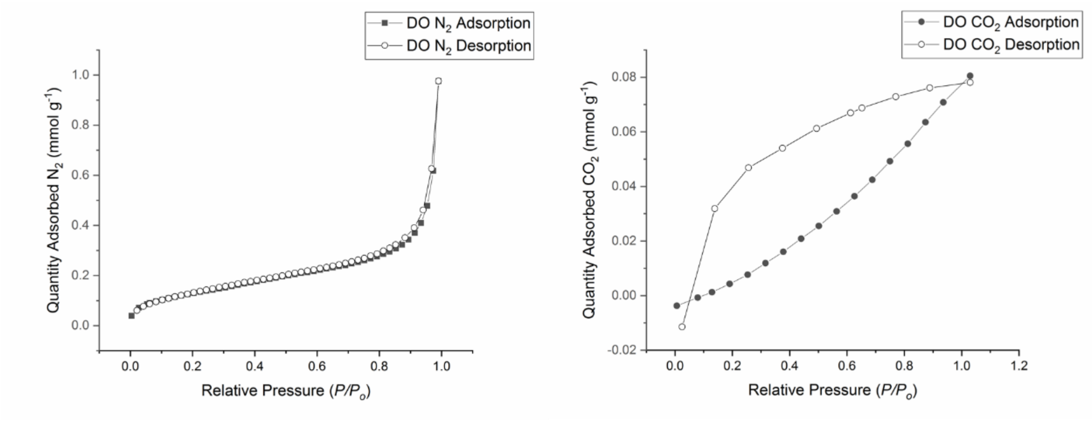

**Figure 6 DO** N$_2$ and CO$_2$ sorption.

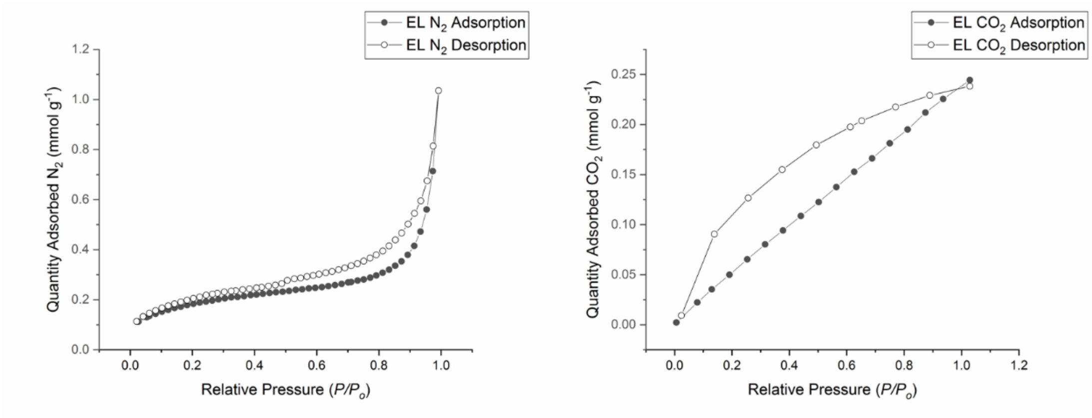

**Figure 7 EL** N$_2$ and CO$_2$ sorption.

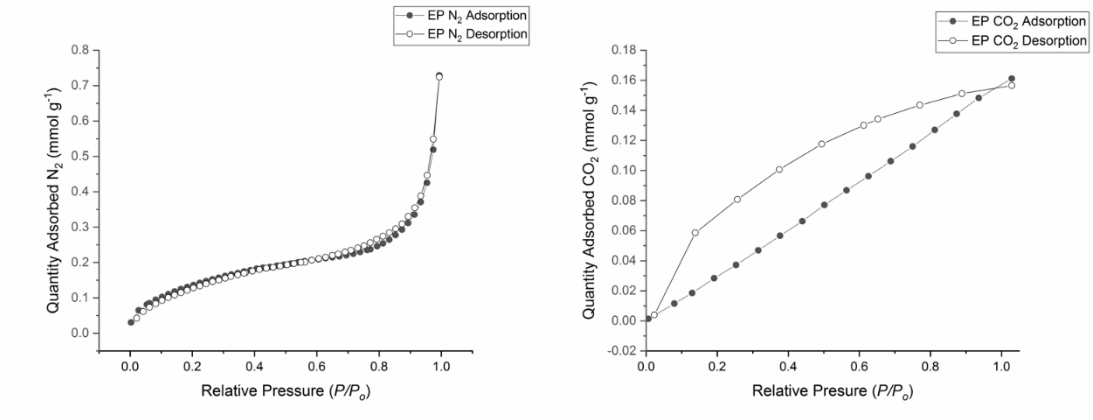

**Figure 8 EP** N$_2$ and CO$_2$ sorption.

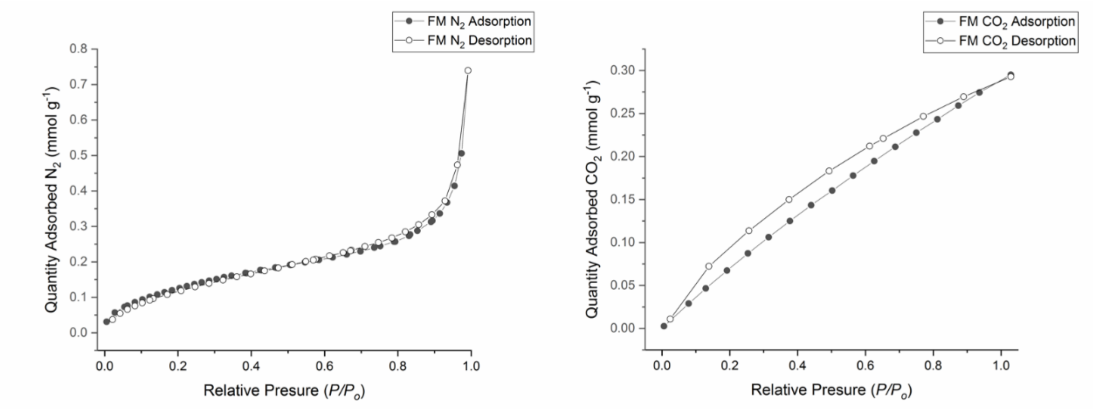

**Figure 9 FM** $N_2$ and $CO_2$ sorption.

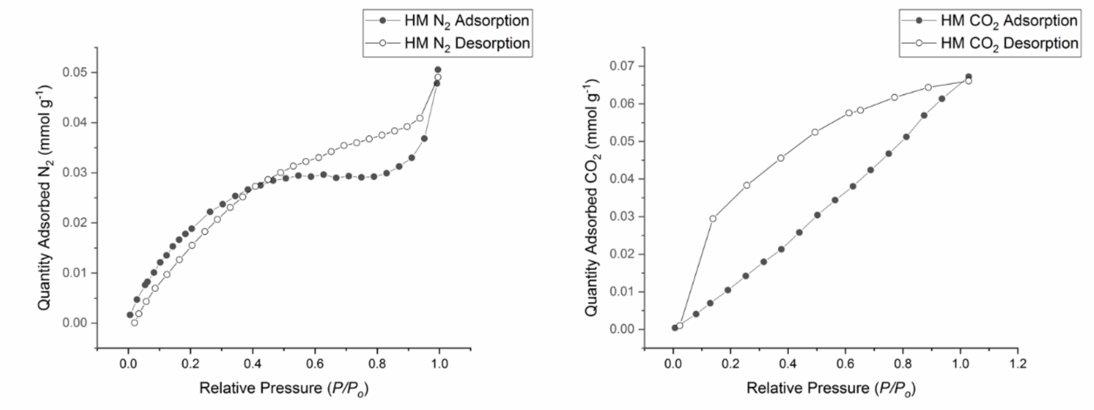

**Figure 10 HM** $N_2$ and $CO_2$ sorption.

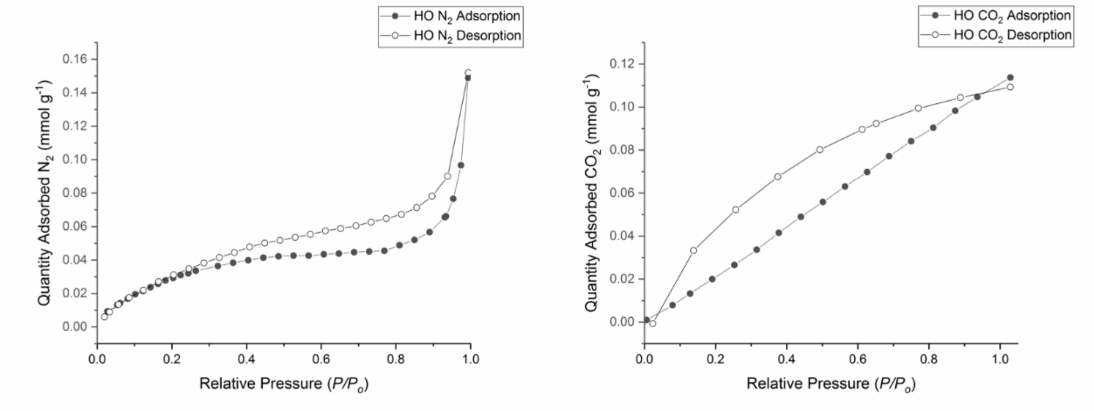

**Figure 11 HO** $N_2$ and $CO_2$ sorption.

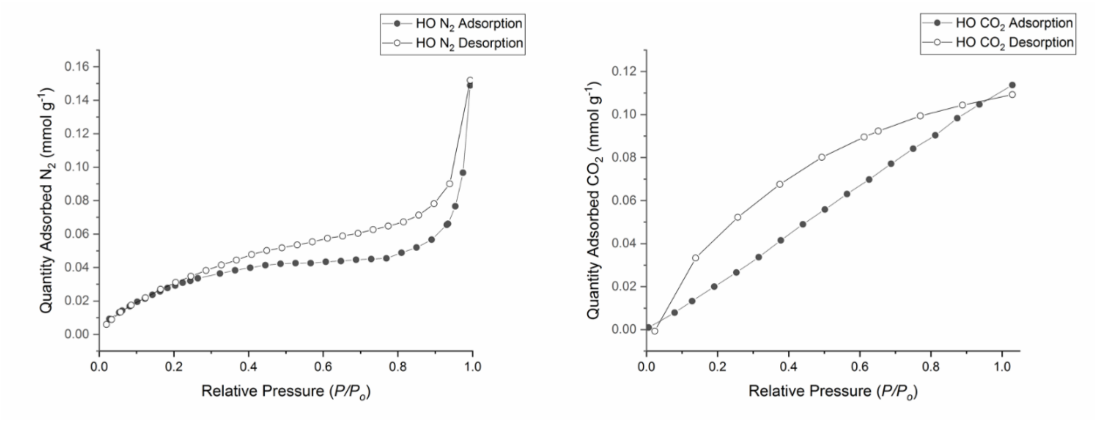

**Figure 12 HP** $N_2$ and $CO_2$ sorption.

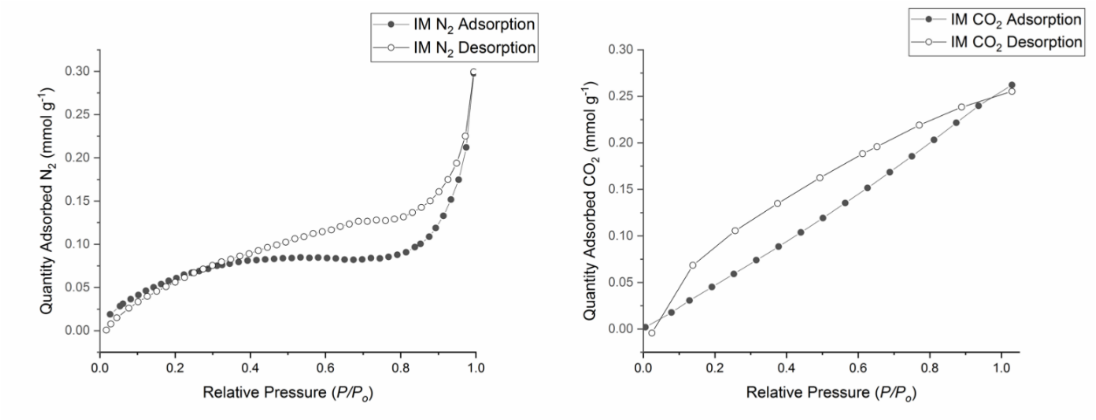

**Figure 13 IM** $N_2$ and $CO_2$ sorption.

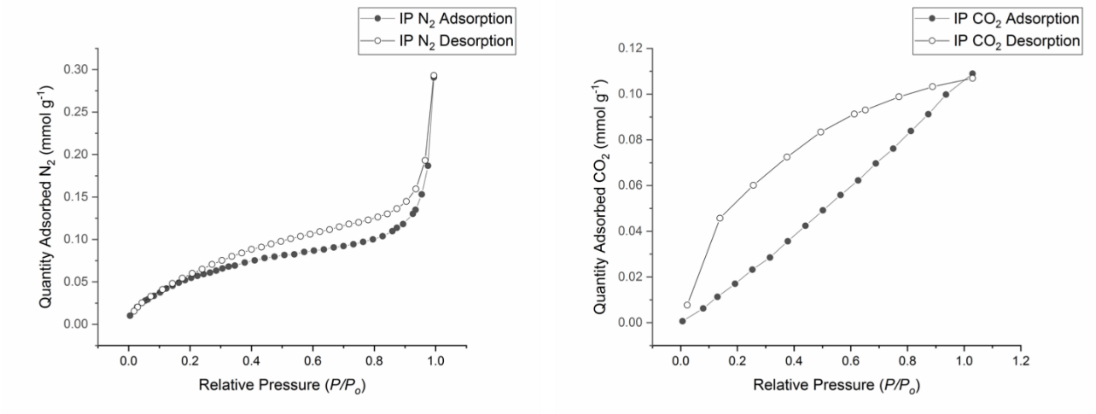

**Figure 14 IP** $N_2$ and $CO_2$ sorption.

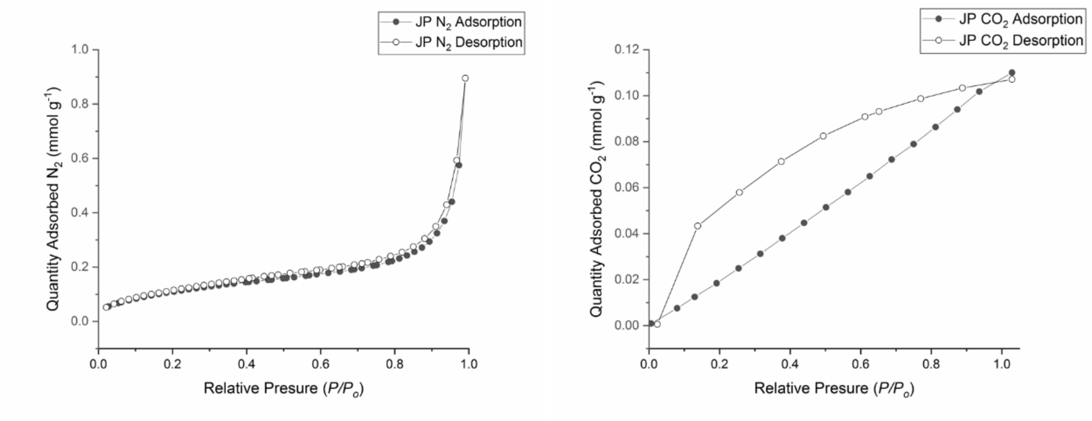

**Figure 15 JP** $N_2$ and $CO_2$ sorption.

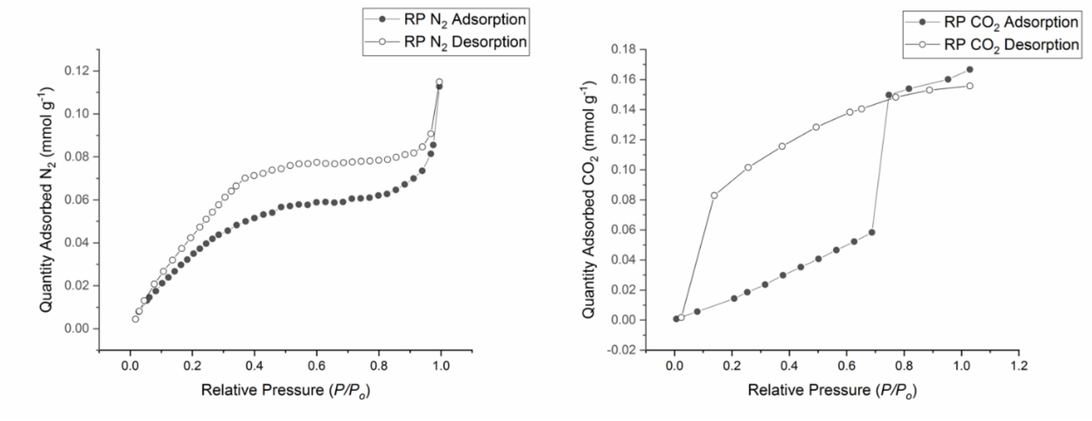

**Figure 16 RP** $N_2$ and $CO_2$ sorption.

# *7 Powder Diffraction Patterns*

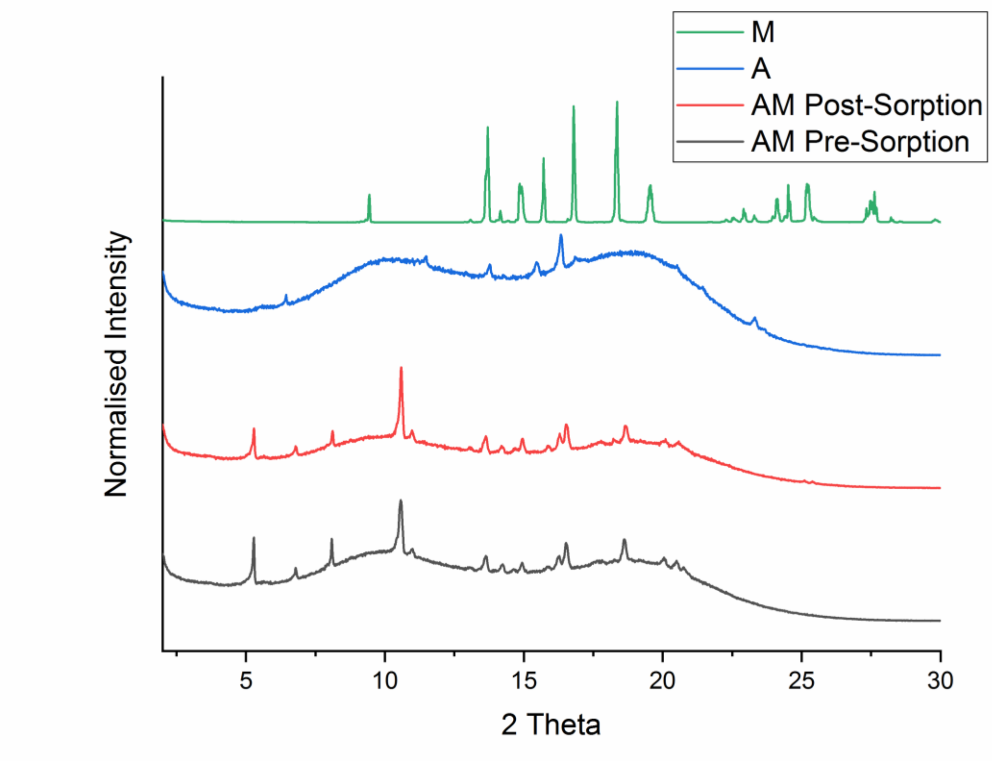

**Figure 17** Powder patterns for **AM**, **A** and **M**.

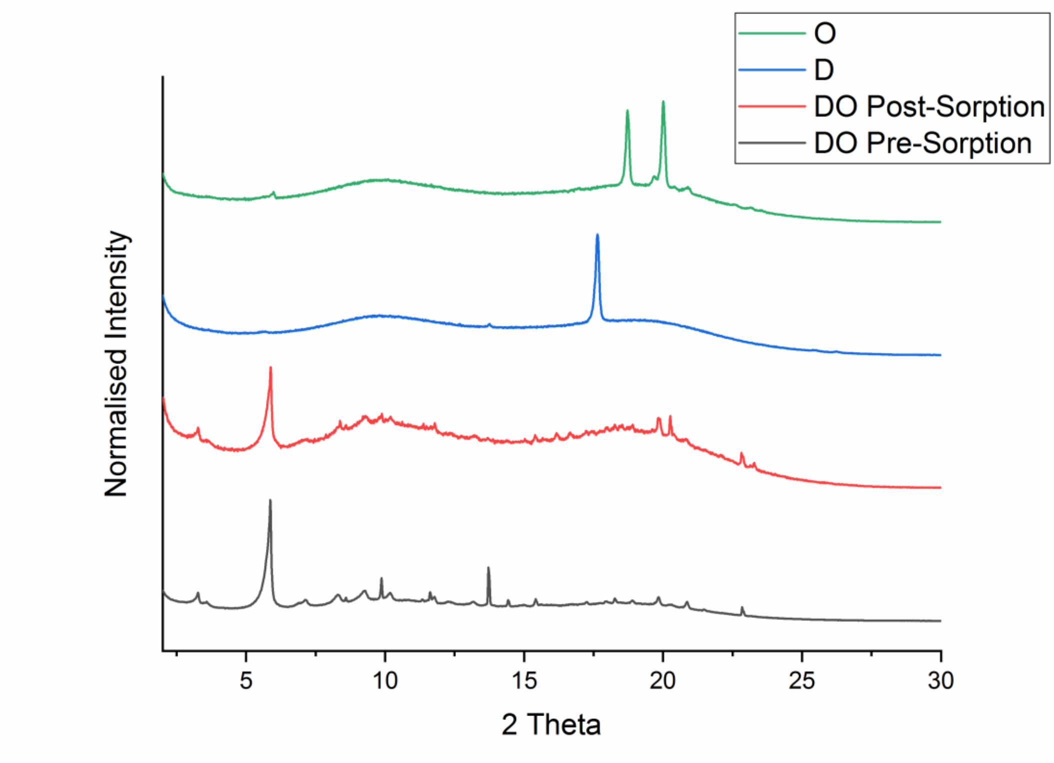

**Figure 18** Powder patterns for **DO**, **D** and **O**.

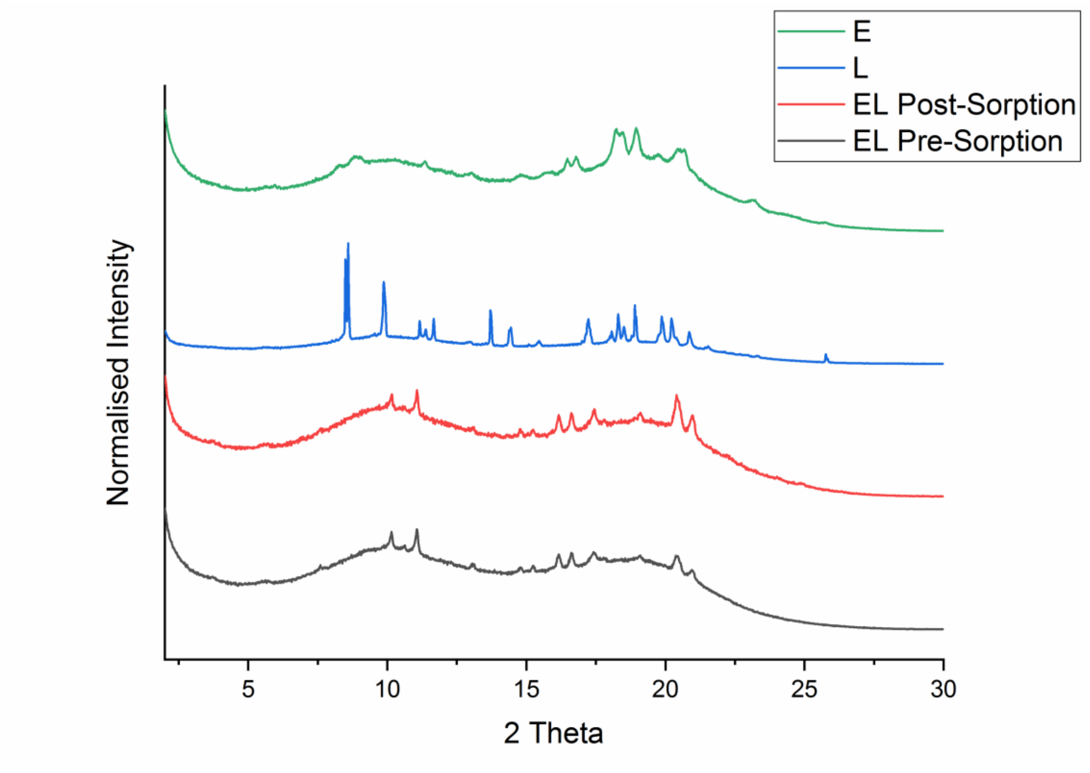

**Figure 19** Powder patterns for **EL**, **E** and **L**.

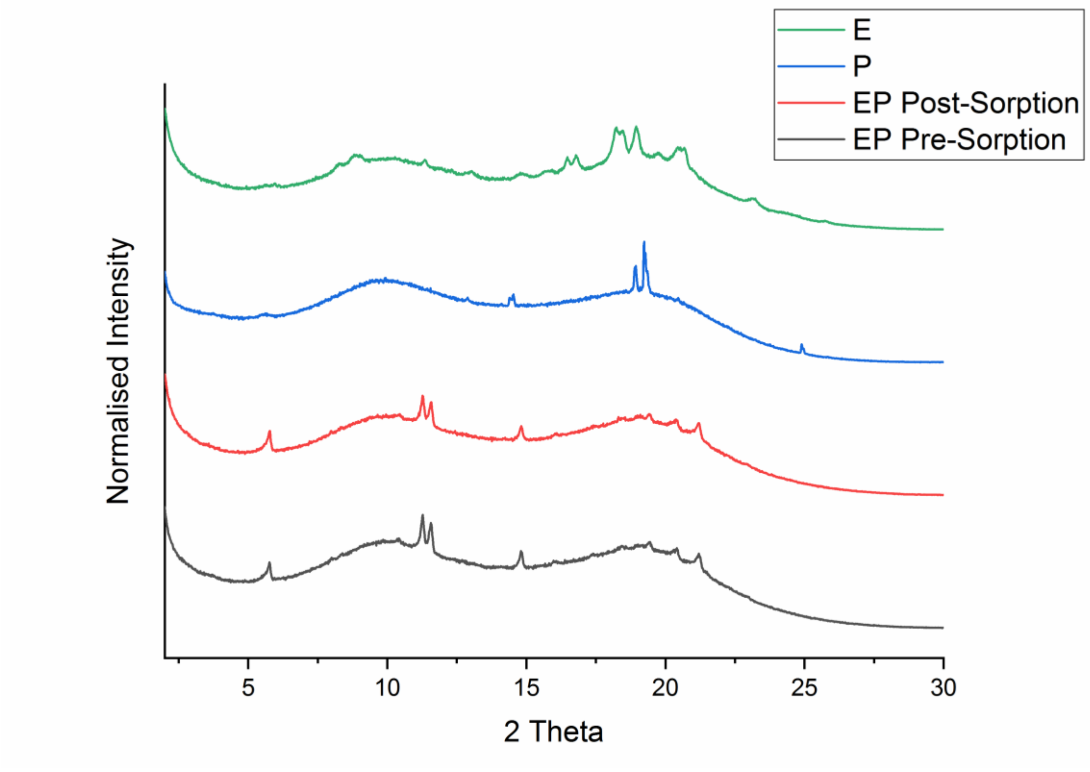

**Figure 20** Powder patterns for **EP**, **E** and **P**.

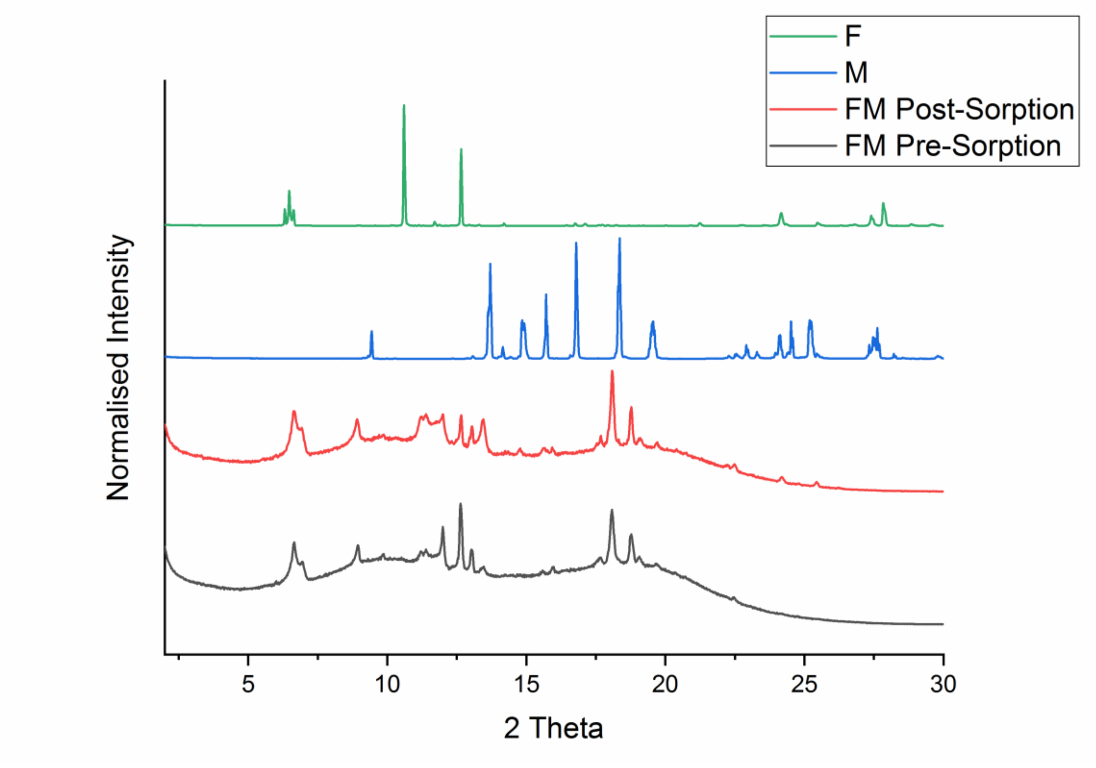

**Figure 21** Powder patterns for **FM**, **F** and **M**.

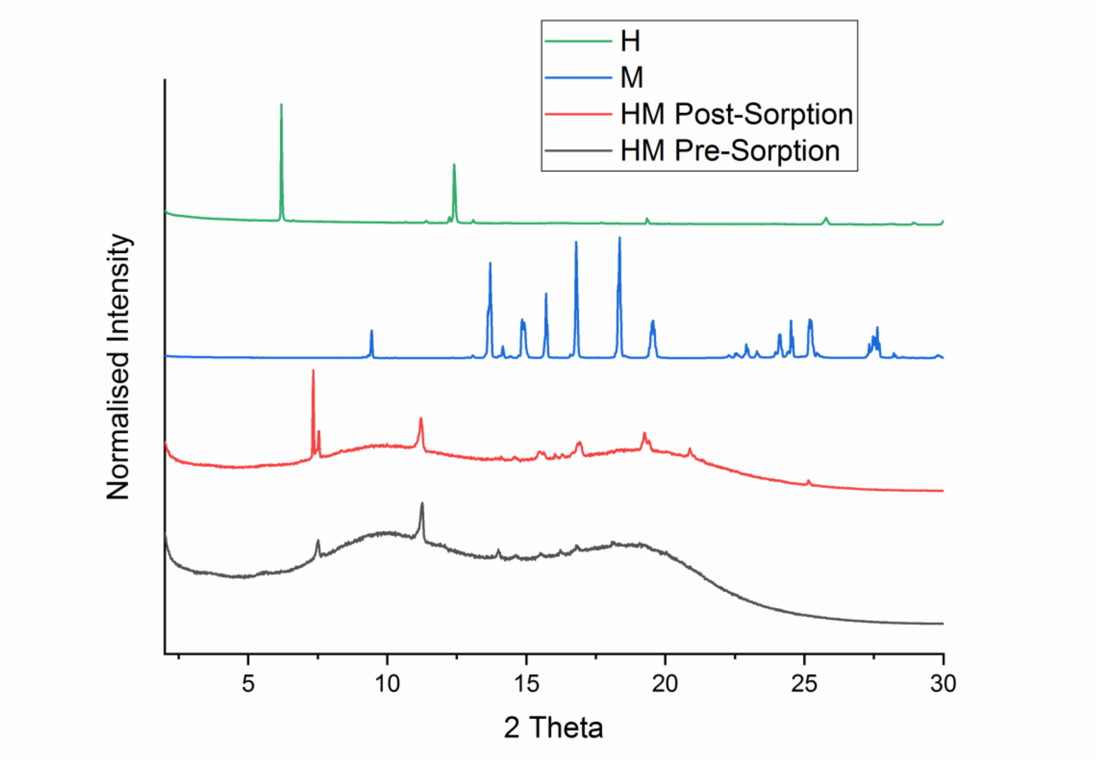

**Figure 22** Powder patterns for **HM**, **H** and **M**.

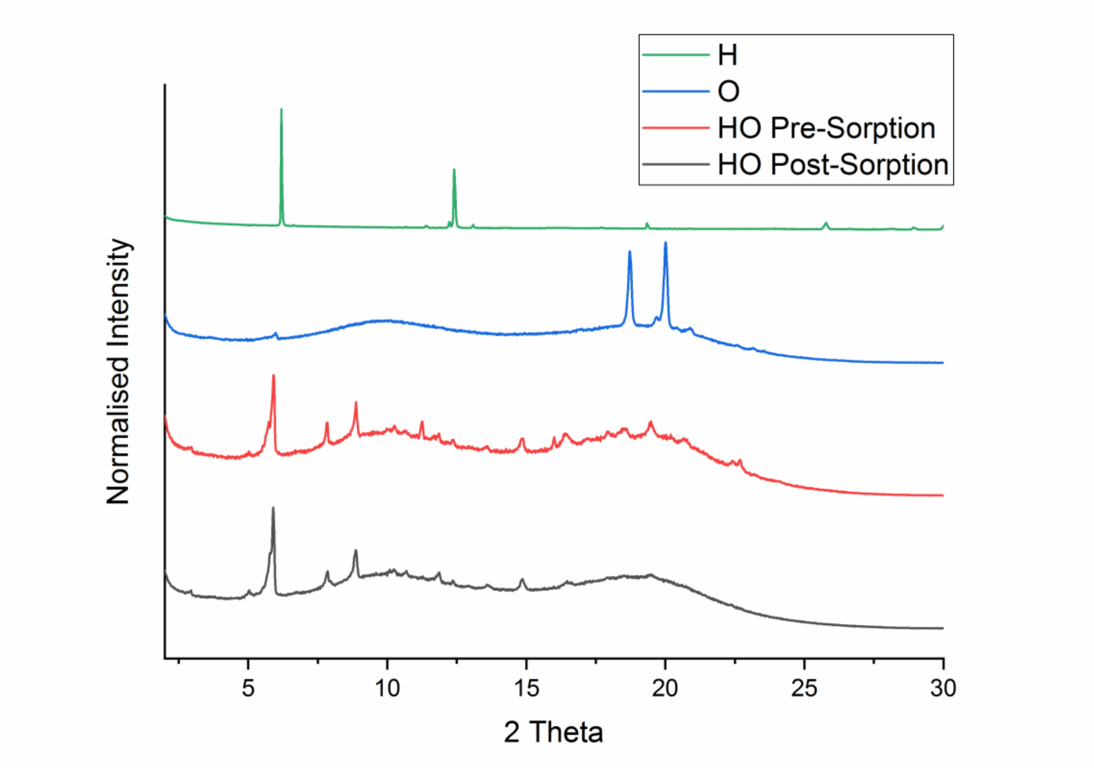

**Figure 23** Powder patterns for **HO**, **H** and **O**.

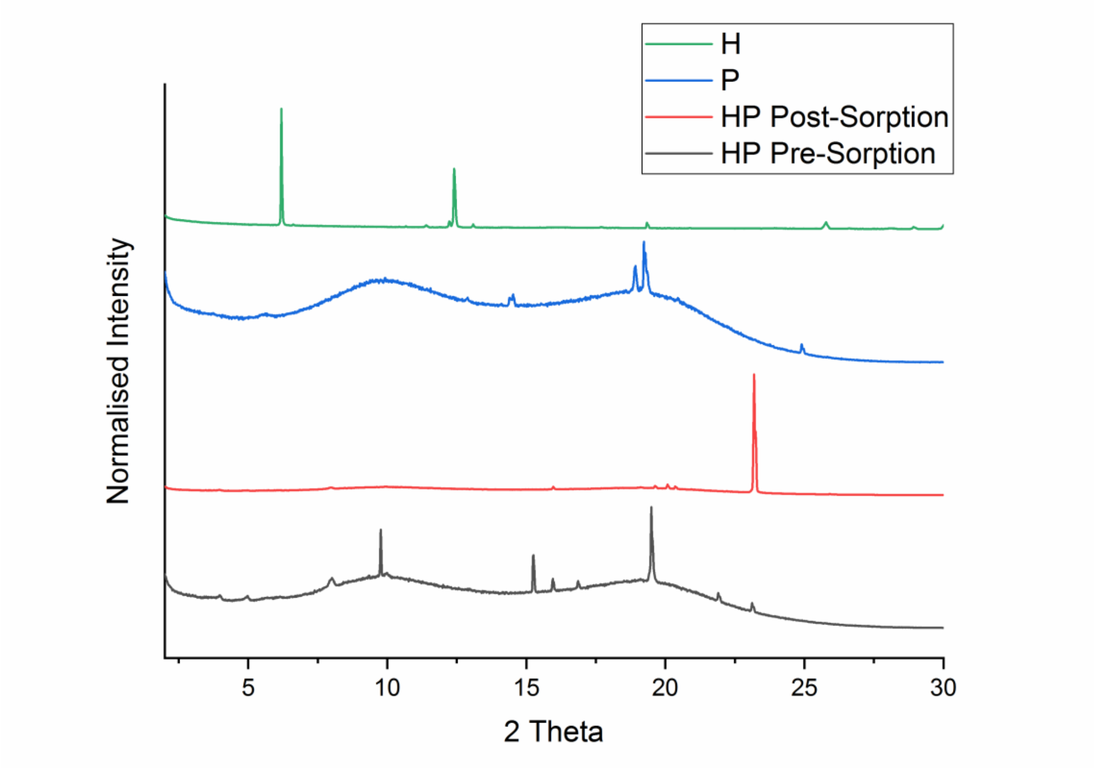

**Figure 24** Powder patterns for **HP**, **H** and **P**.

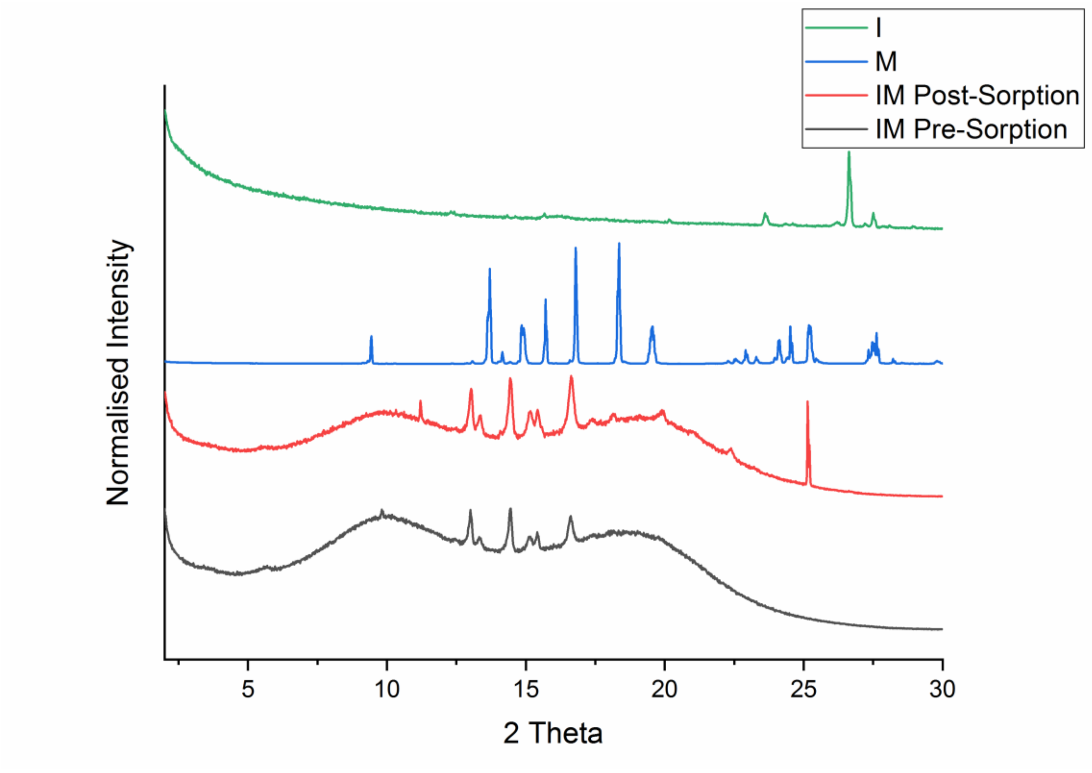

**Figure 25** Powder patterns for **IM**, **I** and **M**.

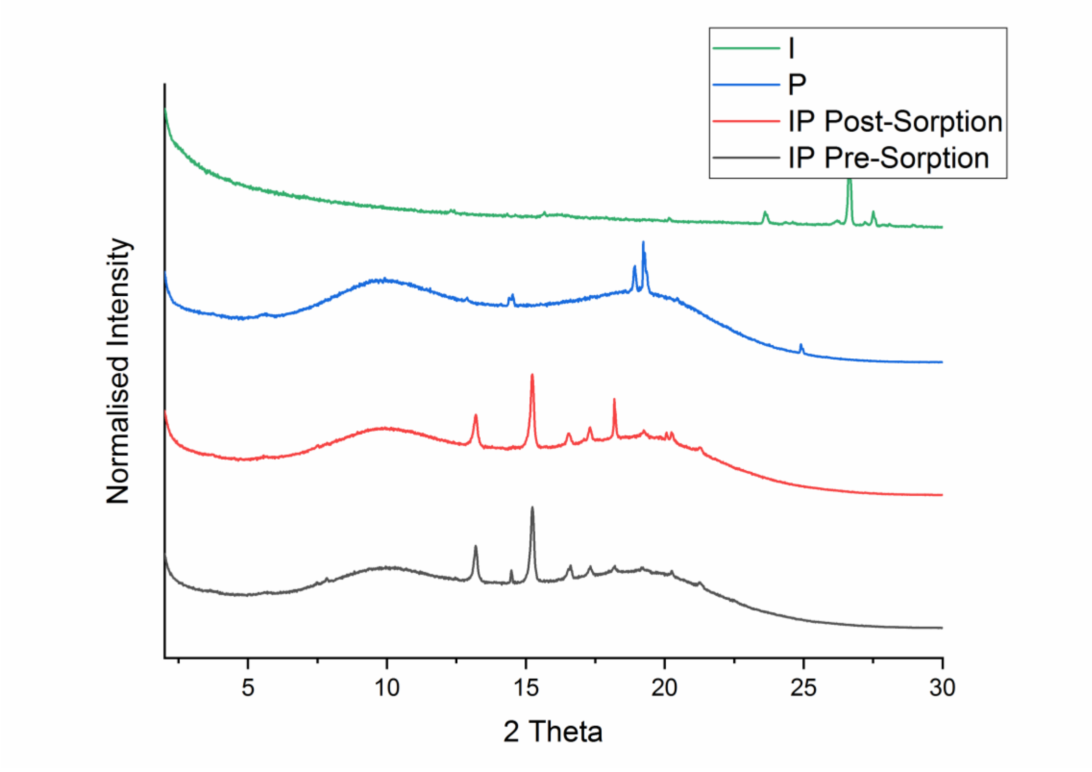

**Figure 26** Powder patterns for **IP**, **I** and **P**.

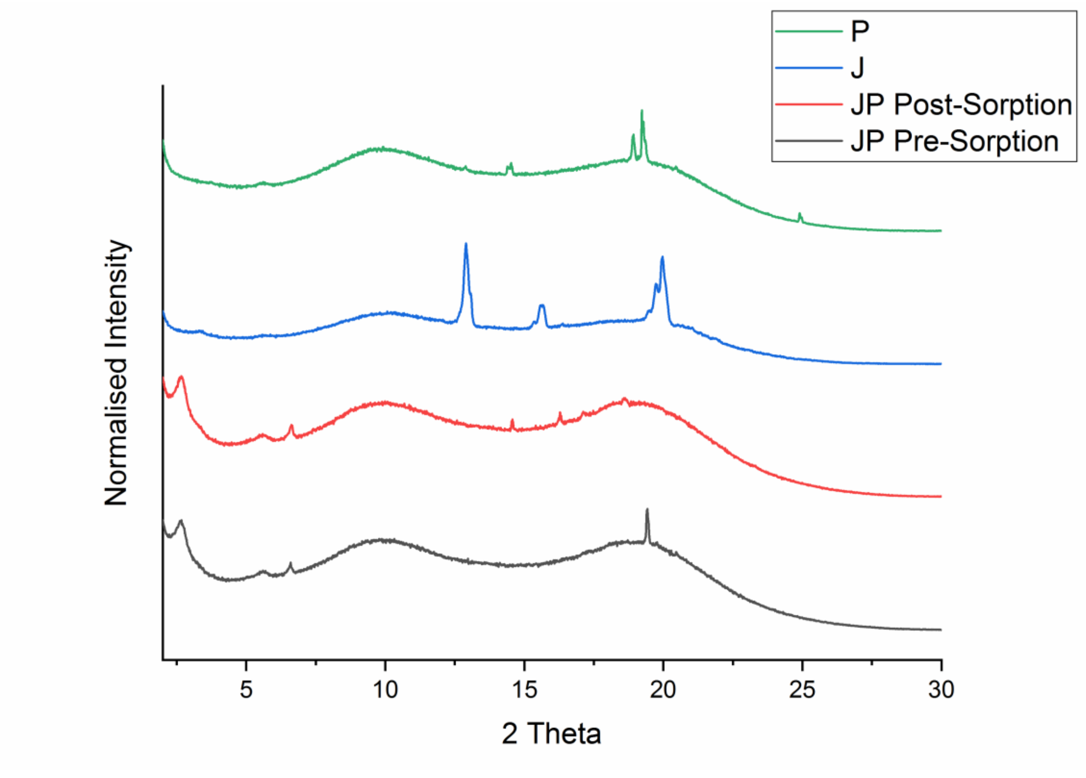

**Figure 27** Powder patterns for **JP**, **J** and **P**.

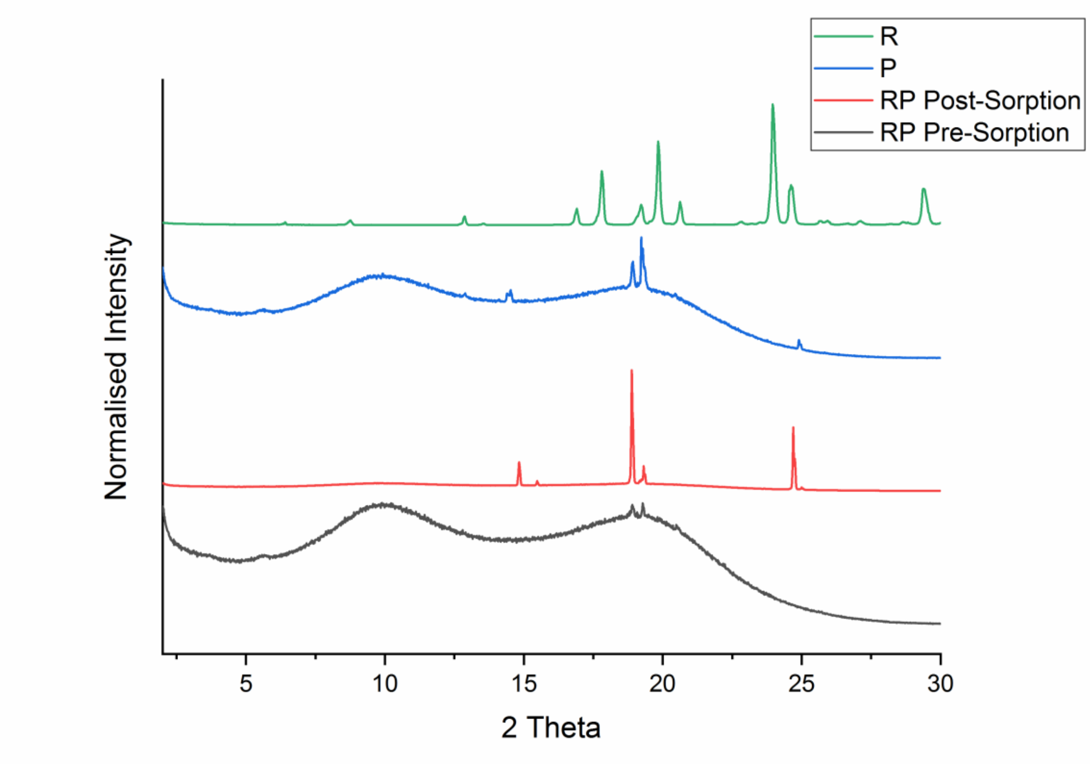

**Figure 28** Powder patterns for **RP**, **R** and **P**.

# Chapter 6

## Conclusions and Future Work

# 1 Conclusions

We have demonstrated it was possible to alter cage topology and geometry from the same pair of precursors. The original cage, **TCC1**$_{[3+6]}$ underwent re-equilibration in solution forming the stoichiometrically twice as large **TCC1**$_{[6+12]}$, with a change in geometry from trigonal prismatic to truncated tetrahedron, and the topology from trigonal prismatic to octahedron. Furthermore, *in silico* analyses provided considerable insight into the cage formation, showing us the formation of energy difference between **TCC1**$_{[3+6]}$ and **TCC1**$_{[6+12]}$ was only 2 kJmol$^{-1}$, hence both existing simultaneously under the same reaction conditions. Experimentally we showed that **TCC1**$_{[6+12]}$ had limited chemical stability, when prep-HPLC was attempted for isolation the resulting material underwent reversal to its constituent components. **TCC2**$_{[3+6]}$ and **TCC3**$_{[3+6]}$ were exposed to the same experimental procedure however there was no evidence of **TCC2**$_{[6+12]}$ or **TCC3**$_{[6+12]}$.

A new high throughput methodology for the discovery of new organic cages was developed using robotics, and furthermore structural studies were performed on these molecules. The studies showed that the cages re-equilibrated dependent on the reaction solvent, **C21**$_{[3+2]}$ was formed preferentially in DCM, whereas a mixture of **C21**$_{[3+2]}$ and **C21**$_{[4+6]}$ in $CHCl_3$. The formation energy for bond in **C21**$_{[3+2]}$ was -10.8 kJmol$^{-1}$, whereas for **C21**$_{[4+6]}$ was -14.1 kJmol$^{-1}$. A new cage topology was also identified, which we have identified as a bridged catenane. **B13** was found from crystallisation, the structure characterised by NMR showed that the cage in solution had a stoichiometry of [4+6], whereas when recrystallised the crystals had a stoichiometry of [8+12], forming an interlocked molecule with a covalent bridge holding them together. This work showed the importance of crystallisation studied in supramolecular chemistry, in particular the discoveries that can be made only through this technique.

Finally, hydrogen-bonded organic frameworks were recrystallised with the aim to combined crystal structure prediction with experimental work and identify potentially new porous polymorphs of known tectons. The results highlighted the importance of hydrogen bonding angles and lengths on the framework structures stability. Comparing **T1** and **T2**, we saw that **T1** had a bond length and angle of 2.897 ad 167.119, whereas **T2** had a shorter bond length of 2.821 Å and a more linear 170.085 °. Hydrogen bonding is strengthened when the bonds are more linear and shorter in length, hence explaining why for **T2** we were able to successfully desolvate **T2**, whereas for **T1** we were unable to isolate a polymorph suitable for gas or guest uptake. Furthermore, we have demonstrated that by using HT methods in order to find new porous materials, identifying two co-crystals, **SA-B**/**AM-P** with a BET surface area of 73.49 $m^2g^{-1}$, and **CA-R/AM-L** 40.69 $m^2g^{-1}$. Despite identifying these porous co-crystals, issues using $CO_2$ as a probe gas proved overwhelming, as multiple hits were found despite showing no potential porosity.

## *2 Future Work*

In Chapter 4, the high throughput method for porous material discovery was introduced, highlighting the benefits of 'trial and error' based screening. This method has proven to be successful, reducing the time taken to identify new HOFs and organic salts which are capable of gas uptake. The next step would be to take forward the two most promising results, **CA-R**/**AM-L** and **SA-B**/**AM-P**, and focus on recrystallisations with alternate stoichiometric equivalents of each precursor. We know from the co-crystal structures **SA-J**/**AM-O** and **SA-J**/**AM-M** that when the original crystallisation were set up, there was a ratio of 1:1.5 acid:amine. Therefore, the next solution would be to consider changing the ratios in order to divert from this ratio and form a potentially more porous materials, generating the clusters seen by Xing *et al.*[1]As well as considering altering the stoichiometry of the stoichiometric ratios, another variable to consider would be solvent changes. It is commonly known that polymorphism is prevalent in organic molecules, shown and discussed throughout. Therefore, recrystallisations in different solvent systems of the precursors could be set up, with the same concept of searching for crystal packing with potentially large pores.

Finally, I focused on commercially available materials in order to gain fast results, without synthesis time factoring into the process. However, the next step which should be considered is to synthesise either sulfonic acid derivatives of rigid molecules such as triptycene or pentiptycene, and co-crystallise these with amines which we have shown have the propensity to co-crystallise and form the porous salts (**Figure 1**).

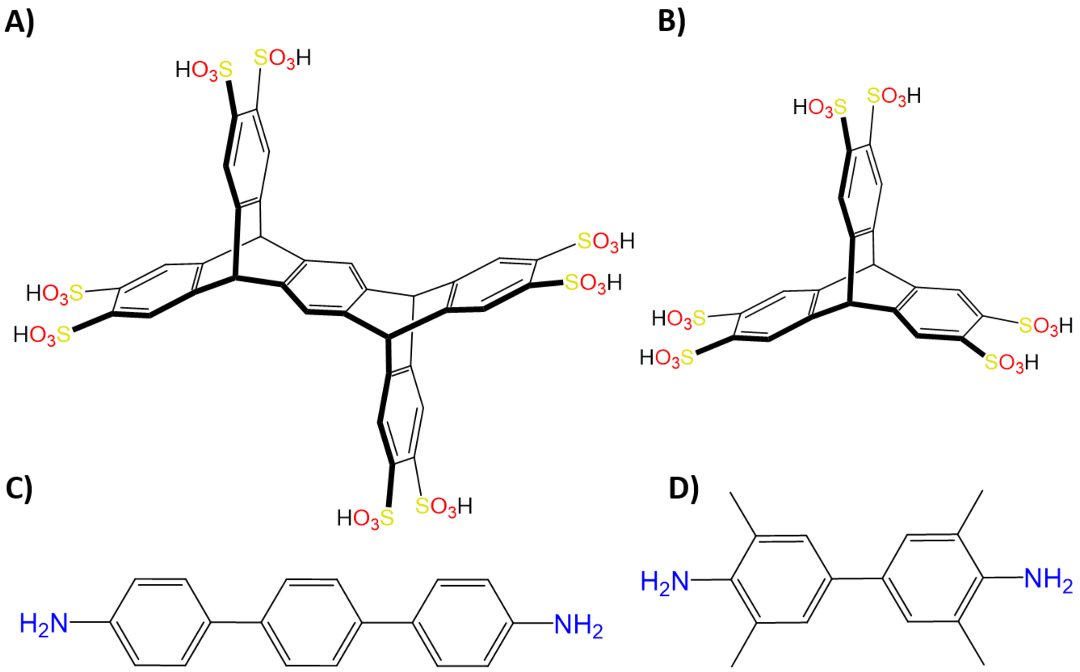

**Figure 1 A)** Octa-substituted pentiptycene; **B)** Hexa substituted triptycene; **C)** 4,4”-diamino-*p*-terphenyl; **D)** 3,3’,5,5’-tetramethylbenzidine.

We have shown that crystal structure prediction and energy-structure-function maps can be used to identify if a molecule has the potential to be porous. Therefore, by using the strategic methods introduced for **T1** and **T2**, and applying them to the preliminary results introduced for **CA-R**/**AM-L** and **SA-B**/**AM-P**, the resulting porous salts would be a vast improvement on the current porous organic salts.[1]

# 3 References

1 G. Xing, T. Yan, S. Das, T. Ben and S. Qiu, *Angew. Chemie Int. Ed.*, 2018, **57**, 5345–5349.